Summer 8-12-2011

NIR-Emissive Polymersomal Markers for Molecular-Level Detection of Metastasis

Wei Qi
University of Pennsylvania, weiqi@sas.upenn.edu

NIR-Emissive Polymersomal Markers for Molecular-Level Detection of Metastasis

Abstract

Noninvasive imaging technologies, capable of visualizing early carcinoma or dormant or latent metastatic tumor cells and evaluating the efficacy of cancer therapies are becoming increasingly important. In this thesis, NIR-emissive polymersomes are engineered for optimal cellular uptake to enable fluorescence-based tumor targeting. A series of benzothiadiazole conjugated porphyrin oligomers with high emission dipole strength and exceptional large quantum yields in the NIR region are synthesized for optimized emissive output would be greatly enhanced. Furthermore, this thesis established for the first time a class of universal chemistry modification methods to directly attach antibody to polymersomes surface with very high antibody coupling efficiency and precise control of antibody density on polymersomes. These antibody conjugated NIR-emissive polymersomes exhibit ideal cell-surface adhesion dynamics and enables future in vivo tracking of labeled tumor cells by NIR fluorescence based imaging. Ultimately, tracking residual disease in vivo requires biodegradable polymersomes. Towards this goal, we fabricated analogous nanoscale NIR-emissive, soft-matter-based vesicles based on already FDA-approved materials poly(caprolactone) (PCL) and poly(trimethylene carbonate) (PTMC) blocks, and involves copolymer synthesis, evaluation of vesicle physical properties, and polymersome functionalization. Finally, a new emissive polymersomes platform is designed by quantitative incorporation of quantum dots into the polymersomes bilayer membranes, featuring a wide range of applications for in vivo diagnostic and drug-delivery applications. In summary, this synthesis developed functionalized nanoscale NIR-emissive polymersomes with optimal fluorescence output and ability to detect limited target cell numbers under clinically relevant diagnostic conditions, and define new tools for the study of metastatic disease.

Degree Type
Dissertation

Degree Name
Doctor of Philosophy (PhD)

Graduate Group
Chemistry

First Advisor
Michael J. Therien

Keywords
NIR imaging, Polymersomes, Functionalization, Targeted delivery, Biodegradable, Nanoparticle incorporation.

Subject Categories
Medicinal-Pharmaceutical Chemistry | Organic Chemistry | Polymer Chemistry

NIR-EMISSIVE POLYMERSOMAL MARKERS FOR

MOLECULAR-LEVEL DETECTION OF METASTASIS

Wei Qi

A DISSERTATION

in

Chemistry

Presented to the Faculties of the University of Pennsylvania

in

Partial Fulfillment of the Requirements for the

Degree of Doctor of Philosophy

2011

Supervisor of Dissertation

Signature _____
Michael J. Therien, Professor of Chemistry

Graduate Group Chairperson

*Signature*_____
Gary A. Molander, Professor of Chemistry

Dissertation Committee

Patrick J. Walsh, Professor of Chemistry
Bradford B. Wayland, Professor of Chemistry
Larry G. Sneddon, Professor of Chemistry

NIR-EMISSIVE POLYMERSOMAL MARKERS FOR MOLECULAR-LEVEL DETECTION OF METASTASIS

ACKNOWLEDGEMENTS

I most graciously thank my advisor, Dr. Michael J. Therien, for the opportunity to work in his first-rated scientific laboratory. He guided me throughout all the difficult times I have both in research and in my life, always providing me with great encouragement and tremendous support. My Ph.D years in this great lab are one of the most joyful days in my life; Mike provided tremendous support for me to try out all my research ideas and introduced me into many fascinating interdisciplinary projects. I have learned a lot of scientific knowledge as well as skills to apply that knowledge in innovative ways. Mike is the most intelligent, generous and kind people I have had the pleasure to work with, I could not ever ask for a better mentor, and I hope to be honored to have your further guidance post-graduation.

I would also like to express my gratitude to members of my thesis committee, Dr. Patrick J. Walsh, Dr. Larry G. Sneddon and Dr. Bradford B. Wayland for your time, commitment, and many fruitful discussions and suggestions.

Thanks also to all the members, past and present, of the Therien lab which has such a great diversity of wonderful people. I am grateful for your friendships, ideas, and support. I especially want to thank: Dr. kimihiro susumu, for teaching me the necessary synthetic skills to succeed in the lab and in science; Dr. Guizhi Li, for all your help on my starting of the polymersomes project and being such a great friend; Dr. Paul Frail, Dr. Tae-Hong Park, and Dr. Pravas Deria, for providing some of the most engaging scientific discussions in all types of unexpected research problems; Dr. Louis Sinks, Jae-Hong Park and Ian Staton, for working with my porphyrin compounds; Dr. Jennifer Ayres and

Joshua Stecher, for working with me on upconverting nanoparticle materials; Dr. Peter Ghoroghchian, Dr. Ying Ma, Dr. Diane Fels and Dr. Gabor Kemeny for all the inspiring and creative thoughts on the polymersomes project; and finally, Christina Hofmann, who will continue to further the polymersomes field, I wish you the best to complete your studies. Especially, I am very grateful to have you read and helped me editing my dissertation. Thank you so much for your time and effort, I really appreciate it!

Other people I must thank for their friendship and support are the collaborators that provided me instrumentation help and training. Dr. Michelle Gignac, I would not have succeeded in running the Cryo-TEM experiments without you. Dr. Michael Cook, thanks for all your insight, time and energy to work with me on the flow cytometry. Dr. Sam Johnson and Dr. Yasheng Gao, thanks for your great help to make me become a laser confocal microscopy expert!

Finally, I would like to express my profound admiration and love to my family for their unconditional support during my Ph.D years. My dad Yichun Qi, who is a chemistry teacher and experienced biological chemist, inspired my initial interest in chemistry. He taught me to read the periodic table of elements in such an interesting way that I was able to memorize all the chemical elements when I was 10 years old. He is the most influential people in my life, and I thank him for the person who I am today. I also would like to profess my inestimable acknowledgements for the endless support, encouragement and unbound love from my mother, Xianqiong Cheng, you always believed in me even when I faced doubt. Finally my wonderful husband, Yang Yang, for your love, patience and steadfast companionship, you have always been my hero since we met each other 15 years ago. I would not have been able to accomplish this without you.

ABSTRACT

NIR-EMISSIVE POLYMERSOMAL MARKERS FOR MOLECULAR-LEVEL DETECTION OF METASTASIS

Wei Qi

Michael. J. Therien

Noninvasive imaging technologies, capable of visualizing early carcinoma or dormant or latent metastatic tumor cells and evaluating the efficacy of cancer therapies are becoming increasingly important. In this thesis, NIR-emissive polymersomes are engineered for optimal cellular uptake to enable fluorescence-based tumor targeting. A series of benzothiadiazole conjugated porphyrin oligomers with high emission dipole strength and exceptional large quantum yields in the NIR region are synthesized for optimized emissive output would be greatly enhanced. Furthermore, this thesis established for the first time a class of universal chemistry modification methods to directly attach antibody to polymersomes surface with very high antibody coupling efficiency and precise control of antibody density on polymersomes. These antibody conjugated NIR-emissive polymersomes exhibit ideal cell-surface adhesion dynamics and enables future in vivo tracking of labeled tumor cells by NIR fluorescence based imaging.

Ultimately, tracking residual disease in vivo requires biodegradable polymersomes. Towards this goal, we fabricated analogous nanoscale NIR-emissive, soft-matter-based vesicles based on already FDA-approved materials poly(caprolactone)

(PCL) and poly(trimethylene carbonate) (PTMC) blocks, and involves copolymer synthesis, evaluation of vesicle physical properties, and polymersome functionalization. Finally, a new emissive polymersomes platform is designed by quantitative incorporation of quantum dots into the polymersomes bilayer membranes, featuring a wide range of applications for in vivo diagnostic and drug-delivery applications.

In summary, this synthesis developed functionalized nanoscale NIR-emissive polymersomes with optimal fluorescence output and ability to detect limited target cell numbers under clinically relevant diagnostic conditions, and define new tools for the study of metastatic disease.

Table of Contents

List of Tables

List of Figures

CHAPTER 1. Introduction to Molecular-Level Detection of Metastasis and the Specific Aims of the Thesis Dissertation

1.1. Molecular Imaging Sciences

1.1.1. Concept of Molecular Biology and Imaging

Molecular imaging is a new discipline that combines molecular biology and *in vivo* imaging. Molecular imaging utilizes new molecular agents with traditional imaging tools for the visualization, characterization, and measurement of biological processes at molecular and cellular levels in the body. Molecular imaging differs from traditional imaging in that new biomarkers are used as imaging probes to help image particular targets or pathways. Biomarkers interact with their surroundings and in turn produce the image according to molecular interactions occurring within the area of interest. This process has significant advantages over the previous imaging methods which primarily imaged differences in qualities such as density or water content. This ability to image fine molecular and cellular pathways *in vivo* opens up an incredible number of exciting possibilities for medical applications, including earlier detection and characterization of metastasis by visualizing the cellular function and following up the molecular process in living organisms without perturbing them. As a result, we will have a better understanding of biology pathology, prospective evaluation of treatment, and basic pharmaceutical development. The multiple and numerous potentialities of this field are applicable to the diagnosis of diseases such as cancer, and neurological and cardiovascular diseases. This technique also contributes to improving the treatment of

these diseases by optimizing the pre-clinical and clinical tests of new medication. They are also expected to have a major economic impact due to earlier and more precise diagnosis. Furthermore, molecular imaging allows for quantitative tests, provides important insights for diagnosis, prognosis, and therapeutic design.

1.1.2. Advantages of Optical Imaging

A number of imaging modalities have current been used in clinical diagnostics, including image via means of x-ray (x-ray computer tomography or CT), sound (ultrasound), magnetism (magnetic resonance imaging or MRI), radiolabeled molecules that produce signals by means of radioactive decay by nuclear imaging (positron emission tomography or PET, and single-photon emission computed tomography or PPECT), and light (optical techniques of bioluminescence and fluorescence).The transparency of date reduction to form the desired images by using these techniques are shown in **Figure 1.1**.
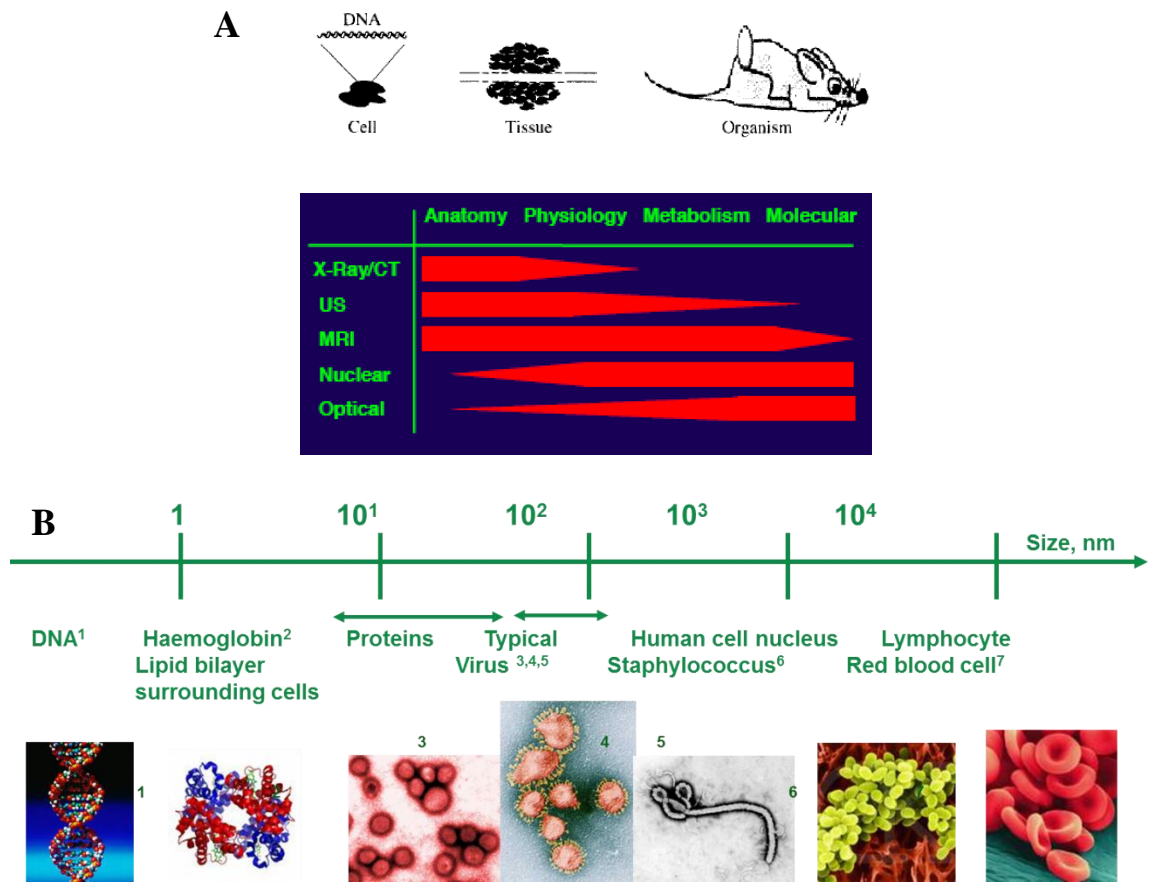
Figure 1.1 A. Comparison of the utility of several commonly available radiological imaging modalities for anatomical, physiological, and molecular-level investigation. CT - x-ray computer tomography; US - ultrasonography; MRI - magnetic resonance imaging; Nuclear - nuclear imaging; Optical - optical imaging. B. Size range of a few common biology molecules.

Therefore, among these different strategies, only MRI, nuclear imaging (PET or PPETC), and optical imaging are suitable for molecular-level investigations. These imaging technologies differ in five main aspects: (1) spatial resolution; (2) depth penetration; (3) sensitivity (4) availability of injectable/biocompatible molecular probes; and (5) tissue safety and facility of use (time and cost), as described in **Table 1.1**. Considering the key advantages and disadvantages of these main available imaging modalities, optical imaging holds the most promise for molecular imaging.

Optical molecular imaging offers significant advantages to nuclear imaging and MRI's capabilities for life science and pre-clinical application. Nuclear imaging requires the expensive process of creating radioisotopes, delivering these radioisotopes for use within a very limited time frame to avoid decay, and the use of a very expensive instrument to examine the results. MRI has the advantages of having very high spatial resolution and has been widely used at morphological imaging and functional imaging. However, MRI has a low sensitivity compared to other types of imaging due to the fact that the difference between atoms in the high energy state and the low energy state in MRI is very small. Therefore, MRI imaging normally requires long acquisition times of limited regions of interest.[1] This means a priori information is necessary to find and image the cells of interest, and whole body imaging is not feasible for MRI.

In contrast to both MRI and nuclear imaging which started in the clinic and were adapted for small animal studies, optical imaging emerged from techniques already established at the molecular and cellular level. The development of fluorescence-based optical imaging methods that utilize exogenous fluorescent dyes has gained a great deal of attention. When introduced within the body, excited with laser diodes, the fluorescent

dyes emit photons that can be detected externally by photomultiplier tubes (PMTs) or with highly sensitive charge- coupled device (CCD) cameras.[2-13] Optical imaging with fluorescent light is particular attractive as the detectors are highly sensitive towards the emitted photons and, hence, require only small amounts of contrast agents (nM) as compared to with MR imaging (mM). Besides, the instruments and probes for optical imaging are generally much cheaper, and can be made more mobile, when compared to those for MRI and nuclear imaging.[14] Further, emission of low-energy photons is concentration-dependent, occurs on the time scale of the fastest molecular processes, and is inherently dependent upon the emissive environment of the fluorescent agent.[9, 10, 14, 15] At shallow depths, picomole quantities of the light emitting source can be detected. There is also no harmful radiation or strong electromagnetic fields, thereby making it a safe method for both the operator and study subjects.[5-7, 12, 16] Image acquisition times are very fast, enabling multiple animals to be imaged in one session. Notely, optical imaging can detect diseases at a very early stage, long before other imaging modalities by allowing nearly real-time monitering of cellular activity. It therefore holds enormous promise for faster treatment of disease and better therapeutic outcomes. Longitudinal studies are easily performed without limitations. Finally, the equipment is very affordable for universities in comparison to the nuclear and MRI instruments.

As a result, fluorescence-based optical imaging is the overall superior modality for small animal imaging research as its enables highly sensitive, safe, and affordable detection of dynamic molecular-level events, with only minimal losses in spatial resolution and signal attenuation due to short optical path lengths.

Table 1.1 Comparison of different molecular imaging approaches.

Imaging Technique	EM Radiation Spectrum	Advantages	Disadvantages
CT	X-rays	Bone and tumor imaging; anatomic imaging	Limited 'molecular' applications; limited soft tissue resolution; radiation
Ultrasound	High-frequency sound	Real time; low cost	Limited spatial resolution; mostly morphologic although targeted microbubbles under development
Nuclear imaging	gamma rays	Most established molecular imaging method; high sensitivity (eed μM contrast agent); many molecular probes available; can image multiple probes simultaneously; may be adapted to clinical imaging systems	Low spatial resolution (mm); radiation of subject; expensive equipment
MRI	Radio waves	Highest spatial resolution (μm); combines morphologic and functional imaging.	Relatively low sensitivity; long scan and post-processing time; Need mass quantity (mM) of contrast probes.
Optical imaging	Visible light or near-infrared	Highest sensitivity (need only nM contrast agent); quantitative analysis with high throughput; safe, quick, easy, low cost and mobile equipment	Minimal losses in spatial resolution and signal attenuation due to short optical path lengths.

1.2. NIR Emissive Polymersomes as Optical Probes for *in vivo* Imaging

1.2.1. NIR Fluorescence for *in vivo* Optical Imaging

The goal for optically based method is to collect light emission in a spatially resolved manner. The energy (E) of each photon of light is inversely proportional to its wavelength (λ) according to the relationship, $E = h\lambda$, where h is Planck's constant. The penetration of photons through a material such as the tissues in the human body is highly dependent on the wavelength, or the energy. *In vivo* imaging with visible fluorophores is inherently limited to very superficial tissue depths as a result of significant light scattering and optical absorption. The main absorbing molecules in the tissue include water, hemoglobin, and deoxyhemoglobin. Absorbance as a function of wavelength for each of these molecules is depicted in **Figure 1.2**. With increasing wavelengths, light scattering decreases appreciably and photon absorption of hemoglobin, and deoxyhemoglobin lessens, approaching a nadir over the near-infrared spectrum (600 - 1000 nm). Therefore, fluorescence-based imaging in this near-infrared spectral has outstanding signal-to-noise ratios (SNR) due to minimum interference from tissue autofluorescence, as seen in **Figure 1.3**. As a result, near-infrared optical imaging can prospectively be used to resolve molecular events through deep tissue volumes at depths of up to 12 cm.[14] Realization of the full potential for fluorescence-based *in vivo* imaging will be dependent upon the design of contrast agents that both absorb and emit in NIR.[5, 7, 9, 11, 17]
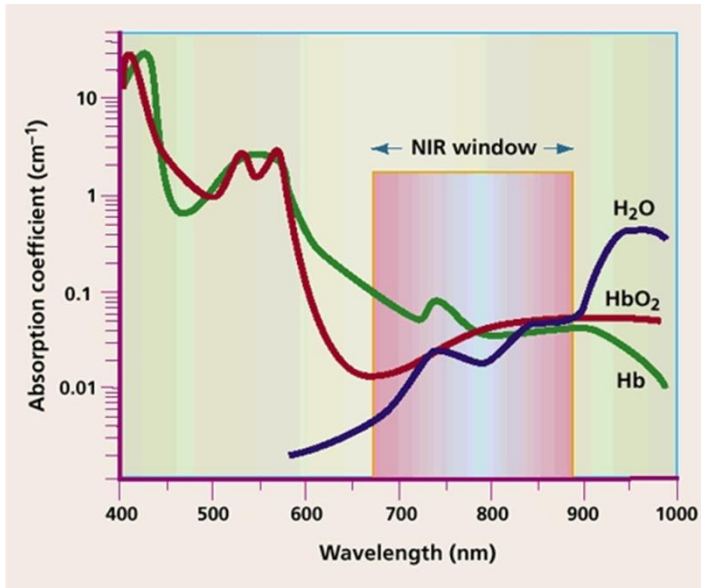
Figure 1.2 The NIR window is ideally suited for *in vivo* imaging because of minimal light absorption by hemoglobin (<650 nm) and water (>900 nm).
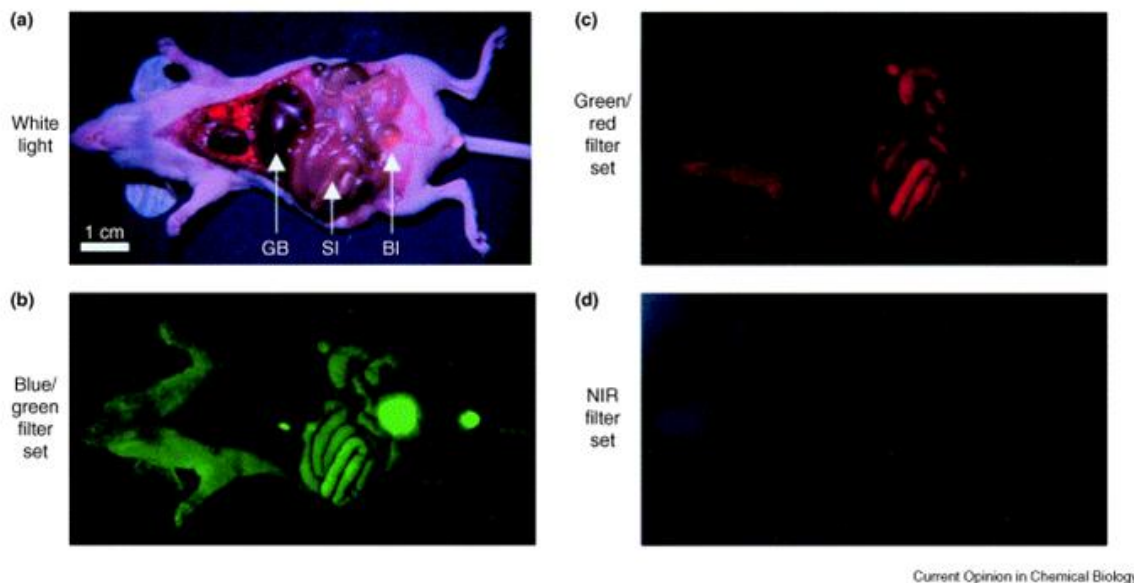
Figure 1.3 Wavelength-dependent autofluorescence of vital organs and bodily fluids.

(a) Immediately after sacrifice, the viscera of a hairless, athymic *nu/nu* mouse were exposed. Tissue autofluorescence was then imaged using three different excitation/emission filter sets: **(b)** blue/green (460–500 nm/505–560 nm); **(c)** green/red (525–555 nm/590–650 nm); and **(d)** NIR (725–775 nm/790–830 nm). The fluence rate provided by each filter set was adjusted to 2 mW/cm^2. To compensate for differences in emission filter wavelength width and camera sensitivity, exposure times were adjusted accordingly. Fluorescence images have identical normalization. For orientation, the white light color image of the animal is shown in (a). Arrows mark the location of the gallbladder (GB), small intestine (SI) and bladder (Bl).[18]

1.2.2. NIR Fluorescence Imaging Probes

The earliest NIR imaging applications utilized fluorochrome indocyanine green (ICG) for the non-invasive detection of tumors in both animals and patients.[5] ICG is a small molecule (M_w = 775 g/mol) that emits NIR light at 800 nm upon optical excitation at 780 nm.[19] It exhibits strong albumin binding and shows preferential uptake and retention in tumors as a result of increased vascular permeability through surrounding leaky blood vessels.[20] However, ICG possesses a short circulation half-life due to its susceptibity to the body's first-pass metabolism, resulted in rapid clearance from the blood.[21] In addition, ICG's spectra are altered[22] and its quantum yield significantly decreases when bound to albumin.[23] In order to improve these optical characteristics and to augment ICG's tumor uptake and contrasting capabilities, dye derivatives that possess better water solubility, decreased protein binding, and more favorable pharmacokinetics have been synthesized.[23, 24] In general, ICG and its derivatives offer basic physiological information such as tissue perfusion and accumulation effects with no additional molecular information.

The energy gap law states that as the energy difference between a fluorophore's ground and excited state decreases, non-radiative decay pathways increasingly dominate its excited state relaxation.[25] As a result, there is a relative small number of organic-based NIR fluorophores, while the existing ones such as ICG and derivatives often lack the ideal properties for generating strong fluorescent signals though deep tissue sections, necessary for both large animal and clinical imaging applications.

One alternative strategy to solve the problems associated with NIR imaging with organic fluorophores is to use inorganic semicondutor nanoparticles (i.e. quantum dots)

Quantum dots are nanocrystals with a core/shell structure comprised of transition metals (e.g. Cd, Se, S, and/or Zn) surrounded by a water-soluble organic coating. [3, 26-29] By controlling the size of quantum dots, the band gap can be adjusted and enables tuning of its narrow fluorescence emission band (25-35 nm) with considerable accuracy. In addition to large extinction coefficients and high fluorescence quantum yields, NIR-emissive quantum dots also possess high photobleaching thresholds.[30] Further, the ready commercial availability of these agents offers exciting opportunities for detection of molecular targets both *in vitro* and *in vivo*.[3, 31-33] However, quantum dots tend to aggregate in aqueous solution, thereby losing their fluorescence.[34] In addition, quantum dots are normally constructed from toxic elemental materials,[35] and the relatively large sizes of their NIR compositions are too large to be cleared via renal filtration, resulting in high fluorescence background noise and increased potential for *in vivo* toxicity.[36]

1.2.3. Novel NIR Emissive Polymersomes

The ideal NIR agent should possess: (1) Large NIR absorption extinction coefficients; (2) High NIR fluorescence quantum yields; (3) High photo-bleaching thresholds; (4) No photo-based cellular toxicity; (5) Good water solubility; (6) Safe and complete *in vivo* clearance. Towards this goal, lots of effort has been devoted to NIR emissive nanocarriers as fluorescence probes, as displayed in **Figure 1.4**.[37]
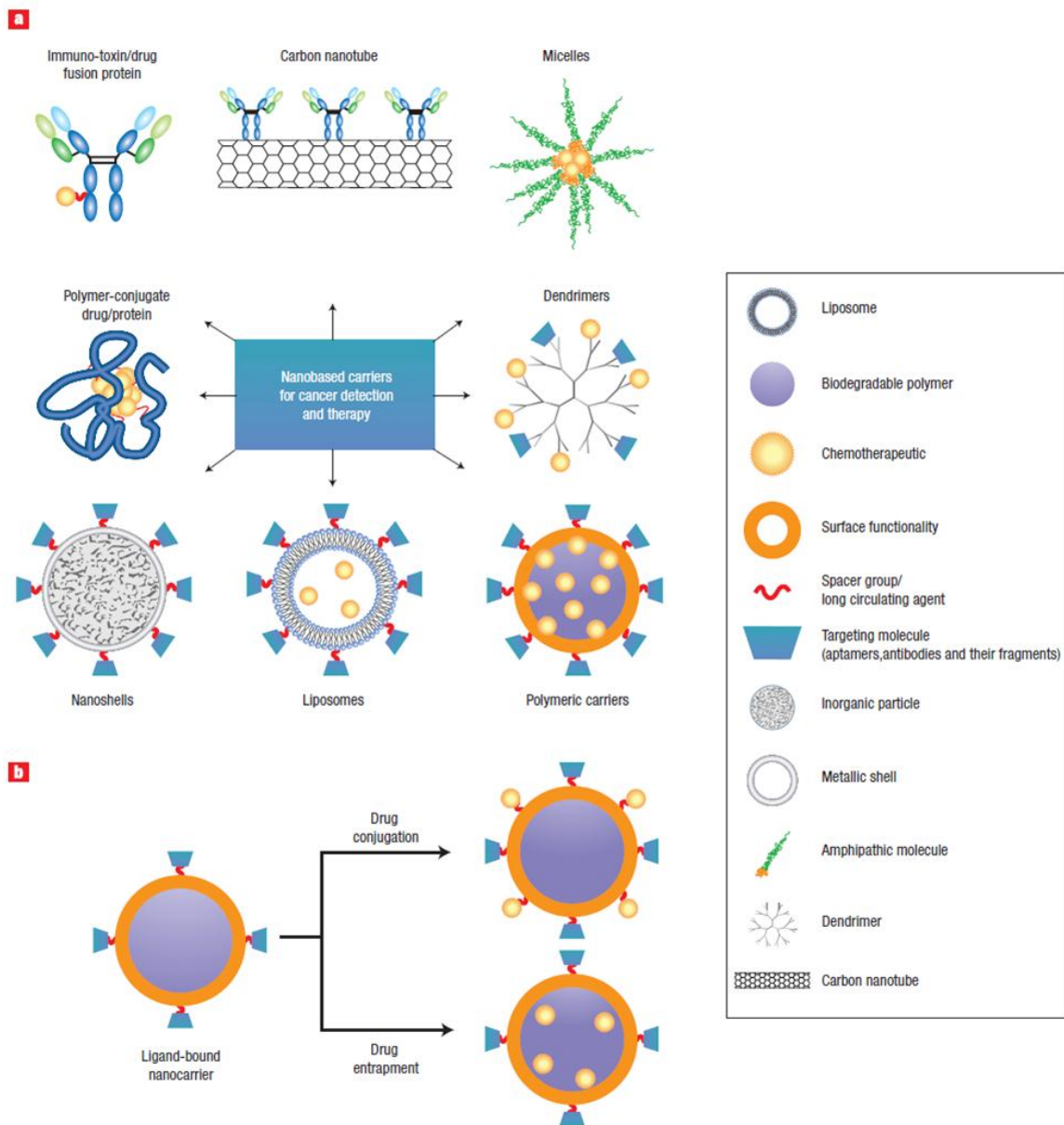
Figure 1.4 a, A whole range of delivery agents are possible but the main components typically include a nanocarrier, a targeting moiety conjugated to the nanocarrier, and a cargo (such as the desired chemotherapeutic drugs). **b**, Schematic diagram of the drug conjugation and entrapment processes. The chemotherapeutics could be bound to the nanocarrier, as in the use of polymer–drug conjugates, dendrimers and some particulate carriers, or they could be entrapped inside the nanocarrier. [37]

Nanocarriers have been classified based on their physical forms to liposomes, polymersomes, microspheres, nanoparticles and etc. Among all these different types of nanocarriers, our lab focused on developing self-assembling polymeric vesicles housing porphyrin-based NIR fluorophores in the hydrophobic bilayer.[38-45] There are significant advantages of using this porphyrin incorporated NIR emissive polymersomes over quantum dots or other types of emissive nanocarries.

Porphyrin is an organic molecule containing four pyrrole (C_4H_5N) rings. The heme structure of hemoglobin is an example of a porphyrin in biology. Nitrogen atoms of porphyrin molecules coordinate to complex with metals such as iron by hemoglobin. By synthesizing porphyrin macromolecules based on conjugating multiple zinc binding porphyrin chromophores together, we can tune their spectral properties including excited-state absorptivity, NIR fluorescence, and achieve high quantum yields in the near-infrared regime.

The most important polymersome feature with regard to fluorophore incorporation is the thick hydrophobic membrane core for incorporation of a large amount of fluorescent contrast agents. For example, the 800 nm NIR dye porphyrin trimer (PZn_3) is a nanometric macromolecule at 3.2 nm in length[46] which is too large for incorporation into liposome membranes.[39] Polymersomes easily accommodate PZn_3 with little change to the fluorescence spectral properties or polymersome mechanical properties. Intermolecular fluorophore quenching is minimized by using high polymer to porphyrin ratios 40:1.

13

Properties of polymersomes which make them optimal delivery vehicles also include the 100% hydrophilic, non-immunogenic PEGylated surfaces with well-proven shielding capacity against protein opsonization,[47] as well as the tunable size from 10 μm to 50 nm in diameter, lead to longer *in vivo* circulation times in comparison to liposomes, the biological counterpart to polymersomes.

In addition to housing fluophores, the vesicular nature of polymersomes makes them adaptable for making multifunctional reagents. These polymer vesicles are multifaceted with mechanically robust membranes, have an ability to sequester both hydrophobic and hydrophilic reagents. Therefore, a second imaging contrast agent could be encapsulated into the aqueous center yielding a dual modality agent. Alternatively, drug can be loaded into the hydrophilic core to combine drug delivery with *in vivo* monitoring of vesicle biodistributions. Attaching receptor ligands on the PEO brush would provide in vivo targeted vesicles to the complimentary receptor for diagnostic purposes. Finally, conjugating tumor targeting antibodies to the exterior brush of the polymersomal nanoscale vesicles would enable cellular uptake and effectively generate NIR-emissive cells.

1.3. Principles of Targeted Delivery

1.3.1. Advantages of Targeted Delivery

The development of successful targeting agents will have dramatic impacts for a number of medical applications, particularly the diagnostic capabilities of imaging agents and improving the specificity of highly toxic drugs used to treat diseases.[48] By far the greatest benefits occurs with the use of chemotherapeutics to treat cancer. Currently, general protocols for the treatment of cancer rely on administering chemotherapeutic

agents as either single agents or in combination with other drugs. Frequently, the use of novel therapeutics in medicine is limited by the lack of efficiency in delivery of these therapeutic agents to the target organs. After a therapeutical agent is administered to the body, it undergoes even bio-distribution throughout the body. In order to reach the therapeutical site, these agents have to cross several biological barriers in the body such as organs, tissues, cells etc., where these agents could be adsorbed, metabolized or excreted out of the body.[49-51] Therefore, to increase the effectiveness of drugs, the doses for these agents are, in most instances, administered at the drug's maximum tolerated dose. The unfortunate impact of treating at such high doses is the undesirable side effects which can be life-threatening. Therefore, most chemotherapeutic agents exhibit very narrow therapeutic windows due to the drug toxicity and poor therapeutic activity at nontoxic doses.

Targeted drug delivery can address the above problems by localizing drugs to a specific target site to provide a major advancement for anti-cancer drug therapy, as it will allow for more effective treatments to be given at doses that are better tolerated. During the last three decades there has been intense effort directed towards the development of targeted drug delivery systems to efficiently transport the drug to its therapeutical site by the appropriate choice of carrier, route, and target. The use of a carrier system for delivering drugs to the body provides several opportunities for achieving the goal of drug targeting. Some potential advantages of targeted drug delivery are: (a) Smaller amounts of drug dosages and facilitation of administration; (b) Maintenance of constant drug levels in the therapeutical range; (c)Reduction of drug toxicity and fewer side effects

when targeted to specific tissues or organs; (d) Protection of biologically active drug molecules like peptides and proteins from degradation during transport.[49, 52]

1.3.2. Passive Targeting vs. Active Targeting

Due to its macromolecular nature, nano-sized delivery vehicles such as micelles, liposomes and polymersomes can accumulate passively in target tissues such as the reticuloendothelial system (RES) through nonspecific uptake by macrophages, or in extravascular disease sites including sites of infection, inflammation, and tumors by a process called the enhanced permeability and retention (EPR) effect.[53, 54] The mechanism of the EPR effect has been summarized according to the following cascade of events: (i) tumor angiogenesis results in hypervasculature, providing increased blood flow to the tumor; (ii) tumor vasculature becomes highly permeable for nano-sized delivery vehicles to escape through blood vessel walls into tissues.; (iii) leaky blood vessels and defective lymphatic drainage, causing nano-sized delivery vehicles to accumulate in them. These factors result in larger carriers having decreased renal clearance, thereby taking longer to be eliminated from the body.[55] Through passive targeting, the nano-sized delivery vehicles accumulation can result in a much larger amount of drug delivery compared to the injection of the same dose of free drug, protecting healthy tissue and greatly reducing adverse side effects.[56, 57] However, the majority of localized nontargeted delivery vehicles do not interact with target cells directly, and the therapeutic activity is a consequence of drug release from nanoparticles within the disease site, a process that does not require direct binding or association with diseased cells.[58]

The facilitation of the binding of the delivery vehicles to target cells through the use of ligands that are capable of recognizing and binding to cells of interest, such as

monoclonal antibodies or peptides, to increase localization of drug and target cell is referred to as active targeting. Active targeting can direct delivery vehicles to tissues where they would not normally accumulate and increasing drug accumulation in the desired tissues and organs.[59] Active targeting can be combined with passive targeting to further reduce the interaction of carried drugs with healthy tissue. Nanotechnology-enabled active and passive targeting can also increase the efficacy of a chemotherapeutic, achieving greater tumor reduction with lower doses of the drug.

Two qualities are important for an active targeting system. One is the specificity of actively targeted delivery vehicles that is dependent upon the surface ligand's affinity for a target cell marker. The second is the ability to enable the deliver the required dose of drug for the required period of time and to overcome biological delivery barriers[50, 51], an important issue for all imaging modalities. Possible solutions[60] to this include targeted local delivery and development of long circulating compounds that provides a more homogeneous distribution of agent. Therefore, the development of targeted probes are composed directly against a specific moiety targeted to the molecule, receptor or enzyme of interest and an imaging component that provides the physical contrast with a prolonged circulation time of the delivery vehicles *in vivo.*

1.3.3. Polymer Functionalization for Targeted Delivery

Polymersomes are a great choice as drug carriers for targeted delivery. Polymersomes have several advantages over other drug delivery systems due to their biocompatibility, capability of self-assembly, ability for loading hydrophobic and hydrophilic encapsulates, broad range of tunable physical properties and a wide diversity of chemistries for polymer modification. These NIR polymersome characteristics led us

to investigate the application of these optical agents for drug delivery and specific tumor cell targeting.

It has been shown that a number of drug molecules improved their therapeutic effects and their targeted delivery *in vivo* when encapsulated inside polymersomes.[61] Such improvement is achieved by (1) retaining the drug molecules inside the polymersomes, therefore avoiding the exposure to tissues or blood and minimizing the nonspecific uptake of drug molecules by normal undiseased tissues; (2) selectively targeting the tissue of interest and releasing the content at the targeted region. These two criteria have been primary reasons for use of polymersomes as drug delivery cargo. In order to make the polymersomes selective for certain tissues and cells, it is important to functionalize the polymersome surface with site-specific ligands.

Functionalized polymersomes provides a versatile carrier platform for the targeted delivery of therapeutics to the interior of the tumor cell and offers the possibility to greatly improve treatment outcomes for diseases by enhancing specificity and minimizing side effects compared to conventional drugs and liposomes.

1.4. Specific Aims of the Thesis Dissertation

The detection of early carcinoma or dormant or latent metastatic tumor cells remains an elusive but important clinical goal. We seek to develop further revolutionary new nanotechnology that enables optically based detection of metastatic cancer cells. Towards this goal, we will further refine design criteria for near infrared (NIR) emissive polymersomes, a promising new soft matter nanoscale platform for *in vivo* diagnostic and drug-delivery applications. This program will develop (i) nanoscale NIR-emissive polymersomes having optimized emissive output; (ii) targeted nanoscale (*diameter ≤ 100*

nm) NIR-emissive polymersomes; (iii) prototype targeted nanoscale vesicles in which the polymeric building blocks are based-upon FDA-approved materials; (iv) targeted NIR-emissive polymersomes with ideal cell-surface adhesion dynamics; and (v) methods and technology that provide not only new insights into metastatic disease, but define an evolvable nanoscale platform for *in vivo* dormant tumor cell detection, diagnosis, and treatment. These efforts involve correlating NIR fluorophore structure and photophysics, polymersome composition of matter, vesicle mechanical and biological properties, nanoscale NIR-emissive polymersome fluorescence output, and the nature of the cellular targeting motif, with *in vivo* function and efficacy. As such, the experimental approach we pursue is cross-cutting and integrative, encompassing supramolecular chemical synthesis, photophysical characterization, *in vivo* imaging, bioengineering, biology, and medicine. We strive to establish design principles that will ultimately enable real-time detection and identification of limited target cell numbers under clinically relevant diagnostic conditions, and define new tools for the study of metastatic disease.

1.4.1. Aim 1- Chapter 2: Engineering and Design of Porphyrin Based Fluorophores for Optimized NIR Emission Output

The first aim of this thesis dissertation involves the synthesis of high emission dipole strength porphyrin-based fluorophores with great enhancement of emission intensity and luminescence quantum yields. A class of quinoidal spacer conjugated (porphinato)zinc(II) (**PZn-(BTD-PZn)$_n$**, **(PZn)$_2$-(BTD-(PZn)$_2$)$_n$**) and **(BTD-(PZn)$_n$-BTD)** complexes that possess intervening conjugated BTD spacer with varying degrees of porphyrin conjugation have been synthesized. These BTD conjugated porphyrin species possess large magnitude NIR $S_1 \rightarrow S_0$ fluorescence quantum yields superior to

the highest reported for NIR laser dyes in the 750−900 nm regime. The synthesis, optical spectroscopy, potentiometric studies, and electronic structural calculations are reported and show that the magnitudes of the potentiometric HOMO−LUMO gap (E_p) and quantum yields in conjugated organic materials can both be modulated.

1.4.2. Aim 2 - Chapter 3: Develop Antibody-Conjugated Polymersomes for Immunochemical Applications

We aim to develop a series of chemical modification procedures to functionalize the hydrophilic PEO terminus with selected activated functional groups. These activated moieties will enable covalent attachment of these species to proteins or antibodies. The optimized procedures for the maximum antibody conjugation efficiency and polymersomes yield are established. The impacts of reactive hydrophilic surface functionality and antibody concentration on maximal loading of targeting antibodies are also assessed to give controlled antibody conjugation degree on polymersomes surface. Antibody conjugation to a functionalized NIR-emissive polymersome having a diameter less than 100 nm provides a nanoscale object targeted to a cell-surface-specific structure. We aim at test the ability of using these antibody-conjugated NIR-emissive polymersomes to label cells and measure fluorescence signal intensity in tumor cells. We will demonstrate the efficiency of these polymersomes to detect metastatic tumor cells and provide fundamental new information regarding metastasis. These studies will correlate NIR optical signal intensity with absolute tumor cell numbers. Detection sensitivity levels will be determined, and the potential for using antibody-conjugated NIR-emissive polymersomes as a detection system for early tumors, as well as dormant or latent metastases, will be assessed.

1.4.3. Aim 3 - Chapter 4:   Elaboration of First-Generation Targeted Nanoscale Emissive Polymersomes on Which the Polymeric Vesicular Building Blocks are Based-Upon FDA-Approved Biodegradable Polymers

The fouth aim of this thesis dissertation involves the formation of functionalized polymersomes through self-assembly of an amphiphilic bioresorbable polymer consisting of previously FDA-approved building blocks: poly(ethyleneoxide) (PEO) , poly(ε-caprolactone) (PCL) and poly(1,3-trimethylene carbonate) (PTMC). A varies of PEO-*b*-PCL, PEO-*b*-PTMC diblock copolymers and PEO-*b*-P(CL-co-TMC)triblock copolymers are synthesized and their ability to self-assembly into meso- and nano-scale polymersomes are examined. Further, we synthesize vinyl sulfone functionalized PEO-*b*-PCl diblock copolymers which can be readily used for peptide conjugation and tumor targeting. As such, these bioresorbable polymersomes hold promise as nanomaterials for future imaging, targeting and drug delivery applications.

1.4.4. Aim 4 - Chapter 5: Develop Nanoparticles Incorporated Polymersomes with Quantitative Membrane Loading

We aim at incorporating various nanoparticles within the thick bilayered membranes of polymer vesicles for wide-ranging potential applications in cellular imaging and manipulation. Methodology for the generation of polymer vesicles with various nanoparticles including different sized CdSe/ZnS quantum dots and gold nanoparticles loaded in the bilayer membrane through a teflon-based thin-film-rehydration method is established. Quantum dots with no aqueous solubility can be quantitatively and reproducibly loaded within polymersome membranes at prescribed molar ratios. The effects of vesicle loading on the absorptive and emissive properties of

quantum dots, as well as whole polymersomal ensembles, are examined. Nanoparticles-loading-dependent changes on vesicle thermodynamic and mechanical stabilities are further tested and the results reported.

1.5. References

1. Mansfield, P.; Morris, P. G., *NMR imaging in biomedicine*. Academic Press New York: 1982; Vol. 37.

2. Weissleder, R.; Mahmood, U. *Radiology* **2001,** 219, 316.

3. Santra, S.; Dutta, D.; Walter, G. A.; Moudgil, B. M. *Technology in cancer research & treatment* **2005,** 4, 593.

4. Thorne, S. H.; Contag, C. H. *Proceedings of the IEEE* **2005,** 93, 750-762.

5. Licha, K.; Olbrich, C. *Advanced drug delivery reviews* **2005,** 57, 1087-1108.

6. Licha, K. *Contrast Agents Ii* **2002**, 1-29.

7. Sevick-Muraca, E. M.; Houston, J. P.; Gurfinkel, M. *Current Opinion in Chemical Biology* **2002,** 6, 642-650.

8. Bremer, C.; Ntziachristos, V.; Weissleder, R. *European radiology* **2003,** 13, 231-243.

9. Ntziachristos, V.; Bremer, C.; Weissleder, R. *European radiology* **2003,** 13, 195-208.

10. Achilefu, S. *Technology in cancer research & treatment* **2004,** 3, 393.

11. Graves, E. E.; Weissleder, R.; Ntziachristos, V. *Current Molecular Medicine* **2004,** 4, 419-430.

12. Zheng, G.; Chen, Y.; Intes, X.; Chance, B.; Glickson, J. D. *Journal of Porphyrins and Phthalocyanines* **2004,** 8, 1106-1117.

13. Gibson, A. P.; Hebden, J. C.; Arridge, S. R. *Physics in Medicine and Biology* **2005,** 50, R1.

14. Weissleder, R.; Ntziachristos, V. *Nature medicine* **2003,** 9, 123-128.

15. Ray, P.; Pimenta, H.; Paulmurugan, R.; Berger, F.; Phelps, M. E.; Iyer, M.; Gambhir, S. S. *Proceedings of the National Academy of Sciences of the United States of America* **2002,** 99, 3105.

16. Shah, K. *Cancer biology & therapy* **2005,** 4, 518-523.

17. Weissleder, R. *Nature biotechnology* **2001,** 19, 316-317.

18. Frangioni, J. V. *Current Opinion in Chemical Biology* **2003,** 7, 626-634.

19. Benson, R. C.; Kues, H. A. *Physics in Medicine and Biology* **1978,** 23, 159.

20. Chance, B. *Annals of the New York Academy of Sciences* **1998,** 838, 29-45.

21. McBride, T. O.; Pogue, B. W.; Jiang, S.; Osterberg, U. L.; Paulsen, K. D.; Poplack, S. P. *Optics Letters* **2001,** 26, 822-824.

22. Landsman, M. L.; Kwant, G.; Mook, G. A.; Zijlstra, W. G. *Journal of applied physiology* **1976,** 40, 575.

23. Licha, K.; Riefke, B.; Ntziachristos, V.; Becker, A.; Chance, B.; Semmler, W. *Photochemistry and photobiology* **2000,** 72, 392-398.

24. Ebert, B.; Sukowski, U.; Grosenick, D.; Wabnitz, H.; Moesta, K. T.; Licha, K.; Becker, A.; Semmler, W.; Schlag, P. M.; Rinneberg, H. *Journal of Biomedical Optics* **2001,** 6, 134.

25. Griesbeck, A. G. *Angewandte Chemie* **1991,** 103, 1554-1555.

26. Dubertret, B.; Skourides, P.; Norris, D. J.; Noireaux, V.; Brivanlou, A. H.; Libchaber, A. *Science* **2002,** 298, 1759.

27. Gao, X.; Cui, Y.; Levenson, R. M.; Chung, L. W. K.; Nie, S. *Nat Biotech* **2004,** 22, 969-976.

28. Smith, A. M.; Gao, X.; Nie, S. *Photochemistry and photobiology* **2004,** 80, 377-385.

29. Michalet, X.; Pinaud, F. F.; Bentolila, L. A.; Tsay, J. M.; Doose, S.; Li, J. J.; Sundaresan, G.; Wu, A. M.; Gambhir, S. S.; Weiss, S. *Science* **2005,** 307, 538.

30. Kim, S.; Lim, Y. T.; Soltesz, E. G.; De Grand, A. M.; Lee, J.; Nakayama, A.; Parker, J. A.; Mihaljevic, T.; Laurence, R. G.; Dor, D. M. *Nature biotechnology* **2003,** 22, 93-97.

31. Chan, W. C. W.; Nie, S. *Science* **1998,** 281, 2016.

32. Han, M.; Gao, X.; Su, J. Z.; Nie, S. *Nature biotechnology* **2001,** 19, 631-635.

33. Schellenberger, E. A.; Reynolds, F.; Weissleder, R.; Josephson, L. *Chembiochem* **2004,** 5, 275-279.

34. Noh, M.; Kim, T.; Lee, H.; Kim, C.-K.; Joo, S.-W.; Lee, K. *Colloids and Surfaces A: Physicochemical and Engineering Aspects* **2010,** 359, 39-44.

35. Hardman, R. *Environmental health perspectives* **2006,** 114, 165.

36. Frangioni, J. V. *Nature biotechnology* **2006,** 24, 326-328.

37. Peer, D.; Karp, J. M.; Hong, S.; Farokhzad, O. C.; Margalit, R.; Langer, R. *Nat Nano* **2007,** 2, 751-760.

38. Discher, D. E.; Ahmed, F. *Annu. Rev. Biomed. Eng.* **2006,** 8, 323-341.

39. Ghoroghchian, P. P.; Frail, P. R.; Susumu, K.; Blessington, D.; Brannan, A. K.; Bates, F. S.; Chance, B.; Hammer, D. A.; Therien, M. J. *Proceedings of the National Academy of Sciences U.S.A* **2005,** 102, 2922-2927.

40. Photos, P. J.; Bacakova, L.; Discher, B.; Bates, F. S.; Discher, D. E. *Journal of Controlled Release* **2003,** 90, 323-334.

41. Wu, S. P.; Lee, I.; Ghoroghchian, P. P.; Frail, P. R.; Zheng, G.; Glickson, J. D.; Therien, M. J. *Bioconjugate Chemistry* **2005,** 16, 542-550.

42. Rubtsov, I. V.; Susumu, K.; Rubtsov, G. I.; Therien, M. J. *Journal of the American Chemical Society* **2003,** 125, 2687-2696.

43. Susumu, K.; Therien, M. J. *Journal of the American Chemical Society* **2002,** 124, 8550-8552.

44. Lin, V. S. Y.; Therien, M. J. *Chemistry – A European Journal* **1995,** 1, 645-651.

45. Lin, V. S.; DiMagno, S. G.; Therien, M. J. *Science* **1994,** 264, 1105-1111.

46. Ghoroghchian, P. P.; Lin, J. J.; Brannan, A. K.; Frail, P. R.; Bates, F. S.; Therien, M. J.; Hammer, D. A. *Soft Matter* **2006,** 2, 973-980.

47. van Vlerken, L. E.; Vyas, T. K.; Amiji, M. M. *Pharmaceutical Research* **2007,** 24, 1405-1414.

48. Roselli, M.; Guadagni, F.; Buonomo, O.; Belardi, A.; Ferroni, P.; Diodati, A.; Anselmi, D.; Cipriani, C.; Casciani, C. U.; Greiner, J. *Anticancer research* **1996,** 16, 2187-2192.

49. Garg, A.; Kokkoli, E. *Engineering in Medicine and Biology Magazine, IEEE* **2005,** 24, 87-95.

50. Jain, R. K. *Microcirculation* **1997,** 4, 1-23.

51. Jain, R. K. *Journal of Controlled Release* **1998,** 53, 49-67.

52. Langer, R. *Nature* **1998,** 392, 5-10.

53. Matsumura, Y.; Maeda, H. *Cancer research* **1986,** 46, 6387.

54. Maeda, H.; Wu, J.; Sawa, T.; Matsumura, Y.; Hori, K. *Journal of Controlled Release* **2000,** 65, 271-284.

55. Noguchi, Y.; Wu, J.; Duncan, R.; Strohalm, J.; Ulbrich, K.; Akaike, T.; Maeda, H. *Cancer Science* **1998,** 89, 307-314.

56. Gabizon, A.; Papahadjopoulos, D. *Proceedings of the National Academy of Sciences* **1988,** 85, 6949.

57. Bakker-Woudenberg, I. A. J. M.; Lokerse, A. F.; ten Kate, M. T.; Storm, G. *Biochimica et Biophysica Acta (BBA) - Molecular Basis of Disease* **1992,** 1138, 318-326.

58. Harasym, T. O.; Cullis, P. R.; Bally, M. B. *Cancer Chemotherapy and Pharmacology* **1997,** 40, 309-317.

59. Pangburn, T. O.; Petersen, M. A.; Waybrant, B.; Adil, M. M.; Kokkoli, E. *Journal of biomechanical engineering* **2009,** 131, 074005.

60. Weissleder, R. *Nat Rev Cancer* **2002,** 2, 11-18.

61. Levine, D. H.; Ghoroghchian, P. P.; Freudenberg, J.; Zhang, G.; Therien, M. J.; Greene, M. I.; Hammer, D. A.; Murali, R. *Methods* **2008,** 46, 25-32.

CHAPTER 2. Synthesis, Characterization and Properties of Conjugated (Porphinato)zinc(II) Compounds Featuring Benzothiadiazole Spacer Units

2.1. Summary

Imaging in the NIR region (700–1100 nm) have numerous advantages for biomedical applications because of low background absorption, low scattering and cheap illumination sources.[1, 2] In the design and synthesis of NIR emissive compounds, problems have been encountered such as aggregation,[3] photobleaching,[4] and low fluorescence quantum yields.[5] There is a pressing need for the identification of highly effective NIR emissive materials. Towards this purpose, we report the synthesis, optical, electrochemical, electronic structural, and transient optical properties of a class of conjugated (porphinato)zinc(II) complexes with an induced spacer group 1,3-benzothiadiazole (BTD) that regulate frontier orbital energy levels and progressively increase the extent of the quinoidal resonance contribution to the ground and electronically excited states, augmenting the magnitude of electronic communication and optimize their optical properties. For (porphinato)zinc(II)-BTD-(porphinato)zinc(II) (**PZn-(BTD-PZn)$_n$** and **(PZn)$_2$-(BTD-(PZn)$_2$)$_n$)** complexes that featuring the BTD spacer in-between the porphyrin monomers and dimers, the potentiometrically determined HOMO-LUMO gaps ($E_{1/2}^{0/+} - E_{1/2}^{-/0}$) display correspondingly diminished energy separations with an increasing in the porphyrin conjugation length, with the emission spectra greatly red-shifts with increasing numbers of conjugated monomeric units, penetrating well into the NIR. Furthermore, these compounds possess very high

oscillator strength and extraordinary large NIR fluorescence quantum yields of 17%-38% in THF, and 18-59% in toluene, while overcoming solvent and stability issues associated with most other NIR laser dyes.[6] The results are remarkable and demonstrate that the S_1 →S_n transition manifolds of these species span an unusually broad spectral domain of the NIR. These data highlight the unusually large quinoidal resonance contribution to the low-lying electronically excited singlet states of these BTD conjugated porphyrin species.

To better understand how the BTD spacer reduces and tunes energy gaps between the highest occupied molecular orbital (HOMO) and the lowest unoccupied molecular orbital (LUMO) of such π-conjugated species and increase the quantum yield, we further design another series of BTD-(porphinato)zinc(II)-BTD **(BTD-(PZn)$_n$-BTD)** supermolecules with the BTD spacer at the end positions of the conjugated multiporphyrin oligomers. These BTD conjugated multiporphyrin compounds show futher red-shifts of the respective x-polarized Q state (S0→S1) transition manifold maxima in the NIR region relative to the BTD spaced porphyrin oligomers, together with very high quantum yields. Electronic structural differences, as well as the relative magnitudes of the optical (E_{op}) and potentiometric (E_p) band gaps of all these BTD conjugated porphyrin structures are rationalized within the context of perturbation theory. The fact that the quantum yields of these BTD conjugated porphyrin possess NIR S_1→S_n manifold absorptions lower in energy with respect to those of classic conducting polymers, yet with an exceptional high quantum yields, underscore the unusual electrooptic properties of these conjugated structures.

2.2.   Introduction

Low band gap organic materials can be used as photonic devices with a wide range of applications as photovoltaics,[7, 8] LEDs,[9, 10] electro-optic modulators[11, 12], optical limiters,[13, 14], and especially *in vivo* biomedical imaging probes.[15] All these applications necessitate highly conjugated materials that manifest at least one type of singlet manifold transition with unusual intensity in the near-infrared (NIR). The excited-states of active conjugated, low band-gap materials usually have shortened excited-state lifetimes due to large magnitude Franck-Condon mediated nonradiative decay, congruent with the energy gap law.[16, 17] Most available NIR-emissive fluorophores possess modest quantum yields with additional undesirable limitations of low chemical and photostability, and a marked sensitivity to solvent polarity.[5, 6] Relative few organic oligomers or polymers have been identified to possess excited singlet states which absorb strongly in the NIR. To enhance electrical properties, small band gap materials have become a synthetic goal in organic/polymer electronics. Construction of either polymers consisting of donor and acceptors or oligomers that have mid gap states is one means to tune the band gap of photonic materials. Another possible method is by addition of monomer repeat units to a monomer unit that possess modest optical, E_{op}, and electropotential, E_{po}, band gaps. Upon addition of monomer repeat units, the band gap sufficiently decreases.

A great candidate for small E_{op} and E_{po} oligomer and polymer electronic material is porphyrins. Porphyrins are a tetrapyrrolic-conjugated macrocycles with large π-conjugated ring systems and heteroatoms that give rise to porphyrin-porphyrin π-interactions and possess modest potentiometrically determined HOMO-LUMO gaps (E_p; $E_{1/2}^{0/+} - E_{1/2}^{-/0}$), relative to those of the common monomeric aromatic building blocks

used to construct traditional electronic polymers. The electronic properties of (porphinato)metal compounds can be modulated extensively by variation of the macrocycle peripheral *meso-* or *β*-substituents, as well as by selection of the central metal ion; further, a variety of modes of porphyrinoid-porphyrinoid connectivity provides sufficiently strong interchromophore electronic interactions to facilitate extensive electronic delocalization.[18-31] In addition, an established means to further reduce the E_{op} and E_p gaps of π-conjugated materials involves introducing quinoid-like character into the conjugation main-chain.[32-34] Porphyrin-to-porphyrin bridging motifs involving ethynes and spacers that induce a quinoidal structural perturbation with appropriately positioned frontier orbital energy levels, can greatly enhance ground- and excited-state π-conjugation, and effect further reduction in E_{op} and E_p in the corresponding oligomeric and polymeric structures.[35]

Our group has synthesized conjugated (porphinato)zinc(II)-spacer-(porphinato)zinc(II) (**PZn-Sp-PZn**) complexes feature Sp moieties 4,7-diethynylbenzo[*c*][1,2,5]thiadiazole (**E-BTD-E**), 6,13-diethynylpentacene (**E-PC-E**), 4,9-diethynyl-6,7-dimethyl[1,2,5]thiadiazolo[3,4-*g*]quinoxaline (**E-TDQ-E**), and 4,8-diethynylbenzo[1,2-*c*:4,5-*c*']bis([1,2,5]thiadiazole) (**E-BBTD-E**). Among these different spacers, BTD was found to demonstrate the highest quantum yield. Thus, we further developed a new class of BTD featured porphyrin supermolecules with both BTD spacer in-between the porphyrin oligomers such as (**PZn-(BTD-PZn**)ₙ and **(PZn)₂-(BTD-(PZn)₂)ₙ)**, as well as BTD spacer at the end positions of the conjugated multiporphyrin oligomers (**BTD-(PZn)ₙ-BTD**). As we expected, all these compounds exhibit very large quantum yields that are superior to the highest reported quantum yields for organic

chromophores in the NIR regime.[36] The synthesis, optical spectroscopy, potentiometric studies, and electronic structural calculations are reported and show that the magnitudes of the potentiometric HOMO−LUMO gap (E_p) and quantum yields in conjugated organic materials can both be modulated.

2.3. Experimental Methods

2.3.1. Materials

All manipulations were carried out under argon previously passed through an O_2 scrubbing tower (Schweitzerhall R3-11 catalyst) and a drying tower (Linde 3-Å molecular sieves) unless otherwise stated. Air sensitive solids were handled in a Braun 150-M glove box. Standard Schlenk techniques were employed to manipulate air-sensitive solutions. Unless otherwise noted, all solvents utilized in this work were obtained from Fisher Scientific (HPLC grade); tetrahydrofuran (THF) was distilled from K/4-benzoylbiphenyl under N_2. Diisopropylamine, Triethylamine, MeOH, $CHCl_3$ and CH_2Cl_2 were distilled from CaH_2 under N_2. Pyridine and piperidine was also dried over CaH_2 and distilled under reduced pressure. The catalysts tetrakis (triphenylphosphine) palladium $Pd(PPh_3)_4$, bis(triphenylphosphine) palladium chloride $Pd(PPh_3)_2Cl_2$, tris(dibenzylideneacetone) dipalladium(0) Pd_2dba_3, copper iodide CuI, triphenylarsine $AsPh_3$ and triphenylphosphine $P(o\text{-tol})_3$ were purchased from Strem Chemicals and used as received. 4-bromo-benzo[c][1,2,5]thiadiazole, 4,7-Dibromobenzo[c][1,2,5]thiadiazole,[37] were prepared by literature methods. All NMR solvents were used as received. The supporting electrolyte used in the electrochemical experiments, tetra-n-butylammonium hexafluorophosphate, was recrystallized twice from

ethanol and dried under vacuum at 70 °C overnight prior to use. All the other chemicals were used as received.

Chemical shifts for ^{1}H NMR spectra are relative to tetramethylsilane (TMS) signal in the deuterated solvent (TMS = 0.00 ppm). All *J* values are reported in Hertz. Flash and size exclusion column chromatography were performed on the bench top, using respectively silica gel (EM Science, 230–400 mesh) and Bio-Rad Bio-Beads SX-1 as media. MALDI-TOF spectroscopic data were obtained with a Perspective Voyager DE instrument in the Laboratory of Dr. W. Degrado (Department of Biophysics, University of Pennsylvania); samples for these experiments were prepared as micromolar solutions in THF or CH_2Cl_2, and dithranol in THF or cyano-4-hydroxycinnamic acid in CH_2Cl_2/isopropyl alcohol (4:1) were utilized as the matrix.

2.3.2.   Instrumentation

Electronic absorption spectra were recorded on a Shimazu UV/vis/near-IR spectrophotometry system that is based on the optics of a Cary 14 spectrophotometer. NMR spectra were recorded on 500 MHz DMX-300 Brüker spectrometers. Cyclic voltammetric measurements were carried out on an EG&G Princeton Applied Research model 273A Potentiostat/Galvanostat.   The electrochemical cell used for these experiments utilized a platinum disk working electrode, a platinum wire counter electrode, and a saturated calomel reference electrode (SCE).   The reference electrode was separated from the bulk solution by a junction bridge filled with the corresponding solvent/supporting electrolyte solution. The ferrocene/ferrocenium redox couple was utilized as an internal potentiometric standard.

PZnE-BTD-EPZn

PZnE-BTD-EPZnE-BTD-EPZn

R =

PZnE-BTD-EPZnE-BTD-EPZnE-BTD-EPZn

BTD-EPZnE-BTD

BTD-EPZnE-PZnE-BTD

BTD-EPZn-EPZnE-PZnE-BTD

BTD-EPZn-EPZnE-PZn-EPZnE-PZnE-BTD

PZn-EPZnE-BTD-EPZnE-PZnE

PZn-EPZnE-BTD-EPZnE-PZnE-BTD-EPZnE-PZn
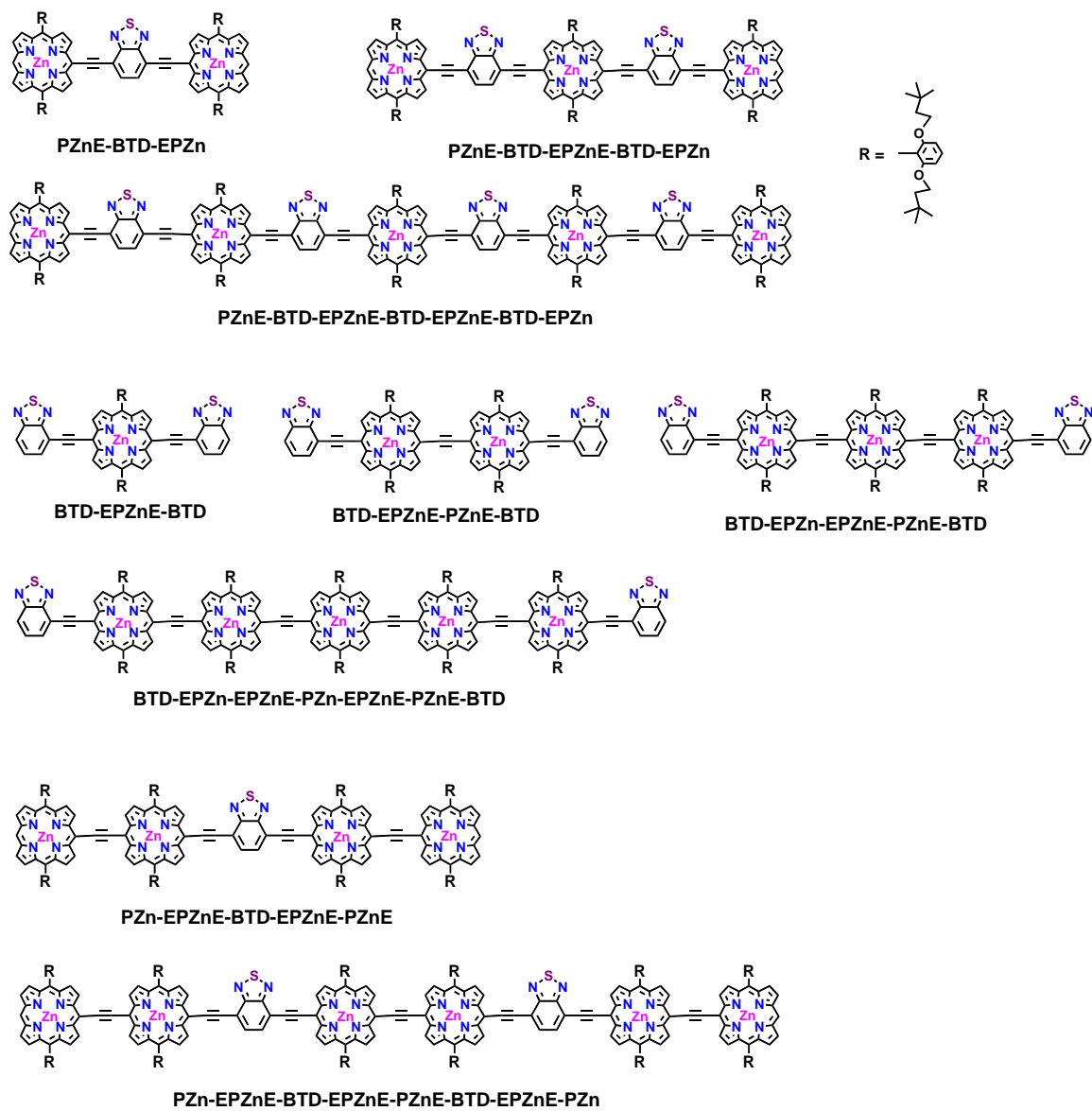
Figure 2.1 Structures of the BTD conjugated porphyrin compounds.

33

2.3.3. Synthesis

Previously made porphyrin compounds see supplemental of literatures.[38, 39]

4,7-Bis[(10,20-bis[2',6'-bis(3'',3''-dimethyl-1''-butyloxy)phenyl]porphinato)zinc(II)-5-ylethynyl]benzo[*c*][1,2,5]thiadiazole (PZnE-BTD-EPZn) (1). (5-Ethynyl-10, 20-bis[2',6'-bis(3,3-dimethyl-1-butyloxy)phenyl]porphinato)zinc(II) (0.100g, 1.05×10^{-4} mol), 4,7-dibromobenzo[*c*][1,2,5]thiadiazole (12.9 mg, 4.4×10^{-5} mol) were charged into a Schlenk Flask with Pd_2dba_3 (12.1 mg, 1.32×10^{-5} mol) and $AsPh_3$ (32.3 mg, 1.05×10^{-4} mol). THF: iPr_2NH (9:1 ml) solvent mixture was degassed with an Ar purge for 30 min prior to solvent transfer. Once solvent was transferred, the reaction mixture was stirred at 50 ℃ overnight under Ar. After the solvent was evaporated, the residue was chromatographed on silica gel using 5:1 hexanes:THF as the eluant. Yield = 82 mg (91.6 % based on 12.9 mg of the dibromobenzo[*c*][1,2,5]thiadiazole starting material). ^{1}H NMR (500 MHz, CDCl$_3$): 10.12 (d, 4H, J = 4.4 Hz, β-H), 10.04 (s, 2H, *meso*-H), 9.21 (d, 4H, J = 4.4 Hz, β-H), 9.06 (d, 4H, J = 4.5 Hz, β-H), 8.92 (d, 4H, J = 4.3 Hz, β-H), 8.37 (s, 2H, Ph-H), 7.74 (t, 4H, J = 8.6 Hz, Ph-H), 7.04 (d, 8H, J = 8.6 Hz, Ph-H), 3.94 (t, 16H, J = 7.2 Hz, -O-CH$_2$-C), 0.87 (t, 16H, J = 7.6 Hz, -O-C-CH$_2$-C), 0.24 (s, 72H, -C-CH$_3$). MALDI-TOF MS m/z : 2029.98 (M$^+$) (calcd 2028.884).

(5-[7'-Bromobenzo[*c*][1,2,5]thiadiazole-ethyn-4'-yl] -10,20-bis[2',6'-bis(3'',3''-dimethyl-1''butyloxy)phenyl]porphinato)zinc(II) (2). (5-Ethynyl-10,20-bis[2',6'-bis(3,3-dimethyl-1-butyloxy)phenyl]porphinato)zinc(II) (0.100g, 1.05×10^{-4} mol), 4, 7-dibromobenzo[*c*][1,2,5]thiadiazole (123.7 mg, 4.21×10^{-4} mol) were charged

into a Schlenk Flask with Pd$_2$dba$_3$ (14.4 mg, 1.57×10^{-5} mol) and AsPh$_3$ (38.5 mg, 1.26×10^{-4} mol). THF: iPr$_2$NH (9:1 ml) solvent mixture was degassed with an Ar purge for 30 min prior to solvent transfer. Once solvent was transferred, the reaction mixture, was stirred at 50 ℃ overnight under Ar. After the solvent was evaporated, the residue was chromatographed on silica gel using 5:1 hexanes:THF as the eluant. Yield = 0.118 g (96.6 % based on 100 mg of the porphyrin starting material). ^{1}H NMR (500 MHz, CDCl$_3$): 10.06 (s, 1H, *meso*-H), 10.01 (d, 2H, J = 4.4 Hz, β-H), 9.22 (d, 2H, J = 4.4 Hz, β-H), 9.02 (d, 2H, J = 4.5 Hz, β-H), 8.91 (d, 2H, J = 4.5 Hz, β-H), 8.07 (d, 1H, J = 7.4 Hz, Ph-H), 8.01(d, 1H, J = 7.5 Hz, Ph-H), 7.71 (t, 2H, J = 8.6 Hz, Ph-H), 7.01 (d, 4H, J = 8.6 Hz, Ph-H), 3.90 (t, 8H, J = 7.3 Hz, -O-CH$_2$-C), 0.87 (t, 8H, J = 7.0 Hz, -O-C-CH$_2$-C), 0.22 (s, 36H, -C-CH$_3$).

(5, 15-Bis[7'-([10''',20'''-bis[2'''',6''''-bis(3''''',3'''''-dimethyl-1'''''-butyloxy)phenyl]porphinato)zinc(II)-5''-ylethynyl]benzo[*c*][1,2,5]thiadiazole-ethyn-4'-yl]-10,20-bis[2',6'-bis(3'',3''-dimethyl-1''butyloxy)phenyl]porphinato)zinc(II) (PZnE-BTD-EPZnE-BTD-EPZn) (3). Compound 2 (0.100g, 8.59×10^{-5} mol), (5, 15-diethynyl-10, 20-bis[2',6'-bis(3,3-dimethyl-1-butyloxy)phenyl]porphinato)zinc(II) (34.9 mg, 3.58×10^{-5} mol) were charged into a Schlenk Flask with Pd$_2$dba$_3$ (9.83 mg, 1.07×10^{-5} mol) and P(*o*-tol)$_3$ (26.1 mg, 8.59×10^{-5} mol). THF: TEA (9:1 ml) solvent mixture was degassed with an Ar purge for 30 min prior to solvent transfer. Once solvent was transferred, the reaction mixture was stirred at 60 ℃ overnight under Ar. The reaction mixture was then poured down a short silica gel column using CHCl$_3$: MeOH (49:1 mL) as the eluent. A large band was collected and the solvent stripped and then the residue

was taken up in THF and put down a size exclusion column (BioRad Biobeads, SX-1) and chromatographed gravimetrically. The first band was collected and solvent removed via vacuum and the residue was purified by silica gel chromatography using $CHCl_3$: MeOH (49:1 mL) as the eluent. Yield = 114 mg (58% based on diethynyl starting material). ^{1}H NMR (500 MHz, $CDCl_3$): 10.02 (d, 4H, J = 4.4 Hz, β-H), 9.94 (d, 4H, J = 4.5 Hz, β-H), 9.86 (s, 2H, *meso*-H), 9.08 (d, 4H, J = 4.2 Hz, β-H), 8.96 (d, 4H, J = 4.3 Hz, β-H), 8.86 (d, 4H, J = 4.5 Hz, β-H), 8.81(d, 4H, J = 4.2 Hz, β-H), 8.26 (s, 4H, Ph-H), 7.70 (t, 6H, J = 8.6 Hz, Ph-H), 7.02 (d, 6H, J = 4.6 Hz, Ph-H), 7.00 (d, 6H, J = 4.7 Hz, Ph-H), 3.89 (m, 24H, -O-CH_2-C), 0.87 (m, 24H, -O-C-CH_2-C), 0.34 (s, 36H, -C-CH_3), 0.30 (s, 72H, -C-CH_3). MALDI-TOF MS m/z: 3136.72 (M^+) (calcd 3133.32).

(5-Ethynyl-15-[7'-Bromobenzo[*c*][1,2,5]thiadiazole- ethyn-4'-yl] -10,20-bis[2',6'-bis(3'',3''-dimethyl-1''butyloxy)phenyl]porphinato)zinc(II) (4). (5-Ethynyl-15-Triisopropylsilylethynyl-10,20-bis[2',6'-bis(3,3-dimethyl-1-butyloxy)phenyl]porphinato)zinc(II) (0.100g, 0.94×10^{-4} mol), 4, 7-dibromobenzo[*c*][1,2,5]thiadiazole (110.7 mg, 3.77×10^{-4} mol) were charged into a Schlenk Flask with Pd_2dba_3 (12.9 mg, 1.40×10^{-5} mol) and $AsPh_3$ (34.5 mg, 1.13×10^{-4} mol). THF: iPr_2NH (9:1 ml) solvent mixture was degassed with an Ar purge for 30 min prior to solvent transfer. Once solvent was transferred, the reaction mixture, was stirred at 50 °C overnight under Ar. After the solvent was evaporated, the residue was chromatographed on silica gel using 5:1 hexanes:THF as the eluant. Yield = 0.117 g (92.4 % based on 100 mg of the porphyrin starting material). ^{1}H NMR (500 MHz, $CDCl_3$): 9.85 (d, 2H, β-H), 9.57 (d, 2H, J = 4.6 Hz, β-H), 8.83 (d, 2H, J = 4.5 Hz, β-H),

8.79 (d, 2H, J = 4.7 Hz, β-H), 7.69 (t, 2H, J = 8.5 Hz, Ph-H), 7.56 (m, 1H, Ph-H), 7.29 (m, 1H, Ph-H), 6.98 (d, 4H, J = 8.6 Hz, Ph-H), 1.43(m, 42H, -SiCH(CH$_3$)$_2$), 3.88 (t, 8H, J = 7.4 Hz, -O-CH$_2$-C), 0.87 (t, 8H, J = 7.3 Hz, -O-C-CH$_2$-C), 0.24 (s, 36H, -C-CH$_3$).

5, 15-Bistriisopropylsilylethynyl- (5, 15-Bis[7'-([10''',20'''-bis[2'''',6''''-bis(3''''',3'''''-dimethyl-1'''''-butyloxy)phenyl]porphinato)zinc(II)-5''-ylethynyl]benzo[*c*][1,2,5]thiadiazole-ethyn-4'-yl]-10,20-bis[2',6'-bis(3'',3''-dimethyl-1''butyloxy)phenyl]porphinato)zinc(II) (5). Coumpound 4 (0.100g, 7.44$\times$10^{-5} mol), (5, 15-diethynyl-10, 20-bis[2',6'-bis(3,3-dimethyl-1-butyloxy)phenyl]porphinato)zinc(II) (30.3 mg, 3.10$\times$10^{-5} mol) were charged into a Schlenk Flask with Pd$_2$dba$_3$ (8.52 mg, 0.93$\times$10^{-5} mol) and P(*o*-tol)$_3$ (22.6 mg, 7.44$\times$10^{-5} mol). THF: TEA (9:1 ml) solvent mixture was degassed with an Ar purge for 30 min prior to solvent transfer. Once solvent was transferred, the reaction mixture was stirred at 60 ℃ overnight under Ar. The reaction mixture was then poured down a short silica gel column using CHCl$_3$: MeOH (49:1 mL) as the eluent. A large band was collected and the solvent stripped and then the residue was taken up in THF and put down a size exclusion column (BioRad Biobeads, SX-1) and chromatographed gravimetrically. The first band was collected and solvent removed via vacuum and the residue was purified by silica gel chromatography using CHCl$_3$: MeOH (49:1 mL) as the eluent. Yield = 56.4 mg (52% based on diethynyl starting material). ^{1}H NMR (500 MHz, CDCl$_3$): 10.02 (d, 4H, J = 4.4 Hz, β-H), 9.94 (d, 4H, J = 4.5 Hz, β-H), 9.86 (s, 2H, *meso*-H), 9.08 (d, 4H, J = 4.2 Hz, β-H), 8.96 (d, 4H, J = 4.3 Hz, β-H), 8.86 (d, 4H, J = 4.5 Hz, β-H), 8.81(d, 4H, J = 4.2 Hz, β-H), 8.26 (s, 4H, Ph-H), 7.70 (t, 6H, J = 8.6 Hz, Ph-H), 7.02 (d, 6H, J = 4.6 Hz, Ph-H), 7.00 (d, 6H, J = 4.7

Hz, Ph-H), 3.89 (m, 24H, -O-CH$_2$-C), 1.42 (m, 42H, -SiCH(CH$_3$)$_2$), 0.87 (m, 24H, -O-C-CH$_2$-C), 0.34 (s, 36H, -C-CH$_3$), 0.30 (s, 72H, -C-CH$_3$). MALDI-TOF MS m/z: 3136.72 (M$^+$) (calcd 3133.32).

5, 15-Ethynyl- (5, 15-Bis[7'-([10''',20'''-bis[2'''',6''''-bis(3''''',3'''''-dimethyl-1'''''-butyloxy)phenyl]porphinato)zinc(II)-5''-ylethynyl]benzo[*c*][1,2,5]thiadiazole-ethyn-4'-yl]-10,20-bis[2',6'-bis(3'',3''-dimethyl-1''butyloxy)phenyl]porphinato)zinc(II) (6). Compound 5 (100 mg, 2.63×10^{-5} mol) were dissolved in THF and cooled down to 0 ℃ under Ar. TBAF (0.526 mL, 0.1 M TBAF in THF solution, 5.26×10^{-5} mol) was then added dropwise and the reaction mixture was allowed to stir for 15 min at 0 ℃. The reaction mixture was then directly poured down a short silica gel column using CHCl$_3$ as the eluent. Yield = 75 mg (82.3% based on compound 5). ^{1}H NMR (500 MHz, CDCl$_3$): 10.05 (d, 4H, *J* = 4.4 Hz, *β*-H), 9.96 (d, 4H, *J* = 4.5 Hz, *β*-H), 9.02 (d, 4H, *J* = 4.2 Hz, *β*-H), 8.96 (d, 4H, *J* = 4.3 Hz, *β*-H), 8.87 (d, 4H, *J* = 4.5 Hz, *β*-H), 8.80 (d, 4H, *J* = 4.2 Hz, *β*-H), 8.26 (s, 4H, Ph-H), 7.72 (t, 6H, *J* = 8.6 Hz, Ph-H), 7.02 (d, 6H, *J* = 4.6 Hz, Ph-H), 7.00 (d, 6H, *J* = 4.7 Hz, Ph-H), 4.13 (s, 2H), 3.89 (m, 24H, -O-CH$_2$-C), 0.87 (m, 24H, -O-C-CH$_2$-C), 0.34 (s, 36H, -C-CH$_3$), 0.30 (s, 72H, -C-CH$_3$).

(5, 15-Bis[7''-([10'''',20''''-bis[2''''',6'''''-bis(3'''''',3''''''-dimethyl-1''''''-butyloxy)phenyl]porphinato)zinc(II)-5'''-ylethynyl]benzo[*c*][1,2,5]thiadiazole-ethyn-4''-yl] -(5, 15-Bis[7'-([10''',20'''-bis[2'''',6''''-bis(3''''',3'''''-dimethyl-1'''''-butyloxy)phenyl]porphinato)zinc(II)-5''-ylethynyl]benzo[*c*][1,2,5]thiadiazole-ethyn-

4'-yl]-10,20-bis[2',6'-bis(3'',3''-dimethyl-1''butyloxy)phenyl]porphinato)zinc(II)

(PZnE-BTD-EPZnE-BTD-EPZn- BTD-EPZnE-BTD-EPZn) (7). Compound 2

(0.100g, 8.59×10^{-5} mol), compound 6 (114.1 mg, 3.58×10^{-5} mol) were charged into a

Schlenk Flask with Pd_2dba_3 (9.83 mg, 1.07×10^{-5} mol) and P(o-tol)$_3$ (26.1 mg, 8.59×10^{-5}

mol). THF: TEA (9:1 ml) solvent mixture was degassed with an Ar purge for 30 min

prior to solvent transfer. Once solvent was transferred, the reaction mixture was stirred at

60 °C overnight under Ar. The reaction mixture was then poured down a short silica gel

column using CHCl$_3$: MeOH (49:1 mL) as the eluent. A large band was collected and the

solvent stripped and then the residue was taken up in THF and put down a size exclusion

column (BioRad Biobeads, SX-1) and chromatographed gravimetrically. The first band

was collected and solvent removed via vacuum and the residue was purified by silica gel

chromatography using CHCl$_3$: MeOH (49:1 mL) as the eluent. Yield = 61.2 mg (32%

based on compound 6). ^{1}H NMR (500 MHz, CDCl$_3$): 10.02 (d, 4H, $J = 4.4$ Hz, β-H), 9.94

(d, 4H, $J = 4.5$ Hz, β-H), 9.86 (s, 2H, $meso$-H), 9.08 (d, 4H, $J = 4.2$ Hz, β-H), 8.96 (d, 4H,

$J = 4.3$ Hz, β-H), 8.86 (d, 4H, $J = 4.5$ Hz, β-H), 8.81(d, 4H, $J = 4.2$ Hz, β-H), 8.26 (s, 4H,

Ph-H), 7.70 (t, 6H, $J = 8.6$ Hz, Ph-H), 7.02 (d, 6H, $J = 4.6$ Hz, Ph-H), 7.00 (d, 6H, $J = 4.7$

Hz, Ph-H), 3.89 (m, 24H, -O-CH$_2$-C), 0.87 (m, 24H, -O-C-CH$_2$-C), 0.34 (s, 36H, -C-CH$_3$),

0.30 (s, 72H, -C-CH$_3$). MALDI-TOF MS m/z: 5366.7 (M$^+$) (calcd 5353.51).

        (**5,   15-Bis[benzo[**c**][1,2,5]thiadiazole-ethyn-4'-yl]   -10,20-bis[2',6'-bis(3,3-**

dimethyl-1-butyloxy)phenyl]porphinato)zinc(II) (BTD-EPZnE-BTD) (8). (5, 15-

Diethynyl-10,20-bis[2',6'-bis(3,3-dimethyl-1-butyloxy)phenyl]porphinato)zinc(II)   (50.0

mg, 5.13×10^{-5} mol), 4-bromobenzo[c][1,2,5]thiadiazole (26.5 mg, 1.23×10^{-4} mol) were

charged into a Schlenk Flask with Pd_2dba_3 (14.1 mg, 1.54×10^{-5} mol) and $AsPh_3$ (37.7 mg, 1.23×10^{-4} mol). THF: iPr_2NH (9:1 ml) solvent mixture was degassed with an Ar purge for 30 min prior to solvent transfer. Once solvent was transferred, the reaction mixture, was stirred at 50 ℃ overnight under Ar. After the solvent was evaporated, the residue was chromatographed on silica gel using 5:1 hexanes:THF as the eluent. Yield = 57.2 mg (90.2 % based on 50 mg of the porphyrin starting material). ^{1}H NMR (500 MHz, $CDCl_3$): 9.82 (d, 4H, J = 4.5 Hz, β -H), 8.85 (d, 4H, J = 4.5 Hz, β-H), 7.97 (d, 2H, J = 6.4 Hz, Ph-H), 7.68 (t, 2H, J = 8.5 Hz, Ph-H), 7.47 (m, 2H, Ph-H), 7.71 (t, 2H, J = 8.6 Hz, Ph-H), 6.98 (m, 6H, Ph-H), 3.86 (t, 8H, J = 7.3 Hz, -O-CH_2-C), 0.77 (t, 8H, J = 7.3 Hz, -O-C-CH_2-C), 0.19 (s, 36H, -C-CH_3). CI MS m/z: 1239.53 [$(M+H)^+$] (calcd 1240.44)

4-(Trimethylsilyl)ethynylbenzo[c][1,2,5]thiadiazole **(9).** 4-Bromobenzo[c][1,2,5]thiadiazole (0.378 g, 1.76×10^{-3} mol), $Pd(PPh_3)_4$ (0.125 g, 1.68×10^{-4} mol), CuI (0.014 g, 7.4×10^{-5} mol), THF (20 ml), diisopropylamine (1.00 ml) and (trimethylsilyl)acetylene (1.00 ml, 7.1×10^{-3} mol) were added to a 50-ml Schlenk tube. N_2 was bubbled through the mixture for 5 min, following which the reaction was stirred at 45 ℃ for 20 h under N_2. After cooling, the solvent was evaporated and the residue was chromatographed on silica gel with 1:1 hexanes:$CHCl_3$ as the eluant. Yield = 0.398 g (97.3 % based on 0.378 g of 4-bromobenzothiadiazole). ^{1}H NMR (500 MHz, $CDCl_3$): 7.88 (m, 1H, Ph-H), 7.67 (m, 1H, Ph-H), 7.45 (m, 1H, Ph-H), 0.33 (s, 9H, -Si-CH_3).

4-Ethynylbenzo[c][1,2,5]thiadiazole **(10).** 4-(Trimethylsilyl)ethynylbenzo[c][1,2,5]thiadiazole (0.100 g, 4.30×10^{-4} mol), K_2CO_3 (78.6

mg, 5.71×10^{-4} mol), THF (3ml), MeOH (2 ml) were added to a 25-ml Schlenk tube. N_2 was bubbled through the mixture for 5 min, following which the reaction was stirred at room temperature for 1.5 h under N_2. The reaction mixture was then filtered and the filtrate was evaporated. The residue was chromatographed on silica gel with 5:1 hexanes:THF as the eluant. Yield = 63 g (91.4% based on 0.100 g of 4-(trimethylsilyl)ethynylbenzothiadiazole). ^{1}H NMR (500 MHz, CDCl$_3$): 8.01 (m, 1H, Ph-H), 7.78 (m, 1H, Ph-H), 7.56 (m, 1H, Ph-H), 3.56 (s, 1H, -CC-H).

(5-Bromo-15-[benzo[*c*][1,2,5]thiadiazole- ethyn-4'-yl] -10,20-bis[2',6'-bis(3'',3''-dimethyl-1''butyloxy)phenyl]porphinato)zinc(II) (11). (5, 15-Dibromo-10,20-bis[2',6'-bis(3,3-dimethyl-1-butyloxy)phenyl]porphinato)zinc(II) (0.200g, 1.84×10^{-4} mol), 4-ethynylbenzo[*c*][1,2,5]thiadiazole (14.8 mg, 8.22×10^{-5} mol) were charged into a Schlenk Flask with Pd(PPh$_3$)$_4$ (26.6 mg, 2.30×10^{-5} mol) and CuI (8.8 mg, 4.62×10^{-4} mol). THF: piperidine (9:1 ml) solvent mixture was degassed with an Ar purge for 30 min prior to solvent transfer. Once solvent was transferred, the reaction mixture, was stirred at 50 ℃ overnight under Ar. After the solvent was evaporated, the residue was chromatographed on silica gel using 5:1 hexanes:THF as the eluant. Yield = 0.076 g (64.9 % based on the 4-ethynylbenzothiadiazole starting material). ^{1}H NMR (500 MHz, CDCl$_3$): 9.75 (d, 2H, *β*-H), 9.57 (d, 2H, *J* = 4.6 Hz, *β*-H), 8.88 (d, 2H, *J* = 4.5 Hz, *β*-H), 8.81 (d, 2H, *J* = 4.7 Hz, *β*-H), 8.00 (m, 1H, Ph-H), 7.69 (t, 2H, *J* = 8.5 Hz, Ph-H), 7.56 (m, 1H, Ph-H), 7.29 (m, 1H, Ph-H), 6.98 (d, 4H, *J* = 8.6 Hz, Ph-H), 3.88 (t, 8H, *J* = 7.4 Hz, -O-CH$_2$-C), 0.87 (t, 8H, *J* = 7.3 Hz, -O-C-CH$_2$-C), 0.24 (s, 36H, -C-CH$_3$).

(5-Triisopropylsilylethynyl-15-[benzo[*c*][1,2,5]thiadiazole- ethyn-4'-yl] -10,20-bis[2',6'-bis(3'',3''-dimethyl-1''butyloxy)phenyl]porphinato)zinc(II) (12). (5-Bromo-15-triisopropylsilylethynyl-10,20-bis[2',6'-bis(3,3-dimethyl-1-butyloxy)phenyl]porphinato)zinc(II) (0.200g, 1.69×10^{-4} mol), 4-ethynylbenzo[*c*][1,2,5]thiadiazole (32.5 mg, 2.03×10^{-4} mol) were charged into a Schlenk Flask with Pd(PPh$_3$)$_4$ (29.3 mg, 2.53×10^{-5} mol) and CuI (9.6 mg, 5.06×10^{-5} mol). THF: piperidine (9:1 ml) solvent mixture was degassed with an Ar purge for 30 min prior to solvent transfer. Once solvent was transferred, the reaction mixture was stirred at 50 ℃ overnight under Ar. After the solvent was evaporated, the residue was chromatographed on silica gel using 5:1 hexanes:THF as the eluant. Yield = 164.4 mg (76.8 % based on the porphyrin starting material). ^{1}H NMR (500 MHz, CDCl$_3$): 9.87 (d, 2H, β-H), 9.61 (d, 2H, $J = 4.5$ Hz, β-H), 8.86 (d, 2H, $J = 4.5$ Hz, β-H), 8.80 (d, 2H, $J = 4.5$ Hz, β-H), 8.07 (m, 1H, Ph-H), 7.67 (t, 2H, $J = 8.5$ Hz, Ph-H), 7.60 (m, 1H, Ph-H), 7.49 (m, 1H, Ph-H), 6.98 (d, 4H, $J = 8.5$ Hz, Ph-H), 3.88 (t, 8H, $J = 7.4$ Hz, -O-CH$_2$-C), 1.41 (m, 21H, -Si-(CH(CH$_3$)$_2$)$_3$), 0.88 (t, 8H, $J = 7.3$ Hz, -O-C-CH$_2$-C), 0.27 (s, 36H, -C-CH$_3$).

(5-Ethynyl-15-[benzo[*c*][1,2,5]thiadiazole- ethyn-4'-yl] -10,20-bis[2',6'-bis(3'',3''-dimethyl-1''butyloxy)phenyl]porphinato)zinc(II) (13). Compound 12 (160 mg, 1.26×10^{-4} mol) were dissolved in THF under Ar. TBAF (2.5 mL, 0.1 M TBAF in THF solution, 2.5×10^{-4} mol) was then added dropwise and the reaction mixture was allowed to stir for 5 min at room temperature. TLC analysis (5:1 Hexanes: THF) showed complete formation of the product and consumption of the starting material. The reaction mixture was then quenched with 10ml water, extracted with CHCl$_3$ and evaporated. The

residue was chromatographed on silica gel using 5:1 hexanes:THF as the eluant. Yield = 125.5 mg (89.5% based on compoud 12). ^{1}H NMR (500 MHz, CDCl$_3$): 9.86 (d, 2H, β-H), 9.57 (d, 2H, J = 4.1 Hz, β-H), 8.85 (d, 2H, J = 4.8 Hz, β-H), 8.81 (d, 2H, J = 4.5 Hz, β-H), 8.03 (m, 1H, Ph-H), 7.69 (t, 2H, J = 8.5 Hz, Ph-H), 7.56 (m, 1H, Ph-H), 7.49 (m, 1H, Ph-H), 6.98 (m, 4H, Ph-H), 4.07 (S, 1H, -CC-H), 3.88 (t, 8H, J = 7.4 Hz, -O-CH$_2$-C), 0.87 (t, 8H, J = 6.8 Hz, -O-C-CH$_2$-C), 0.29 (s, 36H, -C-CH$_3$).

1,2-Bis[(15-(benzo[c][1,2,5]thiadiazole- ethyn-4'-yl)-10,20-bis[3',5'-bis(3'',3''-dimethyl-1''butyloxy)phenyl]porphinato)zinc(II)-5-yl]ethyne (BTD-EPZnE-PZnE-BTD) (14): Compound 11 (50.0 mg, 4.30$\times$10^{-5} mol), Compound 13 (57.0 mg, 5.16$\times$10^{-5} mol) were charged into a Schlenk Flask with Pd$_2$dba$_3$ (5.9 mg, 6.45$\times$10^{-6} mol) and AsPh$_3$ (15.8 mg, 5.16$\times$10^{-5} mol). THF: TEA (9:1 ml) solvent mixture was degassed with an Ar purge for 30 min prior to solvent transfer. Once solvent was transferred, the reaction mixture was stirred at 60 ℃ overnight under Ar. The reaction mixture was then poured down a short silica gel column using CHCl$_3$: MeOH (49:1 mL) as the eluent. A large band was collected and the solvent stripped and then the residue was taken up in THF and put down a size exclusion column (BioRad Biobeads, SX-1) and chromatographed gravimetrically. The first band was collected and solvent removed via vacuum and the residue was purified by silica gel chromatography using CHCl$_3$:MeOH (49:1 mL) as the eluent. Yield = 45 mg (47.8% based on 50 mg of compound 11). [1]H NMR (500 MHz, CDCl$_3$): 10.19 (d, 4H, J = 4.4 Hz, β-H), 9.85 (d, 4H, J = 4.3 Hz, β-H), 8.88 (d, 4H, J = 4.4 Hz, β-H), 8.84 (d, 4H, J = 4.5 Hz, β-H), 8.10 (d, 2H, J = 6.1 Hz, Ph-H), 8.37 (m, 2H, Ph-H), 7.66 (t, 4H, J = 8.6 Hz, Ph-H), 7.00 (d, 8H, J = 8.6 Hz, Ph-H), 3.89 (t, 16H, J =

7.5 Hz, -O-CH$_2$-C), 0.82 (t, 16H, J = 6.6 Hz, -O-C-CH$_2$-C), 0.32 (s, 72H, -C-CH$_3$).

MALDI-TOF MS m/z: 2182.14 (M$^+$) (calcd 2186.88).

(5, 15-Bis[15'-benzo[c][1,2,5]thiadiazole-ethyn-4'-yl-(10''',20'''-bis[2'''',6''''-bis(3''''',3'''''-dimethyl-1'''''-butyloxy)phenyl]porphinato)zinc(II)ethyn-5'-yl]-10,20-bis[2',6'-bis(3'',3''-dimethyl-1''butyloxy)phenyl]porphinato)zinc(II) (BTD-EPZnE-PZn-EPZnE-BTD) (15).

Coumpound 13 (60 mg, 5.42×10^{-5} mol), (5, 15-dibromo-10, 20-bis[2',6'-bis(3,3-dimethyl-1-butyloxy)phenyl]porphinato)zinc(II) (24.5 mg, 2.26×10^{-5} mol) were charged into a Schlenk Flask with Pd$_2$dba$_3$ (6.2 mg, 6.78×10^{-6} mol) and P(o-tol)$_3$ (16.5 mg, 5.42×10^{-5} mol). THF: TEA (9:1 ml) solvent mixture was degassed with an Ar purge for 30 min prior to solvent transfer. Once solvent was transferred, the reaction mixture was stirred at 60 ℃ overnight under Ar. The reaction mixture was then poured down a short silica gel column using CHCl$_3$: MeOH (49:1 mL) as the eluent. A large band was collected and the solvent stripped and then the residue was taken up in THF and put down a size exclusion column (BioRad Biobeads, SX-1) and chromatographed gravimetrically. The first band was collected and solvent removed via vacuum and the residue was purified by silica gel chromatography using CHCl$_3$:MeOH (49:1 mL) as the eluent. Yield = 48.4 mg (68.2% based on dibromo starting material). ^{1}H NMR (500 MHz, CDCl$_3$): 10.16 (d, 4H, J = 4.4 Hz, β-H), 10.14 (d, 4H, J = 4.3 Hz, β-H), 9.81 (d, 4H, J = 4.4 Hz, β-H), 8.87 (d, 4H, J = 4.4 Hz, β-H), 8.85 (d, 4H, J = 4.4 Hz, β-H), 8.81 (d, 4H, J = 4.4 Hz, β-H), 8.02 (d, 2H, J = 6.0 Hz, Ph-H), 7.90 (d, 2H, J = 8.7 Hz, Ph-H), 7.63 (m, 8H, Ph-H), 6.96 (m, 12H, J = 4.6 Hz, Ph-H), 3.89 (m, 24H, -O-CH$_2$-C), 0.81 (m, 24H, -O-C-CH$_2$-C),

0.28 (s, 36H, -C-CH$_3$), 0.26 (s, 72H, -C-CH$_3$). MALDI-TOF MS *m/z*: 3136.80 (M$^+$) (calcd 3133.32).

(5,15-Bis[(15'-triisopropylsilylethynyl-10',20'-bis[2''',6'''-bis(3'''',3''''-dimethyl-1'''''butyloxy)phenyl]porphinato)zinc(II)ethyn-5'-yl]-10,20-bis[2',6'-bis(3'',3''-dimethyl-1''butyloxy)phenyl]porphinato)zinc(II) (16): (5-bromo-15-triisopropylsilylethynyl-10,20-bis[2',6'-bis(3'',3''-dimethyl-1''butyloxy)phenyl]porphinato)zinc(II) (120 mg, 1.01×10^{-4} mol) and (5,15-diethynyl-10,20-bis[2',6'-bis(3'',3''dimethyl-1''-butyloxy)phenyl]porphinato)zinc(II) (41.1 mg, 4.21×10^{-5} mols) were charged into a Schlenk flask with AsPh$_3$ (30.9 mg, 1.01×10^{-4} mols) and Pd$_2$dba$_3$ (11.6 mg, 1.26×10^{-5} mol). THF: TEA (9:1 mL) solvent mixture was degassed with an Ar purge for 30 min and then transferred to the reaction flask. The reaction mixture was stirred at 60 ℃ under Ar overnight. The reaction mixture was then poured down a short silica gel column using CHCl$_3$: MeOH (49:1 mL) as the eluent. A large band was collected and the solvent stripped and then the residue was taken up in THF and put down a size exclusion column (BioRad Biobeads, SX-1) and chromatographed gravimetrically. The first band was collected and solvent removed via vacuum and the residue was purified by silica gel chromatography using CHCl$_3$: MeOH (49:1 mL) as the eluent. Yield = 114 mg (85% based on diethynyl starting material). ^{1}H NMR (500 MHz, CDCl$_3$): 10.35 (d, 8H, *β*-H), 9.64 (d, 4H, *β*-H), 9.01 (d, 8H, *β*-H), 8.86 (d, 4H, *β*-H), 7.72 (d, 6H, *β*-H), 7.05 (d, 12H, *J* = 4.6 Hz, Ph-H), 3.98 (m, 24H, -O-CH$_2$-C), 1.40 (m, 42, -SiCH(CH$_3$)$_2$), 0.89 (m, 24H, -O-C-CH$_2$-C), 0.40 (s, 36H, -C-CH$_3$), 0.37 (s, 72H, -C-CH$_3$).

(5,15-Bis[(15'-ethynyl-10',20'-bis[2''',6'''-bis(3'''',3'''''-dimethyl-1'''''butyloxy)phenyl]porphinato)zinc(II)ethyn-5'-yl]-10,20-bis[2',6'-bis(3'',3''-dimethyl-1''butyloxy)phenyl]porphinato)zinc(II) (17): Compound 16 (114 mg, 3.58×10^{-5} mol) were dissolved in THF and cooled down to 0 ℃ under Ar. TBAF (0.716 mL, 0.1 M TBAF in THF solution, 7.16×10^{-5} mol) was then added dropwise and the reaction mixture was allowed to stir for 15 min at 0 ℃. The reaction mixture was then directly poured down a short silica gel column using CHCl$_3$ as the eluent. Yield = 101.2 mg (98.4% based on compound 16). ^{1}H NMR (500 MHz, CDCl$_3$): 10.35 (d, 8H, β-H), 9.64 (d, 4H, β-H), 9.01 (d, 8H, β-H), 8.86 (d, 4H, β-H), 7.72 (d, 6H, β-H), 7.05 (d, 12H, J = 4.6 Hz, Ph-H), 4.11 (s, 2H), 3.98 (m, 24H, -O-CH$_2$-C), 0.89 (m, 24H, -O-C-CH$_2$-C), 0.40 (s, 36H, -C-CH$_3$), 0.37 (s, 72H, -C-CH$_3$).

[5,15-Bis(15'''-[(15'''''''- benzo[c][1,2,5]thiadiazole-ethyn-4'''''''-yl - 10'''''',20''''''-bis[2''''''',6'''''''-bis(3'''''''',3''''''''dimethyl-1'''''''-butyloxy)phenyl]porphinato)zinc(II)-ethyn-5''''''-yl]-10''',20'''bis[2'''',6''''-bis(3''''',3'''''-dimethyl-1'''''-butyloxy)phenyl]porphinato)zinc(II)-ethyn-5'''-yl)-10,20-bis[2',6'-bis(3'',3''-dimethyl-1''-butyloxy)phenyl)phenyl]porphinato]zinc(II) (BTD-EPZnE-PZn-EPZnE-PZn-EPZnE-BTD) (18): Coumpound 11 (50 mg, 4.13×10^{-5} mol), compound 17 (47.4 mg, 1.65×10^{-5} mol) were charged into a Schlenk Flask with Pd$_2$dba$_3$ (5.7 mg, 4.95×10^{-6} mol) and P(o-tol)$_3$ (12.1 mg, 3.96×10^{-5} mol), CuI (0.31mg, 1.65×10^{-6} mol). THF: TEA (9:1 ml) solvent mixture was degassed with an Ar purge for 30 min prior to solvent transfer. Once solvent was transferred, the reaction mixture was

stirred at 60 °C overnight under Ar. The reaction mixture was then poured down a short silica gel column using CHCl$_3$: MeOH (49:1 mL) as the eluent. A large band was collected and the solvent stripped and then the residue was taken up in THF and put down a size exclusion column (BioRad Biobeads, SX-1) and chromatographed gravimetrically. The first band was collected and solvent removed via vacuum and the residue was purified by silica gel chromatography using CHCl$_3$:MeOH (49:1 mL) as the eluent. Yield = 55 mg (68.2% based on compound 17). ^{1}H NMR (500 MHz, CDCl$_3$): 10.39 (m, 8H, β-H), 10.35 (m, 8H, β-H), 9.84 (d, 4H, β-H), 9.04 (m, 16H, β-H), 8.88 (d, 4H, β-H), 7.77 (d, 2H, Ph-H), 7.74 (m, 12H, Ph-H), 7.55 (d, 2H, Ph-H), 7.07 (m, 20H, Ph-H), 4.03 (m, 40H, -O-CH$_2$-C), 0.89 (m, 40H, -O-C-CH$_2$-C), 0.38 (m, 180H, -C-CH$_3$). MALDI-TOF MS *m/z*: 5016.80 (M$^+$) (calcd 5026.19).

(5- Triisopropylsilylethynyl-15-[10',20'-bis[2''',6'''-bis(3'''',3'''''-dimethyl-1''''butyloxy)phenyl]porphinato)zinc(II)-ethyn-5'-yl] -10,20-bis[2',6'-bis(3'',3''-dimethyl-1''butyloxy)phenyl]porphinato)zinc(II) (19). (5-Bromo-15-triisopropylsilylethynyl-10,20-bis[2',6'-bis(3,3-dimethyl-1-butyloxy)phenyl]porphinato)zinc(II) (74.8 mg, 6.31×10^{-5} mol), (5-ethynyl-10,20-bis[2',6'-bis(3,3-dimethyl-1-butyloxy)phenyl]porphinato)zinc(II) (50 mg, 5.26×10^{-5} mol) were charged into a Schlenk Flask with Pd$_2$dba$_3$ (7.2 mg, 7.89×10^{-6} mol) and AsPh$_3$ (19.2 mg, 6.31×10^{-5} mol). THF: TEA (9:1 ml) solvent mixture was degassed with an Ar purge for 30 min prior to solvent transfer. Once solvent was transferred, the reaction mixture was stirred at 60 °C overnight under Ar. Once solvent was transferred, the reaction mixture was stirred at 60 °C overnight under Ar. The reaction mixture was then poured

down a short silica gel column using CHCl$_3$: MeOH (49:1 mL) as the eluent. A large band was collected and the solvent stripped and then the residue was taken up in THF and put down a size exclusion column (BioRad Biobeads, SX-1) and chromatographed gravimetrically. The first band was collected and solvent removed via vacuum and the residue was purified by silica gel chromatography using CHCl$_3$:MeOH (49:1 mL) as the eluent.   Yield = 82 mg (75.8 % based on the 50 mg of 5-Bromo-15-triisopropylsilylethynyl porphyrin starting material). ^{1}H NMR (500 MHz, CDCl$_3$): 10.43 (d, 2H, J = 4.6 Hz, β-H), 10.42 (d, 2H, J = 4.4 Hz, β-H), 10.03 (s, 1H, *meso*-H), 9.65 (d, 2H, J = 4.5 Hz, β-H), 9.23 (d, 2H, J = 4.4 Hz, β-H), 9.10 (d, 2H, J = 4.6 Hz, β-H), 8.99 (d, 2H, J = 4.4 Hz, β-H), 8.95 (d, 2H, J = 4.4 Hz, β-H), 8.86 (d, 2H, J = 4.4 Hz, β-H), 7.73 (m, 4H, Ph-H), 7.05 (m, 8H, Ph-H), 3.98 (m, 16H, -O-CH$_2$-C), 1.43 (m, 21, -SiCH(CH$_3$)$_2$), 0.89 (m, 16H, -O-C-CH$_2$-C), 0.45 (s, 36H, -C-CH$_3$), 0.42 (s, 36H, -C-CH$_3$).

(5-Ethynyl-15-[10',20'-bis[2''',6'''-bis(3'''',3''''-dimethyl-1''''butyloxy)phenyl]porphinato)zinc(II)-ethyn-5'-yl] -10,20-bis[2',6'-bis(3'',3''-dimethyl-1''butyloxy)phenyl]porphinato)zinc(II) (20). Compound 19 (80 mg, 3.89×10^{-5} mol) were dissolved in THF and cooled down to 0 ℃ under Ar. TBAF (0.778 mL, 0.1 M TBAF in THF solution, 7.78×10^{-5} mol) was then added dropwise and the reaction mixture was allowed to stir for 15 min at 0 ℃. The reaction mixture was then directly poured down a short silica gel column using CHCl$_3$ as the eluent. Yield = 65 mg (87.9% based on compound 16). ^{1}H NMR (500 MHz, CDCl$_3$): 10.43 (d, 2H, J = 4.6 Hz, β-H), 10.42 (d, 2H, J = 4.4 Hz, β-H), 10.03 (s, 1H, *meso*-H), 9.65 (d, 2H, J = 4.5 Hz, β-H), 9.23 (d, 2H, J = 4.4 Hz, β-H), 9.10 (d, 2H, J = 4.6 Hz, β-H), 8.99 (d, 2H, J = 4.4 Hz,

β-H), 8.95 (d, 2H, J = 4.4 Hz, β-H), 8.86 (d, 2H, J = 4.4 Hz, β-H), 7.73 (m, 4H, Ph-H),

7.05 (m, 8H, Ph-H), 4.10 (s, 2H), 3.98 (m, 16H, -O-CH$_2$-C), 0.89 (m, 16H, -O-C-CH$_2$-C),

0.45 (s, 36H, -C-CH$_3$), 0.42 (s, 36H, -C-CH$_3$).

4,7-Diiodobenzo[c][1,2,5]thiadiazole (21). Benzo[c][1,2,5]thiadiazole (3.20 g,

2.35×10^{-2} mol), I$_2$ (13.2 g, 5.20×10^{-2} mol), Ag$_2$SO$_4$ (7.34 g, 2.35×10^{-2} mol) were added

to a 100-ml three neck round bottom flask. 35ml concentrated H$_2$SO$_4$ was added to the

mixture and the reaction mixture was stirred at 110 ℃ for 14 hours under N$_2$. After

cooling, the reaction mixture was poured into ice water and the precipitate was collected

by filtration. This precipitate was washed with CHCl$_3$. The organic solution was then

washed with saturated NaHSO$_3$ aqueous solution and brine respectively for three times,

and dried over Na$_2$SO$_4$. The product was then chromatographed on silica gel with 1:1

hexanes:CHCl$_3$ as the eluant. Yield = 3.95 g (43.3 % based on 3.20 g of

benzothiadiazole). ^{1}H NMR (500 MHz, CDCl$_3$): 7.75 (s, 12H, Ph-H).

4,7-Bis[(15-(10',20'-bis[2'',6''-bis(3''',3''''-dimethyl-1'''-

butyloxy)phenyl]porphinato)zinc(II)   ethyn-5'-yl)-10,20-bis[2',6'-bis(3'',3''-

dimethyl-1''-butyloxy)phenyl]porphinato)zinc(II)-5-

ylethynyl]benzo[c][1,2,5]thiadiazole   (PZn-EPZnE-BTD-EPZnE-PZn)   (22).

Compound 20 (50.0 mg, 2.63×10^{-5} mol), Compound 21 (4.27 mg, 1.10×10^{-6} mol) were

charged into a Schlenk Flask with Pd$_2$dba$_3$ (3.03 mg, 3.31×10^{-7} mol) and AsPh$_3$ (8.05 g,

2.63×10^{-5} mol). THF: iPr$_2$NH (9:1 ml) solvent mixture was degassed with an Ar purge

for 30 min prior to solvent transfer. Once solvent was transferred, the reaction mixture

was stirred at 60 ℃ overnight under Ar. The reaction mixture was then poured down a short silica gel column using $CHCl_3$: MeOH (49:1 mL) as the eluent. A large band was collected and the solvent stripped and then the residue was taken up in THF and put down a size exclusion column (BioRad Biobeads, SX-1) and chromatographed gravimetrically. The first band was collected and solvent removed via vacuum and the residue was purified by silica gel chromatography using $CHCl_3$:MeOH (49:1 mL) as the eluent. Yield = 35 mg (80.6 % based on 4.27 mg of compound 21). ^{1}H NMR (500 MHz, THF-d_8): 10.33 (d, 4H, J = 7.3 Hz, β-H), 10.28 (d, 4H, J = 7.0 Hz, β-H), 10.07 (d, 4H, J = 8.3 Hz, β-H), 9.90(s, 2H, $meso$-H), 9.13 (d, 4H, J = 7.0 Hz, β-H), 9.06 (d, 4H, J = 7.4 Hz, β-H), 8.94 (m, 8H, β-H), 8.88 (d, 4H, J = 4.2 Hz, β-H), 8.40 (s, 2H, Ph-H), 7.79 (m, 8H, Ph-H), 7.17 (m, 16H, Ph-H), 4.01 (m, 32H, -O-CH_2-C), 0.87 (m, 32H, -O-C-CH_2-C), 0.41 (d, 72H, J = 5.2 Hz, -C-CH_3), 0.36 (d, 72H, J = 5.1 Hz, -C-CH_3). MALDI-TOF MS m/z: 3942.10 (M^+) (calcd 3937.79).

1,2-Bis[(15-triisoprpylsilylethynyl-10,20-bis[2',6'-bis(3'',3''-dimethyl-1''butyloxy)phenyl]porphinato)zinc(II)-5-yl]ethyne (23): (5-Bromo-15-triisopropylsilylethynyl-10,20-bis[2',6'-bis(3'',3''-dimethyl-1''butyloxy)phenyl]porphinato)zinc(II) (150 mg, 1.26 x 10^{-4} mol) and (5-ethynyl-15-triisopropylsilylethynyl-10,20-bis[2',6'-bis(3'',3''-dimethyl-1''butyloxy)phenyl]porphinato)zinc(II) (106 mg, 9.40×10^{-5} mol) were charged into a Schlenk flask with $AsPh_3$ (46.3 mg, 1.51×10^{-4} mol) and Pd_2dba_3 (17 mg, 1.89×10^{-5} mol). THF: TEA (9:1 mL) solvent mixture was degassed with an Ar purge for 30 min and then transferred to the reaction flask. The reaction mixture was stirred at 60 ℃ under Ar

overnight. The reaction mixture was then poured down a short silica gel column using CHCl$_3$: MeOH (49:1 mL) as the eluent. A large band was collected and the solvent stripped and then the residue was taken up in THF and put down a size exclusion column (BioRad Biobeads, SX-1) and chromatographed gravimetrically. The first band was collected and solvent removed via vacuum and the residue was purified by silica gel chromatography using CHCl$_3$: MeOH (49:1 mL) as the eluent. Yield = 164mg (78.1% based on 106 mg 5-ethynyl-15-triisopropylsilylethynyl porphyrin starting material). ^{1}H NMR (500 MHz, CDCl$_3$): 10.36 (d, 4H, β-H), 9.67 (d, 4H, β-H), 9.00 (d, 4H, β-H), 8.88 (d, 4H, β-H), 7.75 (m, 4H, Ph-H), 7.06 (m, 8H, Ph-H), 3.98 (m, 16H, -O-CH$_2$-C), 1.46 (m, 21H, -SiCH(CH$_3$)$_2$), 0.91 (m, 16H, -O-C-CH$_2$-C), 0.38 (d, 72H, -C-CH$_3$).

1,2-Bis[(15-ethynyl-10,20-bis[2',6'-bis(3'',3''-dimethyl-1''butyloxy)phenyl]porphinato)zinc(II)-5-yl]ethyne (24): Compound 23 (150 mg, 6.71×10^{-5} mol) was charged in a Schlenk Fask and dissolved in THF and cooled to 0 ℃ while under Ar. Tetrabutylammonium fluoride (TBAF) (1.34 mL, 0.1 M TBAF solution in THF, 1.34×10^{-4} mol) was added dropwise to the reaction mixture and allowed to stir for 15 min at 0 ℃ under Ar. At 15 min the reaction mixture was poured down a pre-packed CHCl3 silica gel plug and the first band was collected and solvent removed via vacuum. Yield = 115 mg (89.1% based on compound 23). ^{1}H NMR (500 MHz, CDCl$_3$): 10.32 (d, 4H, β-H), 9.58 (d, 4H, β-H), 8.96 (d, 4H, β-H), 8.84 (d, 4H, β-H), 7.73 (m, 4H, Ph-H), 7.06 (m, 8H, Ph-H), 4.10 (s, 2H), 3.96 (m, 16H, -O-CH$_2$-C), 0.91 (m, 16H, -O-C-CH$_2$-C), 0.40 (d, 72H, -C-CH$_3$).

(5-(10',20'-Bis[2'',6''-bis(3''',3'''-dimethyl-1'''butyloxy)phenyl]porphinato)zinc(II)-ethyn-5'-yl)-15-[7'-bromobenzo[*c*][1,2,5]thiadiazole- ethyn-4'-yl] -10,20-bis[2',6'-bis(3'',3''-dimethyl-1''butyloxy)phenyl]porphinato)zinc(II) (25). Compound 20 (0.200g, 1.05×10^{-4} mol), 4, 7-dibromobenzo[*c*][1,2,5]thiadiazole (123.8 mg, 4.21×10^{-4} mol) were charged into a Schlenk Flask with Pd$_2$dba$_3$ (14.4 mg, 1.57×10^{-5} mol) and AsPh$_3$ (38.6 mg, 1.26×10^{-4} mol). THF: TEA (9:1 ml) solvent mixture was degassed with an Ar purge for 30 min prior to solvent transfer. Once solvent was transferred, the reaction mixture, was stirred at 50 ℃ overnight under Ar. After the solvent was evaporated, the residue was then poured down a short silica gel column using CHCl$_3$: MeOH (49:1 mL) as the eluent. A large band was collected and the solvent stripped and then the residue was taken up in THF and put down a size exclusion column (BioRad Biobeads, SX-1) and chromatographed gravimetrically. The second band was collected and solvent removed via vacuum and the residue was purified by silica gel chromatography using CHCl$_3$: MeOH (49:1 mL) as the eluent. Yield = 108 mg (48.7 % based on 0.200 mg of the porphyrin starting material). ^{1}H NMR (500 MHz, CDCl$_3$): 10.43 (d, 2H, $J = 4.6$ Hz, β-H), 10.42 (d, 2H, $J = 4.4$ Hz, β-H), 10.03 (s, 1H, *meso*-H), 9.65 (d, 2H, $J = 4.5$ Hz, β-H), 9.23 (d, 2H, $J = 4.4$ Hz, β-H), 9.10 (d, 2H, $J = 4.6$ Hz, β-H), 8.99 (d, 2H, $J = 4.4$ Hz, β-H), 8.95 (d, 2H, $J = 4.4$ Hz, β-H), 8.86 (d, 2H, $J = 4.4$ Hz, β-H), 8.10 (d, 1H, $J = 6.1$ Hz, Ph-H), 7.73 (m, 5H, Ph-H), 7.05 (m, 8H, Ph-H), 3.98 (m, 16H, -O-CH$_2$-C), 1.43 (m, 21, -SiCH(CH$_3$)$_2$), 0.89 (m, 16H, -O-C-CH$_2$-C), 0.45 (s, 36H, -C-CH$_3$), 0.42 (s, 36H, -C-CH$_3$).

1,2-Bis(4-[10,20-bis[2',6'-bis(3'',3''-dimethyl-1''-butyloxy)phenyl]porphinato)zinc(II)-5-ylethynyl],7-[(15-(10',20'-bis[2'',6''-bis(3''',3'''-dimethyl-1''''-butyloxy)phenyl]porphinato)zinc(II)ethyn-5'-yl)-10,20-bis[2',6'-bis(3'',3''-dimethyl-1''-butyloxy)phenyl]porphinato)zinc(II)-5-ylethynyl]benzo[*c*][1,2,5]thiadiazole (PZn-EPZnE-BTD-EPZnE-E-PZnE-BTD-EPZnE-PZn) (26). Compound 25 (181.4 mg, 8.59×10^{-5} mol), compound 24 (68.9 mg, 3.58×10^{-5} mol) were charged into a Schlenk Flask with Pd_2dba_3 (9.83 mg, 1.07×10^{-5} mol) and P(*o*-tol)$_3$ (26.1 mg, 8.59×10^{-5} mol). THF: TEA (9:1 ml) solvent mixture was degassed with an Ar purge for 30 min prior to solvent transfer. Once solvent was transferred, the reaction mixture was stirred at 60 °C overnight under Ar. The reaction mixture was then poured down a short silica gel column using $CHCl_3$: MeOH (49:1 mL) as the eluent. A large band was collected and the solvent stripped and then the residue was taken up in THF and put down a size exclusion column (BioRad Biobeads, SX-1) and chromatographed gravimetrically. The first band was collected and solvent removed via vacuum and the residue was purified by silica gel chromatography using $CHCl_3$: MeOH (49:1 mL) as the eluent. Yield = 68.9 mg (32% based on diethynyl starting material). ^{1}H NMR (500 MHz, $CDCl_3$): 10.02 (d, 4H, *J* = 4.4 Hz, *β*-H), 9.94 (d, 4H, *J* = 4.5 Hz, *β*-H), 9.86 (s, 2H, *meso*-H), 9.08 (d, 4H, *J* = 4.2 Hz, *β*-H), 8.96 (d, 4H, *J* = 4.3 Hz, *β*-H), 8.86 (d, 4H, *J* = 4.5 Hz, *β*-H), 8.81(d, 4H, *J* = 4.2 Hz, *β*-H), 8.26 (s, 4H, Ph-H), 7.70 (t, 6H, *J* = 8.6 Hz, Ph-H), 7.02 (d, 6H, *J* = 4.6 Hz, Ph-H), 7.00 (d, 6H, *J* = 4.7 Hz, Ph-H), 3.89 (m, 24H, -O-CH$_2$-C), 0.87 (m, 24H, -O-C-CH$_2$-C), 0.34 (s, 36H, -C-CH$_3$), 0.30 (s, 72H, -C-CH$_3$). MALDI-TOF MS *m/z*: 6017.79 (M$^+$) (calcd 6006.49).
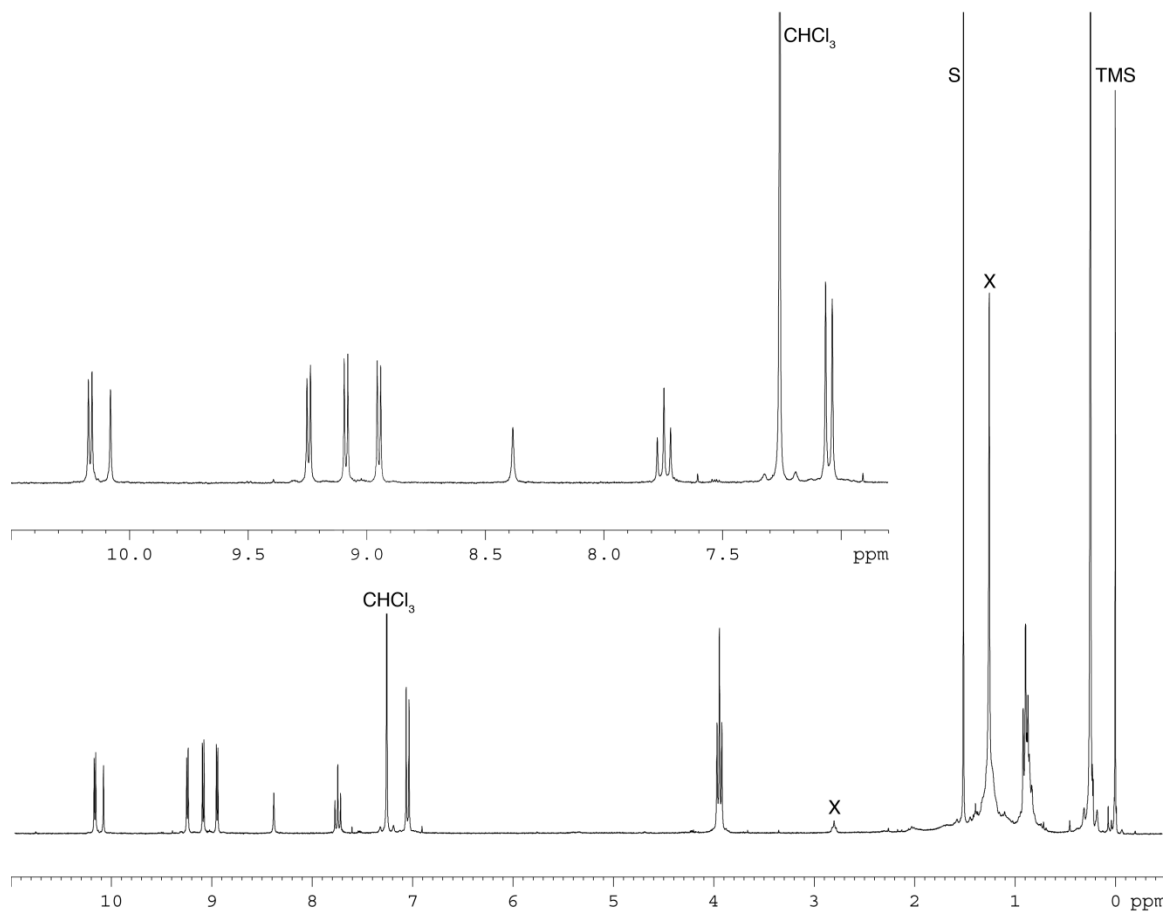
Figure 2.2 ^{1}H NMR (500 MHz) of PZnE-BTD-EPZn in CDCl$_3$. The designations s and x

denote solvent and impurity peaks, respectively.
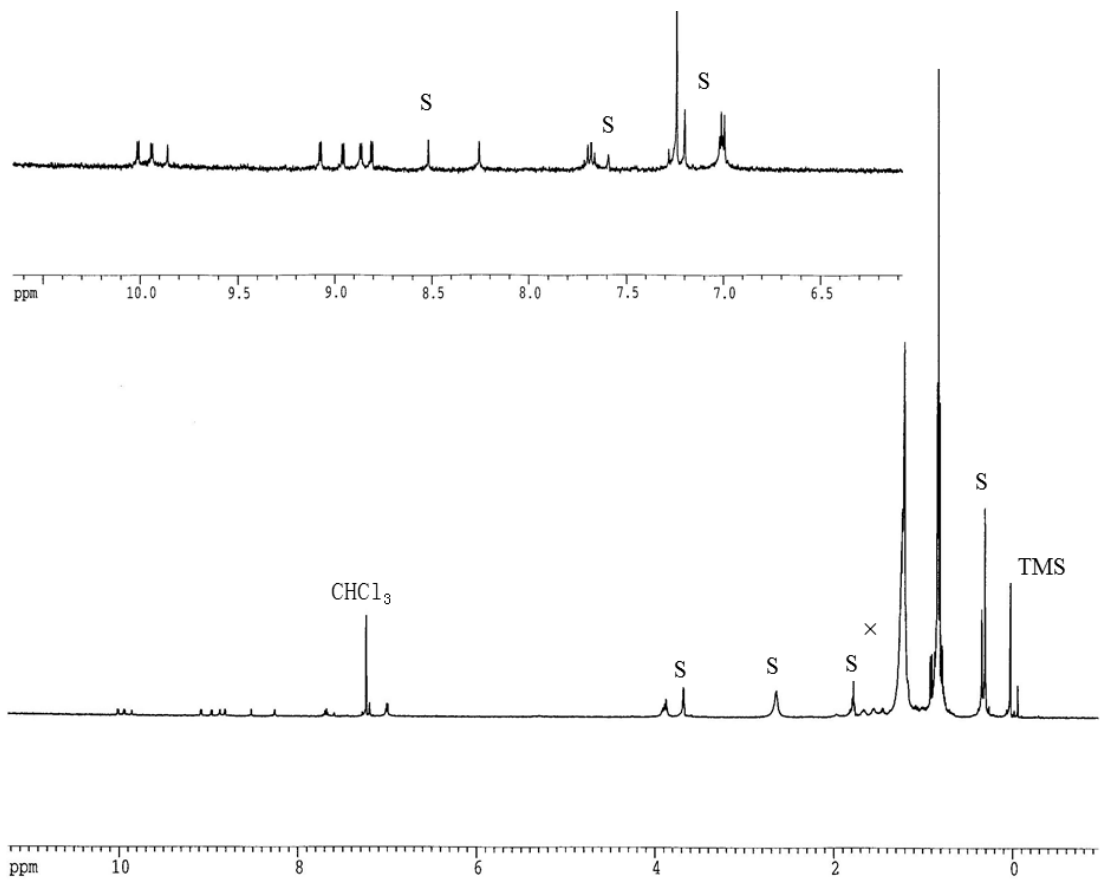
Figure 2.3 ^{1}H NMR (500 MHz) of PZnE-BTD-EPZnE-BTD-EPZn in CDCl$_3$ with 1 drop

of pyridine-d$_5$. The designations s and x denote solvent and impurity peaks, respectively.
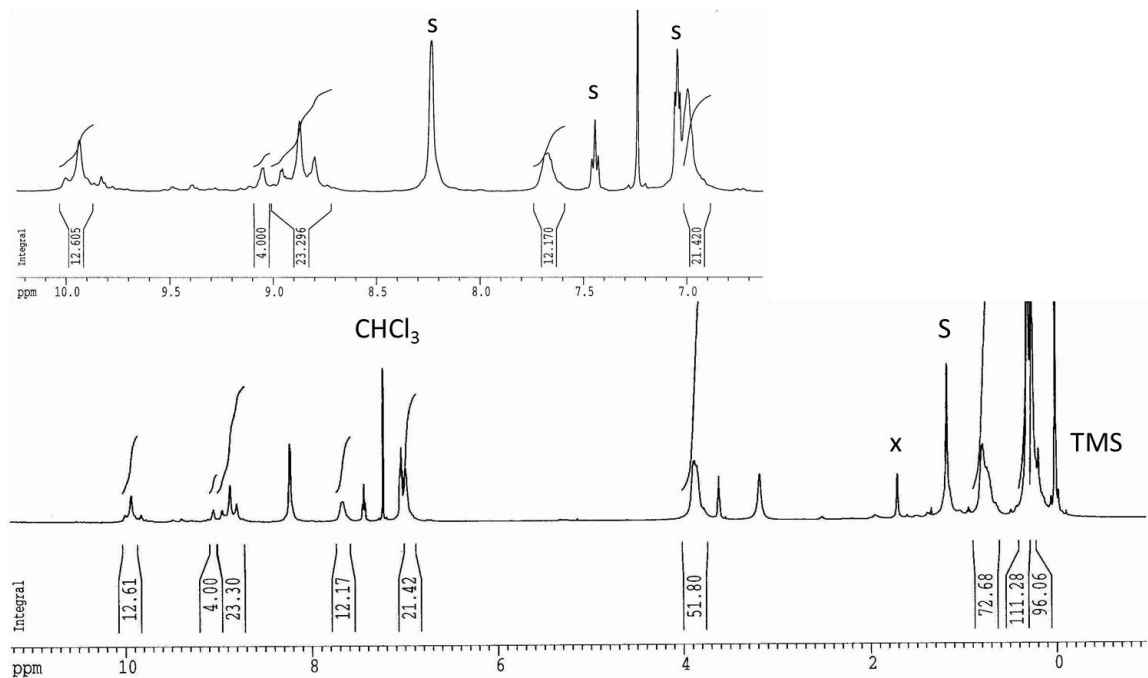
Figure 2.4 ^{1}H NMR (500 MHz) of PZnE-BTD-EPZnE-BTD-EPZnE- BTD-EPZnE-BTD-EPZn in CDCl$_3$ with 1 drop of pyridine-d$_5$. The designations s and x denote solvent and impurity peaks, respectively.
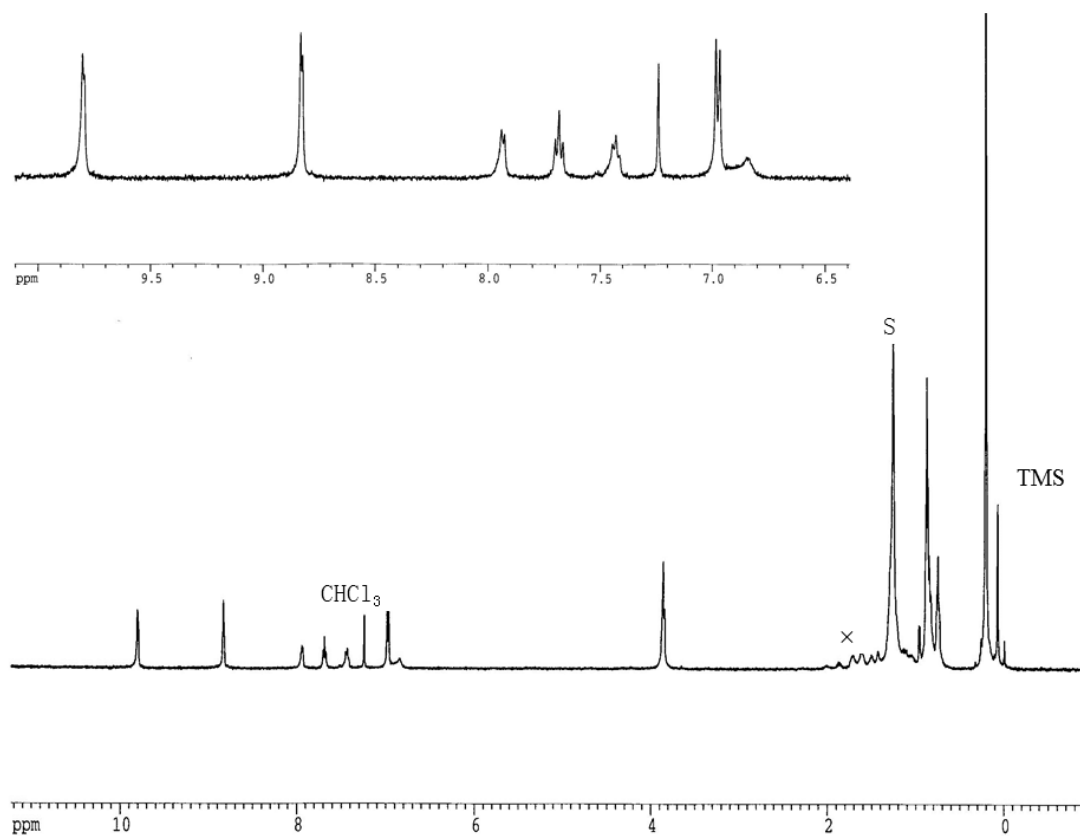
Figure 2.5 ^{1}H NMR (500 MHz) of **BTD-EPZnE-BTD** in CDCl₃. The designations s and

x denote solvent and impurity peaks, respectively.
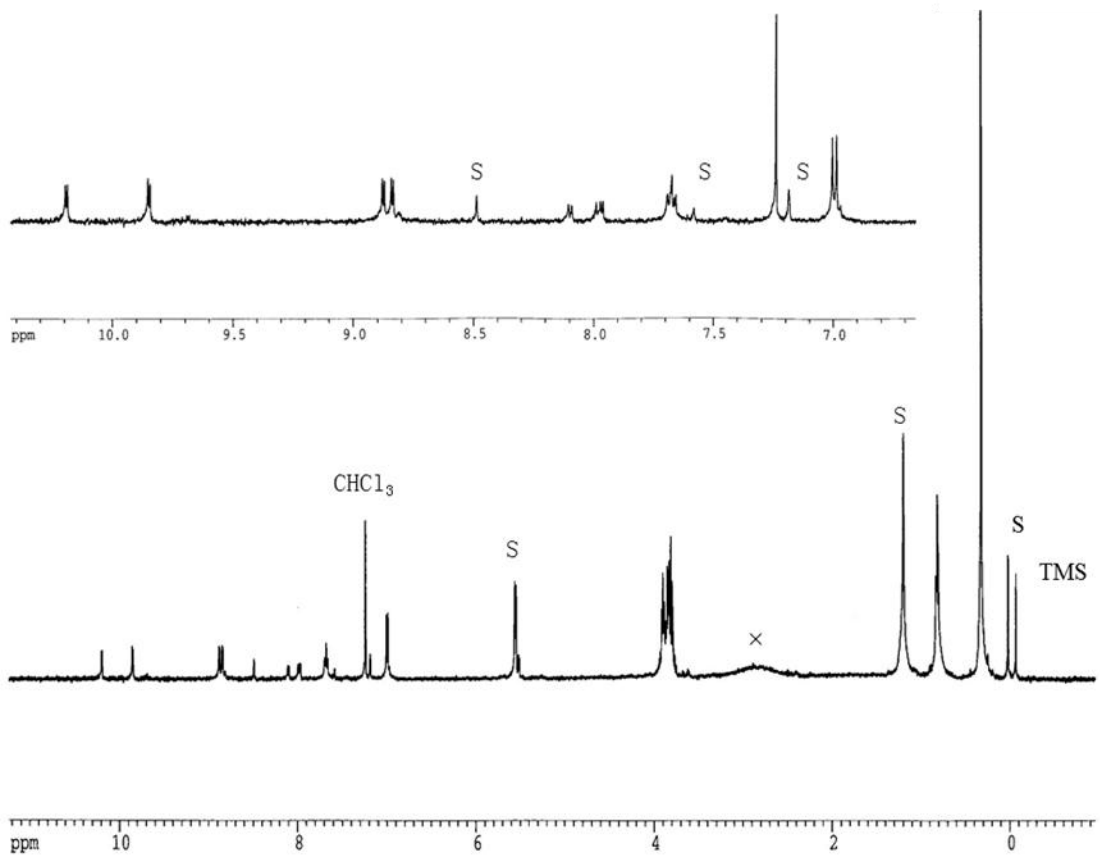
Figure 2.6 ^{1}H NMR (500 MHz) of BTD-EPZnE-PZnE-BTD in CDCl$_3$ with 1 drop of pyridine-d$_5$. The designations s and x denote solvent and impurity peaks, respectively.
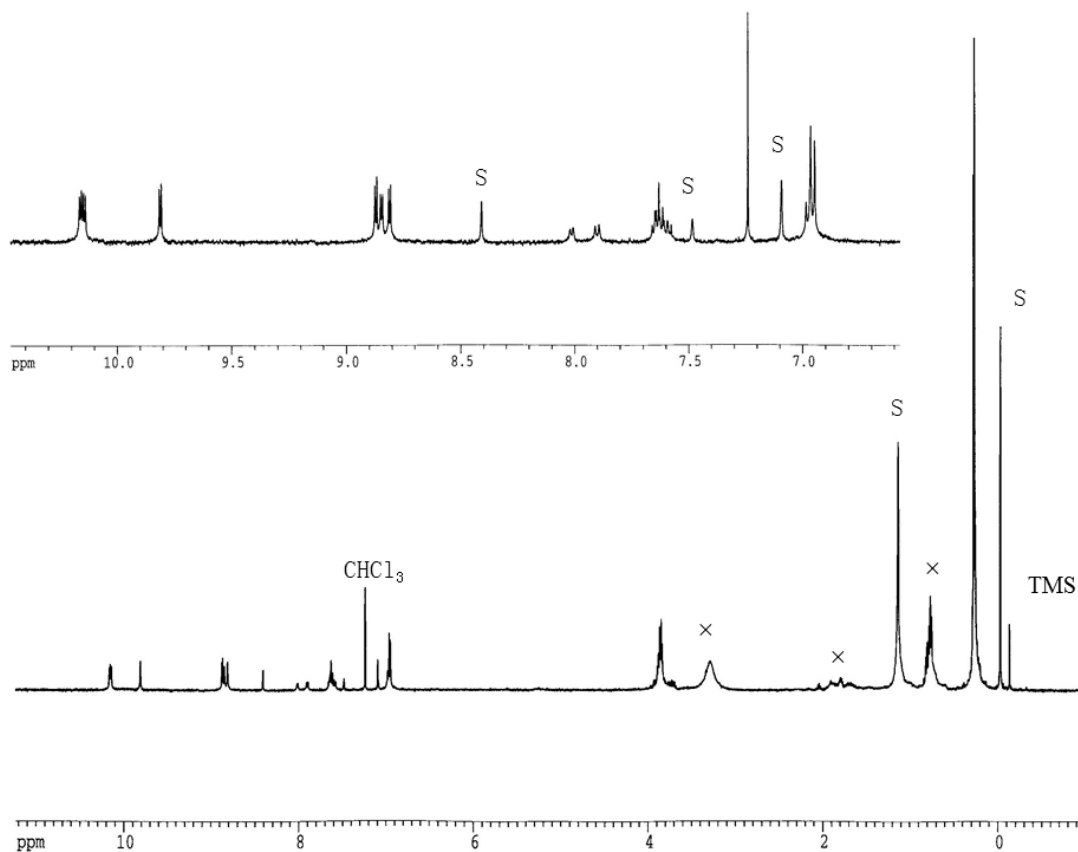
Figure 2.7 ^{1}H NMR (500 MHz) of **BTD-EPZn-EPZnE-PZnE-BTD** in CDCl$_3$ with 1 drop of pyridine-d$_5$. The designations s and x denote solvent and impurity peaks, respectively.
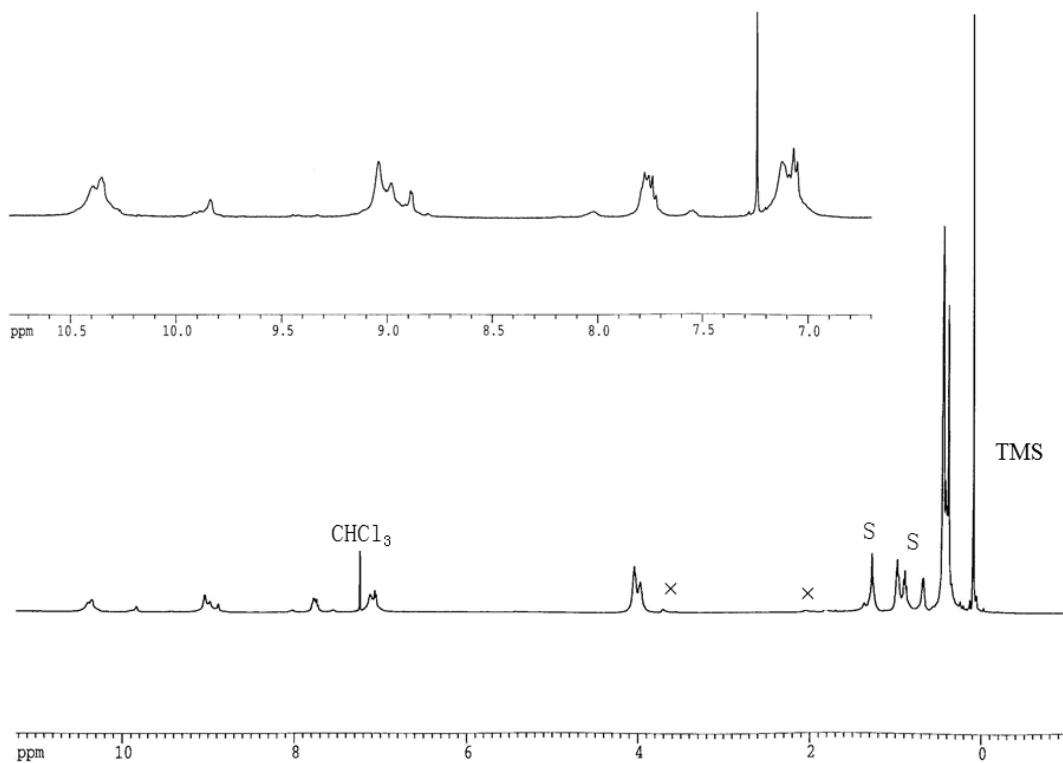
Figure 2.8 ^{1}H NMR (500 MHz) of BTD-EPZnE-PZn-EPZnE-PZn-EPZnE-BTD in CDCl$_3$ with 1 drop of pyridine-d$_5$. The designations s and x denote solvent and impurity peaks, respectively.
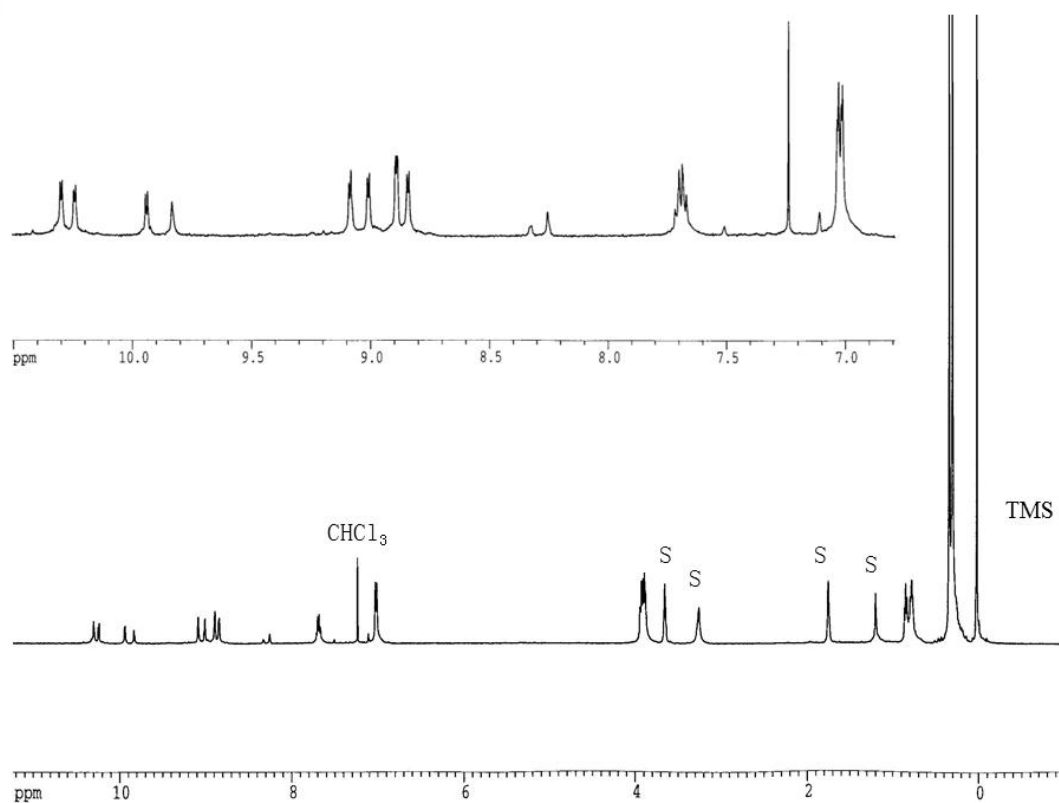
Figure 2.9 ^{1}H NMR (500 MHz) of PZnE-EPZnE-BTD-EPZnE-PZn in CDCl$_3$ with 1 drop of pyridine-d$_5$. The designations s and x denote solvent and impurity peaks, respectively.
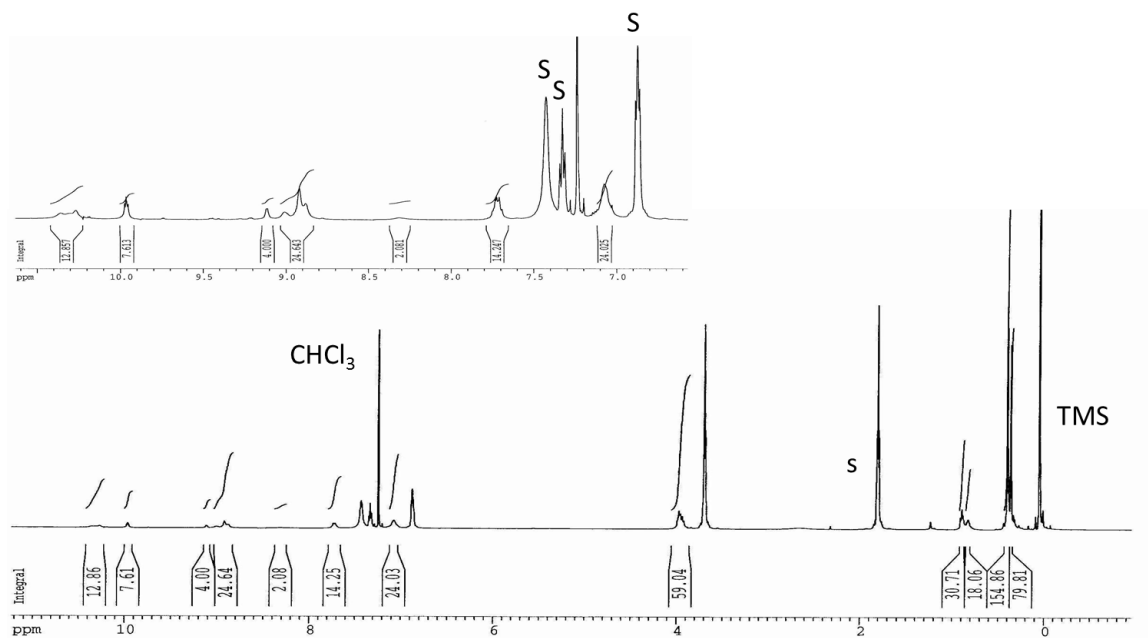
Figure 2.10 ^{1}H NMR (500 MHz) of PZn-EPZnE-BTD-EPZnE-PZnE-BTD-EPZnE-PZn in CDCl$_3$ with 1 drop of pyridine-d$_5$. The designations s and x denote solvent and impurity peaks, respectively.

2.3.4. Fluorescence Quantum Yield Determination

The fluorescence quantum yields ϕ_f of these species were determined by the reference method,[40] using the relation:

$$\emptyset_f^x = \frac{A_S n_x^2 \int F_x}{A_x n_s^2 \int F_S} \emptyset_f^s$$

where $\int F_x$ and $\int F_s$ are the respective, total integrated fluorescence intensities of the unknown and emission standard, A_x and A_s are the corresponding wavelength-specific absorbances of the unknown and standard, respectively, and $\emptyset_f^s$ is the accepted fluorescence quantum yield value for the standard chromophore. The quantity $(n_x/n_s)^2$ represents the solvent refractive index correction. The concentrations of all samples were adjusted such that their absorbance was between 0.005 and 0.05 at the excitation wavelength to minimize complications due to reabsorption effects. Fluorescence spectra obtained for the (porphinato)metal complexes, as well as the chromophores used as emission standards, were corrected to account for the wavelength-dependent efficiency of the detection system which was determined using the spectral output of a calibrated light source. All samples were degassed via purging with a stream of argon gas for ten minutes. Secondary corrections to the emission spectra used to determine ϕ_f (such as energy-dependent intensity corrections necessitated by the variable band pass/constant wavelength resolution data acquisition mode of the grating monochromator) were performed as outlined by Fery-Forgues. Quantum yields were determined using freebase tetraphenylporphyrin ($\phi_f = 0.13$ in benzene[5]) as a standard benchmark. The standard error in quantum yields determined by this method is typically taken as $\pm 10\%$ of the reported value. The ϕ_f entries correspond to the average of values

obtained from at least six independent measurements; corresponding standard deviations from the mean are also listed.

2.4. Results and Discussion

2.4.1. Synthesis

Structures of the BTD conjugated porphyrin supermolecules are shown in **Figure 2.1**. These BTD conjugated porphyrin species were synthesized by palladium (Pd)-mediated cross-coupling reactions involving appropriately substituted (porphinato)zinc(II) (PZn) compounds and BTD units. The PZn-containing structures exploit 2',6'-bis(3,3-dimethyl-1-butyloxy)phenyl groups as 10- and 20-*meso*-porphyrin substituents, which facilitate excellent solubility and straightforward assignment of ^{1}H-NMR spectra.[22, 39] 4,7-Diethynylbenzo[*c*][1,2,5]thiadiazole (**E-BTD-E**) were used as proquinodal spacer units.

The nature of the functionalized PZn and BTD moieties used in the synthesis of the corresponding BTD conjugated porphyrin complexes varied with porphyrin conjugation degree. In our first attempt, **PZn-(BTD-PZn)$_n$** structure featuring a **E-BTD-E** spacer unit in-between porphyrin monomers was synthesized (**Scheme 2.1**). The synthesis of BTD spaced porphyrin dimer **PZnE-BTD-EPZn** was via a Pd-mediated coupling reaction between PZnE and Br-BTD-Br. The synthesis of BTD spaced porphyrin trimer **PZnE-BTD-EPZnE-BTD-EPZn** can be done using two different routes: coupling of PZnE-BTDE and Br-PZn-Br or coupling of PZnE-BTD-Br and EPZnE. The first method has a lower yield than the second method due to the low stability of the PZnE-BTDE compound. For the synthsis of the BTD spaced porphyrin pentamer **PZnE-BTD-EPZnE-BTD-EPZnE-BTD-EPZnE-BTD-EPZn**, there are many

possible routes such as coupling two equivalent of BTD-porphyrin dimer to one equivalent of BTD-porphyrin monomer, or coupling two equivalent of BTD-porphyrin monomer to one equivalent of BTD-porphyrin trimer. The experimental results indicated that the optimized route was to conjugate small porphyrin oliogomers to large porphyrin oligomers. Considering the stability of the starting materials, the coupling reaction was performed between Br-BTD-EPZn monomer and EPZnE-PZn-EPZnE trimer with a 32% yield of **PZnE-BTD-EPZnE-BTD-EPZnE-BTD-EPZnE-BTD-EPZn**, while the yield from other synthetic routes was significantly lower (8-10%).
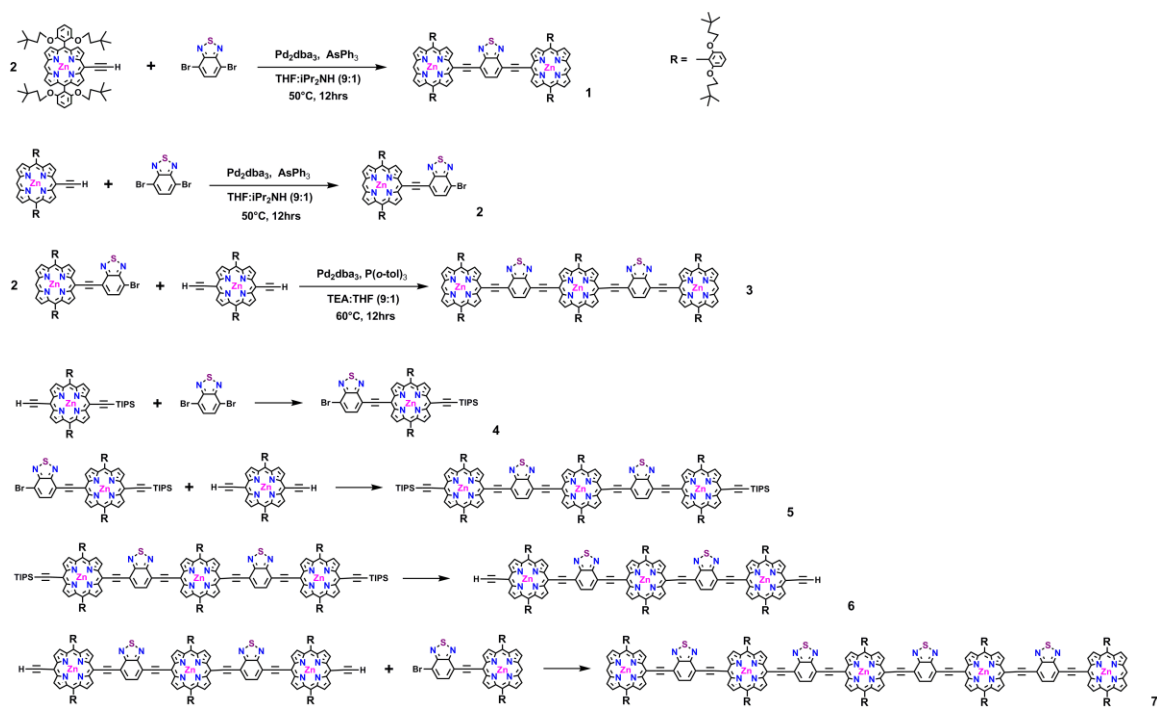
Scheme 2.1 Synthesis of PZn-(BTD-PZn)$_n$ compounds.

Next, we synthesized **BTD-(PZn)ₙ-BTD** compounds featuring the **BTD** spacer unit at the two ends of conjugated porphyrin oligomers (**Scheme 2.2**). The synthesis of **BTD-EPZnE-BTD** monomer was by coupling Br-BTD to EPZnE, considering that E-BTD has a very poor stability. The synthesis of **BTD-EPZnE-PZnE-BTD** dimer was by BTD-EPZnE conjugation with Br-PZnE-BTD. Moreover, the synthesis of **BTD-EPZnE-PZn-EPZnE-BTD** trimer was by coupling BTD-EPZnE to Br-PZn-Br which has a better reaction yield compare to a similar coupling reaction of BTD-EPZn-Br and EPZnE. For synthesis of **BTD-EPZnE-PZn-EPZnE-PZn-EPZnE-BTD** pentamer, as suggested by our previous results that conjugating small porphyrin monomers to large porphyrin oligomers offers a better reaction yield, the optimized route was to conjugate BTD-EPZn-Br with EPZnE-PZn-EPZnE.

Scheme 2.2 Synthesis of BTD-(PZn)$_n$-BTD compounds.
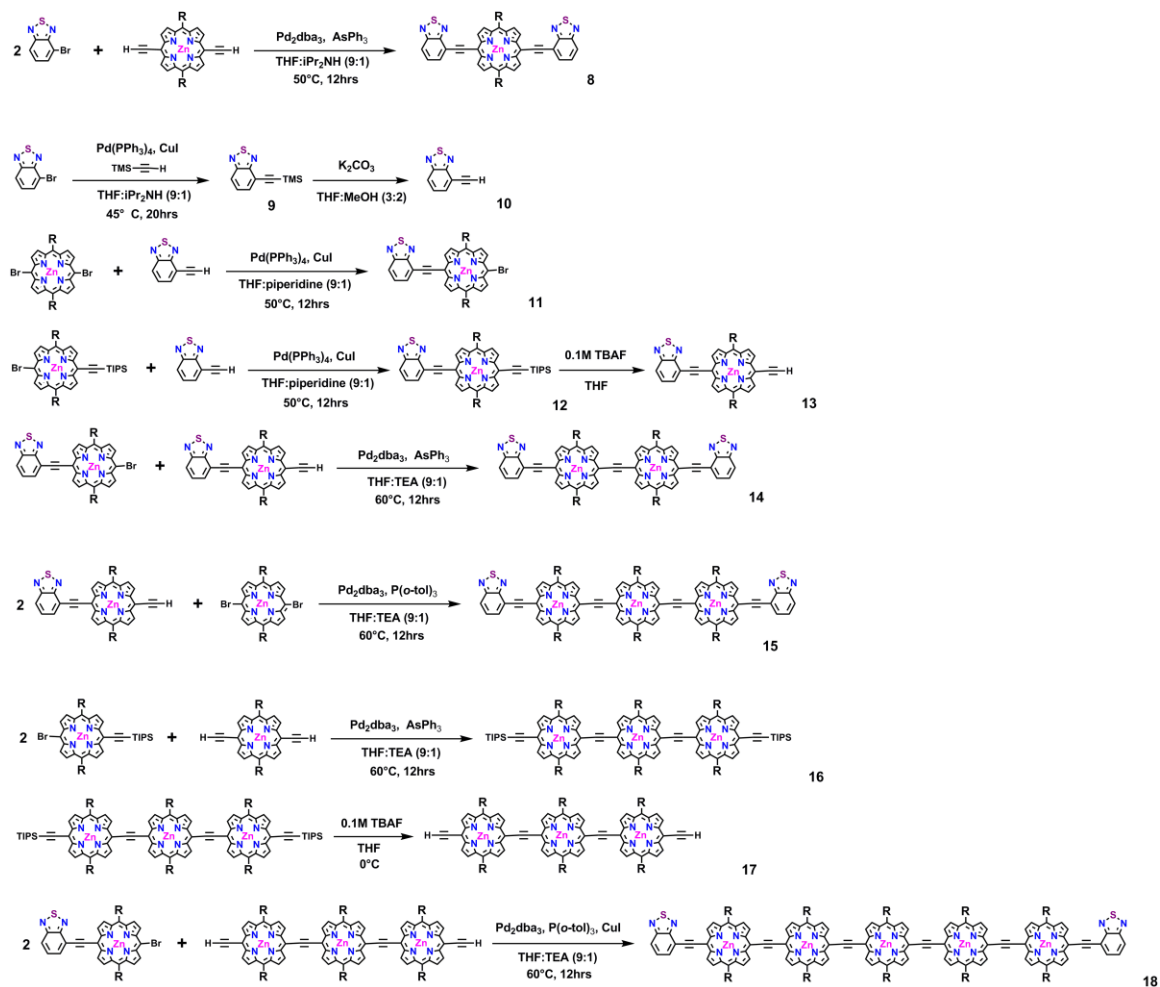
Finally, **(PZn)$_2$-(BTD-(PZn)$_2$)$_n$** with BTD spacer in-between diporphyrin oligomers were synthesized (**Scheme 2.3**). Different from our previous synthetic strategy of coupling small porphyrin monomers to large porphyrin oligomers, the synthesis of **PZn-EPZnE-BTD-EPZnE-PZn** internal tetramer was by adding two equivalents of large porphyrin dimer oligomers to a small BTD monomer. The reason for using this synthetic route rather than conjugating two equivalent of EPZn monomer to one equivalent of Br-PZnE-BTD-EPZn-Br dimer was due to the difficulty of synthesize Br-PZnE-BTD-EPZn-Br dimer which involved very difficult separation steps and low reaction yields. Therefore, Br-BTD-Br monomer was used to react with the PZn-EPZnE to produce the desired **PZn-EPZnE-BTD-EPZnE-PZn** internal tetramer. Similarly, for synthesis of **PZn-EPZnE-BTD-EPZnE-PZnE-BTD-EPZnE-PZn** internal hexamer, PZn-EPZnE-BTD-Br was coupled to EPZnE-PZnE. This reaction scheme was found to involve the least reaction steps and the highest reaction yield out of all possible synthetic routes.
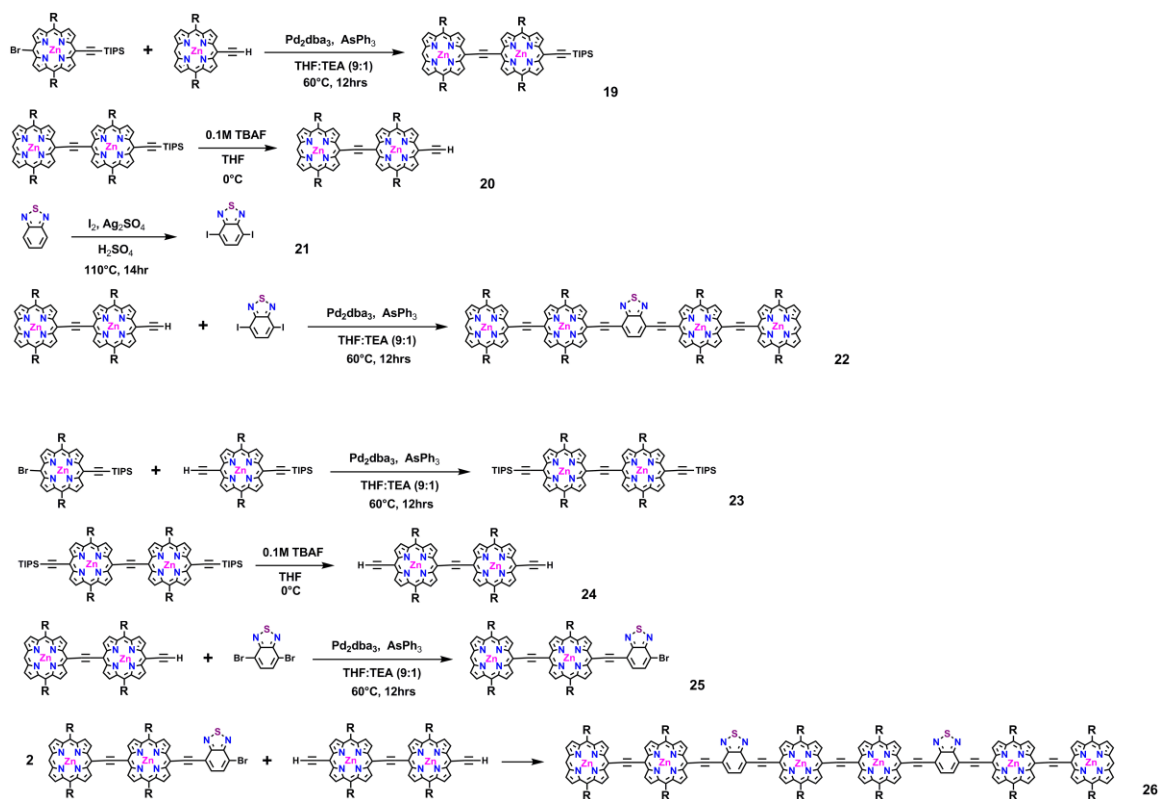
Scheme 2.3 Synthesis of (PZn)$_2$-(BTD-(PZn)$_2$)$_n$ compounds.

2.4.2. Electronic Absorption and Emission Spectra

Figure 2.11 displays the representative electronic absorption and emission spectra of the BTD conjugated porphyrin compounds **PZn-(BTD-PZn)$_n$**, **(PZn)$_2$-(BTD-(PZn)$_2$)$_n$** and **BTD-(PZn)$_n$-BTD**. These BTD spaced (porphinato)zinc(II) oligomers have electronic spectra that are not components of their respective monomer building blocks, due to the large ground state electronic coupling through the cylindrically π-symmetric BTD moiety.

There are several noteworthy characteristics and trends of the Soret region (B-band 300-500 nm) of the electronic spectra: (i) The Soret region shifts to the red with extension of π-conjugation along the x-axis (x being the long molecular axis); (ii) The B-band shows exciton splitting due to the x and y polarizations of the neighboring molecules. The B_x transition has a significant disparity in oscillator strength than the B_y band due to the polarization along the molecular axis. For **PZn-(BTD-PZn)$_n$** oligomers, the B_y-state (high energy portion of the B-band) is dominant. For **BTD-(PZn)$_n$-BTD** oligomers, the B_y band is diminished and there is an enhanced B_x (low energy portion of the B-band) state. Finally, for **(PZn)$_2$-(BTD-(PZn)$_2$)$_n$** oligmers, the B_x and B_y band is further separated and have much less structure than the other two series of oligomers.

The Q-band region (500 - 900 nm) represents the π-π derived transition of the macrocycle and also has several notable characteristics: (i) the Q-band maximum shifts to the red with increasing conjugation length. However, there is not much increasing in the Q-band oscillator strength. This may be due to the broadening of both the B- and Q-band manifold, due to variations in inter porphyfin dihedral angles or due to aggregation; (ii) The lowest energy manifold represents the Q_x-polarization along the molecular axis. The

Q_y-polarization remains unchanged with increasing conjugation and resides underneath the blue edge of the Q-band manifold; (iii) the broad blue edge of the Q-band is due to the large number of rotational conformers that can be accessible at room temperature, which causes a broadening of the Q-band.

The $S_1 \rightarrow S_0$ emission spectra for the series of **PZn-(BTD-PZn)$_n$, (PZn)$_2$-(BTD-(PZn)$_2$)$_n$** and **BTD-(PZn)$_n$-BTD** compounds are also shown in **Figure 2.11**. Reflecting the extended conjugation in **PZn$_n$**, the emission spectra red-shift to the NIR region with increasing numbers of conjugated monomeric units. Upon increasing the number of porphyrins repeat units, a noticeable saturation of the red-shifting begins to develop. The detailed emission data are listed in **Table 2.3**. The decreasing of FWHM and stokes shift with increasing conjugation length for **PZn-(BTD-PZn)$_n$** compounds implying a correlation between the electron-vibrational coupling and chain length. Increasing the conjugation length limits the vibrational activity, therefore decreases the nonradioactive decay process and cause a slow relaxation of the porphyrin oligomer to the lowest vibration S_1 state. However, for **BTD-(PZn)$_n$-BTD** compounds, the trend is opposite that the FWHM and stokes' shift increases with increasing conjugation length. One possible explanation for this trend is that these **BTD-(PZn)$_n$-BTD** compounds are more coplanar and offered good effective conjugation in the π-linked porphyrin compounds, thus tend to aggregate more than the **PZn-(BTD-PZn)$_n$**. This aggregation will causes the energy of the excited state decreasing and results a long-wavelength shift in fluorescence spectrum, as well as increasing stokes' shift with increased conjugation length. For **(PZn)$_2$-(BTD-(PZn)$_2$)$_n$** compounds, they have similar structures to **PZn-(BTD-PZn)$_n$** compounds, but with more porphyrin π-conjugation. Therefore, the conjugation length effect and the

72

aggregation effect balances to give a slight increasing of FWHW while a slight decreasing of stokes' shift. More solvent and time resolved studies will be performed for better understanding of the excited state differences between these compounds.
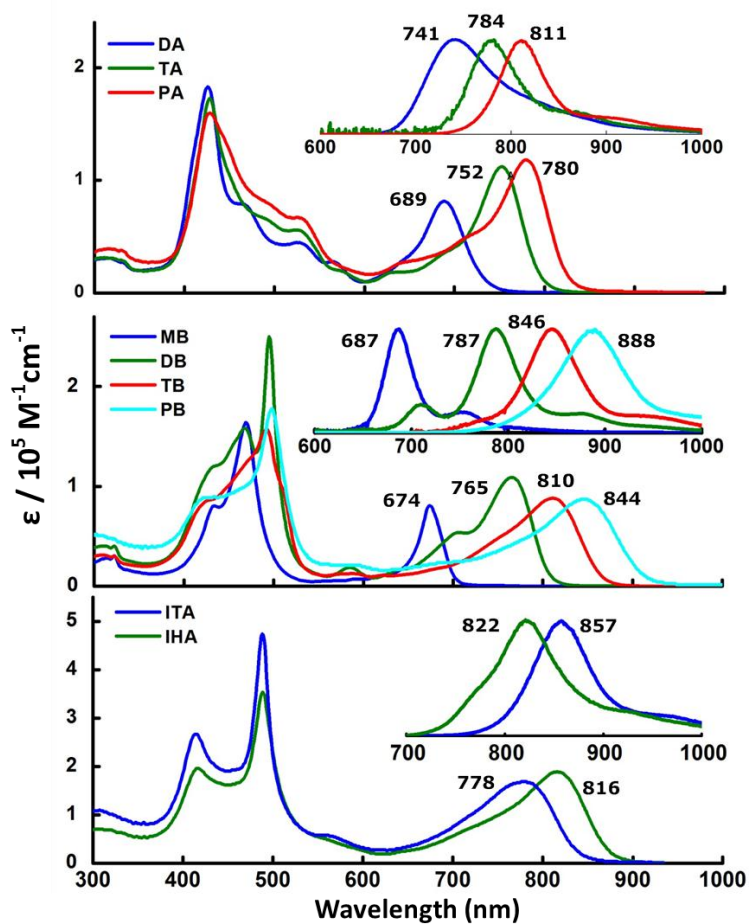
Figure 2.11 Electronic absorption and emission spectra of: PZnE-BTD-EPZn (**DA**); PZnE-BTD-EPZnE-BTD-EPZn (**TA**); PZnE-BTD-EPZnE-BTD-EPZn-EPZnE-BTD-EPZn (**PA**); BTD-EPZnE-BTD (**MB**); BTD-EPZnE-PZnE-BTD (**DB**); BTD-EPZnE-PZn-EPZnE-BTD (**TB**); BTD-EPZnE-PZn-EPZnE- PZn-EPZnE-BTD (**PB**); PZn-EPZnE-BTD-EPZnE-PZn (**ITA**); PZn-EPZnE-BTD-EPZnE-PZnE-BTD-EPZnE-PZn (**IHA**).

Table 2.1 Comparative integrated oscillator strengths and absorptive domains of the blue and red spectral regions of the BTD conjugated porphyrin compounds.[a]

Compound	FWHM[b] B-band region [cm⁻¹, (nm)]		Oscillator Strength B-band region[d]	FWHM[e] Q-band region [cm⁻¹, (nm)]		Oscillator Strength Q-band region[f]	Total Oscillator Strength
PZnE-BTD-EPZn	2323	(426)[c]	2.11	1180	(689)	0.72	3.52
PZnE-BTD-EPZnE-BTD-EPZn	2777	(428)[c]	2.90	1059	(752)	0.75	3.65
PZnE-BTD-EPZnE-BTD-EPZnE-BTD-EPZn	4235	(429)[c]	3.21	1227	(780)	0.97	4.18
BTD-EPZnE-BTD	1850	(469)[c]	2.00	654	(674)	0.35	2.34
BTD-EPZnE-PZnE-BTD	2704 / 1069	(468) / (495)[c]	3.60	1222	(765)	0.89	4.49
BTD-EPZnE-PZn-EPZnE-BTD	4538	(492)[c]	2.99	1597	(811)	0.84	3.83
BTD-EPZnE-PZn-EPZnE-PZn-EPZNE-BTD	3700	(498)[c]	3.33	1689	(844)	1.05	4.38
PZn-EPZnE-BTD-EPZnE-PZn	3920 / 1083	(415) / (488)[c]	7.64	1904	(778)	1.62	9.26
PZn-EPZnE-BTD-EPZnE-PZnE-BTD-EPZnE-PZn	3887 / 1566	(416) / (489)[c]	6.21	1654	(816)	1.65	7.87

[a] From electronic absorption spectra recorded in THF solvent.

[b] Taken as twice value of half the spectral width of the B-band region at half the height of the absorption noted.

[c] Entries correspond to the spectral breadth of the transition envelope centered at the wavelength in parentheses.

[d] Oscillator strengths calculated over the following wavelength domains: **PZnE-BTD-EPZn** (380 ~ 600 nm); **PZnE-BTD-EPZnE-BTD-EPZn** (380 ~ 600 nm); **PZnE-BTD-EPZnE-BTD-EPZn-EPZnE-BTD-EPZn** (380 ~ 600 nm); **BTD-EPZnE-BTD** (360 ~560 nm); **BTD-EPZnE-PZnE-BTD** (360 ~ 560 nm); **BTD-EPZnE-PZn-EPZnE-BTD** (360 ~ 560 nm); **BTD-EPZnE-PZn-EPZnE- PZn-EPZnE-BTD** (360 ~ 560 nm); **PZn-EPZnE-BTD-EPZnE-PZn** (360 ~ 610 nm); **PZn-EPZnE-BTD-EPZnE-PZnE-BTD-EPZnE-PZn** (360 ~ 610 nm).

[e] Entries correspond to the spectral breadth of the transition envelope centered at the wavelength in parentheses.

[f] Oscillator strengths calculated over the following wavelength domains: **PZnE-BTD-EPZn** (600 ~ 760 nm); **PZnE-BTD-EPZnE-BTD-EPZn** (600 ~820 nm); **PZnE-BTD-EPZnE-BTD-EPZn-EPZnE-BTD-EPZn** (600 ~ 900 nm); **BTD-EPZnE-BTD** (560 ~720 nm); **BTD-EPZnE-PZnE-BTD** (560 ~ 850 nm); **BTD-EPZnE-PZn-EPZnE-BTD** (560 ~ 910 nm); **BTD-EPZnE-PZn-EPZnE- PZn-EPZnE-BTD** (560 ~ 1050 nm); **PZn-EPZnE-BTD-EPZnE-PZn** (610 ~ 860 nm); **PZn-EPZnE-BTD-EPZnE-PZnE-BTD-EPZnE-PZn** (610 ~ 920 nm).

Table 2.2 Prominent absorption band wavelength, energies, and extinction coefficients of BTD conjugated porphyrin compounds in THF solvent.

	UV-region			B-band region			Q-band region		
	λ(nm)	ν(cm^{-1})	log(ε)	λ(nm)	ν(cm^{-1})	log(ε)	λ(nm)	ν(cm^{-1})	log(ε)
PZnE-BTD-EPZn	313	31,949	(4.39)	426	23,474	(5.16)	524	19,083	(4.55)
				465	21,505	(4.79)	566	17,667	(4.34)
							689	14,514	(4.81)
PZnE-BTD-EPZnE-BTD-EPZn	311	32,154	(4.50)	428	23,364	(5.24)	525	19,047	(4.75)
				489	20,449	(4.82)	573	17,452	(4.30)
							634	15,772	(4.27)
							689	14,513	(4.56)
							752	13,297	(5.05)
PZnE-BTD-EPZnE-BTD-EPZnE-BTD-EPZnE-BTD-EPZn	316	31,645	(4.59)	429	23,310	(5.20)	525	19,047	(4.83)
							643	15,552	(4.43)
							716	13,966	(4.70)
							780	12,820	(5.07)
BTD-EPZnE-BTD	314	31,847	(4.45)	434	23,041	(4.90)	592	16,892	(3.85)
	322	31,056	(4.48)	469	21,321	(5.21)	619	16,155	(4.02)
							674	14,837	(4.91)
BTD-EPZnE-PZnE-BTD	310	32,258	(4.60)	468	21,367	(5.20)	585	17,094	(4.26)
	323	30,959	(4.60)	495	20,202	(5.40)	638	15,674	(4.21)
							705	14,184	(4.73)
							765	13,072	(5.04)
BTD-EPZnE-PZn-EPZNE-BTD	308	32,467	(4.49)	426	23,474	(4.93)	592	16,891	(4.10)
	323	30,960	(4.48)	492	20,325	(5.20)	621	16,103	(4.03)
							811	12,330	(4.94)
BTD-EPZnE-PZn-EPZnE-PZn-EPZNE-BTD	303	33,003	(4.72)	421	23,753	(4.95)	595	16,807	(4.32)
				498	20,080	(5.25)	681	14,684	(4.37)
							844	11,848	(4.94)
PZn-EPZnE-BTD-EPZnE-PZn	307	32,573	(5.04)	415	24,096	(5.42)	562	17,793	(4.77)
				488	20,491	(5.67)	778	12,853	(5.23)
PZn-EPZnE-BTD-EPZnE-PZnE-BTD-EPZnE-PZn	302	33.112	(4.85)	416	24,038	(5.29)	816	12,254	(5.28)
				489	20,450	(5.55)			

Table 2.3 Spectroscopic Parameters of the porphyrin compounds in THF.

	$\lambda\max(S_0{\to}S_1)$ [nm][a]	ε_g @ $\lambda\max(S_0{\to}S_1)$ [M^{-1} cm^{-1}]	$\lambda\max(S_1{\to}S_0)$ [nm][a]	Stokes' shift (cm^{-1})	$\phi_f^{\,b}$	$\tau_F^{\,c}$ [ns]
PZnE-BTD-EPZn	689(1180)	121 000	741(1605)	1018	0.37 (0.015)	1.6
PZnE-BTD-EPZnE-BTD-EPZn	752(1059)	112 000	784(977)	543	0.36 (0.015)	1.1
PZnE-BTD-EPZnE-BTD-EPZnE-BTD-EPZn	780(1227)	118 000	811(846)	490	0.29 (0.015)	0.8
BTD-EPZnE-BTD	674(654)	81 000	687(727)	281	0.17 (0.005)	1.3
BTD-EPZnE-PZnE-BTD	765(1222)	109 000	787(802)	365	0.33 (0.006)	1.4
BTD-EPZnE-PZn-EPZNE-BTD	811(1597)	87 000	846(872)	510	0.25 (0.015)	0.8
BTD-EPZnE-PZn-EPZnE-PZn-EPZNE-BTD	844(1689)	87 100	888(1008)	587	0.20 (0.025)	0.6
PZn-EPZnE-BTD-EPZnE-PZn	778(1904)	169 000	822(926)	688	0.26 (0.011)	0.6
PZn-EPZnE-BTD-EPZnE-PZnE-BTD-EPZnE-PZn	816(1654)	190 000	857(1154)	586	0.22 (0.01)	0.5

[a] Numbers in parentheses are spectral breadths (FWHM) of the respective transitions in units of cm^{-1}.

[b] Quantum yields were determined relative to H$_2$TPP in benzene ($\phi_f = 0.13$); parenthetical values represent standard deviations from the mean.

[c] All compounds were excited at 405 nm, except TB, PB, ITA, and IHA, which were excited at 780 nm. The lifetime is determined with single exponential fitting using Hamamatsu HPD-TA software with single-photon counting mode. The fitting module is used for fitting analysis with deconvolution method. For the deconvolution method, scattering sample (cream dissolved in water) is used to acquire the instrument response function.

2.4.3. Quantum Yields

The quantum yields (ϕ_f) of these BTD conjugated porphyrin compounds were measured both in THF and toluene solvent as shown in **Table 2.4**. The quantum yields for these compounds are exceptional high in the NIR region, which are 18-38% in THF and 18-59% in toluene. The excited-state lifetimes (τ_f) were also determined which vary from 0.5 ps to 1.6 ns. Trends in φ_f and τ_f are consistent with the expected dependences upon the magnitudes of radiative (k_r) and nonradiative (k_{nr}) rate processes, where k_{nr} includes contributions due to internal conversion (k_{ic}) and intersystem crossing (k_{isc}) rate constants. Except for **BTD-EPZNE-BTD**, the quantum yield and life time decreases with increasing conjugation length in each series of BTD conjugated porphyrin compounds, derives from a larger magnitude k_r, congruent with the Strickler-Berg relation,[41] which predicts that k_r is proportional to the integrated oscillator strength of the lowest-energy ground-state absorption band. The decreasing of the $S_0 \rightarrow S_1$ energy gap with the argument of conjugation length will cause an increasing of the $S_0 \rightarrow S_1$ internal conversion rate (k_{ic}) and therefore the diminishing of the quantum yield and life time. The reason for the low quantum yield of **BTD-EPZNE-BTD** is possible due to the balance of increased number of T_1 state at shorter conjugation length, which causes more $S_0 \rightarrow S_1$ intersystem crossing (k_{isc}) decay and thus a low quantum yield. These results highlight the close correlation of fluorescence quantum yields with $S_0 \rightarrow S_1$ integrated oscillator strength, and demonstrate the ability of broad NIR spectral domain fluorescence energy modulation, where φ_f magnitudes follow a simple Strickler−Berg relationship.

Table 2.4 Comparative quantum yields of conjugated porphyrins in THF and Toluene.

	ϕ_f (THF)	ϕ_f (Toluene)
PZnE-BTD-EPZn	0.39	0.49
PZnE-BTD-EPZnE-BTD-EPZn	0.37	0.49
PZnE-BTD-EPZnE-BTD-EPZnE-BTD-EPZnE-BTD-EPZn	0.29	0.44
BTD-EPZnE-BTD	0.17	0.18
BTD-EPZnE-PZnE-BTD	0.33	0.45
BTD-EPZnE-PZn-EPZnE-BTD	0.25	0.46
BTD-EPZnE-PZn-EPZnE-PZn-EPZNE-BTD	0.21	0.48
PZn-EPZnE-BTD-EPZnE-PZn	0.27	0.59
PZn-EPZnE-BTD-EPZnE-PZnE-BTD-EPZnE-PZn	0.22	0.58

2.4.4.   Electrochemical Properties.

Table 2.5 report the solution electrochemically determined oxidation (HOMO energy level) and reduction (LUMO energy level) levels. As seen with the optical data, the $\pi \to \pi^*$ derived transition shifts to lower energy with increasing conjugation length, the potentiometrically determined band gap, E_{po}, become destabilized and stabilized respectively with increasing number of porphyrins (ie the band gap becomes smaller with larger oligomers in agreement with optical and emission data).

It is also important to note that the optical band gaps (E_{op} values) of these BTD conjugated porphyrin compounds track closely with their corresponding E_ps. These data, coupled with the facts that the steady state absorption spectra indicate that the visible and NIR polarized excitations evince extensive mixing of PZn- and BTD-derived electronic states suggest that the quinoidal resonance contribution to the low lying singlet electronically excited states exceeds greatly that for the ground-state, thus giving rise to the expectation that the excited singlet wavefunctions of these BTD conjugated porphyrin compounds should feature unusual degrees of electronic delocalization.

Table 2.5 Optical HOMO–LUMO gaps (E_{op}s) and potentiometrically determined HOMO–LUMO gaps (E_ps) of the BTD conjugated porphyrins.

	DA	TA	PA	MB	DB	TB	PB	ITA	IHA
$E_{op}(max)^a$	1.80	1.65	1.59	1.84	1.62	1.53	1.47	1.59	1.52
$E_{op}(edge)^b$	1.69	1.54	1.48	1.77	1.54	1.43	1.34	1.46	1.38
E_p^c	1.88	1.58	1.51	1.87	1.75	1.70	1.62	1.76	1.69

[a] Optical HOMO–LUMO gap determined from the lowest absorption maximum measured in THF.
[b] Optical HOMO–LUMO gap determined from the absorption edge measured in THF. The absorption edge was determined as the intersection of the two tangent lines involved.
[c] Potentiometrically determined HOMO–LUMO gap ($E_{1/2}^{0/+} - E_{1/2}^{-/0}$) measured in CH_2Cl_2.

2.5. Conclusions

Quinoidal spacer conjugated (porphinato)zinc(II) (**PZn-(BTD-PZn)$_n$**, **(PZn)$_2$-(BTD-(PZn)$_2$)$_n$)** and **(BTD-(PZn)$_n$-BTD)** complexes that possess intervening conjugated BTD spacer with varying degrees of porphyrin conjugation have been synthesized by palladium-catalyzed cross coupling reactions. The performance of electronic and optical devices based on these conjugated species is optimized by reducing and tuning energy gaps between the highest occupied molecular orbital (HOMO) and the lowest unoccupied molecular orbital (LUMO). Electronic absorption spectra show significant red-shifts of the x-polarized Q state (S$_0$→S$_1$) transition manifold maxima into NIR region. Likewise, the potentiometrically determined HOMO-LUMO gaps (E$_{1/2}^{0/+}$ − E$_{1/2}^{-/0}$) display correspondingly exceptional low band gap. These BTD conjugated porphyrin species possess large magnitude NIR S$_1$ → S$_0$ fluorescence quantum yields superior to the highest reported value for NIR laser dyes in the 700-1000 nm regime. Notely, these emitters do not suffer from commonly cited drawbacks of poor photostability and substantial φ$_f$ sensitivity to solvent polarity for NIR chromophores. These facts underscore the tremendous potential of these species as electrooptic materials in a range of photonic applications.

2.6. Acknowledgements

2.7. References

1. Sowell, J.; Strekowski, L.; Patonay, G. *Journal of Biomedical Optics* **2002,** 7, 571.

2. Mujumdar, S. R.; Mujumdar, R. B.; Grant, C. M.; Waggoner, A. S. *Bioconjugate Chemistry* **1996,** 7, 356-362.

3. Mishra, A.; Behera, R. K.; Behera, P. K.; Mishra, B. K.; Behera, G. B. *Chemical Reviews* **2000,** 100, 1973-2012.

4. Pereverzev, Y. V.; Prezhdo, O. V.; Dalton, L. R. *Chemical Physics Letters* **2003,** 373, 207-212.

5. Reindl, S.; Penzkofer, A.; Gong, S. H.; Landthaler, M.; Szeimies, R. M.; Abels, C.; Baumler, W. *Journal of Photochemistry and Photobiology A: Chemistry* **1997,** 105, 65-68.

6. Lin, Y.; Weissleder, R.; Tung, C.-H. *Bioconjugate Chemistry* **2002,** 13, 605-610.

7. Yu, G.; Gao, J.; Hummelen, J. C.; Wudl, F.; Heeger, A. J. *Science* **1995,** 270, 1789-1791.

8. Brabec, C. J.; Sariciftci, N. S.; Hummelen, J. C. *Advanced Functional Materials* **2001,** 11, 15-26.

9. Segura, J. L. *Acta Polymerica* **1998,** 49, 319-344.

10. Mitschke, U.; Bauerle, P. *J. Mater. Chem.* **2000,** 10, 1471-1507.

11. Katz, H. E. *Journal of material chemistry* **1997,** 7, 369-376.

12. Katz, H. E.; Bao, Z.; Gilat, S. L. *Accounts of Chemical Research* **2001,** 34, 359-369.

13. Nalwa, H. S. *Advanced Materials* **1993,** 5, 341-358.

14. Tykwinski, R. R.; Gubler, U.; Martin, R. E.; Diederich, F.; Bosshard, C.; G 眉 nter, P. *The Journal of Physical Chemistry B* **1998,** 102, 4451-4465.

15. Ghoroghchian, P. P.; Frail, P. R.; Susumu, K.; Blessington, D.; Brannan, A. K.; Bates, F. S.; Chance, B.; Hammer, D. A.; Therien, M. J. *Proceedings of the National Academy of Sciences U.S.A* **2005,** 102, 2922-2927.

16. Caspar, J. V.; Kober, E. M.; Sullivan, B. P.; Meyer, T. J. *Journal of the American Chemical Society* **1982,** 104, 630-632.

17. Englman, R.; Jortner, J. *Molecular Physics* **1970,** 18, 145-164.

18. Lin, V. S.-Y.; DiMagno, S. G.; Therien, M. J. *Science* **1994,** 264, 1105–1111.

19. Lin, V. S.-Y.; Therien, M. J. *Chem. Eur. J.* **1995,** 1, 645–651.

20. Kumble, R.; Palese, S.; Lin, V. S.-Y.; Therien, M. J.; Hochstrasser, R. M. *J. Am. Chem. Soc.* **1998,** 120, 11489–11498.

21. Shediac, R.; Gray, M. H. B.; Uyeda, H. T.; Johnson, R. C.; Hupp, J. T.; Angiolillo, P. J.; Therien, M. J. *J. Am. Chem. Soc.* **2000,** 122, 7017–7033.

22. Susumu, K.; Therien, M. J. *J. Am. Chem. Soc.* **2002,** 124, 8550–8552.

23. Rubtsov, I. V.; Susumu, K.; Rubtsov, G. I.; Therien, M. J. *J. Am. Chem. Soc.* **2003,** 125, 2687–2696.

24. Ostrowski, J. C.; Susumu, K.; Robinson, M. R.; Therien, M. J.; Bazan, G. C. *Adv. Mater.* **2003,** 15, 1296–1300.

25. Angiolillo, P. J.; Uyeda, H. T.; Duncan, T. V.; Therien, M. J. *J. Phys. Chem. B* **2004,** 108, 11893–11903.

26. Anderson, H. L. *Inorg. Chem.* **1994,** 33, 972–981.

27. Taylor, P. N.; Wylie, A. P.; Huuskonen, J.; Anderson, H. L. *Angew. Chem. Int. Ed.* **1998,** 37, 986–989.

28. Taylor, P. N.; Huuskonen, J.; Rumbles, G.; Aplin, R. T.; Williams, E.; Anderson, H. L. *Chem. Commun.* **1998**, 909–910.

29. Arnold, D. P.; Heath, G. A.; James, D. A. *J. Porphyrins Phthalocyanines* **1999,** 3, 5–31.

30. Beljonne, D.; O'Keefe, G. E.; Hamer, P. J.; Friend, R. H.; Anderson, H. L.; Brédas, J. L. *J. Chem. Phys.* **1997,** 106, 9439–9460.

31. Susumu, K.; Maruyama, H.; Kobayashi, H.; Tanaka, K. *J. Mater. Chem.* **2001,** 11, 2262–2270.

32. Roncali, J. *Chem. Rev.* **1997,** 97, 173-205.

33. van Mullekom, H. A. M.; Vekemans, J. A. J. M.; Havinga, E. E.; Meijer, E. W. *Mater. Sci. Eng.* **2001,** 32, 1-40.

34. Ajayaghosh, A. *Chem. Soc. Rev.* **2003,** 32, 181–191.

35. Susumu, K.; Duncan, T. V.; Therien, M. J. *Journal of the American Chemical Society* **2005,** 127, 5186-5195.

36. Benson, R. C.; Kues, H. A. *Journal of Chemical & Engineering Data* **1977,** 22, 379-383.

37. Pilgram, K.; Zupan, M.; Skiles, R. *J. Heterocycl. Chem.* **1970,** 7, 629–633.

38. Susumu, K.; Therien, M. J. *Journal of the American Chemical Society* **2002,** 124, 8550-8552.

39. Uyeda, H. T.; Zhao, Y.; Wostyn, K.; Asselberghs, I.; Clays, K.; Persoons, A.; Therien, M. J. *J. Am. Chem. Soc.* **2002,** 124, 13806–13813.

40. Fery-Forgues, S.; Lavabre, D. *Journal of chemical education* **1999,** 76, 1260.

41. Strickler, S. J.; Berg, R. A. *The Journal of Chemical Physics* **1962,** 37, 814.

CHAPTER 3. Antibody Conjugated Near-Infrared Emissive Polymersomes for Active Targeting

3.1. Summary

Polymersomes have emerged as versatile carrier systems for delivering active molecules in the organism, and demonstrated enhanced efficiency compared to conventional drugs and liposomes. The design of immunopolymersomes (IPs) for targeted cancer therapies by endocytosis of the targeting molecule and delivery of therapeutic agents to the interior of the tumor cell remains an ongoing research goal. This is accomplished by highly specific chemical modifications to the bilayers of the polymersomes for the attachment of antibodies that recognize and bind specifically to target cells. Therefore, active, targeting antibodies conjugated near infrared (NIR) emissive polymer vesicles will be a perfect system for *in vivo* diagnostic and drug-delivery applications. The efficiency, stability of the resulting antibody to polymersomes bond, and biocompatibility are essential criteria for such conjugation chemistry. To this end, various techniques have been developed, including covalent and noncovalent approaches, with emphasis on the major differences between the coupling reactions, on their advantages and drawbacks, on the surface functionalization degree effect, antibody concentration effect, polymersome recovery yields and the coupling efficiencies obtained. The optimized coupling method was by using 5% maleimide functionalized PEO(3600)-*b*-PBD(6800) (PEO$_{80}$-*b*-PBD$_{125}$: OB18) mixture with PEO(1300)-*b*-PBD(2500) (PEO$_{30}$-*b*-PBD$_{46}$: OB2) to preform polymersomes, followed by addition of thiol-activated antibody at mole ratio of 1:40 IgG antibody to functionalized polymer, resulted in ~ 64

IgG antibody per 100 nm polymersomes with conjugation efficiency as high as 80.6%. Furthermore, the antibody-conjugated polymersomes were characterized by confocal microscope, cryogenic transmission electron microscopy (Cryo-TEM), Enzyme-linked immunosorbent assay (ELISA), and Licor-Odyssey imaging experiments. All of these characterizations showed direct province of successful antibody conjugation to the polymersome surface.

Based on the functionalization techniques we developed for direct conjugation of antibodies to the polymersome surface, anti-ErbB2 NIR emissive IPs were developed to enable efficient delivery to HER2 breast cancer cells. Flow cytometry and confocal microscopy analysis indicated that anti-ErbB2 IPs delivery to HER2 cells was concentration dependent, and resulted in punctate intracellular localization. The extent of anti-ErbB2 IPs delivery was estimated to be $86,000 \pm 2,500$ vesicles per BT474 cell with uptake efficiency as high as 37%. In summary, we developed NIR emissive IPs based on universal chemical modification methods for targeted delivery and optically based detection of metastatic cancer cells *in vivo*.

3.2. Introduction

In recent years, an increasing number of studies have been devoted to the development of drug delivery methods that are aimed at targeting cancer chemotherapeutics to tumors. Systemic administration of chemotherapeutic agents results in indiscriminate drug distribution and severe toxicity, so specific targeting to tumor cells is a great advantage. The first attempt toward this goal was accomplished by utilization of antibody coupled anti-tumor drugs.[1] However, one major difficulty was to preserve of both pharmacological and immunological activities of the antibody-drug conjugates.

Only a relatively low amount of drug can be coupled to the antibody to maintain the binding activity, which is often insufficient to obtain the desired therapeutic effect. Therefore, other strategies for targeted delivery have been developed by the entrapment of drugs into liposomes or nanoparticles. Liposomes offer a suitable means for drug delivery by protecting encapsulated drugs from enzymatic degradation and rapid clearance *in vivo*, thereby improving drug pharmacokinetics, and leading to increased accumulation of the drug at the tumor site. However, phospholipids have their physicochemical limitations, and hence limited options are available to tailor their properties.

Polymersomes are a new class of self-assembled vesicles based on amphiphilic block copolymers with thicker and tougher membranes than lipids, with critical strains before rupture as much as seven times larger than those for lipid vesicles, and with toughnesses up to 50 times that of phopholipid vesicles.[2-4] The sizes of polymersomes can be easily tuned to 100-200 nm scale following self-assembly by techniques such as sonication, freeze-thaw cycles and extrusion through appropriately sized membranes.[5] At this length scale the polymersomes can most effectively leverage the Enhanced Permeability and Retention (EPR) effect and leave the bloodstream at the site of tumors.[6] In addition, polymersomes also offer the advantage of prolonged circulation *in vivo*, resulted in increased biological stability, slow uptake by phagocytic cells of the reticuloendothelial system (RES)[7-9] and thus strong targeting specificity.[10-12] Moreover, the physical and chemical properties of polymersomes including particle size, drug loading, surface modification, and even prolonged circulation *in vivo* behavior may be broadly tunable through rich diversity of block copolymer chemistries.[2, 3, 13-15] Another

advantage of polymersomes is their unique ability to encapsulate hydrophobic components, owing to the hyperthickness of the polymersome membrane. The most compelling example of this is the encapsulation of hydrophobic light emitting porphyrinic dyes, ranging in size from 1.1 to 5.5 nm in length, to yield NIR emissive polymersomes that have exceptional potential to facilitate deep-tissue fluorescence-based imaging for in vivo diagnostic and drug-delivery applications.[16]

These polymersomal vesicles are promising systems to be used as molecular imaging modalities[16, 17], targeted drug-delivery devices[18-21], biosensors, and nanoreactors.[22-29] The attachment of targeting ligands to the polymersomes is of crucial importance in these applications. By tethering ligands that are specific to receptors overexpressed on the surface of diseased cells to the delivery vehicles, it is possible to achieve specific binding between delivery vehicles and target cells.[30] Developing polymersomes that have targeting vectors attached to the bilayer surface has attracted increasing attention.[31] These vectors have included ligands such as peptides, enzymes and proteins. However, very few studies have focused on antibody conjugates. Developing antibody-polymersome conjugation techniques is very important since procedures for producing highly specific monoclonal antibodies are well established, and the antibody-polymersomes conjugates will become immunogenic which is ideal for various immunochemical and diagnostic purposes.

IPs are polymersomes that have been specially designed for active targeting to a given type of tissue or organ that the polymersome is able to recognize by its molecular fingerprint. This is accomplished by conjugating an antibody or an antibody fragment which is responsible for cell recognition to the bilayer surface of the polymersomes.

Antibodies are immunoglobulins, which are glycoproteins produced by the body's immune system. Therefore, the attachment of specific antibodies to the surface of the polymersomes enables them to bind to cells bearing antigens, and subsequently be internalized into the cells for the immuno-specific delivery of drugs or other materials to the antigenic target cells. To note, the liposome-based antigen delivery is more immunogenic than the antigen alone. This effect is attributed to the particulate nature of liposomes which more closely mimic the uptake of viruses or bacteria.[32] It is possible that polymersomes would possess this adjuvant quality as well.

There are two basic approaches to the attachment of ligands to polymersomes. The first involves the direct attachment of a ligand to a preformed polymersome that will contain functionalized headgroups which are predisposed to react with the ligand. The major advantage of this approach is that it allows the use of any polymersomes preparation procedure, and avoids exposure of the ligand to the conditions of polymersome preparation. The second type of approach involves functionalization of block copolymers at their hydrophilic chain end with ligands such as carbohydrates, peptides and proteins and subsequently self-assembly into polymer vesicles with surface functionalization.[33-43] This strategy allows the functionalized copolymer to be purified and fully characterized as a non-aggregated species. Thus, the ligands density on polymersomes surface can be better controlled by simply adjusting the ratio of functionalized to non-functionalized block copolymer prior to vesicle formation. However, the assembly behavior of the block copolymers might be affected by the end-functionalization, so that their ability to form vesicles has to be confirmed by experimental data. Also, the protein may be denatured or deactivated during the polymersomes self-assembling process which normally involves harmful organic solvent or sonication, and thus carefully chosen of polymersomes formation

method is required. Finally, only about half of the ligand that is conjugated to the polymer will be positioned in the inner membrane of the polymer vesicles during self-assembly and will not be accessible for targeting; therefore, this method has a low ligand coupling efficiency on the outer surface of the polymersomes and is not suitable for costly proteins.

For the conjugation of a targeting ligand to polymersomes particles, there are two main options: non-covalent linkage, such as the avidin-biotin interaction,[19, 23, 44-48] or covalent binding. The noncovalent avidin-biotin linkage has been exploited for conjugating polymersomes with a biotinylated ligand, e.g. a peptide or antibody. Avidin is a tetrameric protein with a molecular weight of 68 kDa which can strongly bind to four biotins. By using noncovalent avidin-biotin conjugation, a polymer vesicle carrying biotin functionalities is first incubated with avidin. In a second step, the avidin-polymersomes conjugate is incubated with biotinylated ligands. Although this method is simple and effective, the introduction of avidin into the conjugate has certain drawbacks. First, conjugation of avidin to polymersomes will considerably increase its size and thereby alter its pharmacokinetics. More importantly, avidin is known[49] to be rapidly cleared by the liver. In fact, this property of avidin has been exploited to chase and clear antibodies[50] and MRI contrasting agents from the circulation.[51]

Covalently linking the ligand to the polymersome directly would lead to a smaller conjugate, which has more favorable pharmacokinetic properties. Covalent conjugation of ligands to polymersomes is achieved with several methods. Roughly, these methods can be divided in the formation of (i) a triazole bond, between alkyne groups and azide groups as so called "click chemistry", [27, 52-55] (ii) a C-S bond, between N-hydroxysuccinimidyl ester or vinyl sulfone and thiol groups, [13, 56] (iii) an imine bond, between aldehyde groups and amino groups, [57] (iv) a hydrazone bond, between two

different amide groups. [58] To avoid possible interactions between targeting ligands and cargo (drugs, RNA, etc.) and to prevent interference with self-assembly, attachment of ligands is normally take place after vesicle formation. Several approaches to attach ligands have been reported as shown above, for example biotin-streptavidin binding or azide-alkyne click chemistry. Although these approaches have proven feasible, they exhibit problems in terms of application in therapy, including human intolerance to streptavidin and toxic effects due to possible copper residues used to catalyze the alkyne-azide click reaction. Therefore, the challenge was to devise a biocompatible conjugation chemistry that would facilitate precise control of antibody density on polymersomes surface and stable chemical bonding while avoiding toxic reaction additives and catalysts. Also, in most of these coupling methods, the block copolymer vesicle surfaces are functionalize by chemical means with small ligands such as adhesion moieties[23, 44, 57, 59], carbohydrates[33, 34], fluorophores[41, 42, 55, 58, 60] and peptides[35-40, 43, 56]. Very few works have been done on large moieties such as antibody conjugation to polymersomes. In addition, previous work on conjugating antibodies to polymersomes has either resulted in low antibody conjugation efficiency[58] or lacks systematic information to study the factors that affect the antibody conjugation efficiency.[13, 58]

Toward this goal, OB18 diblock copolymers with five different functionalities at the hydrophilic terminus (**Scheme 3.1**) are synthesized for antibody conjugation. The schemetic structure of functionalized polymersome system for targeted drug delivery and imaging is shown in **Scheme 3.2**. The polymersomes are comprised of a mixture of functionalized OB18 diblock copolymer and nonfunctionalized OB2 diblock copolymer with highly NIR emissive fluorescent hydrophobic porphyrin fluorophores incorporated

in the bilayer membrane. The longer functionalized OB18 will be in both the inner and outside surface of the polymersomes bilayer membrane, and the schemetic structure only displays them as on the outside of the polymersomes bilayer membrane. The thick polymersome hydrophobic bilayer membrane enables the incorporation of NIR emissive porphyrin dyes for optical based NIR molecular imaging; the functionalized polymersome surface enables the antibody conjugation for specific cell targeting; and the large aqueous inner core of the polymersomes facilitates hydrophilic drug encapsulation for drug delivery. All these features of this antibody conjugated NIR emissive polymersomes suggest a promising new soft matter nanoscale platform for *in vivo* diagnostic and drug-delivery applications.
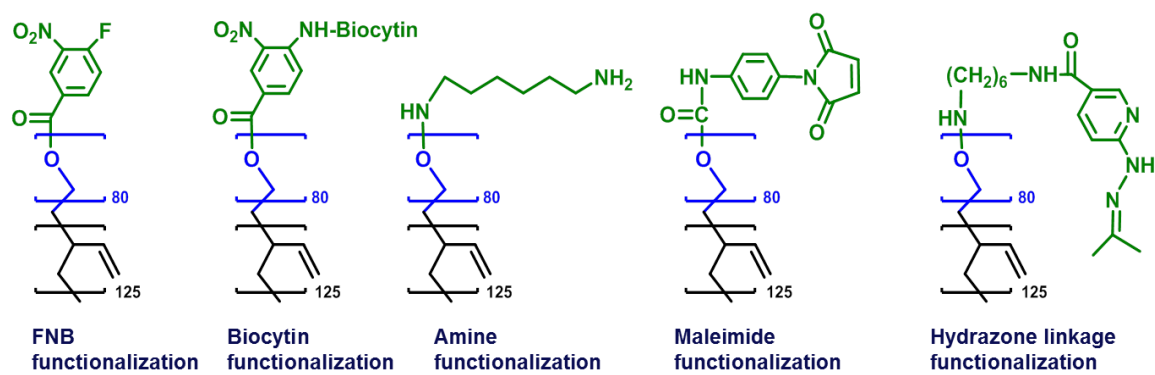
Scheme 3.1 Schematic structures of OB18 diblock copolymers with different functionalities.
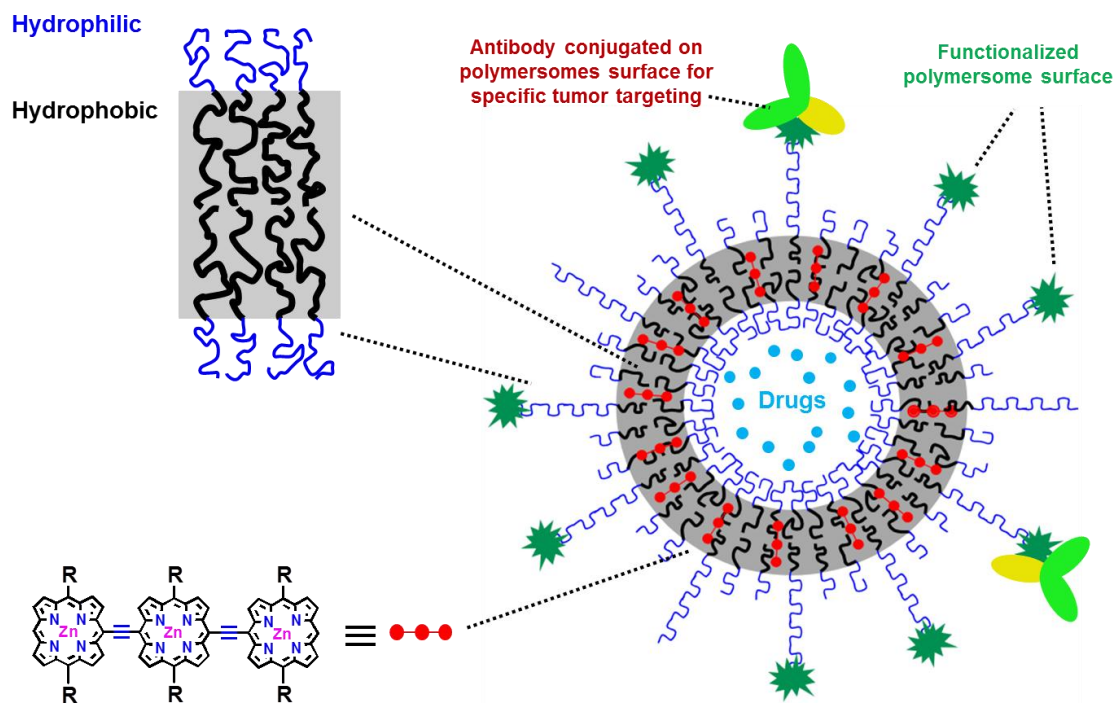
Scheme 3.2 Schematic structures of antibody conjugated NIR emissive polymersomes.

The functionalized end groups of OB18 can react with amino groups on antibodies or thio-activated antibodies. In summary, these five different functionalized end groups features the four chemistries of forming (i) a ester bond, between 4-Fluoro-3-nitrobenzoic ester (FNB) functionalized polymers and amino antibodies; (ii) a biotin-avidin bond, between biotin functionalized polymers and avidin, followed by addition of biotinlated antibodies; (iii) a urea bond or hydrazine bond, between isocyante groups and amino antibodies or amide groups and amide-activated antibodies, (iiii) a thioester bond, between maleimide and thiol. Six coupling procedures have been developed from the five functionalized polymers described above, and all these coupling method were evaluated, compared and optimized in terms of antibody conjugation efficiency and polymersome recovery yield. The number of exposed functionalities on the surface was controlled by varying the molar percentage of the functional OB18 polymer. The antibody concentration effect was also studied by varying the mole ratio of antibody concentration and polymersomes concentration. Among all these approaches for antibody conjugation, the maleimide method is found to give the highest protein conjugation yield and is broadly applicable. To apply this maleimide method, the ligand should contain a free thiol group, necessary for bond formation. Proteins, antibody and peptides exposing a free cysteine group can directly be used for coupling to maleimide. For proteins that don't have cysteine, thiol groups can be introduced by different thiolation methods such as: (1) reducing the disulfide crosslinks of cystines in proteins by using dithiothreitol (DTT).[61] However, the reduction will alter the protein conformation and may result in loss of protein activity or specificity; (2) thiolating the amines with succinimidyl 3-(2-pyridyldithio)-propionate (SPDP), followed by reduction with DTT;[62] (3) thiolating the

amines with succinimidyl acetylthioacetate (SATA), followed by deprotection generating sulfhydryl groups in the biopolymer.[63] This reagent is most useful when disulfides are essential for activity. And it also circumvents the separation step of the ligand-SH with other reagents and to allow a "one-pot" conjugation method. In this work, an alternate thiolation agent, 2-iminothiolane (Traut's reagent) is used to modify primary amines by adding a small spacer arm (8.1 Å) terminated by a free sulfhydryl group while maintaining charge properties similar to the original amino group for immediate use. Traut's reagents have several advantages over the other described thiolation reagents in light of its simplicity, specificity, flexibility and solubility.[64-67] It is a one-step conversion of amines to sulfhydryls with selective and spontaneous modification of primary amines at pH 7-10. And it incorporates a space arm to reduce steric hindrance. Moreover, it preserves the original positive charge to preserve protein solubility. Finally, the thiol containing ligands is utilized to react with maleimide-containing particles and form a covalent thioether linkage.

After the attachment of the antibody to NIR emissive polymersomes, the morphology and immunogenic effect were also characterized by using confocal microscopy, cryogenic transmission electron microscopy (Cryo-TEM), Enzyme-linked immunosorbent assay (ELISA) experiments, and Licor-Odyssey imaging experiments. The results indicate successful antibody conjugation on polymersomes surface, as well as highly specific and selective activity of these antibody conjugated IPs towards other antigens or antibodies.

Using the estabilished functionalization methods, we further developed IPs to combine the tumor-targeting properties and delivery advantages of long circulating

polymersomes. The IPs system we studied was the anti-ErbB2 NIR emissive polymersomes. HER2 (also known as ErbB2) is a member of the epidermal growth factor receptor family that has been found to be overexpressed or amplified in approximately 20-30% of breast cancers.[68] Overexpression of this receptor in breast cancer is associated with increased disease recurrence and worse prognosis. Because of its prognostic role, breast tumors are routinely checked for overexpression of HER2. Overexpression also occurs in other cancer such as ovarian cancer, stomach cancer, and biologically aggressive forms of uterine cancer, such as uterine serous endometrial carcinoma.[69] As a target antigen, HER2 is a readily accessible cell surface receptor for selective immunotargeting of tumor cells when overexpressed. By conjugating anti-ErbB2 antibody to the surface of NIR-emissive polymersomes, we were able to use these IPs for HER2 cell targeting and imaging.

Confocal microscope imaging experiments indicates that the anti-ErbB2 IPs bind specifically to HER2 overexpressed tumor cell lines BT474, SKBR3, HCC1569, and showed minimal binding towards low HER2 expressing tumor cell line MCF7 (the ErbB2 receptors per MCF7 cell is two to three orders of magnitude less than the ErbB2 overexpression cell lines). Nonconjugated polymersomes and irrelevant rat-IgG conjugated polymersomes were used as negative controls towards those tumor cells and all of them showed minimal binding to the cells. In addition, the anti-ErbB2 IPs demonstrated intense focus of fluorescence both at the ErbB2 overexpression tumor cell surface and intracellularly.

In order to maximize the intracellular uptake of polymersomes necessary for optimal cellular labeling, the effects of varying both the polymersome concentration and

incubation time on polymersomes uptake were examined. Flow cytometry and Licor-Odyssey imaging were used to measure the intensity of cellular-associated PZn$_3$ based fluorescence following cell incubation and washing *in vitro*. These experiments evaluated the uptake of both anti-ErbB2 IPs and nonconjugated polymersomes controls in order to distinguish the impact of antibody conjugation on intracellular delivery. The results indicate that a single BT474 cell can be effectively labeled with 86000 ± 2500 IPs, and 800 ± 50 control polymersomes. For MCF7 cells, they can only be labeled with 1700 ± 130 IPs per cell, and 830 ± 200 control polymersomes per cell. The maximum IP uptake percentage for BT474 cells is $37.9 \pm 1.8\%$, and $0.60 \pm 0.18\%$ for MCF7 cells; while the maximum control polymersomes uptake percentage for BT474 cells is $0.19 \pm 0.03\%$, and $0.19 \pm 0.05\%$ for MCF7 cells. The incubation times of one hour and overnight have also been studied. We found for overnight incubation, the IP uptake slightly increased while the control polymersomes uptake greatly increased. This indicates a higher level of nonspecific binding with increased incubation time.

3.3. Experimental Methods

3.3.1. Polymer Functionalization

3.3.1.1. Synthesis of FNB Modified Polymer
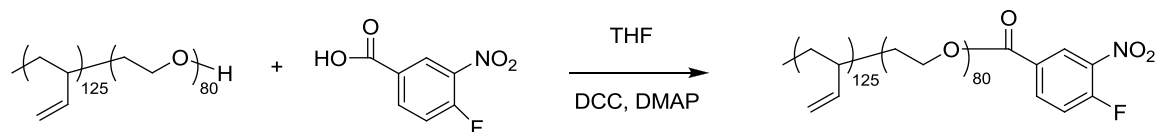
Scheme 3.3 Reaction scheme for terminal hydroxyl derivatization to 4-Fluoro-3-nitrobenzoic ester.

The PEO terminal hydroxyl of the copolymer was derivatized with 4-Fluoro-3-nitrobenzoic acid (FNB) as presented in **Scheme 3.3** and as previously drecribed.[48] Briefly, in round bottom flask, 100 mg OB18 was added to 1.1 equivalents of 4-fluoro-3-nitrobenzoic acid (Sigma-Aldrich, St. Louis, MO), with catalytic dimethylaminopyridine (Sigma-Aldrich), followed by the addition of 35 mL dry methylene chloride (Fisher). To a dried septum-seal vial we added 1.1 equivalents of dicyclohexylcarbodiimide (Sigma-Aldrich) and 5 mL methylene chloride, which was then injected into round bottom flask with the polymer. The reaction was allowed to proceed for 48 hours, and the resulting solution was purified by filtration and high-performance liquid chromatography (HPLC). The final product was vacuum dried and stored under argon gas at -20 ℃ until use. The extent of derivatization of the polymer was determined by ^{1}H NMR to be 88%.

3.3.1.2. Synthesis of Biocytin Modified Polymer
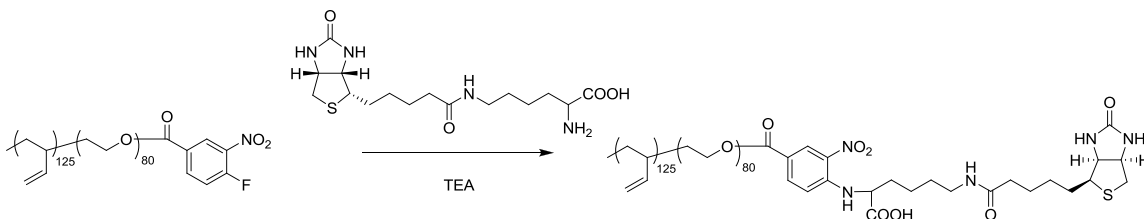
Scheme 3.4 Reaction scheme for terminal hydroxyl derivatization to biocytin.

The terminal end of the PEO block was modified to display biocytin through a two-step synthesis. 4-fluoro-3-nitrobenzoic acid was attached to the hydroxyl polymer terminus through an esterification in methylene chloride as described in 3.3.1. After filtration and HPLC purification, biocytin was attached to the modified polymer through a nucleophilic aromatic substitution in 50% THF / 50% DI water (by volume) at 5 mM in a glass screw

top vial. FNB functionalized polymer, biocytin and triethylamine were combined at 1:1.5:10 (molar ratio, FNB-polymer : biocytin : triethylamine). Reaction proceeded at 37-40 °C, while stirring for 24 hours. The mixture was dried by rotary evaporation to remove water and THF, resolvated in 100% THF at 0.1 mg mL^{-1}, and then filtered and purified by HPLC. Characterization of the biotin functionalization percentage in the final polymer was quantified via the established extinction coefficients (5449 M^{-1} cm^{-1}) of the biotinylated PEG at 428 nm[70] and was calculated to be 68%. The reaction scheme is shown in **Scheme 3.4**.

3.3.1.3. Synthesis of Amine Modified Polymer
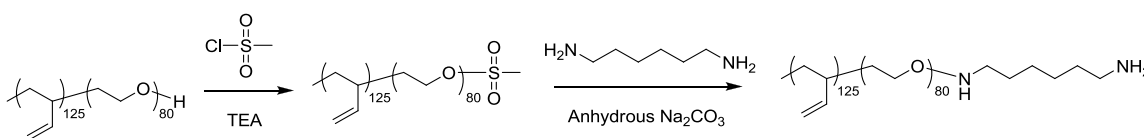
Scheme 3.5 Reaction scheme for terminal hydroxyl derivatization to amine.

As shown in **Scheme 3.5**, methanesulfonyl chloride (5.4 mg, 50 μmol) in 1 mL methylene chloride were mixed at 0 °C with 100 mg (10 μmol) OB2 and 2 mg (20 mmol) triethylamine dissolved in 1 mL methylene chloride. The reaction mixture was then stirred overnight under Ar at room temperature, and the product was purified by filtration and HPLC. Yield was 88 mg. ^{1}H NMR showed 94% functionalization. The mesylated OB18 (88 mg, 8 μmol) and hexamethylenediamine (10 mg, 80 μmol) were dissolved in benzene (5 mL) with a suspension of 15 mg anhydrous sodium carbonate. This mixture was stirred at reflux for 3 days, and then the product was purified by filtration and HPLC. Yield was 69 mg, ^{1}H NMR showed an overall of 54% substitution.

3.3.1.4. Synthesis of HyNic Modified Polymer
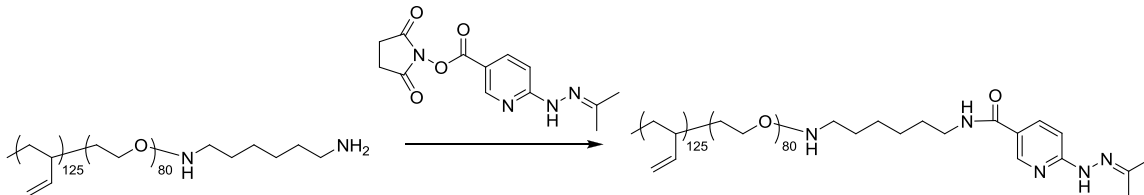
Scheme 3.6 Reaction scheme for terminal hydroxyl derivatization to HyNic.

50 mg amine functionalized OB18 diblock copolymer was dissolved in 1ml methylene chloride, and 1.5 mL of 10 mg mL^{-1} (100 μmol) succinimidyl 6-hydrazinonicotinate acetone hydrazone (S-HyNic) in anhydrous DMSO were added. After reaction overnight at room temperature, the hydrazine functionalized polymers were purified by HPLC. The functionalization degree calculated by ^{1}H NMR was 63%.

3.3.1.5. Synthesis of Maleimide Modified Polymer
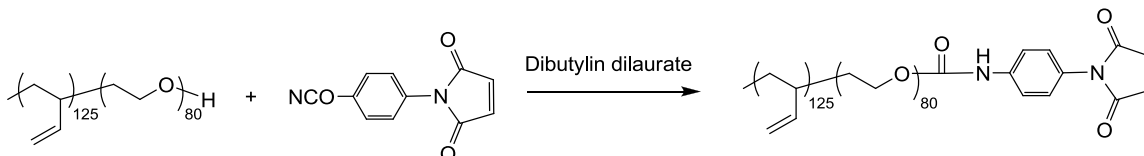
Scheme 3.7 Reaction scheme for terminal hydroxyl derivatization to maleimide.

100 mg OB18 diblock copolymer was dried under vacuum and dissolved under nitrogen in 2 mL of methylene chloride at room temperature, after which 6 mg (5 mM) catalyst dibutylin dilaurate (DBTDL) was added. *p*-maleimidophenyl isocyanate (PMPI) (20 mg; Pierce Chemical Co., Rockford, IL) was dissolved in 2 mL of anhydrous DMSO and then added to the diblock copolymer solution. The reaction was performed under Ar in the dark overnight. The solution was filtered and puried by HPLC to remove any residual traces of DMSO and catalyst, dried at room temperature under Ar, and stored at -20 ℃. The functionalization degree was calculated by ^{1}H NMR to be 72%.

3.3.2. Preparation and Characterization of OB18 and OB2 Mixed Polymersomes

All Near-infrared fluorophores incorporated polymersomes were prepared as described by Ghoroghchian et al.[16] A schematic vesicle formation via thin film rehydration is shown in **Scheme 3.8**. In brief, a different ratio of OB18 and OB2 diblock copolymer (Polymer Source Inc., Montreal, Quebec) was mixed at a mole ratio of 0%, 10%, 20%, 30%, 40%, 50%, 60%, 70%, 80%, 90% and 100%. The mixed diblock copolymer and porphyrin fluorophore trimer (PZn_3) were dissolved in methylene chloride at a 40:1 molar ratio of polymer to NIRF. The solution was then plated onto a roughened Teflon film and dried under vacuum overnight. Polymersomes were formed upon the addition of DI water and sonicated (1 h) in a bath sonicator. A narrow size distribution of nano-sized polymersomes was achieved with serial extrusion using a Liposofast Basic hand-held extruder equipped with 400-, 200- and 100-nm polycarbonate membranes (Avestin Inc., Ottawa, Ontario). The morphology of polymersomes samples was observed by Cryo-TEM as described in 3.3.8.
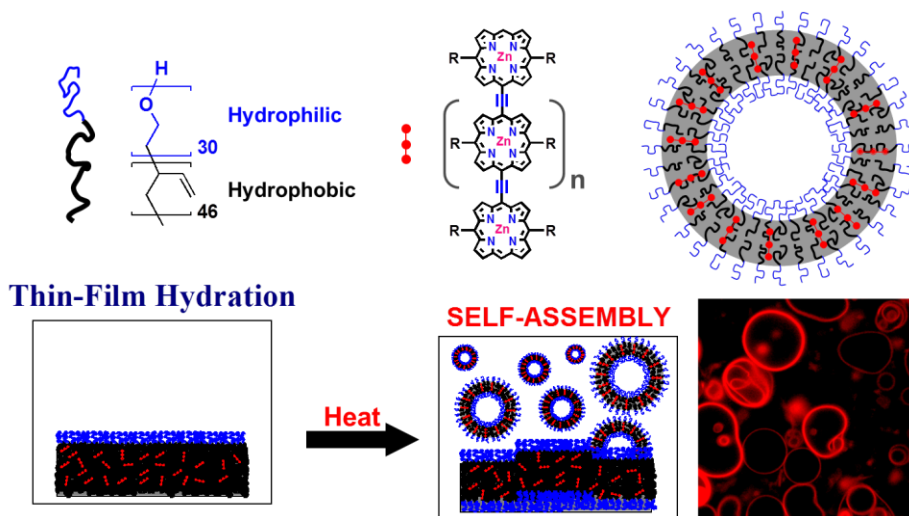
Scheme 3.8 Schematic formation of polymersomes by thin film rehydration.

3.3.3. Functionalized Polymersomes Formulation

The formation of functionalized polymersomes is similar to the procedures described in 3.3.2. Functionalized OB18 diblock copolymer was mixed with OB2 diblock copolymer and porphyrin fluorophore trimer (PZn_3). The polymer and porphyrin were codissolved in methylene chloride at a 40:1 molar ratio of polymer to porphyrin, plated on a square roughened Teflon film and dried under vacuum overnight. FNB functionalized polymersomes were formed upon the addition of 290 mOsm 0.1M pH 8.5 sodium borate buffer; biocytin, amine and HyNic functionalized polymersomes were formed upon the addition of 290 mOsm 0.1M pH 7.4 phosphate buffered saline (PBS) buffer solution; and the maleimide functionalized polymersomes were formed in 290 mOsm pH 4.0 2-(N-morpholino)ethanesulfonic acid (MES) buffer solution. Heating at 60 ℃ for 24 hours yielded micron-sized polymersomes while sonication (1 h) in a bath sonicator yielded nanoscale polymersomes. For nanosized polymersomes, a narrow size distribution of nano-sized polymersomes was achieved with serial extrusion using a Liposofast Basic hand-held extruder equipped with 400-, 200- and 100-nm polycarbonate membranes (Avestin Inc., Ottawa, Ontario). The morphology of polymersomes samples was observed by Cryo-TEM as described in 3.3.8.

3.3.4. Protein Conjugation to Functionalized Polymersomes by Different Coupling Procedures

3.3.4.1. Synthesis of ANHP Modified Polymers and Self-Assemble into Polymersomes

The terminal end of the PEO block was modified with ANHP peptide (a 1.5KDa anti-HER2-neu peptide mimic designed by Murali et al.)[71] through a two-step syntheses.

4-fluoro-3-nitrobenzoic acid was attached to the hydroxyl polymer terminus through an esterification in methylene chloride as described in 3.3.2.1. After filtration and HPLC purification, ANHP was attached to the modified polymer through a nucleophilic aromatic substitution in 50% THF (HPLC grade, Sigma-Aldrich) / 50% DI water (by volume) at 5 mM in a glass screw top vial. FNB functionalized polymer, ANHP and triethylamine (Sigma-Aldrich) were combined at 1:2:10 (molar ratio, FNB-polymer : ANHP : triethylamine). Reaction proceeded at 37-40 ℃, while stirring for 48 hours. The mixture was dried by rotary evaporation to remove water and THF, resolvated in 100% THF at 0.1 mg mL^{-1}, and then filtered and purified by HPLC. Characterization of the final polymer using ^{1}H NMR showed that 42.4% of the polymer was modified with ANHP. The ANHP functionalized 100 nm polymersomes were then prepared from a mixture of ANHP functionalized OB18 and OB2 at mole ratio of 1:99, 5:95 and 10:90 as described in 3.3.3. The polymersomes samples were then examined by Cryo-TEM (as described in 3.3.8) and DLS (as described in 3.3.9).

3.3.4.2. ANHP Peptide Conjugation to Preformed FNB Functionalized Polymersomes

100 nm FNB functionalized polymersomes were formed from a mixture of FNB functionalized OB18 and OB2 at mole ratio of 5:95, 10:90 and 30:70 as described above in 3.3.3. ANHP peptides were added to the preformed FNB functionalized polymersomes at a mole ratio of 1:10 in 0.1M Sodium borate buffer, PH 8.5. After reaction under Ar at 37℃ for 48 hours, the free ANHP peptide was separated by passing the mixture through a Sephacryl S-500 column (GE Healthcare Biosciences, Piscataway, NJ) with pH 7.4 PBS as eluent. The polymersomes samples were then examined by Cryo-TEM (as described in 3.3.8) and DLS (as described in 3.3.9).

3.3.4.3. Protein Conjugation to FNB Functionalized Polymersomes

100 nm FNB functionalized polymersome samples were prepared from a mixture of FNB functionalized OB18 and OB2 at mole ratio of 5:95 as described in 3.3.3. FNB functionalized 100 nm polymersomes were then mixed with streptavidin (Jackson ImmunoResearch Laboratories, PA) at a mole ratio of 10:1 functionalized polymer to streptavidin, or with rat-IgG antibody (Jackson ImmunoResearch Laboratories, PA) at a mole ratio of 40:1 functionalized polymer to rat IgG in 0.1M sodium borate buffer, pH 8.5. After reaction under Ar at 37 ℃ for 48 hours, the unbound antibody is separated by passing the mixture down a Sephacryl S-500 column with pH 7.4 PBS as eluent. The protein coupling efficiency to polymersomes was quantified by BCA protein assay as described in 3.3.7.

3.3.4.4. Antibody Conjugation to Biotin Functionalized Polymersomes
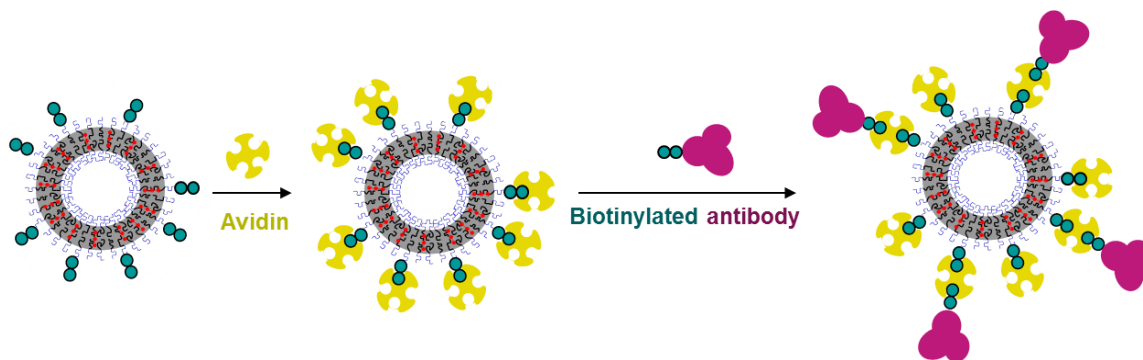
Scheme 3.9 Reaction scheme for biotinylated antibody conjugation to streptavidin polymersomes.

100 nm biotin functionalized polymersome samples were prepared from a mixture of biotin functionalized OB18 and OB2 at mole ratio of 1:99 as described in 3.3.3. The polymersomes were diluted to 0.5 mg mL^{-1}, mixed with streptavidin at a mole ratio of 1:

10 functionalized polymer to streptavidin in PBS buffer, pH 7.4 and stirred at room temperature for 1 hour. After reaction, the unreacted streptavidin is separated by passing the mixture down a Sephacryl S-500 column with pH 7.4 PBS as eluent. The streptavidin concentration was quantified by BCA protein assay as described in 3.3.7. For biotinylated antibody conjugation (**Scheme 3.6**), biotin-rat-IgG antibody (Jackson ImmunoResearch Laboratories, PA) is added to the streptavidin conjugated polymersomes at a mole ratio of 10:1 biotin-rat-IgG antibody to streptavidin conjugated polymersomes. After reaction under Ar at room temperature for 1 hour, the unbound biotin-rat-IgG antibody is separated by passing through a Sephacryl S-500 column with pH 7.4 PBS as eluent. The protein coupling efficiency to polymersomes was quantified by BCA protein assay as described in 3.3.7.

For micron-sized biotin functionalized polymersomes, they were also prepared from a mixture of biotin functionalized OB18 and OB2 at mole ratio of 1:99 as described in 3.3.3. The meso-scale polymersome samples were mixed with FITC-streptavidin (Jackson ImmunoResearch Laboratories, PA) at a mole ratio of 1: 10 biotin functionalized polymer to FITC-streptavidin in pH 7.4 PBS buffer containing 3% bovine serum albumin (BSA). The vesicles were allowed to bind 1 hour at room temperature, the unreacted FITC-streptavidin was separated by using a 1000 KDa dialysis tube (Spectrum Laboratories, Inc.). The morphology of FITC-streptavidin conjugated μm-sized NIR emissive polymersomes was observed by confocal laser scanning microscope.

3.3.4.5. Protein Conjugation via TDIC Linkage to Amine Functionalized Polymersomes
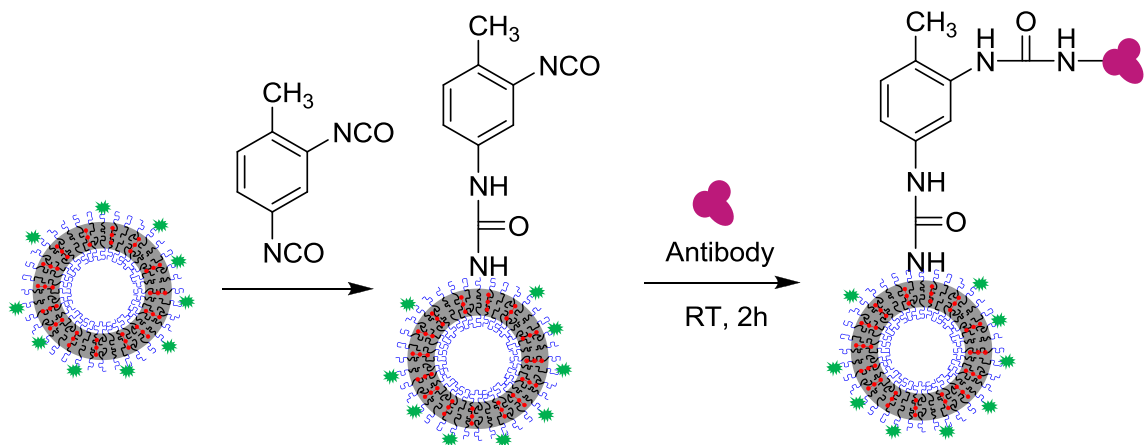
Scheme 3.10 Reaction scheme for antibody conjugation via TDIC linkage.

To 2 ml of 20 nM 100 nm amine functionalized polymersomes prepared from a mixture of amine functionalized OB18 and OB2 at mole ratio of 5:95 as described in 3.3.3, 200 μl of a 2% solution of TDIC in p-dioxane was added. The reaction mixture was incubated at room temperature for 2 hours with stirring. The resulting supernatant was then mixed with 50 μl of streptavidin (10 mg/ml in PBS) or 200 μl of rat-IgG solution (2 mg/ml in PBS) and incubated at 37 ℃ for 2hr to produce antibody-modified polymersomes. To separate noncovalently bound antibody, the polymersome solution was then passed down a sephacryl S-500 HPLC column with pH 7.4 PBS as eluent. The protein coupling efficiency to polymersomes was quantified by BCA protein assay as described in 3.3.7.

3.3.4.6. Antibody Conjugation via Sulfo-SMCC Linkage to Amine Functionalized Polymersomes
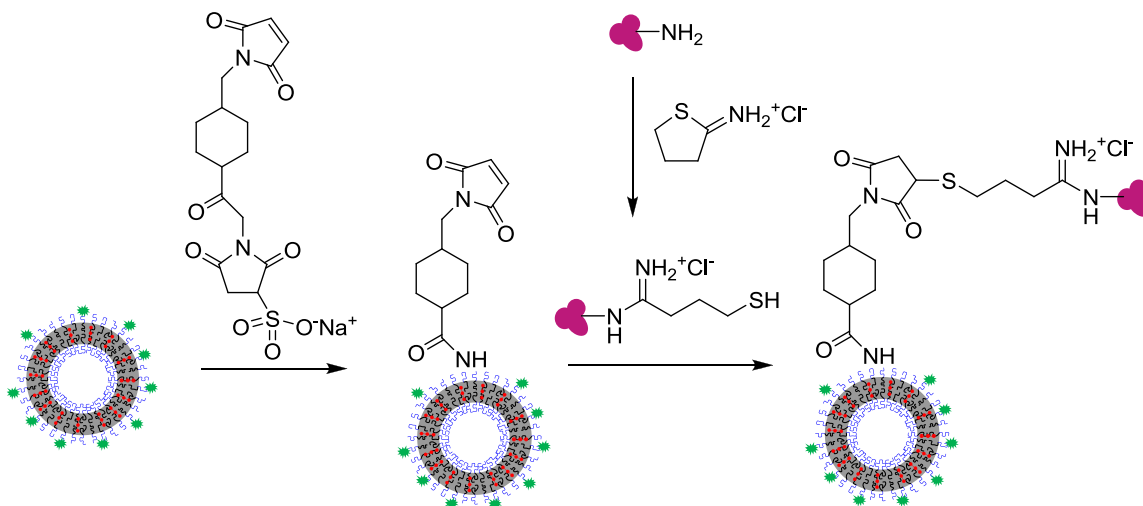
Scheme 3.11 Reaction scheme for antibody conjugation via sulfo-SMCC linkage.

To 2 ml of 20 nM 100 nm amine functionalized polymersomes prepared from a mixture of amine functionalized OB18 and OB2 at mole ratio of 5:95 as described in 3.3.3, 1 ml of 5 mg/ml sulfo-SMCC in PBS buffer was added. Reaction was continued at RT for 1 hour. Excess sulfo-SMCC was removed by passing the reaction mixture through a sephacryl S-500 HPLC column with pH 7.4 PBS as eluent. Streptavidin or rat-IgG antibody was thiolated using 2-iminothiolane (Traut's reagent). 2-iminothiolane was dissolved at 2mg/ml in pH 8 0.1M sodium borate buffer containing 5mM EDTA. The molar ratio of 2-iminothiolane added to antibody was 40:1.[13, 72] The reaction was performed at RT for 1 hour under Ar. The thiol modified antibody was then desalted into conjugation buffer (pH 7.4, PBS buffer). The thiolated streptavidin or rat-IgG was then incubated with concentrated sulfo-SMCC polymersomes overnight with stirring under Ar flow at room temperature. The molar ratio of thiolated streptavidin to maleimide was

1:10 and thiolated rat-IgG to maleimide was 1:40. The reaction mixture was then applied to a sephacryl S-500 HPLC column and eluted with 0.01 M PBS buffer (pH 7.4) to remove unbound antibody. The protein coupling efficiency to polymersomes was quantified by BCA protein assay as described in 3.3.7.

3.3.4.7. Antibody Conjugation to HyNic Functionalized Polymersomes
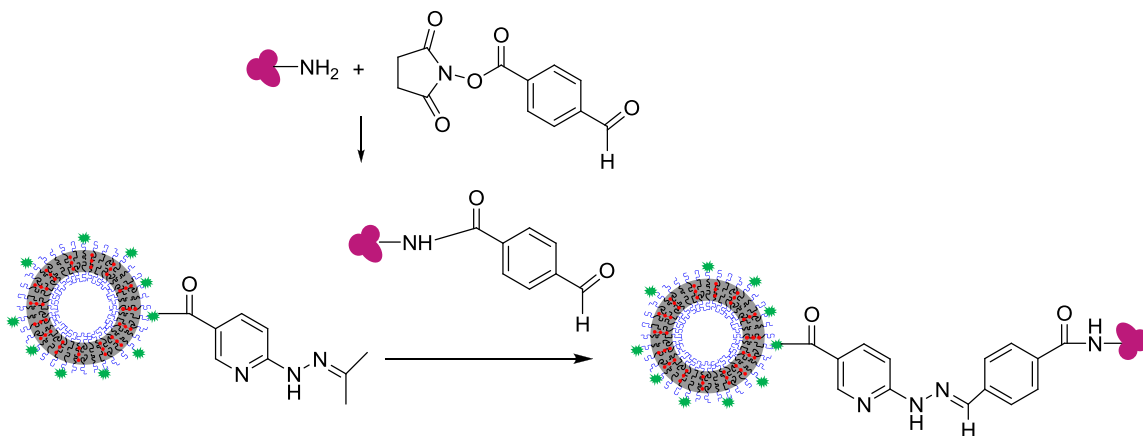
Scheme 3.12 Reaction scheme for antibody conjugation via hydrazone linkage.

Streptavidin and rat-IgG antibody were passed through a 40k desalting column (Thermofisher) before modification. 1.0 mg succinimidyl 4-formylbenzoate (SFB) was dissolved in 100 µl anhydrous DMF. The required volume of SFB (20 mole equivalents/mole antibody, and the percentage of DMF (vol/vol) in the final SFB modification reaction was maintained below 5% of the total reaction volume) was added to the antibody solution in modification buffer (2-4 mg/ml concentration, 0.1 M PBS, 150 mM NaCl, pH 7.4) and mixed thoroughly. The reaction was incubated at room temperature for 1.5 hour. The SFB modified antibody was purified by desalting into conjugation buffer (100 mM phosphate, 150 mM NaCl, pH 6.0) using a 40k desalting column.

Polymersome-antibody conjugate was synthesized by adding SFB modified streptavidin or rat-IgG to 100nm HyNic modified polymersomes prepared from a mixture of HyNic functionalized OB18 and OB2 at mole ratio of 5:95 as described in 3.3.3, at mole ratio of 10:1 functionalized polymer: streptavidin or 40:1 functionalized polymer: rat-IgG. The non-conjugated antibody was subsequently removed by a sephacryl S-500 HPLC column with pH 7.4 PBS as eluent. The protein coupling efficiency to polymersomes was quantified by BCA protein assay as described in 3.3.7.

3.3.4.8. Antibody Conjugation to Maleimide Functionalized Polymersomes

Streptavidin, rat-IgG or Goat-Anti-Mouse IgG (5 nm Gold conjugated) antibody (Ted-pella Inc, Redding, CA) were thiolated using 2-iminothiolane. 2-iminothiolane as described in 3.3.4.6. The 100 nm maleimide functionalized polymersomes were prepared from a mixture of maleimide functionalized OB18 and OB2 at mole ratio of 5:95 as described in 3.3.3 at pH 4.0 in MES buffer. The pH of maleimide functionalized polymersomes was adjusted to pH 6.5 by adding NaOH dropwise. The thiolated streptavidin or rat-IgG was incubated with maleimide functionalized polymersomes overnight with stirring under Ar flow at room temperature. The molar ratio of thiolated streptavidin to maleimide was 1:10 and thiolated rat-IgG or Goat-Anti-Mouse IgG (5 nm Gold conjugated) antibody to maleimide was 1:40. The reaction mixture was then applied to a sephacryl S-500 HPLC column and eluted with pH 7.4 PBS buffer. The protein coupling efficiency to polymersomes was quantified by BCA protein assay as described in 3.3.7. The morphology of Goat-Anti-Mouse IgG (5nm Gold conjugated) antibody conjugated polymersomes was observed by TEM, negative staining TEM and Cryo-TEM as described in 3.3.8.

For micron-sized maleimide functionalized polymersomes, they were also prepared from a mixture of maleimide functionalized OB18 and OB2 at mole ratio of 5:95 as described in 3.3.3. The pH of the maleimide functionalized polymersome samples were adjusted to 6.5 and then mixed with thiol activated FITC-rat IgG (Jackson ImmunoResearch Laboratories, PA) at a mole ratio of 1: 40 maleimide functionalized polymer to thiol-activated FITC-rat IgG. The vesicles were allowed to bind overnight at room temperature; the free unbound FITC-rat IgG was separated by using a 1000 KDa dialysis tube. The morphology of FITC-rat IgG conjugated μm-sized NIR emissive polymersomes was observed by confocal laser scanning microscope.

3.3.5. Antibody Conjugation Efficiency with Different Functionalization Degree

Streptavidin and rat-IgG antibody were conjugated to functionalized polymersomes by both FNB coupling method and Maleimide method at different functionalized polymer degrees. For FNB coupling method, 0.05%, 0.1%, 0.5%, 1%, 2%, 3% and 4% FNB functionalized polymersomes were conjugated with streptavidin at mole ratio of 2:1; while 0.1%, 0.2%, 0.3%, 0.5%, 0.75% and 1% FNB functionalized polymersomes were conjugated with rat-IgG antibody at mole ratio of 2:1. For Maleimide coupling method, 0.5%, 1%, 2%, 3%, 4% and 5% Maleimide functionalized polymersomes were conjugated with thiolated streptavidin at mole ratio of 2:1; while 0.2%, 0.3%, 0.5%, 0.75%, 1%, 2% and 3% FNB functionalized polymersomes were conjugated with thiolated rat-IgG antibody at mole ratio of 2:1. Conjugated antibody concentration per polymersome was quantified by BCA protein assay.

3.3.6. Antibody Conjugation Efficiency with Different Antibody Concentration

5% Maleimide functionalized polymersomes were conjugated with thiolated rat-IgG antibody at mole ratio of 80:1, 40:1, 20:1 and 10:1 maleimide functioanlzied polymer to antibody. Conjugated antibody concentration per polymersome was quantified by BCA protein assay. Antibody (AB) conjugation efficiency was calculated using the equation below:

AB conjugation efficiency = AB conjugated / AB initially added

3.3.7. Quantification of Protein concentration by BCA protein assay

Bicinchoninic acid (BCA) protein assay (ThermoScientific, USA) was used to quantify the extent of protein coupling to the polymersomes. First, we constructed a protein calibration curve by preparing a serial dilution of antibodies in PBS and analyzing each solution for protein content with the BCA protein assay kit. Next, the protein concentrations of protein-conjugated polymersome sample and the blank polymersome sample were both measured by using the BCA assay. The blank polymersomes sample was prepared by mixing the same amount of nonfunctionalized polymersomes with protein, followed by passing down the sephacryl S-500 column. The amount of protein that was covalently coupled to the polymersomes was determined by subtracting the calculated amount of the blank polymersomes sample from the protein conjugated polymersomes sample. The experiment was repeated three times with three different polymersomes samples prepared on different days to get the average value of protein concentration. The number of antibodies per 100nm polymersomes was then calculated as below: computations assume a 1 nm^2 projected area per PBD block composing the polymersome's bilayer membrane, therefore each 100nm polymersomes is composed of

~62,800 PEO-*b*-PBD polymer.[73] There are approximate $4*10^{14}$ peptides per ug ANHP, $1*10^{13}$ proteins per ug streptavidin, $4*10^{12}$ antibodies per ug rat IgG antibody, and $9.6*10^{12}$ polymersomes per umol polymer. The polymer concentration was directly related to the porphyrin concentration by the initial molar ratio deposited as a thin film (40:1 polymer:porphyrin).[16, 74] The concentration of the PZn_3 porphyrin emitterS in the polymersomal membrane was quantified via the established extinction coefficients of the far red absorbance of these species PZn_3 (λ = 795 nm). Upon measurement of fluorophore absorbance in solution, the concentration of PZn_3 was obtained using Beer's Law and previously established extinction coefficients (PZn_3 λ_{795nm} ε = 25000 $M^{-1}cm^{-1}$).[17, 75-78] The concentration of protein is quantified by BCA assay, therefore, we could calculate the number of protein per 100nm polymersome using the method described here.

3.3.8. Transmission Electron Microscopy (TEM)

<u>TEM</u>

Nanometric polymersomes were formulated as described above. A droplet of solution (5 μl) was deposited on TEM grid, any excess solution was removed with filter paper. Sample grids were examined in a FEI Tecnai G ² Twin transmission electron microscope operating at 200 kV, and images were recorded with a Gatan 724 multiscan digital camera.

<u>Negative staining TEM</u>

For the negative staining, a droplet of sample solution, DI water and phosphotungstic acid (Ted Palla, USA) were deposited on a parafilm. The TEM grid was insert into the sample drop (30 s), then in a distilled water drop for washing (10 s) and finally in a phosphotungstic acid (PTA) drop for staining (10 s). Any excess solution was

removed with filter paper. Sample grids were examined in a FEI Tecnai G ² Twin transmission electron microscope operating at 200 kV, and images were recorded with a Gatan 724 multiscan digital camera.

<u>Cryogenic Transmission Electron Microscopy (Cryo-TEM)</u>

Vitreous samples were prepared within a controlled environment vitrification system (Vitrobot). A droplet of solution (10 μl) was deposited on a copper TEM grid coated with a porous polymer film. A thin film (< 300 nm) was obtained by blotting with filter paper. After allowing the sample sufficient time to relax from any residual stresses imparted during blotting (30 s), the grid was plunge cooled in liquid ethane at its freezing point (-180 ℃), resulting in vitrification of the aqueous film. Sample grids were examined in a FEI Tecnai G ²Twin transmission electron microscope operating at 200 kV, and images were recorded with a Gatan 724 multiscan digital camera.

3.3.9. Dynamic Light Scattering (DLS)

Dynamic light scattering was performed using a DynaPro Titan dynamic light-scattering instrument (Wyatt Technology Inc.) that applied vertically polarized laser light of wavelength 829 nm. The DLS instrument was calibrated with BSA standard (2 mg ml^{-1} in PBS buffer, 25 ℃). Light-scattering studies were carried out in the concentration range of 0.1-0.5 mg mL^{-1} polymersomes in DI H_2O. Prior to DLS, The quartz cell was rinsed several times with filtered water and then filled with the filtered sample solution. The data obtained in each case were the average of 50 runs, each of 10 s duration. The temperature was maintained at 25 ℃. Data were collected and analyzed using the DYNAMICS software for the DynaPro Titan instrument (Wyatt Technology Inc.)

3.3.10. Confocal Laser Scanning Microscopy

Fluorescence scanning confocal microscope images were obtained with a Leica SP5 Confocal Microscope (Oberkochen, Germany) equipped with a CApochromat $40\times/1.2$ W objective. Both FITC and PZn_3 excitation were achieved with a 488 nm Argon laser. Fluorescence emission was captured using either 505-530 nm band pass (FITC) or 650 nm long-pass (YZ112) filters. Polymersomes were imaged by directly plating 10 μL on a glass slide and covering with coverslip. Images were modified for contrast and brightness using Leica SP5 software.

3.3.11. Enzyme-linked Immunosorbent Assay (ELISA) Experiments

Equilibrium binding of conjugated rat IgG polymersomes by maleimide method to recombinant goat-anti-rat IgG antigen was determined by a modified ELISA assay. ELISA was performed at room temperature. NUNC MaxiSorpTM High Protein-Binding Capacity ELISA plates (NUNC, Rochester, NY, USA) were coated with goat-anti-rat IgG antibody (100 μg mL^{-1}) and incubated overnight at 4°C. After rinsing the plates three times with PBS buffer, blocking was performed with 3% bovine serum albumin (BSA) in the washing buffer for 1 h at RT. After being washed, different concentrations of test samples (Rat-IgG antibody conjugated polymersomes) and control samples (non-conjugated polymersomes) were incubated for 1 hour at RT. The wells were washed, and 1/5000 diluted Goat-anti-Rat HRP was then incubated for 1 h at RT. After a final wash, the enzyme substrate (100 μg mL^{-1} TMB12 in 100mM sodium acetate, PH 6.0, with 10 μl of 30% hydrogen peroxide added to 50ml of this solution directly before use) was added and incubated for 10 min at RT. The reaction was then stopped by the addition of 1 N

HCl. The absorbance was read at 520 nm using an ELISA plate reader (Dynatech, MR-5000, Chantilly, Va., USA).

3.3.12. Licor-Odyssey Experiments to Measure Polymersomes Binding Sensitivity

Binding of streptavidin conjugated polymersomes by maleimide coupling method to biotinylated 96 well plates were determined by direct Licor-Odyssey imaging. Purified streptavidin conjugated polymersomes or unconjugated polymersomes alone (1.68-200 fmol polymersomes/well) were immobilized on a biotinlated plate (Pierce) with a 2 times serial dilution per well for l hr at room temperature in PBS. Commercially available DyLight 680 conjugated streptavidin and DyLight 800 conjugated streptavidin were used at the same concentration as the streptavidin conjugated polymersomes for comparision. Excess polymersomes or DyLight streptavidin samples were then washed 3 times by using excessive PBS buffer. Images were acquired by excite using a solid-state diode laser at 685nm or 785 nm and collected with a dichroic mirror filter below 750nm (700 nm chanel) and above 810nm (800 nm chanel) with an Odyssey Infrared Imaging System (LI-COR, Lincoln, NE). Emission readings (700 nm and 800 nm chanel) of the samples were determined by integration of the image intensity.

3.3.13. Preparation of anti-ErbB2 IPs

Anti-ErbB2 antibody (Abcam, USA) was thiolated using 2-iminothiolane as described in 3.3.4.6. The maleimide functionalized polymersomes prepared from maleimide functionalized OB18 diblock copolymer mixture with OB2 diblock copolymer at a mole ratio of 5:95 as described in 3.3.3 was incubated with the thiolated antibody overnight under Ar flow at room temperature. The molar ratio of the thiolated anti-ErbB2

antibody to maleimide was 1:40. The reaction mixture was then applied to a sephacryl S-500 HPLC column and eluted with 0.1 M PBS buffer (pH 7.4).

3.3.14. Cell Culture and Harvest

The human breast cancer cell lines BT474, HCC1569 cells, SKBR3, and MCF7 were purchased from the American Type Tissue Culture Collection. BT474 cells and HCC1569 cells were cultured in Roswell Park Memorial Institute medium (RPMI) with penicillin:streptomycin (PenStrep), 10% fetal bovine serum (FBS), 1% glutamine and 10 μg/mL of insulin. SKBR3 cells were cultured in Dulbecco's modified eagle's medium (DMEM) growth medium supplemented with 10% fetal bovine serum, 1% penicillin, 10,000 μg/mL streptomycin, 2 mM L-glutamine and 1 mM pyruvate. MCF7 cells were cultured in DMEM with PenStrep and 10% FBS and 1% glutamine. Cells were grown in a humidified incubator (HERA Cell 150, Thermo Scientific, Germany) at 37 ℃ in a 5% CO_2 atmosphere. The medium was replenished every two days and the cells were harvested as follows. Following removal of the growth medium, cells were first washed with 5 mL of phosphate buffered saline (PBS). PBS was removed and the cells were disassociated with 2 mL PBS containing 2 mM ethylenediamine tetraacetate (EDTA) and subcultured by trypsinization.

3.3.15. Internalization of Anti-ErbB2 IPs in Cells

Human breast cancer cells BT474, HCC1569 cells, SKBR3, and MCF7 were seeded at a density of 1×10^6 cells per well in a 6-well plate and incubated for 24 h to allow attachment of cells to the plate prior to the uptake experiments. Both live cells and fixed cells (fixed by using 4% formaldehyde at room temperature for 15 mins and then washed 3 times with PBS buffer) were incubated with anti-ErbB2 810 nm emissive

polymersomes with and without conjugated anti-ErbB2 antibody, or with conjugated irrelevant rat-IgG antibody. For fixed cells, 4 nM polymersomes were incubated with the cells for 30 mins at room temperature. For live cells, 1 nM polymersomes were incubated with the cells for 4 hours at room temperature. Following incubation, cells were washed 3 times with PBS buffer to remove non-internalized polymersomes. The cells were analyzed for the uptake of polymersomes with and without conjugated anti-ErbB2 antibody with confocal laser scanning microscopy.

3.3.16. Cell Imaging by Laser Confocal Scanning Microscopy

Cells pre-treated with 810 nm emissive polymersomes with and without conjugated anti-ErbB2 antibody were incubated with nuclei staining Hoechest dye 33258 followed by 3 PBS washes before imaging. The cell suspensions were visualized with a confocal laser scanning microscope (Leica SP5) equipped with $40\times$ oil lens (Olympus). The measurements were performed in sequential mode, and the intensity of each fluorescent dye was adjusted individually: both FITC and PZn_3 excitation were achieved with a 488 nm Argon laser. Fluorescence emission was captured using either 505-530 nm band pass (FITC) or 650 nm long-pass (YZ112) filters. Images were modified for contrast and brightness using Leica SP5 software.

3.3.17. Quantification of IP Uptake

BT474 cells and MCF7 cell lines were passaged when confluency reached 70%. These adherent cells were detached from culture plates with addition of 0.05% trypsin and 2 mM EDTA and incubation at 37C for 5 min. The single cell suspensions were counted to have a cell concentration of 1×10^6 cells/mL. The cells were fixed by using 4% formaldehyde at room temperature for 15 mins, followed by washing 3 times with PBS

buffer. The cell suspensions were then incubated with either PBS buffer (control), NIR emissive polymersomes, or ErbB2-NIR emissive polymersomes at controlled concentrations (0.22 nM to 3.52 nM polymermersomes) for 1 hour at RT or overnight at 4 ℃. Following incubation, cells were collected using three PBS washes with an additional volume of PBS added (10 times cell incubation volumes) before centrifugation (2 min, 5000 rpm). The polymersome containing supernatant was then removed and the wash cycle subsequently repeated twice.

The dissociation constant of the polymersome-cell complex (K_{diss}) and the maximum polymersome-cell binding ($[P]_{max}$) was determined as best fit parameters of the dose response equation:

$$[P] = [P]_{max}[P]_0/(K_{diss}+[P]_0)$$

where [P] is the amount of cell-bound polymersomes per cell and $[P]_0$ is the concentration of unbound polymersomes in the incubation medium.

3.3.17.1. Flow Cytometry for Quantification of anti-ErbB2 IP Uptake in HER2 Cells

A BD FACSCalibur flow cytometer (BD Biosciences, Franklin Lakes, NJ) was employed to determine the extent of fluorescent labeling achieved by NIR emissive polymersome uptake. Cells were gated using the forward versus side scatter parameters. All experiments analyzed a minimum of 10 000 cell events. The NIR fluorophores were excited using an argon ion laser (15 mW, 488 nm) and probed with fluorescence detection in the FL3 channel (650 nm longpass filter). The uptake of polymersome-anti-ErbB2 conjugates at different polymersome concentrations (0.22 nM to 3.52 nM) by BT474 cells and MCF7 cells were analyzed based on the measurement of cellular-associated fluorescence of cells and the mean fluorescence intensity of gated viable cells.

The cell detection studies based on the uptake of polymersome-anti-ErbB2 conjugates by BT474 cells and MCF7 cells were performed in a 96-well plate (BD Falcon, Franklin Lakes, NJ). Labeled cells from 4.3.4 were plated at dilutions of 25000, 5000, 1000, or 200 cells per well. NIR emissive polymersomes were plated in parallel with 2-fold dilutions ranging from 1.6 to 0.012 fmol of polymersomes per well for calibration purposes. Images were acquired by excitation using a solid-state diode laser at 785 nm and collected with a dichroic mirror filter above 810nm with an Odyssey Infrared Imaging System (LI-COR, Lincoln, NE).

3.4. Results and Discussion

3.4.1. Functionalized Block Copolymer Synthesis and Characterization

We developed five different chemistry modification methods to synthesize functionalized PEO-*b*-PBD diblock copolymers to provide an amphiphilic polymer with functional properties suitable for the conjugation of antibody to polymersomes, as shown in **Scheme 3.1**. OB18, a member of the PEO-*b*-PBD family, was used for our functionalization. The terminal hydroxyl on the PEG end of OB18 was linked to different moieties. For FNB functionalization, FNB was used to functionalize the hydroxyl end group of OB18 via an esterification reaction. The functionalization degree for this step has been measured by NMR to be 88%, and the resulting product was stable at least 30 days at neutral pH and 20 ℃. For biotin functionalization, a two-step functionalization was utilized by adding biocytin to FNB functionalized OB18. In the second step, the terminal amine in the lysine tail of biocytin nucleophilically displaces an optical absorber that can be used to monitor the progression of the reaction at 428 nm.[70] We measured that

the success of biotinylation is about 68% of all terminal hydroxyl groups by using the extinction coefficient of the biotin functionalized OB18 at 428 nm. For amine functionalization, a two-step reaction was also used by first mesylating the hydroxyl group of OB18. The functionalization degree for this step was measured by ^{1}H NMR to be as high as 94%. Hexamethylenediamine was then added to the mesylated OB18 to form the amine functionalized OB18, the functionalization degree for this step was measured by NMR to be 54% of the overall polymer. The maleimide functionalization was carried out by adding PMPI to give a maleimide functionality of OB18. The functionalization degree was calculated from NMR to be 72%. Finally, the hydrazone linkage functionalization was using HyNic to functionalize the hydroxyl group of OB18, and the functionalization degree was measured by NMR to be 63%.
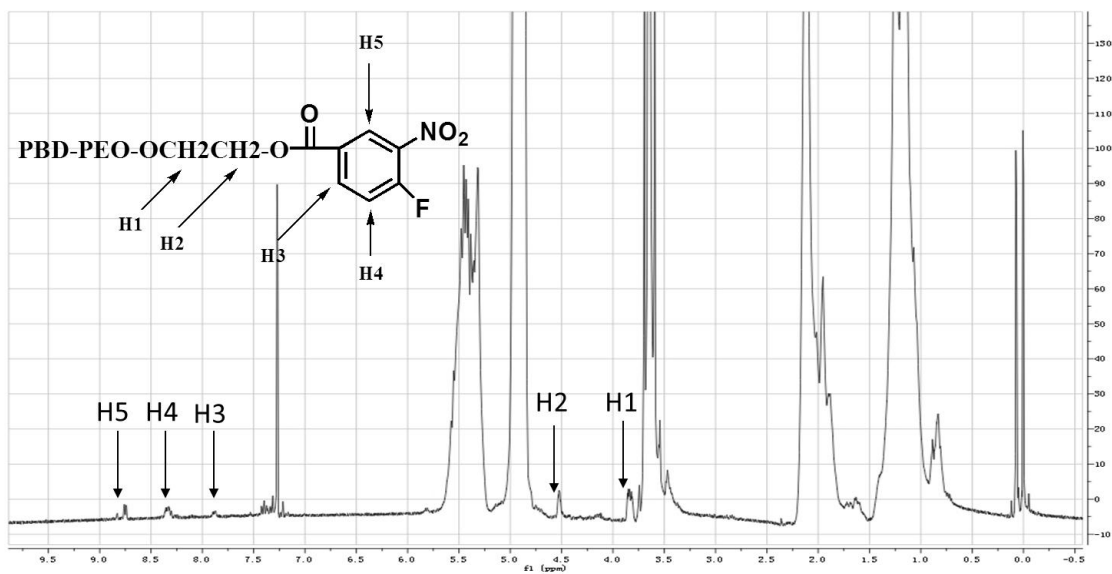
Figure 3.1 ^{1}H NMR of FNB functionalized OB18.
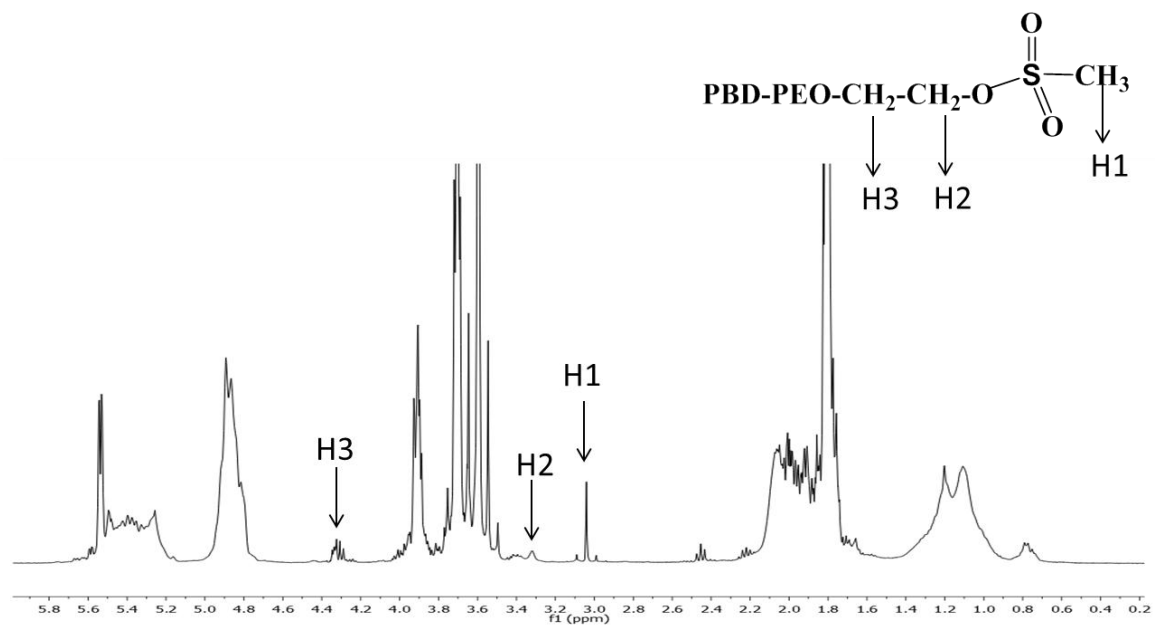
Figure 3.2 ^{1}H NMR of mesylated OB18.
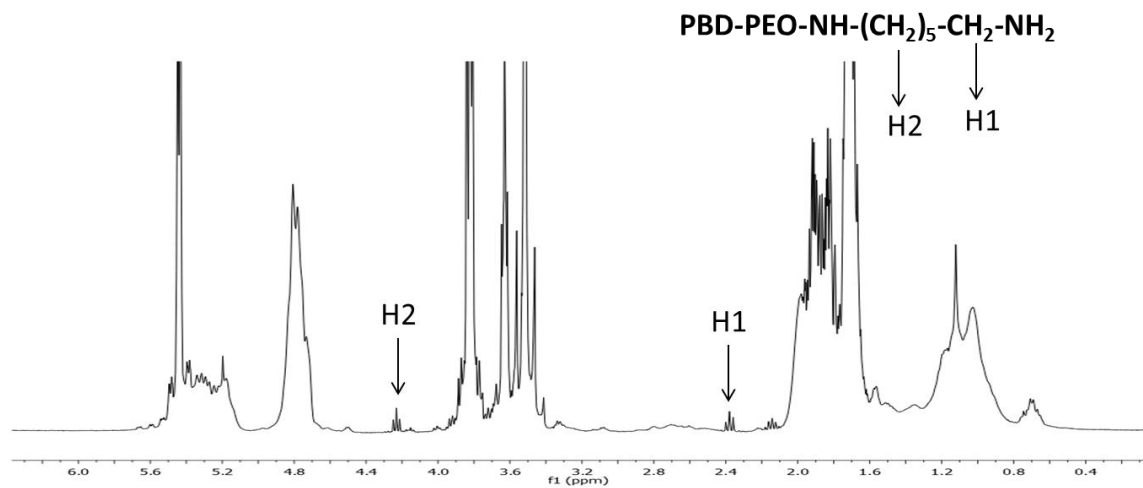
Figure 3.3 ^{1}H NMR of amine functionalized OB18.
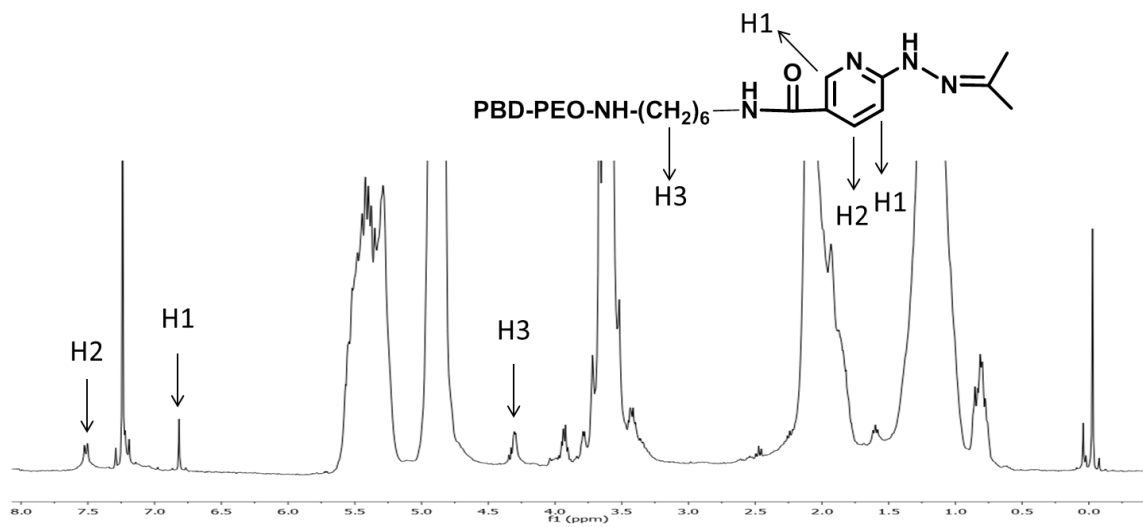
Figure 3.4 ^{1}H NMR of HyNic functionalized OB18.
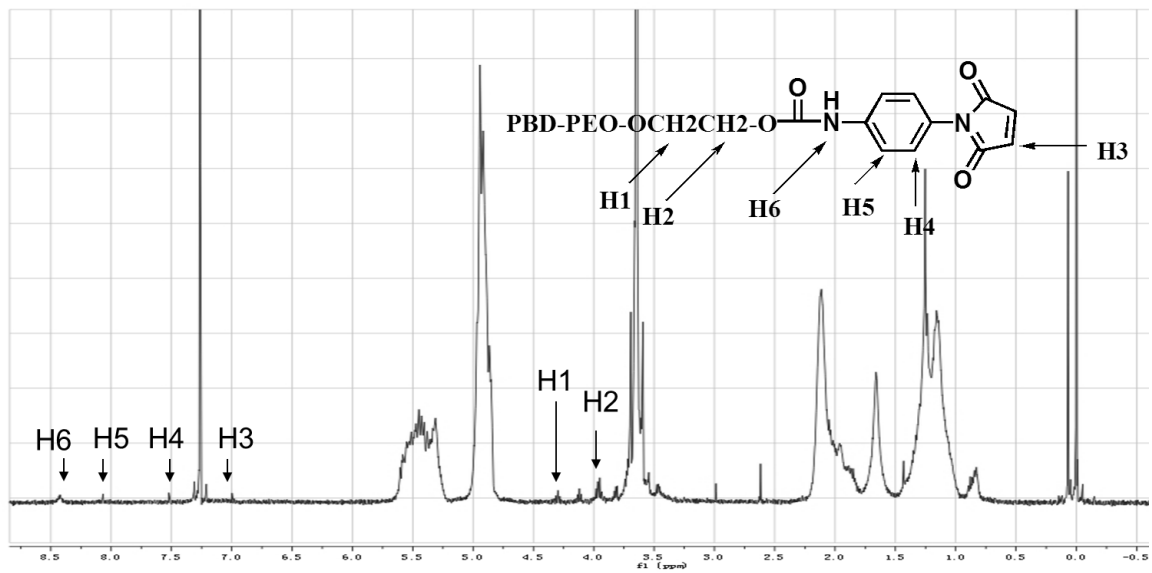
Figure 3.5 ^{1}H NMR of maleimide functionalized OB18.

3.4.2. Functionalized Polymersome Formation and Characterization

3.4.2.1. Functionalized Polymersome Composition

A polymer mixture of functionalized OB18 and OB2 was used to preform functionalized polymersomes. The reason we used this polymer mixture is because the OB18 diblock copolymer has a much longer PEO chain length compared to the OB2 diblock copolymer and will be able to extend its hydrophilic functionalized end group to a further region on the polymersome outer surface, therefore there is less possibility for the functionalized end group to bend back towards the bilayer membrane and become less accessible to the antibody conjugation. Also, the steric hindrance effect on the polymersomes surface which prevents the antibody conjugation will be minimal because of the increased PEO chain length. Previous studies on conjugating antibodies to liposomes prepared from carboxyacyl derivatives of phosphatidylethanolamine with different chain length showed that with an increasing in PEG chain length from PEG_2 to PEG_{20}, the antibody conjugation efficiency greatly increased from 1% to 63%.[79]

To make sure the mixture of the two different PEO-b-PBD diblock copolymers OB18 and OB2 would produce a uniform distribution of the two polymers in polymersomes, rather than a mixture of separate OB18 polymersomes and OB2 polymersomes, we prepared 11 samples with different OB18 mole percentages ranging from 0% - 100% in the OB18/OB2 mixture as shown below in **Figure 3.6**. The morphology of all these samples was observed by Cryo-TEM, which showed a mixture of mostly polymersome vesicle structures together with a small amount of worm-like micelle structures in all the samples. The membrane thickness of the OB18/OB2 polymersomes was also measured by Cryo-TEM. Previous literature results indicate that

OB2 polymersomes have a membrane thickness of 9.6nm and OB18 polymersomes has a membrane thickness of 14.8nm.[74] The membrane thickness of our OB18/OB2 polymersomes was right within this range of 9.6nm to 14.8nm. In addition, the membrane thickness increased linearly with the OB18 content in the OB18/OB2 mixture which was used to prepare OB18/OB2 polymersomes. All these results indicate that the mixtures of OB18 and OB2 diblock copolymers have a homogenous distribution of the two polymers in polymersomes, and this polymer mixture system could be used to prepare functionalized OB18/OB2 polymersomes.

The functionalization end group is very small compare to the OB18 diblock copolymer, and thus should not change the morphology of the self-assembled OB18/OB2 polymersomes. As expected, Cryo-TEM showed no structure change of 5% FNB functionalized OB18/OB2 polymersomes compared to the 5% OB18/OB2 polymersomes (**Figure 3.7**).

Samples   **Membrane thickness**
1.   100% OB2   9.6nm
2.   10% OB2 / 90% OB18
3.   20% OB2 / 80% OB18
4.   30% OB2 / 70% OB18
5.   40% OB2 / 60% OB18
6.   50% OB2 / 50% OB18
7.   60% OB2 / 40% OB18
8.   70% OB2 / 30% OB18
9.   80% OB2 / 20% OB18
10. 90% OB2 / 10%OB18
11. 100% OB18   14.8nm
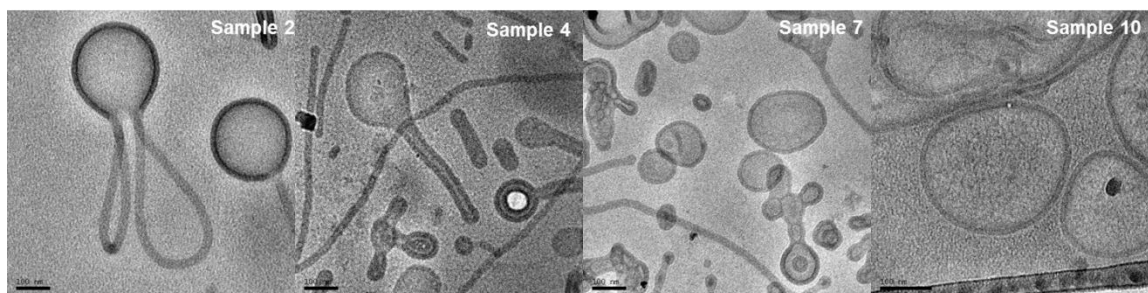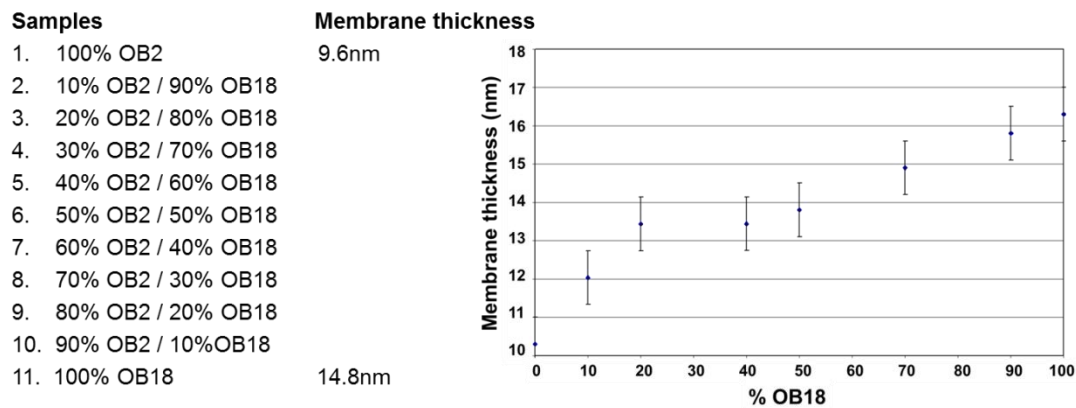
Figure 3.6 Polymersome membrane thickness vs. different OB18 content.
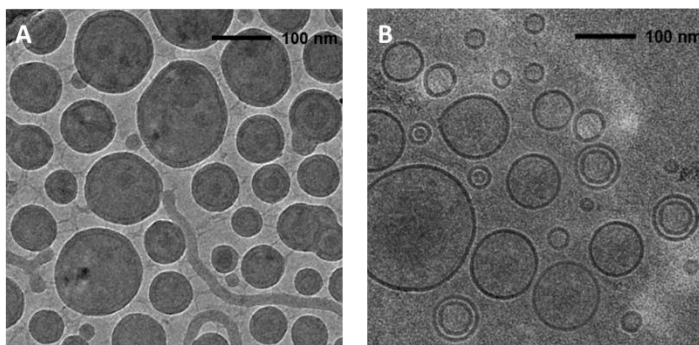
Figure 3.7 Cryo-TEM images of (A) 5% OB18/OB2 polymersomes and (B) 5% FNB functionalized OB18/OB2 polymersomes.

3.4.2.2. Peptide Conjugation by Using Functionalized Polymer vs. Preformed Functionalized Polymersomes

As described in 3.2, there are two different methods to prepare ligand conjugated polymersomes. The first coupling procedure involves attachment of ligands to functionalized diblock copolymer to synthesize ligand-conjugated polymers, followed by using these ligand-conjugated polymers to self-assemble into polymersomes. The other method is to first form polymersomes from end-functionalized block copolymers, and then conjugate ligands to the preformed functionalized polymersomes surface. A small peptide ANHP was chosen to conjugate to FNB functionalized polymer or polymersomes to compare these two methods. For the first coupling method, we conjugated the ANHP peptide to the polymersomes via FNB functionalization, as shown in **Scheme 3.13**. The ANHP functionalized OB18 was mixed with OB2 at 1%, 3% and 5% to form 100nm-sized polymersomes. Cryo-TEM images and DLS data of these three samples were taken and shown in **Figure 3.8**. In 1% and 3% ANHP peptide functionalized polymersomes, a lot of polymersome vesicle structures together with some worm-like micelle structures were observed by Cryo-TEM. However, in 5% ANHP peptide functionalized polymersomes, very few polymersomes structures were observed. DLS data also confirmed this. In 1% and 3% ANHP peptide functionalized polymersomes, the average particles size was ~100nm, while in 5% ANHP peptide functionalized polymersomes, the particles size greatly increased to 1-10 μm, indicated large aggregate formation in solution. Therefore, by using this method, the maximum functionalization degree to form polymersomes is ~3% for ANHP peptide functionalized polymers.
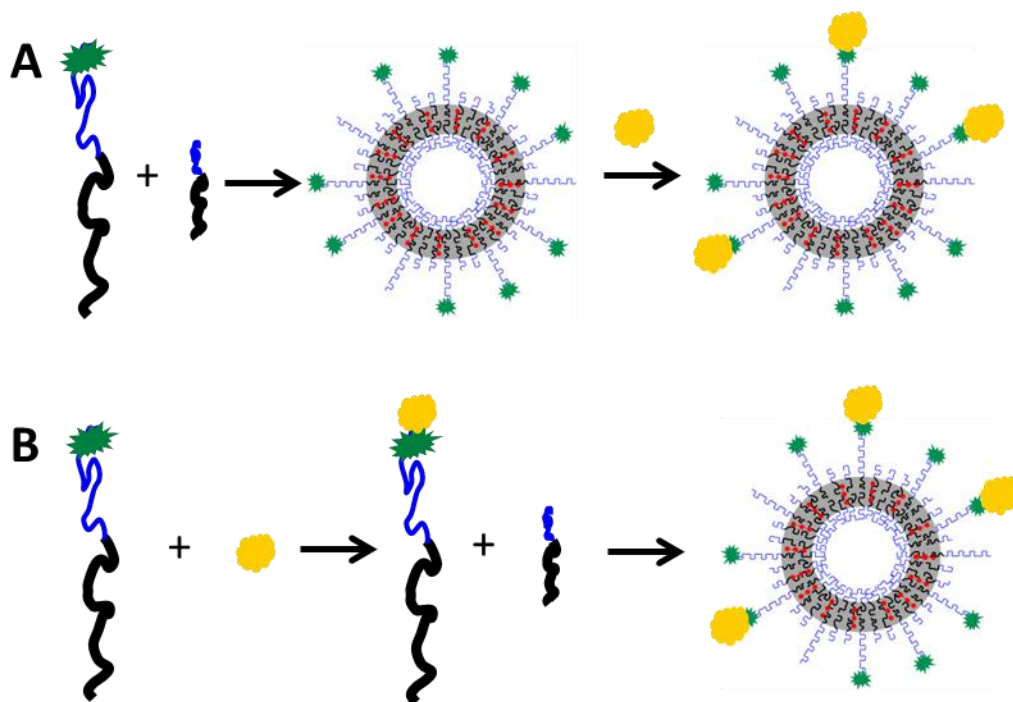
Scheme 3.13 Preparation of ANHP conjugated polymersomes by using (A) preformed FNB functionalized polymersomes to conjugate ANHP peptide. (B) ANHP peptide functionalized polymer to self-assemble into polymersomes.
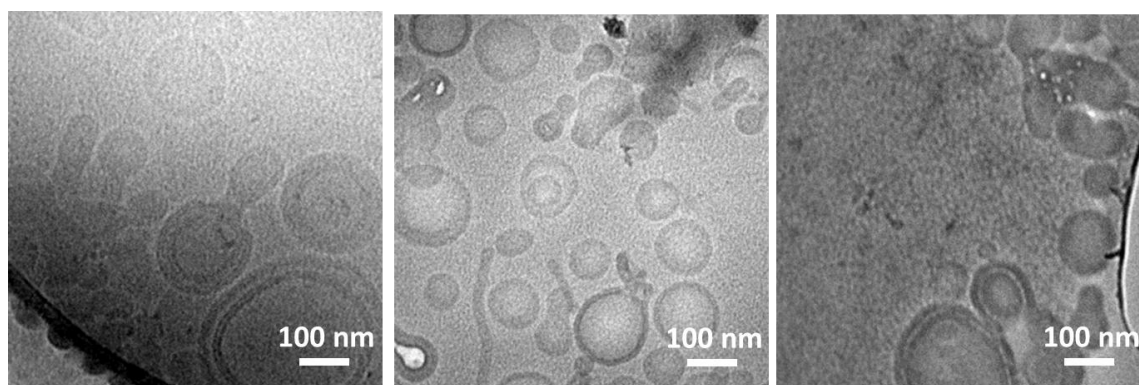
1% OB18-ANHP/OB2　　　**3% OB18-ANHP/OB2**　　　**5% OB18-ANHP/OB2**
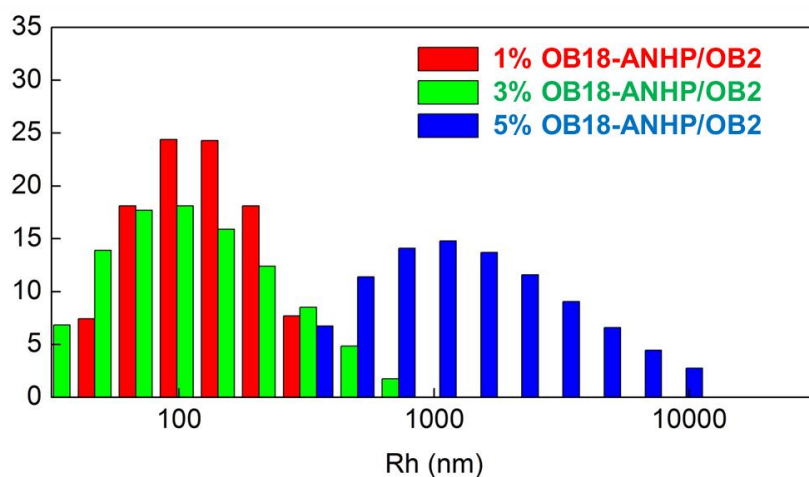
Figure 3.8 Cryo-TEM images and DLS data of 1%, 3% and 5% ANHP peptide conjugated polymersomes made from ANHP functionalized polymers.

For the second method, the ANHP peptide conjugation was performed with the FNB functionalized polymersomes. 5%, 10% and 30% FNB functionalized polymersomes were then used for the ANHP conjugation reaction as shown in **Scheme 3.13**. Cryo-TEM images and DLS data of these three samples were also taken and shown in **Figure 3.9**. A lot of polymersome vesicle structures together with some worm-like micelle structures were observed in ANHP peptide conjugated 5% and 10% FNB functionalized polymersomes, while in ANHP peptide conjugated 30% FNB functionalized polymersomes, the main structure were long worm-like micelles with a small amount of polymersomes. DLS data also showed the same morphology change for conjugation with increased FNB functionalization. In 5% and 10% FNB functionalized polymersomes, the average particles size was ~100 nm and didn't change much after ANHP peptide conjugation. However, in 30% FNB functionalized polymersomes, the particle size changed from average ~100 nm to a very wide size distribution from nm-sized to um-sized particles, suggested formation of aggregated structures. Based on these results, the maximum functionalization degree was determined to be ~10% for ANHP peptide conjugation to FNB functionalized polymersomes.

5% FNB-OB18/OB2 + ANHP   **10% FNB-OB18/OB2 + ANHP**   **30% FNB-OB18/OB2 + ANHP**
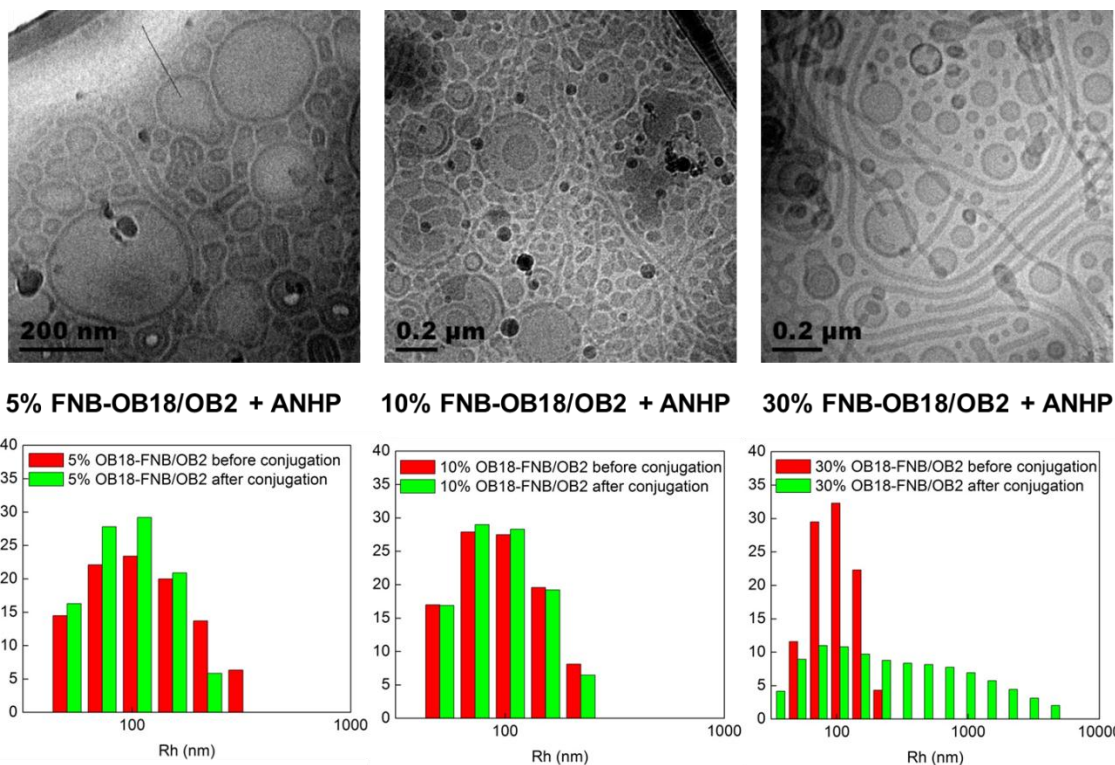
Figure 3.9 Cryo-TEM images and DLS data of ANHP peptide conjugation to preformed

5%, 10% and 30% FNB functionalized polymersomes.

In summary, both of these methods work well for conjugating small peptides such as ANHP on the polymersome surface, while the maximum functionalization degree we can reach by using peptide functionalized polymer is significantly lower (3%) compared to preformed FNB functionalized polymersomes (10%). For antibody conjugation, the second method by making antibody conjugated polymersomes from the preformed functionalized polymersomes is preferred. Preparing antibody polymersomes self-assembled from antibody-conjugated polymers has a few significant drawbacks. First of all, as predicted from the ANHP peptide conjugation results, the maximum functionalization degree for antibody conjugation should also be much lower by using the antibody-conjugated polymer self-assembling method. In addition, antibodies are normally very expensive and precious; we would hope to have a high antibody coupling efficiency to the polymersomes. When using the antibody-conjugated polymer to form polymersomes, about half of the antibody will be lost in the aqueous inner core of the polymersomes, resulted in low antibody conjugation efficiency on the polymersomes outer layer. Besides, considering most antibodies are much larger than small peptides and ligands, the polymersomes need to be pre-formed before the addition of antibody to prevent phase separation of antibody-modified and nonmodified block copolymers in the membrane.[80] Therefore, antibody conjugated polymersomes are all prepared from the preformed functionalized polymersomes.

3.4.3. Coupling Antibodies to Polymersomes: Evaluation and Comparison of the Different Methods

We have developed a series of different chemical modification methods for attachment of proteins and antibodies to nanoscale NIR-emissive polymersomes. Using

these chemical modification procedures, we first functionalized the hydrophilic PEO terminus of OB18 diblock copolymers with selected activated functional groups. From these functionalized diblock copolymers, we then constructed polymersomes that vary with respect to the extent of reactive hydrophilic surface functionality. These surface-modified vesicles will be subjected to coupling reactions with antibodies.

There are two main approaches to attach antibodies on the surface of NIR-emissive polymersomes: non-covalent linkage, such as the avidin-biotin interaction, or covalent binding. In the biotin-avidin method, avidin, with its four biotin binding sites, functions to crosslink the biotinylated antibody to biotinylated polymer at the polymersome surface. In this first approach (**Figure 3.10B**), the hydroxyl end groups of OB18 dilock copolymers were functionalized with FNB followed by conjugation to biocytin. Biotinylated OB18 diblock copolymers were mixed with nonfunctionalzed OB2 and self-assemble into NIR-emissive polymersomes. These polymersomes were then conjugated to streptavidin and finally, biotinylated antibody was added and conjugated to these avidin-conjugated, biotinylated NIR-emissive polymersomes.

The second approach involves the direct attachment of antibody to a preformed polymersome by covalent coupling. The polymersome will contain specifically functionalized end groups that are predisposed to react with the antibody. Five different functionalization chemistries have been used in this approach. The first functionalization method (**Figure 3.10** A) involves using FNB functionalization by creating an active fluoride end group on the polymersome surface which can then be conjugated to amino bearing antibody. The FNB terminated OB18 diblock copolymers were mixed with nonfunctionalized OB2 and self-assemble into polymersomes. These FNB functionalized

polymersomes were then conjugated to antibodies. The second functionalization method (**Figure 3.10C**) uses TDIC as a linking group between antiboby and amine functionalized polymersomes. OB18 diblock copolymers were first functionalized with methanesulfonyl chloride. These mesylated OB18 diblock copolymers then reacted with hexamethylenediamine to form amine terminated OB18 diblock copolymers. Amine functionalized OB18 diblock copolymers were mixed with nonfunctionalized OB2 diblock copolymers and self-assembled into polymersomes. TDIC was then added to this polymersome solution followed with antibody conjugation. The third functionalization method (**Figure 3.10D**) facilitates a hydrazone bond linkage motif by using the HyNic functionalized polymersomes to react with SFB modified antibody thus form a hydrazone bond. Finally, the maleimide (**Figure 3.10E**) and sulfo-SMCC methods (**Figure 3.10F**) involve the formation of a covalent thioether bond between the thiol groups on the antibody and maleimide groups on the polymersome surface. For the maleimide method, OB18 diblock copolymers were functionalized with N-(p-maleimidophenyl)isocyanate (PMPI), and the antibodies were functionalized by Traut's reagent. PMPI functionalized OB18 diblock copolymers were then mixed with unfunctionalized OB2 diblock copolymers and self-assembled into polymersomes, and conjugated to the thiol-actived antibody. For the sulfo-SMCC method, Sulfo-SMCC was added to the amine functionalized polymersome solution followed by thiol-activated antibody conjugation.
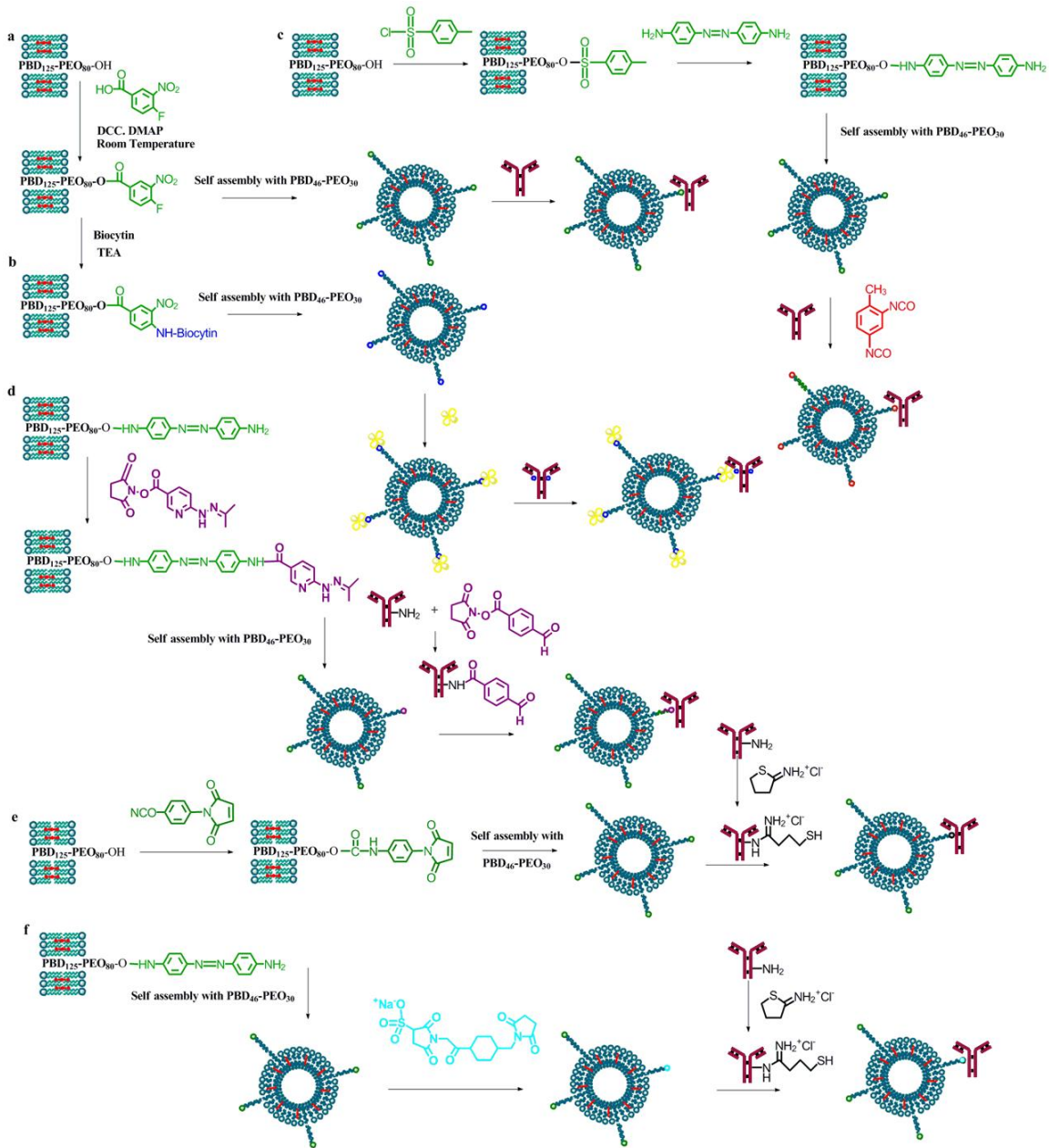
Figure 3.10 Reactions to attach an antibody to the polymersome surface.

(A). Polymersomes are self-assembled from a blend of OB2 and FNB functionalized OB18. Amino-group-containing antibodies are then attached by the conjugation to the distant terminus of polymersome surface.

(B). Attachment of biotinylated antibody to polymersomes by noncovalent biotin-avidin coupling. Avidin-conjugated, biotinylated OB18 diblock copolymers in self-assembled polymersomes are used to conjugate biotinlated antibody.

(C). Diblock copolymer OB18 is initially functionalized to feature an amino-group on the PEO terminus. Attachment of amino-group-containing antibody to amino-group-containing polymersomes is carried out by using a bifunctional reagent TDIC.

(D) In a particular case of amino-mediated coupling, SFB-containing antibody can be attached to HyNic functionalized polymersome with the formation of a hydrazone bond.

(E) Attachment of thio-activated antibody to the maleimide-activated polymersomes. The sulphydryl group can be introduced into the amino-group-containing antibody by Traut's reagent. The maleimide group is introduced onto the polymersome surface by the activation of diblock copolymer with N-(p-maleimidophenyl)isocyanate (PMPI). SH-containing antibody then interacts with maleimide-polymersome.

(F). Attachment of thio-activated antibody to the amine-activated polymersomes via Sulfo-SMCC linkage. The maleimide group is introduced onto the polymersome surface by the activation of the amine group with Sulfosuccinimidyl 4-[N-maleimidomethyl] cyclohexane-1-carboxylate (Sulfo-SMCC), followed by conjugation to SH-containing antibody.

The reason we chose these chemistries is based on the following requirements for a successful antibody to polymersome conjugation: (1) the polymersomal integrity have to be preserved during the binding procedure; (2) the reaction conditions need to be mild, in an aqueous solution at a neutral PH range (pH 6-8), to preserve the antibody specificity and affinity; (3) a sufficient quantity of antibody molecules should be firmly bound to the polymersome surface; (4) the binding procedure should be simple with a high yield of antibody binding to the polymersome. The advantages and disadvantages of these six coupling methods are discussed below.

The avidin-biotin noncovalent strategy has become a very commonly used method for active targeting. However, it involves multiple conjugation steps, and at a higher biotin functionalization degree, the polymersomes tend to aggregate,[81] so we can only use a very low functionalization degree. All of these factors lead to a low antibody conjugation efficiency and polymersome yield.

The FNB method is straightforward and only takes one-step. However, the reactivity of the FNB group towards antibody is relatively low and requires a very long reaction time (48 hours) at a relative high temperature (37-40 ℃) which might denature the antibody and make them unreactive. Besides, the ester bond which forms between the FNB functionalized polymersomes and the antibody tends to hydrolyze over time and decreases the stability of this bond.

The TDIC method is at a much milder condition and can be performed at room temperature for only 2 hours. However, as TDIC is sparingly soluble in water, organic solvent must be used; and TDIC polymerizes during the coupling reaction which decreases the polymersome recovery yield.

The hydrazone method requires multistep reaction and involves the use of HyNic and SFB reagent, both of which are pretty expensive. The main reason for us to choose this method is that the hydrazone bond formed between the functionalized polymersomes and antibody is fluorescent, and the conjugation degree could be directly quantified by measuring the absorbance of this hydrazone bond. However, in our NIR-emissive polymersomes, the absorbance of the hydrazone bond (λ_{max} = 354 nm) is overlapped with our porphyrin soret band (250- 450 nm) and this fluorescent hydrazone bond could not be used for quantification. We expect this method to work well for other fluophore incorporated polymersomes in which the hydrazone bond absorbance is distinct from the incorporated fluorophore absorbance spectrum.

The sulfo-SMCC and maleimide method both use a single-step reaction for polymer functionalization, and the reactivity of the functionalized maleimide group towards the thiol-actived antibody is very high. Also, the antibody is conjugated to polymersomes by thioether bond, which is very stable and will not hydrolyze over time. Therefore, both methods results in rather high antibody conjugation efficiencies. However, for the sulfo-SMCC method, there are two HPLC separation steps for first removing the excess Sulfo-SMCC in solution and then removing the unbound antibody. Both HPLC purification loses some polymersomes and causes a lower polymersome recovery yield. This is consistent with the experimental results showing 45-50% polymersome recovery yield with the Sulfo-SMCC method.

Table 3.1 compares the number of streptavidin and rat IgG antibody bound to the polymersomes for the non-covalent biotin-avidin method, and the five covalent coupling methods. Functionalized polymers were incorporated into polymersomes at 5 mol%

except for biotin functionalized polymer which was incorporated at 1 mol%. Using the biotin-avidin method, there are low levels of antibody attached to the polymersome surface with low efficiency. For the FNB, TDIC, Hydrazone, and Sulfo-SMCC methods, a moderate amount of antibody was bound to the polymersome surface. The maleimide method gave the highest amount of antibody bound to the polymersome surface. The polymersome recovery yields are also calculated by comparing the mass of the polymer recovered after antibody conjugation to the mass used to prepare the polymersomes. The recovery yields of the FNB and maleimide methods are ~30% higher than the non-covalent biotin-avidin method and the hydrozone, TDIC, and sulfo-SMCC method. Considering both the antibody conjugation efficiency and the polymersome recovery yield, we conclude that the maleimide method is the best out of these six methods for antibody conjugation, which is well rationalized by the described advantages and disadvantages of these methods.

Table 3.1 Comparison of polymersomes preparation and conjugation procedures.

Method	Polymersomes composition	# of streptavidin per 100nm polymersome	# of rat IgG per 100nm polymersome	Polymersome Recovery Yield
Biotin	1% OB18-Biotin/ 99% OB2	62 ± 9	11 ± 4	41% - 46%
FNB	5% OB18-FNB/ 95% OB2	92 ± 13	37 ± 6	72% - 81%
TDIC	5% OB18-NH2/ 95% OB2	78 ± 11	23 ± 5	45% - 52%
Hydrazone	5% OB18-SANH/ 95% OB2	114 ± 15	38 ± 7	70% - 76%
Sulfo-SMCC	5% OB18-NH2/ 95% OB2	142 ± 22	50 ± 12	42% - 50%
Maleimide	5% OB18-PMPI/ 95% OB2	162 ± 31	64 ± 11	75% - 84%

The antibody was coupled to 100 nm polymersomes at an antibody/functionalized polymer molar ratio of 1:10 for streptavidin or 1:40 for rat-IgG, and a polymersome concentration of 20 nM. The conversion from antibody concentration to the approximate number of antibodies per polymersome was based on the following assumptions: the area per polar head group for PEO-PBD diblock copolymer is 1 nm^2 and that there are approximately 9.6×10^{12} polymersomes per μmol polymer[73] and 4×10^{12} antibodies per μg protein.

3.4.4. Factors Affecting Antibody Coupling Efficiency

Understanding and controlling the density of reactive antibodies on the polymersome surface is of great importance for applications such as targeted drug delivery. In order to investigate the effects of functional group concentration on polymersome surface modification, we produced different batches of polymersomes consisting of various molar percentages of the reactive functionalized OB18 diblock polymer and nonfunctionalized OB2 copolymers. We have investigated, for the FNB and maleimide coupling procedure, two main factors affecting coupling of antibody to functionalized diblock copolymer: (1) the concentration of FNB or Maleimide functionalized OB18 polymer incorporated into the polymersomes (**Figure 3.11**) , (2) the antibody concentration (**Figure 3.12**). For the FNB method, a 20-fold increase in the amount of incorporated FNB functionalized OB18 diblock copolymer, from 0.05 to 1.0 mol% resulted in a 30-fold increase in the amount of bound streptavidin (**Figure 3.11** A); a 3-fold increase in the amount of incorporated FNB functionalized ob18 diblock polymer, from 0.1 to 0.3 mol% resulted in a 2-fold increase in the amount of bound rat-IgG (**Figure 3.11** B). The conjugation of antibody reaches a plateau at 1% FNB functionalization degree for streptavidin conjugation and at 0.3% FNB functionalization degree for rat-IgG conjugation. The maximum number of streptavidin that can be conjugated to polymersomes by FNB coupling method is ~230 per 100 nm polymersome while the maximum number of rat-IgG that can be conjugated to polymersomes is ~47 per 100 nm polymersome. For maleimide method, a 6-fold increase in the amount of incorporated maleimide functionalized OB18 diblock copolymer, from 0.5 to 3.0 mol% resulted in a 4-fold increase in the amount of bound streptavidin (**Figure 3.11A**); a 5-fold

increase in the amount of incorporated maleimide functionalized ob18 diblock polymer, from 0.2 to 1 mol% resulted in a 3-fold increase in the amount of bound rat-IgG (**Figure 3.11B**). The conjugation of antibody reaches a plateau at 3% maleimide functionalization degree for streptavidin conjugation and at 1% maleimide functionalization degree for rat-IgG conjugation. The maximum number of streptavidin that can be conjugated to polymersomes by maleimide coupling method is ~447 per 100 nm polymersome while the maximum number of rat-IgG that can be conjugated to polymersomes is ~158 per 100 nm polymersome. Similarly, as the antibody concentration increased, the total amount of bound antibody also increased substantially, while the antibody conjugation efficiency decreased with the increasing antibody concentration (**Figure 3.12**).
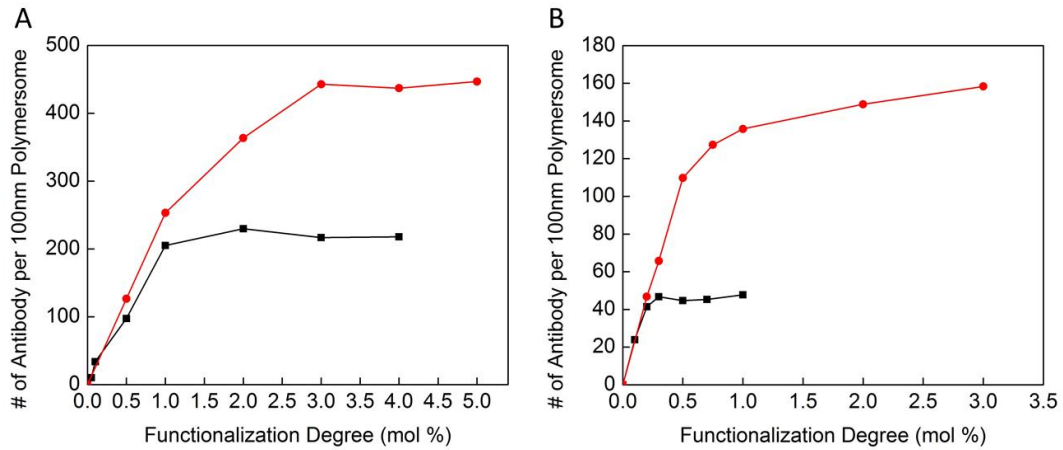
Figure 3.11 Effect of funtionalized polymer content on coupling of protein streptavidin (A) and rat IgG (B) to polymersomes by FNB method (black line) and maleimide method (red line).

Polymersomes were 100 nm in diameter, composed of streptavidin or rat-IgG. (A) Polymersomes containing 0 to 5 mol% functionalized-polymer were incubated with streptavidin at an antibody to functionalized polymer molar ratio of 1:2; (B) Polymersomes containing 0 to 1 mol% functionalized-polymer were incubated with SH-rat-IgG at an antibody to functionalized polymer molar ratio of 1:2.
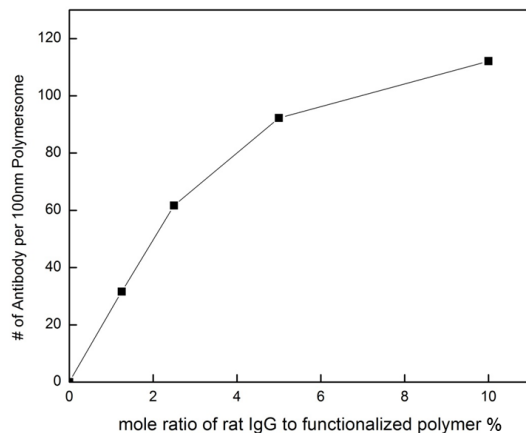
Mole ratio of rat IgG antibody to functionalized polymer	AB conjugation efficiency
1:10	35.7 ± 3.2%
1:20	58.7 ± 2.4%
1:40	78.6 ± 6.3%
1:80	80.6 ± 6.8%

Figure 3.12 Effect of antibody concentration on coupling of antibody (rat-IgG) to polymersomes by maleimide method.

5 mol% maleimide-OB18/OB2 polymersomes were incubated with various amounts of rat-IgG at a constant polymersome concentration of 20 nM.

The maximum functionalization degree and number of antibody per 100 nm polymersomes is calculated, assuming the polymersomes surface is 100% cover with the antibodies are spherical particles. Considering the diameter of streptavidin is ~ 5nm[82] and the diameter of IgG is ~10nm,[83] the projected area of each streptavidin on polymersomes surface is 19.6 nm^2 and for rat-IgG is 78.5 nm^2. The surface area of 100 nm polymersomes is 31346 nm^2, therefore the maximum number of streptavidin per 100 nm polymersome is 1600 and the corresponding maximum functionalization degree is 5.3%; while the maximum number of rat-IgG per 100 nm polymersome is 400 with 1.3% maximum functionalization degree. Taken into account the steric hindrance effect on the polymersomes surface, the experimental numbers of antibody per polymersome will be much smaller than these theoretical calculated numbers. Our measured values correspond well with the calculated numbers. The rat-IgG antibody, a much larger particle than streptavidin, has a low conjugation degree on the polymersome surface and the maximum functionalization degree is much smaller. Also, by comparing the numbers from FNB coupling method and maleimide coupling method, we could conclude that the maleimide method has a much stronger reactivity towards antibody conjugation than the FNB coupling method based on the increasing number of antibodies on the polymersome surface at the same functionalization degree.

3.4.5. Confocal Microcope Imaging of Antibody Conjugated Polymersomes

Meso-scale biotin functionalized polymersomes were prepared and conjugated to FITC-streptavidin. The morphology of the formed vesicles is shown in **Figure 3.13**. The polymer vesicle structures were very robust and didn't change after the antibody conjugation. The fluorescence from the FITC green chanel indicated uniform binding of

151

FITC-streptavidin on the polymersomes surface. However, streptavidin conjugated polymersomes formed by using this noncovalent method via streptavidin-biotin interaction were observed to be highly aggregated. This aggregation is due to the cross-linking of streptavidin to biotinylated polymersomes.

Similarly, meso-sized maleimide functionalized polymersomes were prepared and conjugated to SH-functionalized FITC-rat IgG antibody. The morphology of the formed antibody conjugated vesicles is shown in **Figure 3.14**. While the noncovalent biotin-avidin conjugation method caused polymersome aggregation, the maleimide coupling procedures had a minimal aggregation effect and produced well dispersed, non-aggregated antibody conjugated polymersome suspension.
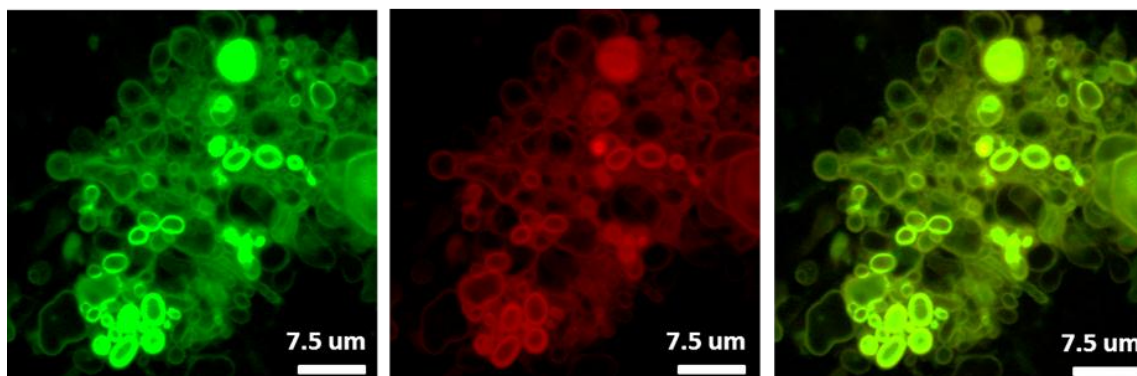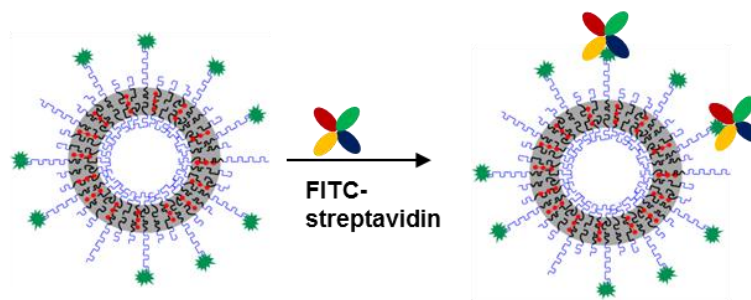
Figure 3.13 Functionalized polymersomes labeled with FITC-streptavidin by biotin functionalization show uniform labeling. Green chanel: FITC emission, Red chanel: porphyrin emission, Orange chanel: overlapped.
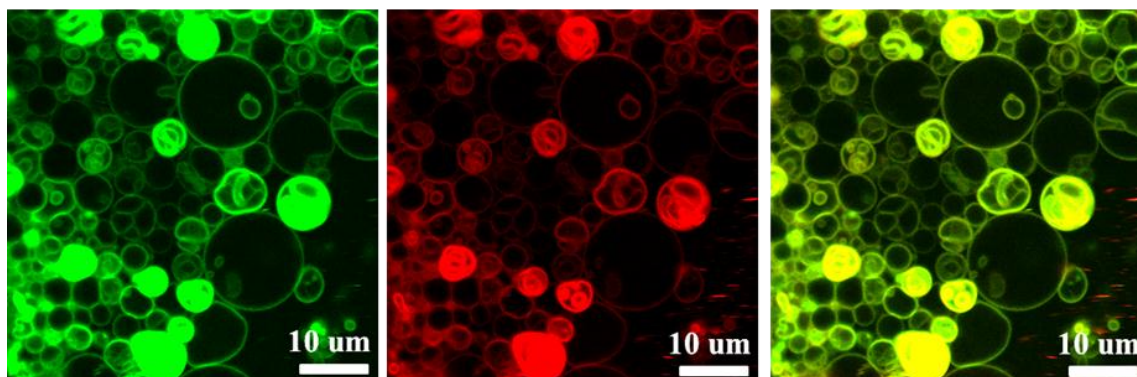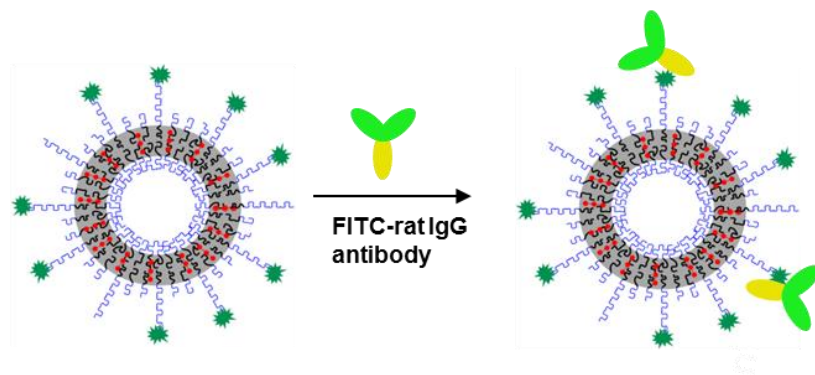
Figure 3.14 Functionalized polymersomes labeled with FITC-rat IgG by maleimide functionalization show uniform labeling. Green chanel: FITC emission, Red chanel: porphyrin emission, Orange chanel: overlapped.

3.4.6. Cryo-TEM of nm-sized AB Conjugated Polymersomes

After the conjugation of 10 nm gold-labeled goat-anti-mouse IgG antibody to nano-sized polymersomes, the structure of gold- labeled IgG antibody conjugated polymersomes was examined by multiple TEM techinques (**Figure 3.15**). The TEM images revealed that nano-scale antibody conjugated polymersomes were generally round and of vesicle-like shape, indicating that polymersomes were tough and the conjugation with the antibody did not rupture the polymersome structure. Conjugation of the antibody with the polymersome was also confirmed by gold labeled antibody visualized by TEM. Antibodies have very low scattering contrast and could not be visualized by TEM; by labeling them with electron-dense gold nanoparticles, the observation of the gold nanoparticles under TEM will indicate the presence of antibody. In TEM experiments (**Figure 3.15A and B**), polymersome samples were air dried, with aqueous solution trapped in the hydrophilic core, and appeared as black spheres without showing the subtle bilayer structure, with gold-labeled antibodies as the darker dots surround them. To confirm the black sphere structures we saw in classic TEM are truly polymersomes other than possible exist water droplets, negative staining TEM was employed by embedding the polymersomes in an electron dense material (PTA) providing high contrast, and polymersomes were seen as white spheres with a black edge which is the bilayer membrane of the vesicles. Furthermore, to allow the indicative evaluation of the polymersomal internal structure without discriminating on the fine details, Cryo-TEM was performed. In Cryo-TEM experiments, polymersome solution was frozen into a thin water film, thus the vesicle structures were well preserved and the bilayer structure was clearly revealed.
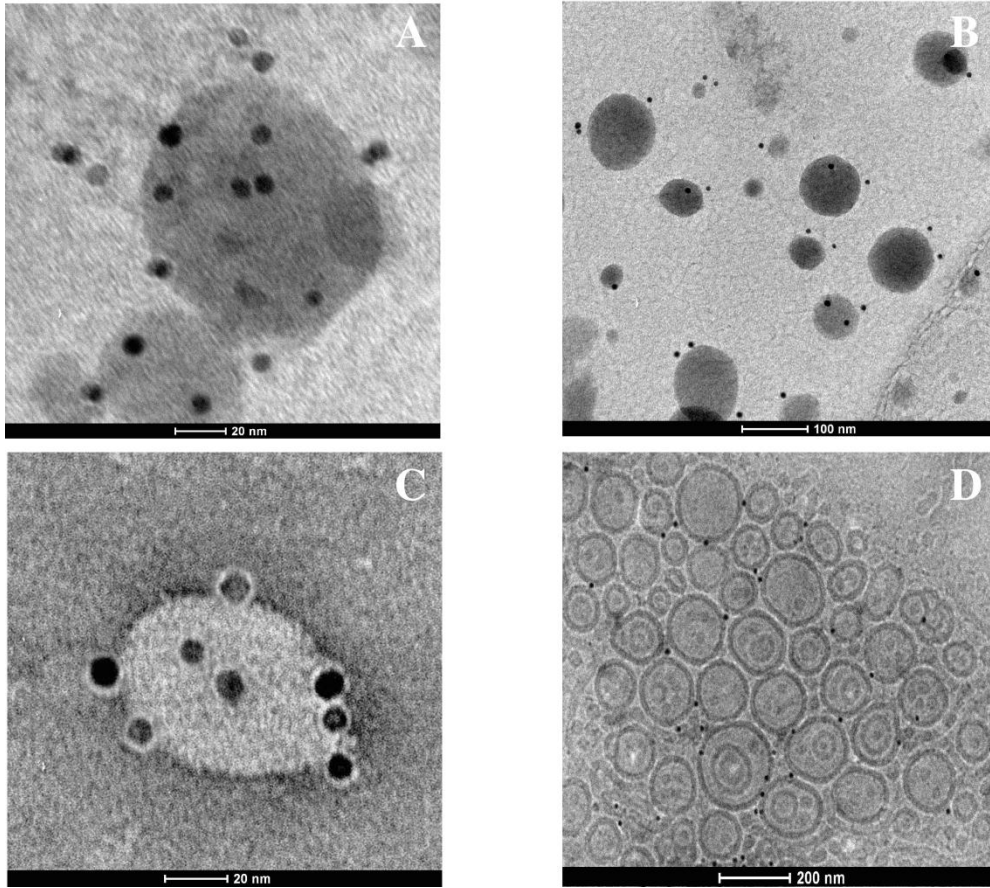
Figure 3.15 TEM images of Gold (10nm)-antibody conjugated polymersomes (PO-Gold): (A) and (B) PO-Gold in PBS buffer. (C) TEM images of PO-Gold negatively stained with PTA solution. (D) Cryo-TEM images of PO-Gold in PBS buffer.

3.4.7. ELISA of Antibody Conjugated Polymersomes

Nanoscale polymersomes (100nm diameter) prepared using functionalized OB18 blended with OB2 in 5:95 and polymer with porphyrin trimer (λ_{max} = 798 nm) in 40:1 were conjugated with rat-IgG and goat-anti-mouse IgG antibody. First, the binding of rat-IgG antibody conjugated polymersomes towards goat-anti-rat IgG antibody was studied by ELISA experiments (**Figure 3.16**). The rat-IgG antibody conjugated polymersomes showed positive titers against goat-anti-rat IgG antibody, with enhanced absorbance intensities by increasing rat-IgG conjugated polymersomes concentration. The very obvious and quick color change even in dilute rat-IgG polymersome samples (0.37 fmol) proved the successful antibody conjugation on polymersomes. All of the control samples showed negative results which indicated that the non-conjugated polymersomes have minimal non-specific binding to the goat-anti-rat IgG antibody.

Furthermore, the specificity and cross-reactivities of goat-anti-mouse IgG antibody and rat-IgG antibody conjugated polymersomes were also tested by ELISA experiments (**Figure 3.17**). Different IgG antibodies (mouse IgG antibody and rabbit IgG antibody) were used for ELISA plates coating. ELISA experiments (**Figure 3.17**) showed that the goat-anti-mouse IgG antibody conjugated polymersomes were only positive with plates coated with mouse IgG antibody, and were negative towards rabbit IgG. As expected, rat-IgG antibody conjugated polymersomes were also negative both to mouse-IgG AND rabbit-IgG. This result indicates species-specific reactions. There are no non-specific or cross-reactivities of antibody conjugated polymersomes. In summary, the ELISA results show that the conjugation of antibody to polymersomes was successful, with specific and selective binding towards 96 well plates.
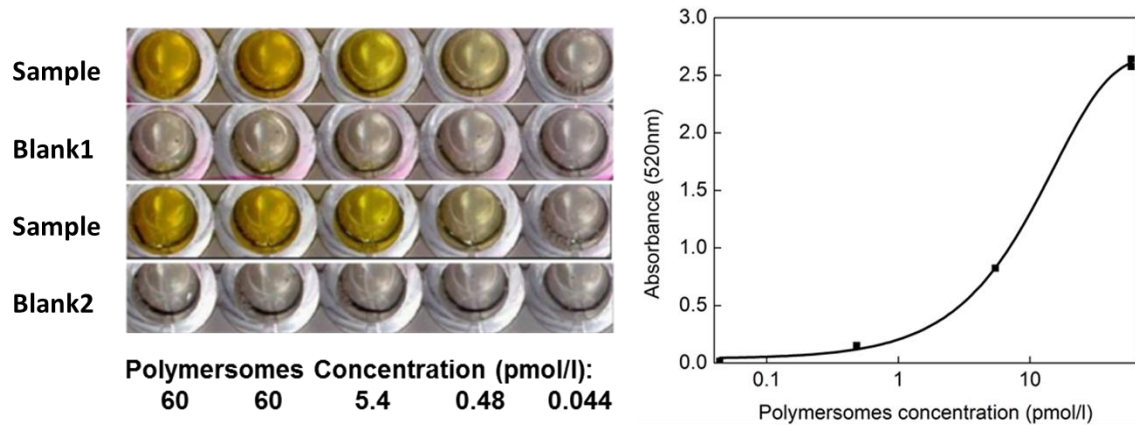
Figure 3.16 ELISA plate images (left) and polymersomes standard curve (right).

Sample: Rat IgG antibody conjugated 100 nm polymersomes.

Blank1: functionalized, nonconjugated 100 nm polymersomes.

Blank2: nonfunctionalized nonconjugated 100 nm polymersomes.
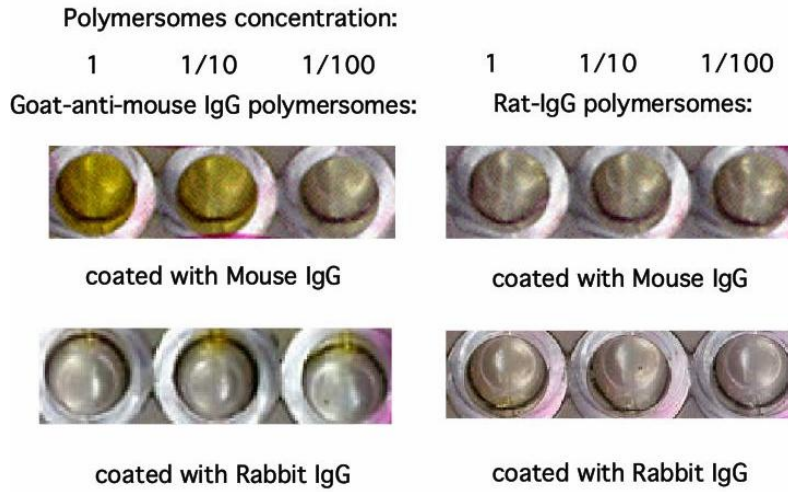
Figure 3.17 ELISA plate images for specificity tests.

Polymersomes are dilute in 10 times series in each well (from left to right).

3.4.8. Licor-Odyssey Imaging of Antibody Conjugated Polymersomes

The binding sensitivity of streptavidin conjugated polymersomes to biotinylated 96 well plates was measured by Licor-Odyssey imaging system as shown in **Figure 3.18**. Different amounts (0.9-120 fmol) of PZn_3 incorporated streptavidin conjugated polymersomes ($\lambda_{em\ max}$=810 nm), and PZn_2 incorporated streptavidin conjugated polymersomes ($\lambda_{em\ max}$=723 nm) were added to the biotinlayted 96 well plate, with DyLight 680 streptavidin and DyLight 800 streptavidin added at the same concentration as the polymersomes for comparison. Serial dilutions of the DyLight or polymersome based NIR emissive probe concentrations in lanes A-D demonstrate that polymersome enable analyte detection 2-3 orders of magnitude more sensitive than that provided by commercially available organic fluorophores.

Polymersome particles are much more sensitive than the DyLight streptavidin particles because each 100 nm polymersome made from 40:1 polymer:porphyrin contains ~ 1,570 copies of porphyrin fluorophores in the bilayer membrane (there are 9.6 $\times 10^{12}$ polymersomes per umol PEO-*b*-PBD polymer, [73] so each polymersomes are comprised of 62,800 copies of polymer); while each DyLight streptavidin contains only a few copies of DyLight fluorophores per DyLight streptavidin particle. Therefore, each polymersome particle is thousands of times brighter than each DyLight streptavidin particle, and will greatly increases the detection sensitivity.

From the Licor-Odyssey imaging experiments shown below in **Figure 3.18**, the minimal detection concentration (average from 3 measurements) is calculated using the equation:

Minimal detection concentration = 3*SD$_{blank}$/slope

The SD$_{blank}$ is the standard deviation of blank wells. Slope is from the linear regression fit of a series dilution curve. The minimal detection concentration calculated for PZn$_3$ incorporated streptavidin conjugated polymersomes ($\lambda_{em\ max}$=810 nm) is 0.012 fmol, DyLight 800 streptavidin is 2.37 fmol; for PZn$_2$ incorporated streptavidin conjugated polymersomes ($\lambda_{em\ max}$=723 nm) is 0.69 fmol, DyLight 680 streptavidin is 46.07 fmol. Comparing these numbers, the PZn$_3$ incorporated streptavidin conjugated polymersomes ($\lambda_{em\ max}$= 810 nm) is 197.5 times more sensitive than DyLight 800 streptavidin, and PZn$_2$ incorporated streptavidin conjugated polymersomes ($\lambda_{em\ max}$= 723 nm) is 66.7 times more sensitive than DyLight 680 streptavidin.
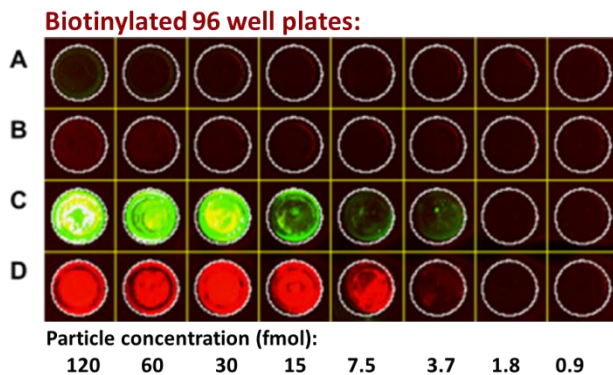
Figure 3.18 Licor Odyssey Imaging experimental results.

Streptavidin, DyLight 800; B. Streptavidin, DyLight 680 conjugated; C. Streptavidin-810 nm emissive polymersomes conjugate; D. Streptavidin-723 nm emissive polymersomes conjugate. All samples are incubated in biotinylated 96 well plates for 1 hour at RT with SEA blocking buffer and then rinsed with PBS three times before imaging using Licor Odyssey Imaging System. Red chanel: 700 nm emission, green chanel: 800 nm emission.

3.4.9. Anti-ErbB2 IPs for Targeting HER2 Cells

We have generated anti-ErbB2 IPs consisting of functionalized polymersomes linked to anti-ErbB2 monoclonal antibody, to provide targeted delivery to HER2 overexpression cells. Anti-ErbB2 IPs bound efficiently to and internalized in HER2 overexpression cells *in vitro* as determined by confocal fluorescence microscopy and quantitative analysis of fluorescent probe delivery.

3.4.9.1. In Vitro Optical Imaging of Labeled Human Breast Cancer Tumor Cells

Anti-ErbB2 antibodys are readily internalized in HER2-overexpression tumor cells via receptor-mediated endocytosis.[84] To assess whether anti-ErbB2 IPs also internalize within target cells in vitro, a series of studies using confocal fluorescence microscopy were performed. As seen in **Figure 3.19**, anti-ErbB2 IPs labeled with 810 nm emissive porphyrin, were incubated with HCC1569, BT474, SKBR3 fixed breast cancer cells, which overexpress HER2 (10^6 molecules/cell), and with MCF-7 fixed breast cancer cells which have very low or basal levels of HER2 expression (10^4 receptors/cell).[85] The anti-ErbB2 IPs significantly bind to HCC1569, BT474, SKBR3 cells as evident from images **Figure 3.19A-C**, demonstrated intense fluorescence at the cell surface by 30 min, indicating rapid internalization. In addition, the anti-ErbB2 IPs were localized intracellular and distributed throughout the cytoplasm as clearly evident in **Figure 3.20**. MCF7 cells similarly incubated with anti-ErbB2 IPs showed minimal uptake of anti-ErbB2 IPs (**Figure 3.19D**), indicating very weak non-specific binding of anti-ErbB2 IPs with cells with low HER2 expression.

Furthermore, the specificity of anti-ErbB2 IP uptake was confirmed by incubation of SKBR3 cells with irrelevant rat-IgG conjugated polymersomes and nonconjugated

polymersomes in both live and fixed SKBR3 and MCF7 cells lines (**Figure 3.21**). The confocal microscope results demonstrated strong specific binding of anti-ErbB2 IPs to HER2 overexpressed SKBR3 cells, and no detectable interaction of irrelevant rat-IgG conjugated polymersomes and nonconjugated polymersomes in SKBR3 cells. As expected, live cells also exhibit similar anti-ErbB2 IP binding properties as fixed cells.

Taken together, these studies demonstrated the ability of anti-ErbB2 IPs to selectively internalize in target cells, thus the potential for intracellular delivery. This targeting strategy can provide a critical advantage to the therapeutic action of many anticancer agents.
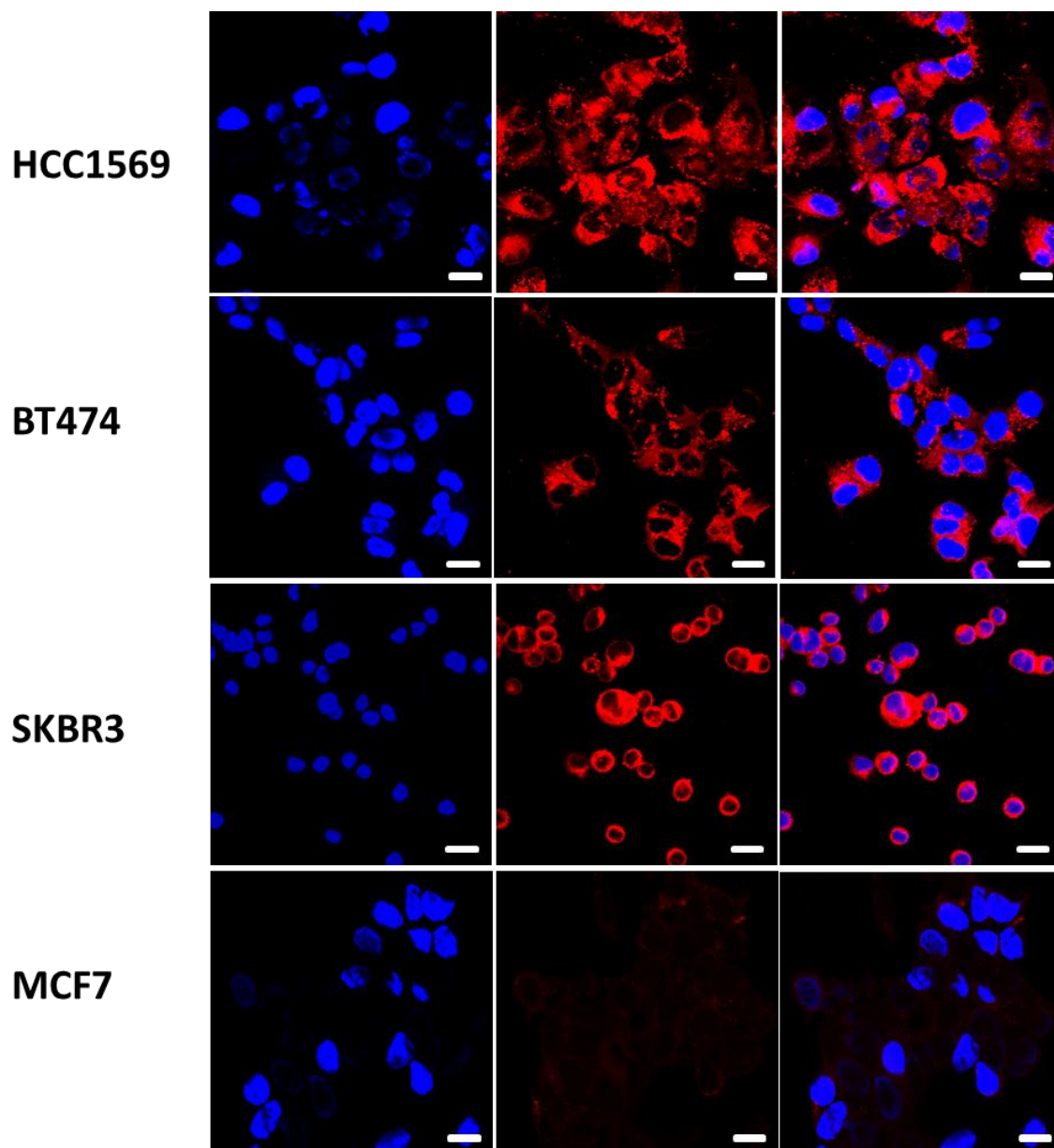
Figure 3.19 Confocal microscopy of fixed cells coincubated at RT 30mins with anti-ErbB2 emissive IPs (5 mol % Maleimide functionalization, ErbB2 antibody conjugated, 723nm emissive) and Hoechst 33258.

Left column, Hoechst 33258 (blue); central column, emissive polymersomes (red); right column, overlapped images. (A). HCC1569 cells. (B). BT474 cells. (C). SKBR3 cells. (D). MCF7 cells. Scale bar: 25 μm.
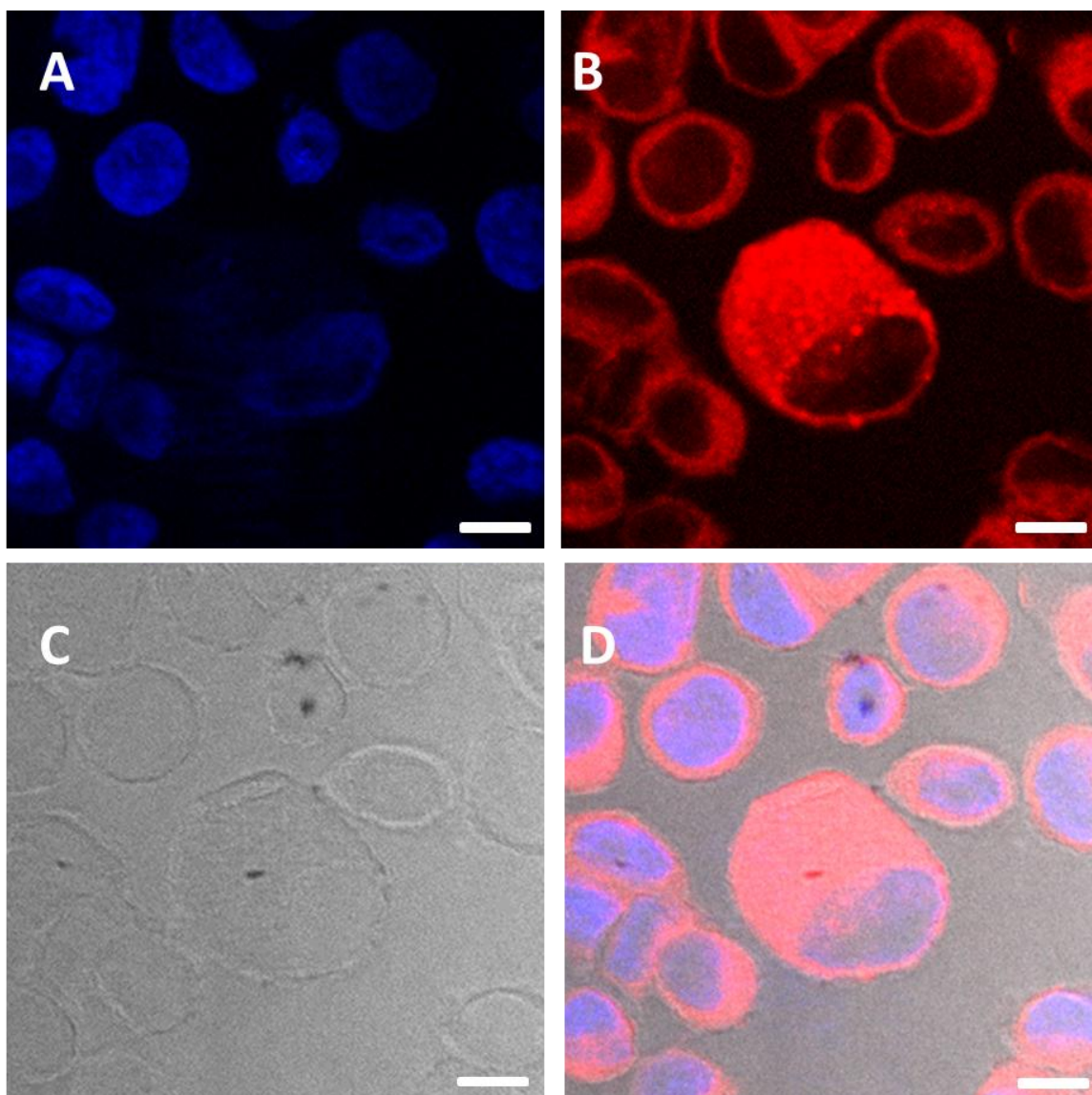
Figure 3.20 Detailed confocal microscope images of fixed SKBR3 cells coincubated at RT 30mins with anti-ErbB2 emissive IPs (5 mol % Maleimide functionalization, ErbB2 antibody conjugated, 723nm emissive) and Hoechst 33258.

A: Hoechst 33258 (blue); (B) emissive polymersomes (red); (C) differential interference contrast (DIC) image of cells; (D) overlapped images. Scale bar: 10 μm.
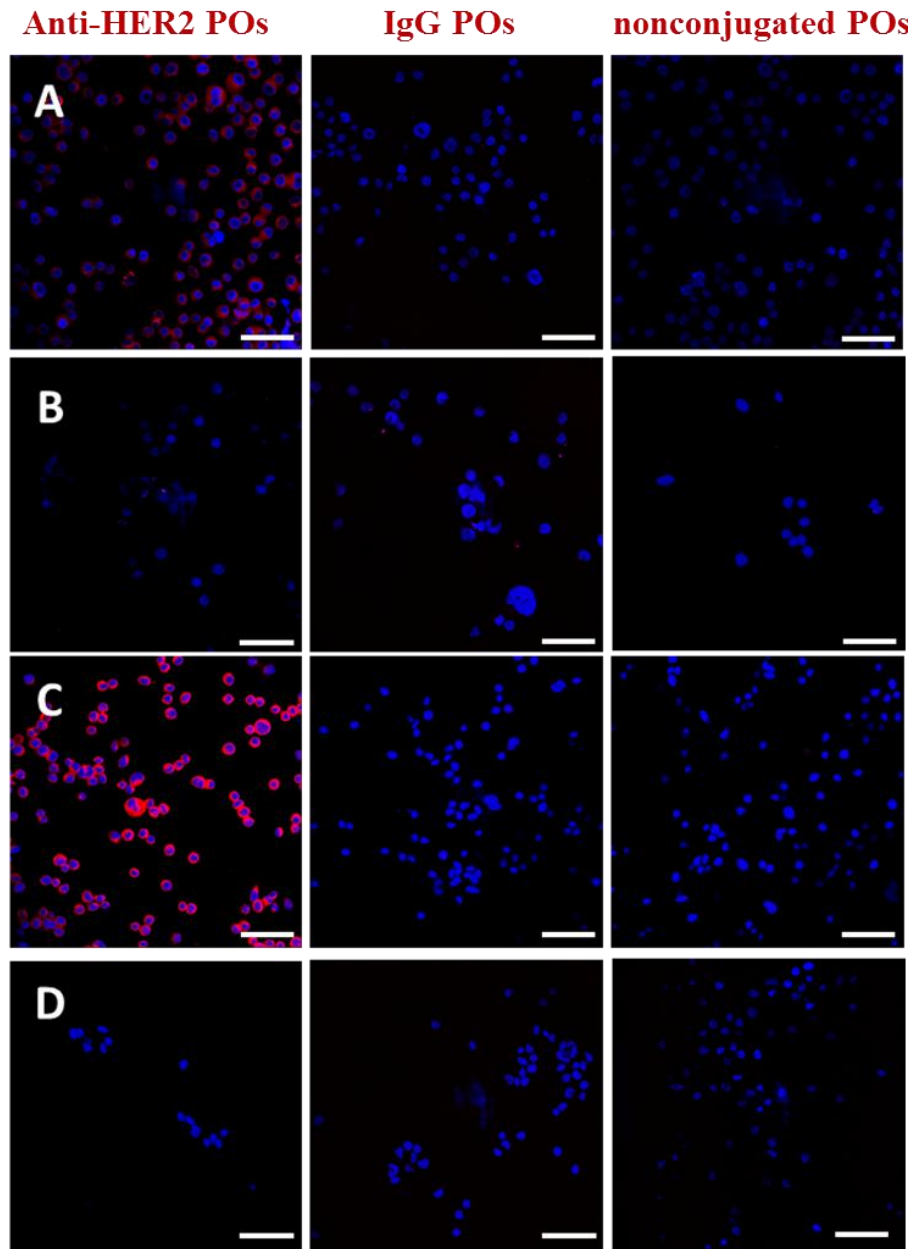
Figure 3.21 Confocal microscopy of cells coincubated at RT 30mins (fixed cells) or 4 hours (live cells) with different polymersomes (red) and Hoechst 33258 (blue).

Left column: anti- ErbB2 IPs; central column: irrelevant IgG conjugated polymersomes; right column: nonconjugated polymersomes. (A). live SKBR3+ cells. (B). live MCF7- cells. (C). fixed SKBR3+ cells. (D). fixed MCF7- cells. Scale bar: 75 um.

3.4.9.2. Concentration Dependence Anti-ErbB2 IPs Uptake

In order to maximize the intracellular uptake of polymersomes necessary for optimal cellular labeling, the maximum uptake concentration on HER2 cell uptake were examined. Flow cytometry was used to measure the intensity of cellular-associated PZn_3-based fluorescence following cell incubation and washing. The uptake of both anti-ErbB2 IPs and nonconjugated polymersomes controls at various polymersome concentrations was evaluated in order to distinguish the impact of anti-ErbB2 conjugation on intracellular delivery. The histograms presented in **Figure 3.22** demonstrate clear dose-dependent uptake of anti-ErbB2 IPs in HER2 overexpressing BT474 cells, while the nonconjugated control polymersomes had minimal nonspecific binding in BT474 cells. The MCF7 cells that lack ErbB2 overexpression showed minimal uptake of both polymersomes with or without anti-ErbB2 antibody conjugation.

The concentration dependence of anti-ErbB2 IPs uptake is also evident for both anti-ErbB2 antibody conjugated and nonconjugated (control) polymersomes. The uptake of anti-ErbB2 NIR emissive polymersomes becomes saturated after incubation with a concentration of 0.88 nM polymersomes. This saturation is clearly observed in **Figure 4B** where the geometric mean fluorescence intensities of the presented histograms are plotted against the treatment concentration.
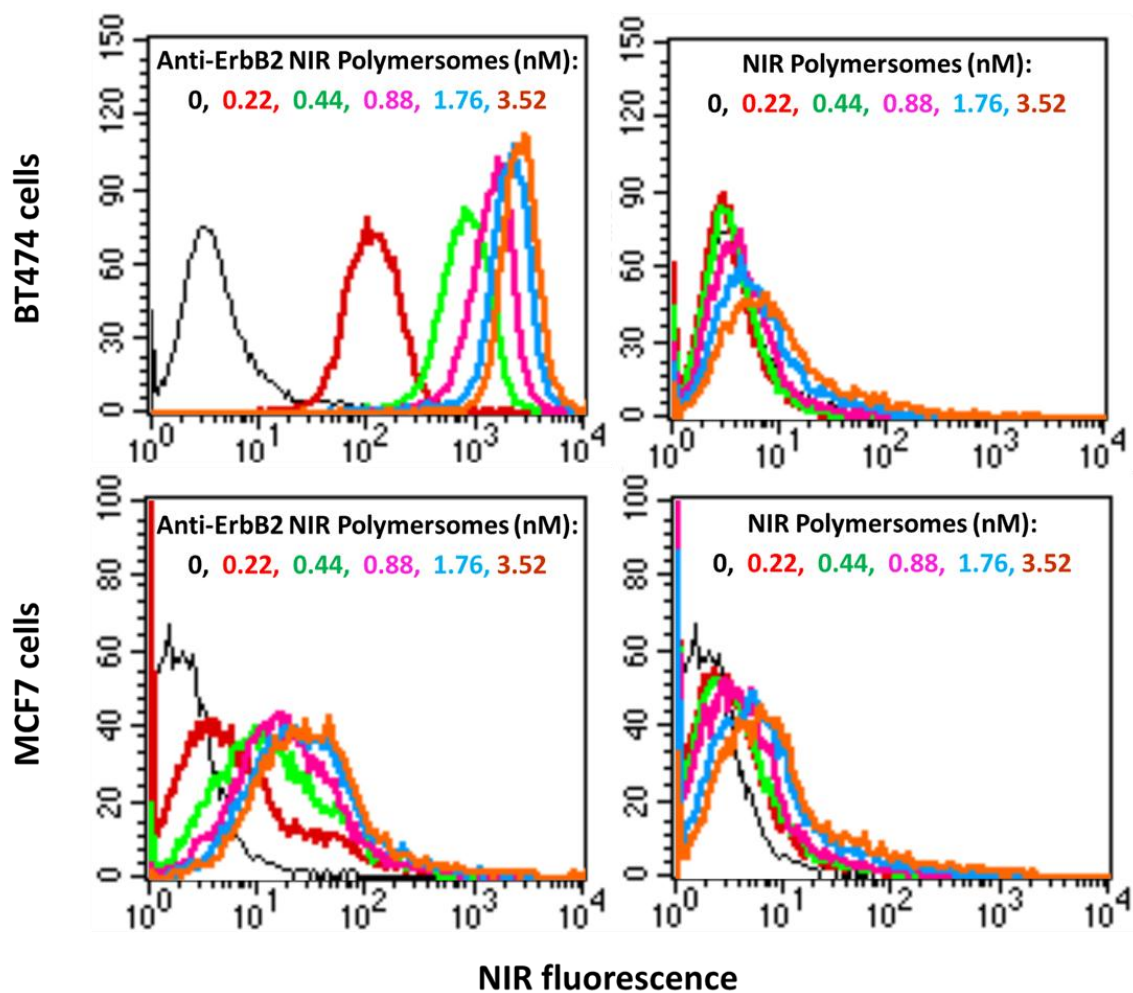
Figure 3.22 Representative histograms for BT474 and MCF7 cells treated at room temperature 1 hour with either control or anti-ErbB2 NIR emissive polymersomes at the indicated polymer dose.
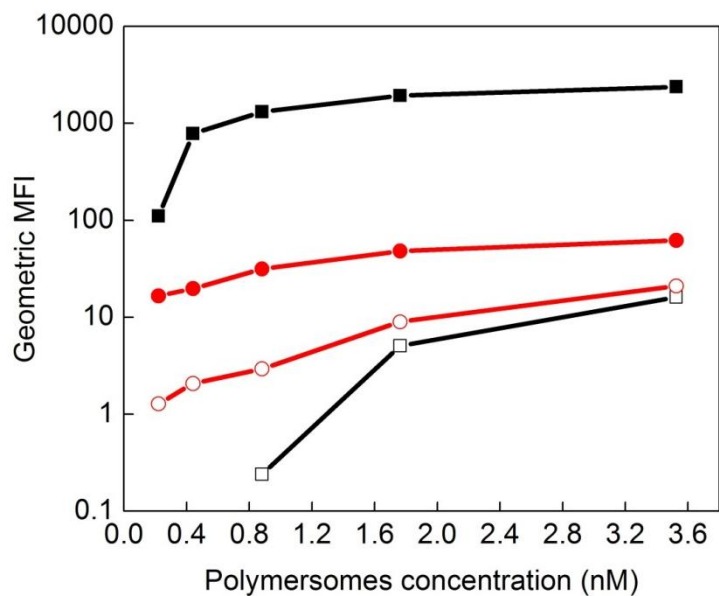
Figure 3.23 Geometric mean fluorescent intensity from flow cytometry analysis with different polymersome concentration for BT474 cells (black line) and MCF7 cells (red line) treated with anti-ErbB2-conjugated NIR emissive polymersomes (solid dots) or control NIR emissive polymersomes (hollow dots).

Furthermore, for quantitative studies of anti-ErbB2 IP uptake, internalization and intracellular delivery, Licor-Odyssey imaging system was used to assay the number of anti-ErbB2 IPs binding to HER2 cells. HER2 cells that were stained with NIR emissive polymersomes at different cell concentrations were plated in 96 well plates and the cell emission from each well were integrated. NIR imaging allows quantitative and repetitive detection of fluorophore-labeled cells without disturbing cellular function. The representative images of plated cells are presented in **Figure 3.24 and Figure 3.26**. Similar to the flow cytometry results, we observed a clear dose-dependent uptake of anti-ErbB2 IPs in HER2 overexpression BT474 cells while the nonconjugated control polymersomes had minimal staining in BT474 cells, while MCF7 cells that lack ErbB2 overexpression showed minimal uptake of both polymersomes with or without anti-ErbB2 antibody conjugation. For each single Licor-Odyssey imaging measurement, a standard calibration curve created from the number of NIR fluorophores versus total photon counts per well (**Figure 3.25A** and **Figure 3.27A**) was used for the estimation of the amount of fluorophore associated with each cell population and ultimately the number of polymersomes per cell. The number of polymersomes per cell as a function of polymersome treatment concentration is presented in **Figure 3.25B** and **Figure 3.27B**. A single BT474 cell can be effectively labeled with 86,000 ± 2,500 anti-ErbB2 IPs, and 800 ± 50 control polymersomes. However, for MCF7 cells, they can only be labeled with 1,700 ± 130 anti-ErbB2 IPs per cell, or 830 ± 200 control polymersomes per cell. These results were represented in **Figure 3.28** for easy comparison. The binding curve of anti-ErbB2 IPs to BT474 cells fit very well to the simple Langmuir-type dose response equation of the equilibrium binding assuming all binding sites equal and independent

(**Figure 3.25C**). The maximum number of anti-ErbB2 IPs per cell is calculated to be 88,751 $\pm$ 5151, and the dissociation constant is 0.84 $\pm$ 0.37 min^{-1}.

The maximum polymersomes uptake percentage which equals the number of polymersome uptake up divided by the polymersomes initially added for staining is also calculated and the results are represented in **Figure 3.29**. The maximum IP uptake is 37.9 $\pm$ 1.8% for BT474 cells, and 0.60 $\pm$ 0.18% for MCF7 cells. The maximum cellular uptake for the control polymersomes is 0.19 $\pm$ 0.03% for BT474 cells, and 0.19 $\pm$ 0.05% for MCF7 cells.
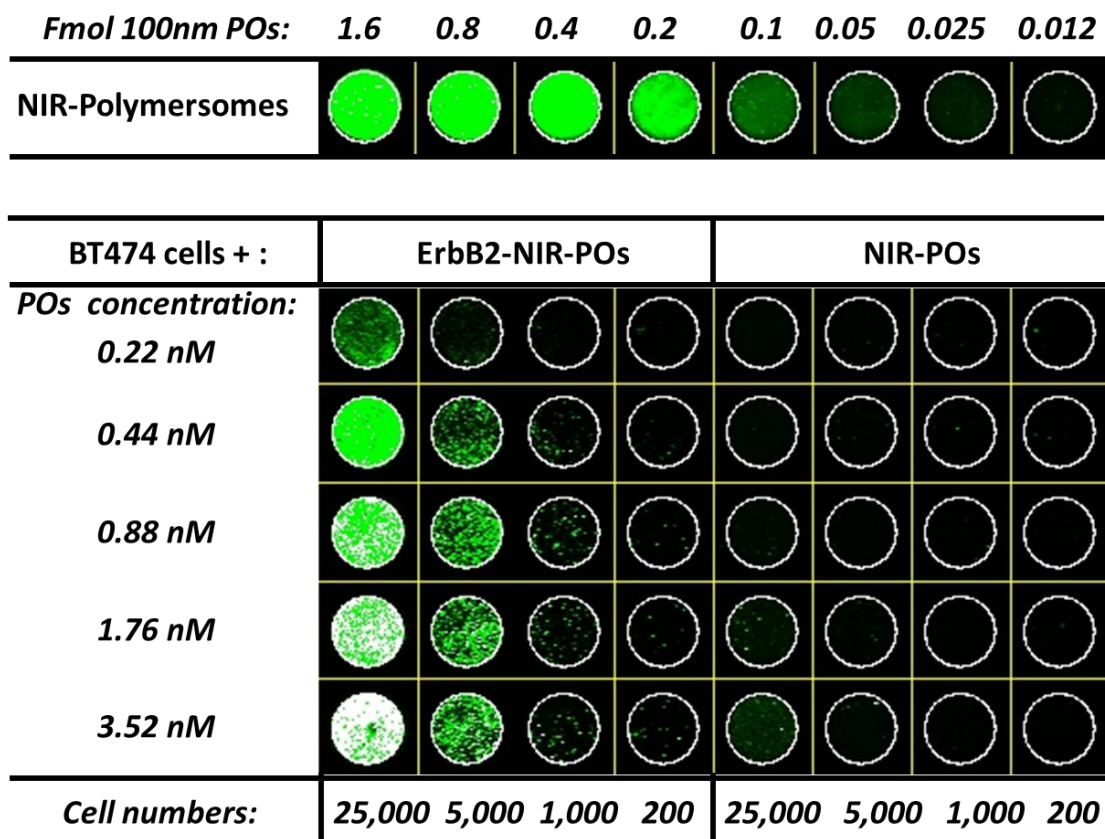
Figure 3.24 Representative Licor-Odyssey image of 96-well plate with 5-fold serial dilutions of BT474 cells with different concentrations of anti-ErbB2-NIR-polymersomes and control NIR-polymersomes.
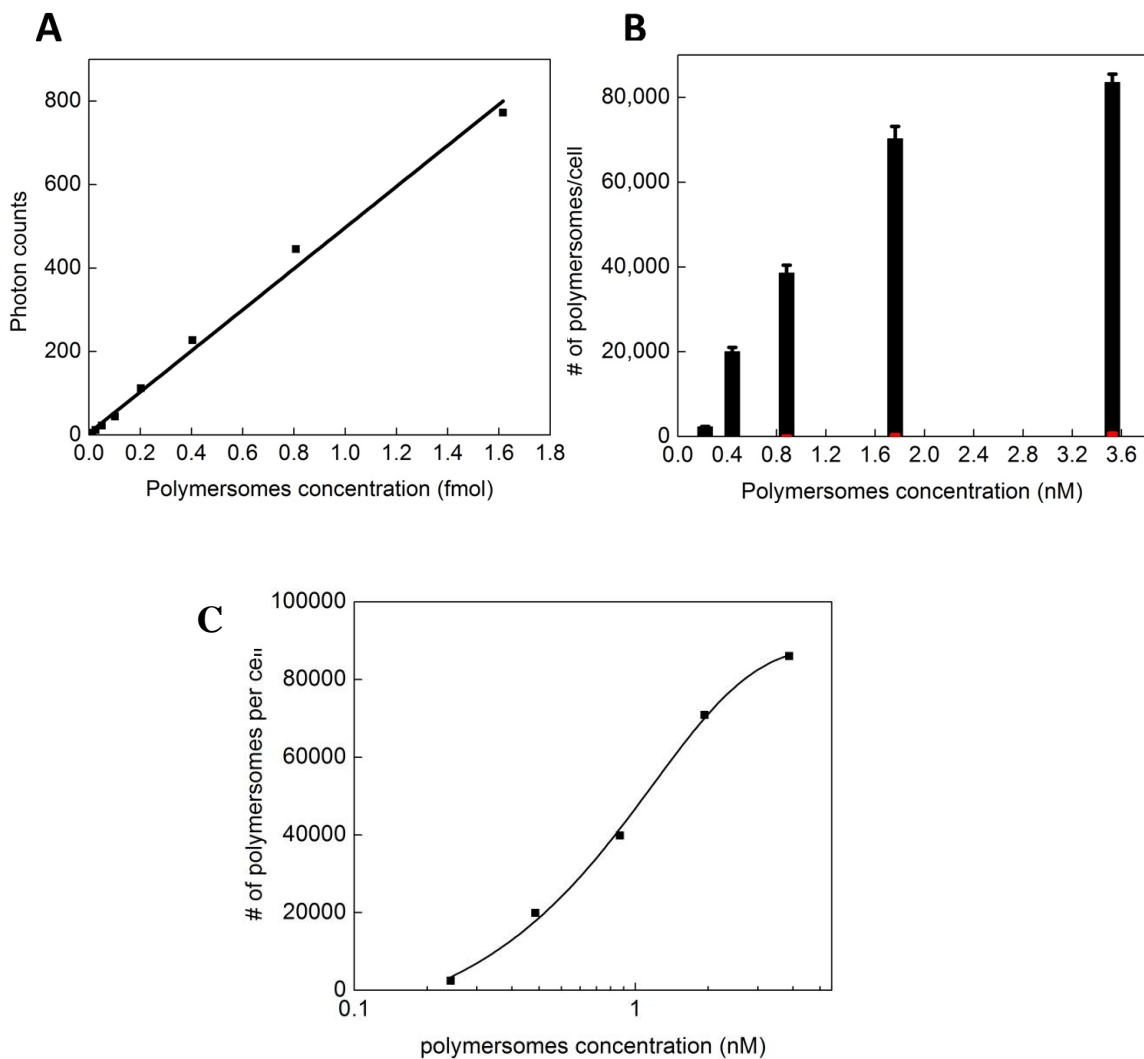
Figure 3.25 (A) Fluorescence calibration with total photon counts versus the number of NIR-polymersomes (PO) per well ($n = 8$); linear fit $R^2 = 0.99$. (B) The calculated number of polymersomes per cell as a function of cellular treatment condition. (C). Fitted curve for binding of anti-ErbB2 immunoliposomes to BT474 cells.

Black bars represent BT474 cells treated with anti-ErbB2-NIR-polymersomes, and the red bars represent BT474 cells treated with control NIR-polymersomes. Error bars represent standard deviation.

Fmol 100nm POs:	1.6	0.8	0.4	0.2	0.1	0.05	0.025	0.012
NIR-Polymersomes								

MCF7 cells + :	ErbB2-NIR-POs				NIR-POs			
POs concentration: 0.22 nM								
0.44 nM								
0.88 nM								
1.76 nM								
3.52 nM								
Cell numbers:	25,000	5,000	1,000	200	25,000	5,000	1,000	200
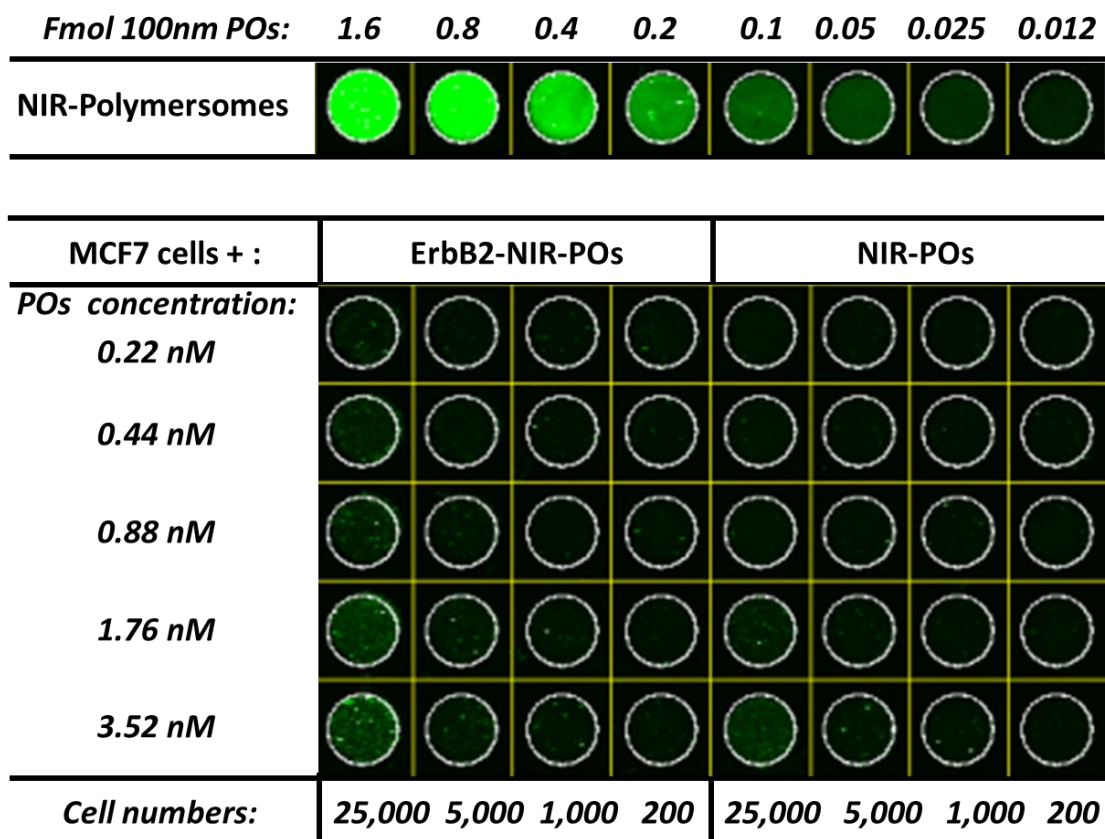
Figure 3.26 Representative Licor-Odyssey image of 96-well plate with 5-fold serial dilutions of MCF7 cells with different concentrations of anti-ErbB2-NIR-polymersomes and control NIR-polymersomes.
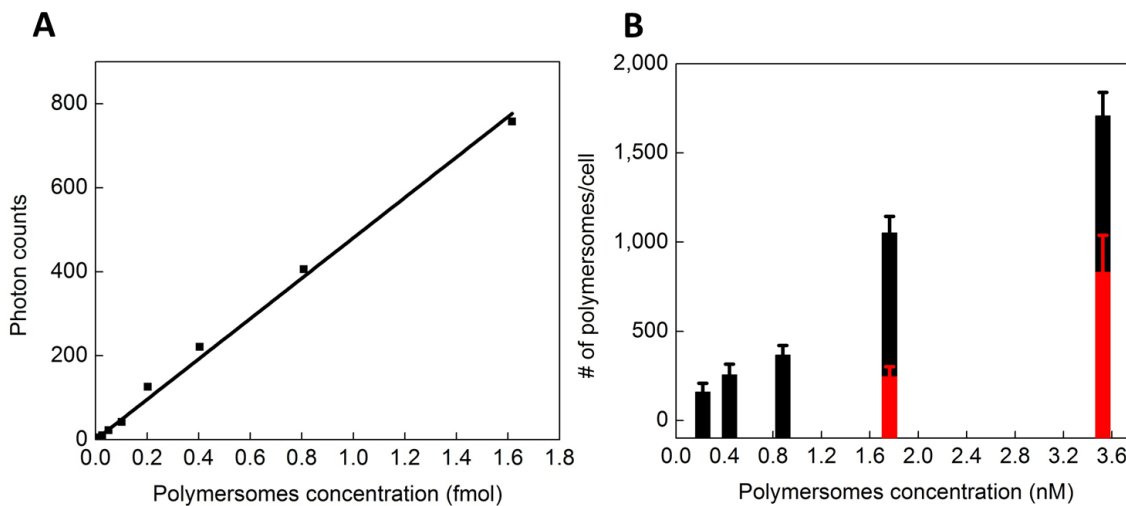
Figure 3.27 (A) Fluorescence calibration with total photon counts versus the number of NIR-polymersomes (PO) per well ($n = 8$); linear fit $R^2 = 0.99$. (B) The calculated number of polymersomes per cell as a function of cellular treatment condition.

Black bars represent MCF7 cells treated with anti-ErbB2-NIR-polymersomes, and the red bars represent MCF7 cells treated with control NIR-polymersomes. Error bars represent standard deviation.
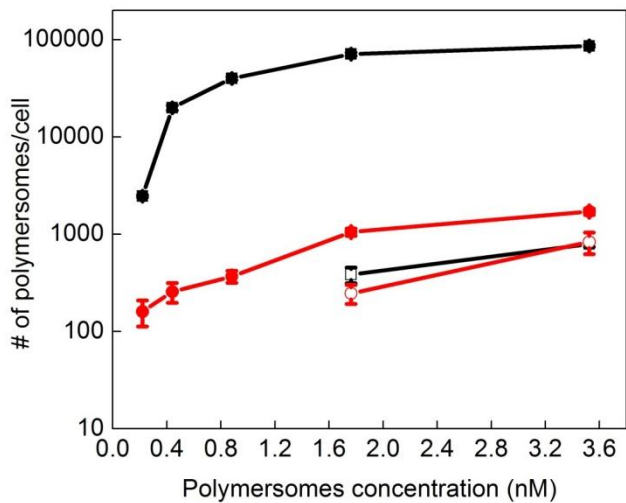
Figure 3.28 Number of polymersomes per cell with different polymersome concentrations for BT474 cells (black line) and MCF7 cells (red line) treated with anti-ErbB2-conjugated NIR emissive polymersomes (solid dots) or control NIR emissive polymersomes (hollow dots) measured by Licor-Odyssey experiments.
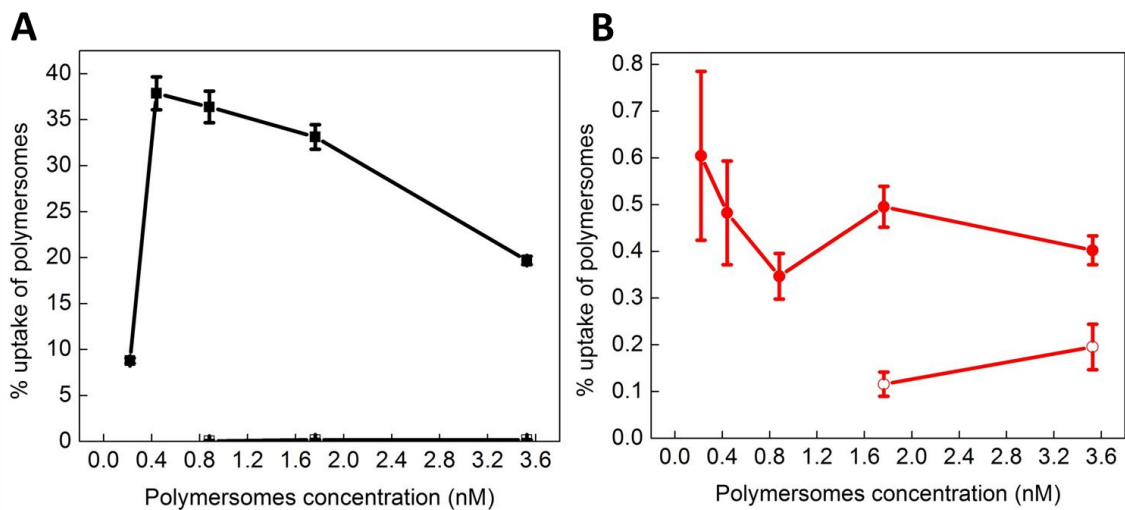
Figure 3.29 Relative uptake, percentage of polymersomes added/10^6 cells (A) BT474 cells and (B) MCF7 cells treated with different polymersome concentration of anti-ErbB2-conjugated NIR emissive polymersomes (solid dots) or control NIR emissive polymersomes (hollow dots) measured by Licor-Odyssey experiments.

Finally, since both Licor-Odyssey imaging and flow cytometry measure the fluorescence per cell, we compared results from each of these assays by normalizing individual values with the maximum fluorescence signal intensity observed in each method. These results are presented in **Figure 3.23** and summarized in **Table 3.2** which shows that the independent assays are in close agreement. In both assays, the extent of labeling is greatest for BT474 cells labeled with anti-ErBb2 NIR emissive IPs. Cellular labeling levels in the absence of anti-ErbB2 antibody are two orders of magnitude lower for ErBb2 overexpression BT474 cells and one order of magnitude lower for non-ErbB2 overexpression MCF7 cells. The corroboration of both the NIR imaging and flow cytometry-based assays shows the reliability of our imaging methods.

Table 3.2 Comparison of fluorescence per cell value generated from Licor-Odyssey imaging or flow cytometry analysis.

	Normalized fluorescence/cell									
	BT474 cells					MCF7 cells				
Concentration (nM)	*0.22*	*0.44*	*0.88*	*1.76*	*3.52*	*0.22*	*0.44*	*0.88*	*1.76*	*3.52*
	Flow cytometry[a]									
Anti-ErbB2 IPs	4.67	32.98	55.18	81.39	100	0.70	0.83	1.33	2.03	2.61
Control POs	-	-	0.01	0.21	0.68	0.05	0.09	0.12	0.38	0.89
	Licor-odyssey imaging[b]									
Anti-ErbB2 IPs	4.12 (0.18)	31.37 (1.60)	57.84 (2.74)	79.55 (4.31)	100 (5.91)	0.09 (0.09)	0.62 (0.13)	0.67 (0.11)	1.30 (0.07)	2.77 (0.20)
Control POs	-	-	-	0.29 (0.06)	0.98 (0.08)	-	-	-	0.32 (0.10)	1.51 (0.70)

[a] Normalized average photon counts per cell (mean ±SD) by Licor-Odyssey image.

[b] Normalized geometric mean fluorescence of 10 000 events by flow cytometry analysis.

3.5. Conclusions

The goal of this work was to design and implement a simple, efficient, and universal method to covalently attach big biological ligands, such as antibodies, to polymersomes in order to provide a platform for targeting experiments. Amphiphilic PEO-*b*-PBD diblock copolymers comprising FNB, biotin, amine, amide and maleimide functionalities at their hydrophilic ends were synthesized and characterized. Six different antibody coupling procedures were developed based on these five different functionalities on polymersomes surface. All these coupling procedures were evaluated and compared in terms of antibody conjugation efficiency and polymersome receovery yield. The maleimide coupling procedure was concluded to be the optimized method for antibody conjugation, which yields ~162 streptavidin molecules and ~64 rat-IgG antibodies per 100 nm polymersomes at ~80% antibody conjugation efficiency with a high polymersome yield of 75-84%. The covalent attachment of antibody to polymersomes can be controlled by varying the molar percentage of functionalized polymer in the polymersome. The effect of antibody concentration on conjugation efficiency was also studied. Characterization of the antibody conjugated polymersomes by confocal microscope and Cryo-TEM experiments showed successful conjugation of antibody to the surface of polymersomes. The reactivity and specifity of the antibody after conjugation to polymersomes was also studied by ELISA. The results demonstrated that antibody conjugated polymersomes showed speficic and selective binding in immunoassays. Furthermore, the sensitivity of antibody polymersomes conjugates for optical based NIR imaging was studied by Licor-Odyssey imaging. The antibody

conjugated polymersomes appear to be 1-2 orders more sensitive than the commercially available fluorescent-tagged antibodies.

Finally, anti-ErbB2 NIR emissive IPs were developed based on these established functionalization chemistries to combine the tumor-targeting propertied of anti-ErbB2 monoclonal antibodies with the pharmacokinetic and delivery properties of long circulating polymersomes. Anti-ErbB2 IPs bound efficiently to and internalized in HER2 overexpressing cells, resuling in intracellular delivery *in vitro,* as determined by fluorescence confocal microscopy and quantitative analysis of fluorescent probe delivery. HER2 overexpression tumor cells uptake of the probes was saturated at high concentrations. Optimized cellular uptake of NIR emissive polymersomes was achieved in BT474 cells incubated with anti-ErbB2 IPs at 0.88 nM concentration in 1 h, with uptake efficiency as high as 37.3%. This high efficiency uptake of IPs in BT474 cells corresponds to $86,000 \pm 2,500$ polymersomes per cell. This number is much higher than the anti-HER2 immunoliposomes uptake which is only 8,000-23,000 IPs per cell.[86] Although this maximum number of polymersomes per cell is similar to other peptide conjugated polymersomes, for example, the uptake of Tat-polymersomes into dentric cells resulted in ~ 70,000 polymersomes per cell,[39] the uptake of our antibody conjugated IPs is much more rapid (within 1 hour incubation) compared to the small peptide conjugated polymersomes (over 10 hours incubation), suggests a much stronger interaction of IPs with the cells than peptide conjugated polymersomes. In summary, we developed a new antibody-polymersome platform, based on a series of different conjugation chemistries that allows multifaceted and stable attachment of targeting antibodies. This targeting strategy can provide a critical advantage to the therapeutic

182

action of many anticancer agents and presents new opportunities to make highly sensitive and effective immunoassays for *in vivo* imaging and biomedical applications.

3.6. Acknowledgements

3.7. References

1.   Adams, G. P.; Weiner, L. M. *Nature biotechnology* **2005,** 23, 1147-1157.

2.   Discher, B. M.; Won, Y. Y.; Ege, D. S.; Lee, J.; Bates, F. S.; Discher, D. E.; Hammer, D. A. *Science* **1999,** 284, 1143.

3.   Discher, D. E.; Eisenberg, A. *Science* **2002,** 297, 967-973.

4.   Bermudez, H.; Brannan, A. K.; Hammer, D. A.; Bates, F. S.; Discher, D. E. *Macromolecules* **2002,** 35, 8203-8208.

5.   Lee J.C.M., B. H., Discher B.M., Sheehan M.A., Won Y-Y, Bates F.S. and Discher D.E. . *Biotechnology and Bioengineering* **2001,** 73, 135-145.

6.   Unezaki, S.; Maruyama, K.; Hosoda, J. I.; Nagae, I.; Koyanagi, Y.; Nakata, M.; Ishida, O.; Iwatsuru, M.; Tsuchiya, S. *International journal of pharmaceutics* **1996,** 144, 11-17.

7.   Senior, J. H. *Critical reviews in therapeutic drug carrier systems* **1987,** 3, 123.

8.   Allemann, E.; Gurny, R.; Doelker, E. *European journal of pharmaceutics and biopharmaceutics* **1993,** 39, 173-191.

9.   Couvreur, P.; Fattal, E.; Andremont, A. *Pharmaceutical Research* **1991,** 8, 1079-1086.

10. Vaage, J.; Barber Guillem, E.; Abra, R.; Huang, A.; Working, P. *Cancer* **1994,** 73, 1478-1484.

11. Harasym, T. O.; Bally, M. B.; Tardi, P. *Advanced drug delivery reviews* **1998,** 32, 99-118.

12. Forssen, E.; Willis, M. *Advanced drug delivery reviews* **1998,** 29, 249-271.

13. Pang, Z.; Lu, W.; Gao, H.; Hu, K.; Chen, J.; Zhang, C.; Gao, X.; Jiang, X.; Zhu, C. *Journal of Controlled Release* **2008,** 128, 120-127.

14. Ahmed, F.; Discher, D. E. *Journal of Controlled Release* **2004,** 96, 37-53.

15. Meng, F.; Engbers, G. H. M.; Feijen, J. *Journal of Controlled Release* **2005,** 101, 187-198.

16. Ghoroghchian, P. P.; Frail, P. R.; Susumu, K.; Blessington, D.; Brannan, A. K.; Bates, F. S.; Chance, B.; Hammer, D. A.; Therien, M. J. *Proceedings of the National Academy of Sciences U.S.A* **2005,** 102, 2922-2927.

17. Ghoroghchian, P. P.; Frail, P. R.; Susumu, K.; Park, T. H.; Wu, S. P.; Uyeda, H. T.; Hammer, D. A.; Therien, M. J. *Journal of the American Chemical Society* **2005,** 127, 15388-15390.

18. Ahmed, F.; Pakunlu, R. I.; Brannan, A.; Bates, F.; Minko, T.; Discher, D. E. *Journal of Controlled Release* **2006,** 116, 150-158.

19. Broz, P. B., S.M.; Saw, C.; Burger, P.; Heider, H.; Pfisterer, M.; Marsch, S.; Meier, W.; Hunziker, P. . *Journal of Controlled Release* **2005,** 102, 475-488.

20. Uchegbu, I. F. *Expert Opinion in Drug Delivery* **2006,** 3.

21. Upadhyay, K. K. B., A.N.; Mishra, A.K.; Dwarakanath, B.S.; Jain, S.; Schatz, C.; Le Meins, J.-F.; Farooque, A.; Chandraiah, G.; Jain, A.K.; Misra, A.; Lecommandoux, S. *Biomaterials* **2010,** 31, 2882-2892.

22. Renggli, K. B., P.; Langowska, K.; Onaca, O.; Bruns, N.; Meier, W. *Advanced Functional Materials* **2010,** in presss.

23. Grzelakowski, M. O., O.; Rigler, P.; Kumar, M.; Meier, W. *Small* **2009,** 5, 2545-2548.

24. Nardin, C. T., S.; Widmer, J.; Winterhalter, M.; Meier, W. *Chemical Communications* **2000,** 36, 1433-1434.

25. Axthelm, F. C., O.; Koppenol, W.H.; Nauser, T.; Meier, W.; Palivan, C.G. 2008, 112, 8211-8217. . *The Journal of Physical Chemistry B* **2008,** 112, 8211-8217.

26. De Vocht, C. R., A.; Willaert, R.; Van Ginderachter, J.A.; Vanhaecke, T.; Rogiers, V.; Versees, W.; van Gelder, P.; Steyaert, J. . *Journal of Controlled Release* **2009,** 137, 246-254.

27. van Dongen, S. F. M. N., M.; Cornelissen, J.J.L.M.; Nolte, R.J.M.; van Hest, J.C.M. *Chemistry - A European Journal* **2009,** 15, 1107-1114.

28. Onaca, O. H., D.W.; Balasubramanian, V.; Grzelakowski, M.; Meier, W.; Palivan, C.G. *Macromolecular Bioscience* **2010,** 10, 531-538.

29. Broz, P. D., S.; Ziegler, J.; Ben-Haim, N.; Marsch, S.; Meier, W.; Hunziker, P. *Nano Letters* **2006,** 6, 2349-2353.

30. Minko, T.; Dharap, S. S.; Pakunlu, R. I.; Wang, Y. *Current Drug Targets* **2004,** 5, 389-406.

31. Egli, S.; Schlaad, H.; Bruns, N.; Meier, W. *Polymers* **2011,** 3, 252-280.

32. Brewer, J. M.; Pollock, K. G. J.; Tetley, L.; Russell, D. G. *The Journal of Immunology* **2004,** 173, 6143-6150.

33. Kim, B. S.; Yang, W. Y.; Ryu, J. H.; Yoo, Y. S.; Lee, M. *Chem. Commun.* **2005**, 2035-2037.

34. Kim, B. S.; Hong, D. J.; Bae, J.; Lee, M. *Journal of the American Chemical Society* **2005,** 127, 16333-16337.

35. Toyotama, A.; Kugimiya, S.; Yamanaka, J.; Yonese, M. *Chemical & pharmaceutical bulletin* **2001,** 49, 169-172.

36. Yang, X.; Grailer, J. J.; Rowland, I. J.; Javadi, A.; Hurley, S. A.; Matson, V. Z.; Steeber, D. A.; Gong, S. *ACS nano* **2010**, 1532-1555.

37. Yang, X.; Grailer, J. J.; Rowland, I. J.; Javadi, A.; Hurley, S. A.; Steeber, D. A.; Gong, S. *Biomaterials* **2010**.

38. van Dongen, S. F. M.; Verdurmen, W. P. R.; Peters, R. J. R. W.; Nolte, R. J. M.; Brock, R.; van Hest, J. *Angewandte Chemie International Edition* **2010,** 49, 7213-7216.

39. Christian, N. A.; Milone, M. C.; Ranka, S. S.; Li, G.; Frail, P. R.; Davis, K. P.; Bates, F. S.; Therien, M. J.; Ghoroghchian, P. P.; June, C. H. *Bioconjugate chemistry* **2007,** 18, 31-40.

40. Demirgoz, D.; Pangburn, T. O.; Davis, K. P.; Lee, S.; Bates, F. S.; Kokkoli, E. *Soft Matter* **2009,** 5, 2011?019.

41. Chang, Y.-W.; Silas, J. A.; Ugaz, V. M. *Langmuir* **2010,** 26, 12132-12139.

42. Rajagopal, K.; Christian, D. A.; Harada, T.; Tian, A.; Discher, D. E. *International Journal of Polymer Science* **2010,** 2010, 379286-179296.

43. Marsden, H. R.; Handgraaf, J.-W.; Nudelman, F.; Sommerdijk, N. A. J. M.; Kros, A. *Journal of the American Chemical Society* **2010,** 132, 2370-2377.

44. Lin, J. J.; Silas, J. A.; Bermudez, H.; Milam, V. T.; Bates, F. S.; Hammer, D. A. *Langmuir* **2004,** 20, 5493-5500.

45. Broz, P.; Ben-Haim, N.; Grzelakowski, M.; Marsch, S.; Meier, W.; Hunziker, P. *Journal of Cardiovascular Pharmacology* **2008,** 51, 246-252.

46. Rigler, P.; Meier, W. *Journal of the American Chemical Society* **2006,** 128, 367-373.

47. Nilsson, K.; Mosbach, K. *Methods in enzymology* **1984,** 104, 56-69.

48. Hammer, D. A.; Robbins, G. P.; Haun, J. B.; Lin, J. J.; Qi, W.; Smith, L. A.; Ghoroghchian, P. P.; Therien, M. J.; Bates, F. S. *Faraday discussions* **2008,** 139, 129.

49. Phillips, N. C.; Gagne, L.; Tsoukas, C.; Dahman, J. *The Journal of Immunology* **1994,** 152, 3168.

50. Paganelli, G.; Pervez, S.; Siccardi, A. G.; Rowlinson, G.; Deleide, G.; Chiolerio, F.; Malcovati, M.; Scassellati, G. A.; Epenetos, A. A. *International Journal of Cancer* **1990,** 45, 1184-1189.

51. Dafni, H.; Gilead, A.; Nevo, N.; Eilam, R.; Harmelin, A.; Neeman, M. *Magnetic resonance in medicine* **2003,** 50, 904-914.

52. van Dongen, S. F. M.; Nallani, M.; Schoffelen, S.; Cornelissen, J. J. L. M.; Nolte, R. J. M.; van Hest, J. *Macromolecular Rapid Communications* **2008,** 29, 321-325.

53. Li, B.; Martin, A. L.; Gillies, E. R. *Chemical Communications* **2007**, 5217-5219.

54. Martin, A. L.; Li, B.; Gillies, E. R. *Journal of the American Chemical Society* **2008,** 131, 734-741.

55. Opsteen, J. A.; Brinkhuis, R. P.; Teeuwen, R. L. M.; Leowik, D. W. P. M.; van Hest, J. C. M. *Chemical Communications* **2007**, 3136-3138.

56. Petersen, M. A.; Yin, L.; Kokkoli, E.; Hillmyer, M. A. *Polymer Chemistry* **2010**.

57. Domes, S.; Filiz, V.; Nitsche, J.; Fro msdorf, A.; Fo rster, S. *Langmuir* **2010,** 26, 6927-6931.

58. Egli, S.; Nussbaumer, M. G.; Balasubramanian, V.; Chami, M.; Bruns, N.; Palivan, C.; Meier, W. *Journal of the American Chemical Society* **2011**, 629.

59. Lin, J. J.; Bates, F. S.; Hammer, D. A.; Silas, J. A. *Physical review letters* **2005,** 95, 26101.

60. Nehring, R.; Palivan, C. G.; Casse, O.; Tanner, P.; Tuxen, J.; Meier, W. *Langmuir* **2008,** 25, 1122-1130.

61. Cleland, W. W. *Biochemistry* **1964,** 3, 480-482.

62. Carlsson, J.; Drevin, H.; Axen, R. *Biochemical Journal* **1978,** 173, 723.

63. Derksen, J. T. P.; Scherphof, G. L. *Biochimica et Biophysica Acta (BBA)-Biomembranes* **1985,** 814, 151-155.

64. Traut, R. R.; Bollen, A.; Sun, T. T.; Hershey, J. W. B.; Sundberg, J.; Pierce, L. R. *Biochemistry* **1973,** 12, 3266-3273.

65. Jue, R.; Lambert, J. M.; Pierce, L. R.; Traut, R. R. *Biochemistry* **1978,** 17, 5399-5406.

66. Newton, D. L.; Hansen, H. J.; Mikulski, S. M.; Goldenberg, D. M.; Rybak, S. M. *Blood* **2001,** 97, 528.

67. D'Oro, U.; Munitic, I.; Chacko, G.; Karpova, T.; McNally, J.; Ashwell, J. D. *The Journal of Immunology* **2002,** 169, 6269-6278.

68. Beeghly-Fadiel, A.; Kataoka, N.; Shu, X. O.; Qiuyin, C. A. I.; Deming, S. L.; Gao, Y. T.; Wei, Z. *Oncology reports* **2008,** 19, 1347-1354.

69. Santin, A. D.; Bellone, S.; Roman, J. J.; McKenney, J. K.; Pecorelli, S. *International Journal of Gynecology & Obstetrics* **2008,** 102, 128-131.

70. Ladd, D. L.; Snow, R. A. *Analytical Biochemistry* **1993,** 210, 258-261.

71. Park, B.-W.; Zhang, H.-T.; Wu, C.; Berezov, A.; Zhang, X.; Dua, R.; Wang, Q.; Kao, G.; O'Rourke, D. M.; Greene, M. I.; Murali, R. *Nat Biotech* **2000,** 18, 194-198.

72. Huwyler, J.; Wu, D.; Pardridge, W. M. *Proceedings of the National Academy of Sciences of the United States of America* **1996,** 93, 14164.

73. Won, Y. Y.; Brannan, A. K.; Davis, H. T.; Bates, F. S. *The Journal of Physical Chemistry B* **2002,** 106, 3354-3364.

74. Ghoroghchian, P. P.; Lin, J. J.; Brannan, A. K.; Frail, P. R.; Bates, F. S.; Therien, M. J.; Hammer, D. A. *Soft Matter* **2006,** 2, 973-980.

75. Rubtsov, I. V.; Susumu, K.; Rubtsov, G. I.; Therien, M. J. *Journal of the American Chemical Society* **2003,** 125, 2687-2696.

76. Susumu, K.; Therien, M. J. *Journal of the American Chemical Society* **2002,** 124, 8550-8552.

77. Lin, V. S. Y.; Therien, M. J. *Chemistry – A European Journal* **1995,** 1, 645-651.

78. Lin, V. S.; DiMagno, S. G.; Therien, M. J. *Science* **1994,** 264, 1105-1111.

79. Kung, V. T.; Redemann, C. T. *Biochimica et Biophysica Acta (BBA) - Biomembranes* **1986,** 862, 435-439.

80. Christian, D. A.; Tian, A.; Ellenbroek, W. G.; Levental, I.; Rajagopal, K.; Janmey, P. A.; Liu, A. J.; Baumgart, T.; Discher, D. E. *Nat Mater* **2009,** 8, 843-849.

81. Loughrey, H.; Bally, M. B.; Cullis, P. R. *Biochimica et Biophysica Acta (BBA) - Biomembranes* **1987,** 901, 157-160.

82. Moudgil, A. L. K. R. S. V. A. H. A. K. P. J. S. B. M. *Materials Research Society Symposia Proceedings* **2007,** 1019E, 1019-FF05-01.

83. Yang, J.; Mayer, M.; Kriebel, J. K.; Garstecki, P.; Whitesides, G. M. *Angewandte Chemie International Edition* **2004,** 43, 1555-1558.

84. J.W. Park, R. S., G.D. Lewis, P. Carter, D. Maneval, D.J. Slamon, H. Jaffe and H.M. Shepard. *Advances in Cellular and Molecular Biology of Breast Cancer* **1992**, 193-211.

85. Lewis, G. D.; Figari, I.; Fendly, B.; Lee Wong, W.; Carter, P.; Gorman, C.; Shepard, H. M. *Cancer Immunology, Immunotherapy* **1993,** 37, 255-263.

86. Kirpotin, D.; Park, J. W.; Hong, K.; Zalipsky, S.; Li, W. L.; Carter, P.; Benz, C. C.; Papahadjopoulos, D. *Biochemistry* **1997,** 36, 66-75.

CHAPTER 4. Synthesis, Characterization, Polymersome Preparation, Morphology Assessment and Functionalization of Biodegradable Diblock Copolymers

4.1. Summary

Polymersomes have been shown to possess a number of attractive biomaterial properties including prolonged circulation times, increased mechanical stability, and the unique ability to non-covalently incorporate numerous high-molecular-weight hydrophobic molecules within their thick lamellar membranes. A long-standing challenge in materials chemistry, however, has been the development of polymersomes comprised entirely of biodegradable, non-toxic synthetic amphiphiles that would make these vesicles truly competitive with liposomes for in vivo applications. In this chapter, we described the formation of polymersomes through self-assembly of an amphiphilic bioresorbable polymer consisting of three previously FDA-approved building blocks: poly(ethyleneoxide) (PEO) , poly(ε-caprolactone) (PCL) and poly(1,3-trimethylene carbonate) (PTMC). Unlike other published reports of degradable peptide, polyester, or polyanhydride-based polymersomes, these biodegradable vesicles are formed spontaneously through self-assembly without the addition of co-solvent or blending with other non-degradable vesicle-forming polymers, enabling facile, large-scale synthesis and thus obviating the need for post-assembly processing. We found the PEO-*b*-PCL diblock copolymer compositions that form none or very little meso-scale polymersomes could

form ~100% nano-scale polymersomes, implicates various *in vivo* applications for this diblock copolymers as nano-sized drug delivery vesicles.

Furthermore, by copolymerizing TMC, soft, bioresorbable vesicles with reduced membrane crystallinity were prepared. Notely, the vesicles prepared from these TMC containing materials have much smaller sizes compare to classic polymer vesicles, suggests prolonged *in vivo* circulation time and thus delayed clearance by the reticuloendothelial system (RES), a highly desired property for *in vivo* applications. In addition, these PEO-*b*-PTMC and PEO-*b*-P(CL-co-TMC) can also self-assemble into uniform distributed large spherical micelles at very high yields, enable the arising of new promising nanomaterials for various biomedical applications.

Finally, we synthesized vinyl sulfone functionalized PEO-*b*-PCl diblock copolymers which can be readily used for peptide conjugation and tumor targeting. As such, these bioresorbable polymersomes hold promise as nanomaterials for future imaging, targeting and drug delivery applications.

4.2. Introduction

Polymersomes (50 nm - 50 μm diameter polymer vesicles) formed from amphiphilic block copolymers have attracted much attention due to their superior mechanical stabilities and unique chemical properties relative to those of conventional lipid-based vesicles (liposomes) and micelles.[1-5] Polymer vesicles have not only proven capable of entrapping water-soluble hydrophilic compounds (drugs, vitamins, fluorophores, etc.) inside of their aqueous cavities, but have been shown to disperse hydrophobic molecules[5] within their thick lamellar membranes. Moreover, the size, membrane thickness, and stability of these synthetic vesicles can be rationally tuned via

various preparation methods[1, 4] through modulation of block copolymer chemical structure, number-average molecular weight, and hydrophilic to hydrophobic volume fraction: polymersomes thus have adjustable characteristics that lend to their potential function in medical imaging, drug delivery, and cosmetic applications.[1, 5, 6]

To date, polymersomes have been formed predominantly from amphiphilic diblock copolymers that include poly(ethylene oxide)-*b*-polybutadiene (PEO-*b*-PBD),[1, 5, 7] poly(ethylene oxide)-*b*-polyethylethylene (PEO-*b*-PEE),[7] polystyrene-*b*-poly(ethylene oxide) (PS-*b*-PEO),[8-10] polystyrene-*b*-poly(acrylic acid) (PS-*b*-PAA),[1, 9, 11] poly(ethylene oxide)-*b*-poly(propylenesulfide) (PEO-PPS),[12] [13, 14] poly(2-(methacryloyloxy) ethylphosphorylcholine)-*b*-poly(2-(diisopropylamino)ethylmethacrylate) (PMPC-PDPA)[15, 16] and polystyrene-*b*-polyisocyanoalanine(2-thiophene-3-yl-ethyl)amide (PS-PIAT)[17-20]. None of these well-established polymersome formulations, however, yields self-assembled fully-biodegradable polymer-based vesicles useful for *in vivo* applications. A few biodegradable polymersomes prepared from amphiphilic biodegradable diblock copolymers of PEO and aliphatic polyesters/polycarbonates using an organic co-solvent/water injection/extraction system have been reported;[21-23] in contrast with other polymersome preparation procedures based on self-assembly (i.e. film hydration, bulk hydration, or electroformation), a drawback of the co-solvent method is that the organic co-solvent must be completely removed from the aqueous polymersome suspension post-assembly; in addition to this required processing, the presence of any residual organic solvent in such vesicles constitutes an additional concern in the transition of these polymersomes for *in vivo* application. The other drawback of the co-solvent method is that the self-assembling process of diblock copolymer are affected by many different

factors, such as the diblock copolymer concentration, the water content, temperature, the mixing time and order of aqueous phase and organic phase.[22, 24-26] Therefore the cosolvent method is relatively hard to control and repeat, whereas the thin-film hydration method is not affected by these factors and is much more facile.

We have previously reported the generation of self-assembled polymersomes comprised entirely of an amphiphilic diblock copolymer PEO(2K)-*b*-PCL(12K) by thin film hydration featuring two previously FDA-approved polymers, poly(ethylene oxide) (PEO) and polycaprolactone (PCL).[27] Unlike degradable polymersomes formed from blending "bio-inert" and hydrolysable components,[28, 29] these PEO-*b*-PCL-based vesicles promise to be fully bioresorbable,[30] leaving no potentially toxic byproducts upon their degradation. Besides, unlike published reports of other degradable (polypeptide-, polyester-, or polyanhydride-based) polymersomes,[21, 22, 31-33] these bioresorbable vesicles are formed through spontaneous self-assembly of their pure amphiphile component, offering manufacturing advantages in terms of cost, tune, and safety. Moreover, these self-assembled vesicular architectures allow for the economic generation of mesoscopic colloidal devices, enabling large-scale production while eliminating the need for costly removal of organic cosolvents post assembly. These polymersomes are also found to possess slow *in vivo* drug release kinetics which makes them appropriate for potential intravascular drug delivery applications. However, it is well known that the size of particles has a big influence on blood circulation times, RES recognition, biodistribution and the mechanism of cell uptake.[34-36] The *in vivo* uptake of particles and the extent of drug absorption increase with decreasing particle size and increasing specific surface area; the optimum size for circulation in the blood stream is around 80-150 nm, and the uptake

of particles larger than 1 μm in diameter is minimal.[37-39] Therefore, it is very important to make nano-sized vesicles for *in vivo* applications using the vesicle morphology for encapsulation and drug delivery, which implicates an urgent need to screen for PEO-*b*-PCL diblock copolymer compositions that can self-assemble into nano-scale polymersomes by examining the effect of hydrophilic fraction and PEO chain length on the formation of nano-sized vesicles. Butler et al.[22] have looked into the formation of nano-sized vesicles from a number of PEO-*b*-PCL block copolymers. However, they were using co-solvent method for the vesicle preparation, and only checked on a very narrow range of commercial available PEO-*b*-PCL polymers at small PEO chain length and low copolymer molecular weights. Besides, they only checked on the effect of hydrophilic fraction on the formation of vesicles. In this work, we report the synthesis, characterization, and morphologies formed via aqueous self-assembly, of a very wide range of amphiphilic PEO-*b*-PCL compositions varying both the hydrophilic fraction and the PEO chain length.

These biodegradable PEO-*b*-PCL diblock copolymers were fabricated by: (i) ring-opening polymerization of ε-caprolactone monomer (ε-CL) followed by coupling to commercially available monomethoxyl PEO (MePEO); and (ii) sequential anionic living polymerization of ethylene oxide and caprolactone monomers. The number-average molecular weight and molecular weight distribution were characterized for each copolymer formulation by nuclear magnetic resonance (NMR) spectroscopy and gel permeation chromatography (GPC). These PEO-*b*-PCL diblock copolymers possessed number-average molecular weights spanning 3.6-57K, PEO block weight fractions ranging from 0.08-0.33 and polydiserpsity index (PDI) ranging between 1.14 and 1.37.

The thin film hydration method and organic co-solvent water injection/extraction method were employed to self-assemble diblock copolymers into various aqueous morphologies. The resultant structures were visualized by confocal, optical, and cryogenic transmission electron microscopic imaging.

PEO was chosen as the hydrophilic block for increasing of vesicles surfaces biocompatibility and prolonged blood circulation times.[40-42] PCL constitutes the hydrophobic membrane portion of the vesicles. PCL is degraded by hydrolysis of its ester linkages in physiological conditions and has therefore received lots of attention for use as an implantable biomaterial in drug delivery devices, bioresorbable structures, adhesion barriers, and as scaffolds for injury repair via tissue engineering.[43-46] PCL has several advantageous properties compared to other biodegradable aliphatic polyesters: (1) high permeability to small drug molecules; (2) maintenance of neutral pH upon degradation; (3) facility in forming blends with other polymers; and (4) suitability for long-term delivery afforded by slow erosion kinetics as compared to polyglycolide (PGA), polylactide (PLA), and polylactic-co-glycolic acid (PLGA).[44] Therefore, the utilization of PCL as the hydrophobic block promises that the resultant polymersomes should have safe and complete *in vivo* degradation. However, different from the PEO-*b*-PBD polymersomes that are "stealth" like, the biodegradable PEO-*b*-PCL polymersomes are found to be highly crystallized as determined by differential scanning calorimetry (DSC).[27] It is known that membrane rheology can significantly influence how polymersomes interact with their surroundings.[47] Soft membranes have several advantages over rigid membranes, the contact area between a soft vesicle and substrate is increased as the soft vesicle can deform and flatten on a surface, while no conformational

change can occur to improve the contact area for rigid vesicles. Consequently, the binding between soft vesicles and a substrate (i.e. a tissue) would be enhanced compared to a rigid vesicle's binding.[48] Another advantage of soft membrane vesicles is their ability to successfully passivate tumor tissue *in vivo* by deform-to elongate-to fit through the endothelial pore,[49] since the leaky junction pathway of tumor vasculatures is only 40-80 nm, which is smaller than the typical polymersome diameter.[50] In addition, crystallized polymers easily form multi-molecular aggregates which could accumulate undesirably in cells and kidneys as crystalline aggregates.

To decrease the crystallization of PCL blocks in PEO-*b*-PCL polymersomes and make soft polymersomes which can easily go through flesh and skin cells, poly(1,3-trimethylene carbonate) (PTMC), a rubbery and amorphous polymer with low glass transition temperatures, was taken as a starting point in the design of alternative synthetic materials with suitable mechanical properties. Poly(trimethylene carbonate) (PTMC) is a valuable candidate for biomedical applications in light of its biodegradability, biocompatibility and low toxicity.[51] Due to its excellent flexibility and poor mechanical strength, PTMC have been evaluated as flexible synthetic materials for the preparation of tissue engineering scaffolds or as depots for controlled release systems,[52-61] as well as in the design of implants, such as anti-adhesion membranes or vascular prostheses.[62] *In vivo*, PTMC degrades relatively rapid without the release of acidic degradation products.[51, 63,51, 64] Unlike the PCL, PMTC undergo surface degradation, the degradation and erosion are only limited to the polymer surface and the mass loss is linear. Therefore, the molecular weight of the polymer should be constant and the mechanical strength of the polymer should slowly decrease during the degradation process.

Seeing the promise in this material, biodegradable amphiphilic Poly(ethylene oxide)-*b*-Poly(trimethylene carbonate) (PEO-*b*-PTMC) diblock copolymers and Poly(ethylene oxide)-*b*-Poly(ε-caprolactone-co- trimethylene carbonate) (PEO-*b*-P(CL-co-TMC) diblock tripolymers varying in a number average molecular weight (M_n: 5.7-35.6k) and PEO weight fraction (f_{PEO}: 0.10-0.25) and TMC molar fraction of the hydrophobic block (30%, 50%, 100 %) were synthesized. The number-average molecular weight and molecular weight distribution were characterized for each copolymer formulation by nuclear magnetic resonance (NMR) spectroscopy and gel permeation chromatography (GPC). The chemical and thermal properties of these polymers in bulk were characterized by differential scanning calorimetry (DSC). The polymers were also subsequently screened for their ability to self-assemble into meso-scale and nano-scale polymersomes in dilute aqueous solution. All copolymers robustly assembled into both micron-sized and nano-sized vesicles. These vesicles were characterized for their mechanical rigidity, and stability properties.

Finally, as described in Chapter 3, actively targeted carriers have proven to be particularly promising for enhancing the specificity of drug delivery systems.[65] However, very little study has done on the functionalization of biodegradable PEO-*b*-PCL polymersomes. Jiang etc. reported functionalized vesicles formed from maleimide functionalized PEO-*b*-PCL; [66-68] the maleimide functionalized PEO-*b*-PCL diblock copolymer synthesis is based upon custom-synthesized hydroxy-polyethyleneglycol-maleimide, which is costly and have very few options of PEO molecular weight. Herein we report the synthesis of vinyl sulfone functionalized PEO-*b*-PCL diblock copolymer with a wide molecular weight distribution and capable of reacting with targeting ligands

under mild conditions via conjugate addition following vesicle formation. Following a related procedure by Bae et al., the functionalized diblock copolymers were synthesized by preferentially modifying one end of PEO diol with divinyl sulfone (VS).[69] To allow thiol-reactivity of the copolymer, heterobifunctional PEG with a VS group at one terminus was prepared by a multi-step synthetic procedure and PCL was then introduced to the remaining terminal hydroxyl group of PEG using ring opening polymerization. Compared to maleimide-PEG, which has been widely used to make targeted and long-circulating nanocarriers,[70-72] VS-PEO are reported to have several advantages: (1)The reaction rate of VS-PEO towards peptides and proteins is relative faster than maleimide-PEG; (2) The specificity is slightly better at pH below 8 and the thioether linkage formed with thiol compounds is much more stable than the linkage formed with maleimides;[73] (3) The VS group is quite stable in aqueous solution[74, 75] while maleimide group is easy to hydrolysis. This VS functionalized block copolymer self-assembles in water to form polymersomes containing the VS functionality at the hydrophilic PEO corona terminus, which can undergo an efficient, site-selective attachment to thiol-containing peptides under mild conditions and did not react with targeting peptides lacking a thiol. Properties of these obtained VS functionalized block copolymer were fully characterized, and the reactivity of the VS functionalized vesicles toward thiols was investigated using peptide-based cancer targeting molecules. Overall, this work develops a versatile platform for the targeted delivery of therapeutics and offers the possibility to greatly improve treatment outcomes for diseases by enhancing specificity, thus minimizing detrimental side effects.

4.3. Experimental Methods

4.3.1. Synthesis, Characterization, Polymersome Preparation and Morphology Assessment of Biodegrable PEO-*b*-PCl, PEO-*b*-PTMC and PEO-*b*-P(CL-co-TMC) Polymers

4.3.1.1. Materials

ε-caprolactone (ε-CL, Aldrich) was dried over calcium hydride (CaH$_2$) at room temperature for 48 h, and distilled under reduced pressure. Monomethoxyl poly(ethylene oxide) (MePEO) homopolymers featuring a terminal -OH group and molecular weights of 5000, 2000, 1100 and 750, were purchased from Fluka. Higher molecular weight MePEO homopolymers (M$_n$ = 1100, 2000 and 5000) were purified by dissolution in tetrahydrofuran (THF), followed by precipitation into ether, and subsequent drying at 40 ℃ under reduced pressure (10 mm Hg) for 24 h. Polymer grade 1, 3-trimethylene carbonate (TMC) (Boehringer Ingelheim, Germany) were used without further purification. Stannous octoate (SnOct$_2$) (stannous 2-ethylhexanoate) (Sigma, USA) and 1,6-hexanediol (Aldrich, Germany) were used as received. Stannous (II) octonate (SnOct$_2$, Sigma) was used as received. Ethylene oxide (EO, Aldrich) was purified by passage through potassium hydroxide, condensed onto CaH$_2$, stirred for 2h, and distilled. Naphthalene was recrystallized from ether. THF was distilled over Na mirror under nitrogen. Other chemicals were commercially available and used as received.

4.3.1.2. General Polymerization Reaction Conditions
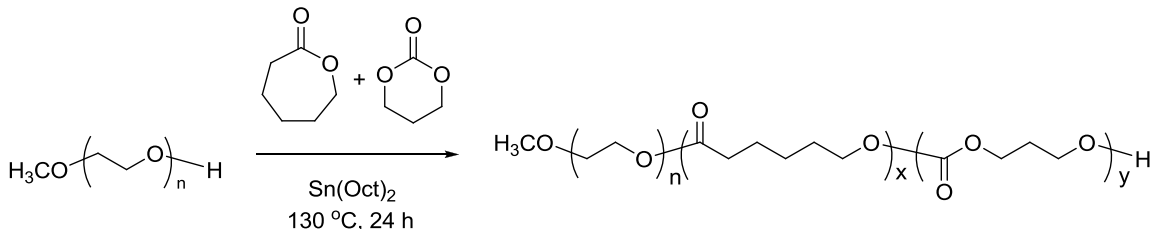
Scheme 4.1 Synthesis of PEO-b-P(CL-co-TMC) diblock copolymers by ring-opening polymerization.

Ring-opening polymerization: Monomethoxyl poly(ethylene oxide) (MePEO) was delivered to a flamed-dried flask under argon. A known mass of ε-caprolactone (CL) monomer and 1, 3-trimethylene carbonate (TMC) monomer were then injected into the flask via syringe, was then injected into the flask via syringe, following which two drops of SnOct$_2$ were added to the reaction mixture. The flask was connected to a vacuum line, evacuated, and immersed in an oil bath at 130 ℃. A progressive increase in viscosity of the homogeneous mixture was evident as the polymerization reaction progressed. After 24 h, the volatiles were removed; the recovered solid residue was dissolved in methylene chloride, precipitated with cold methanol/hexane (4 ℃), and dried under vacuum.
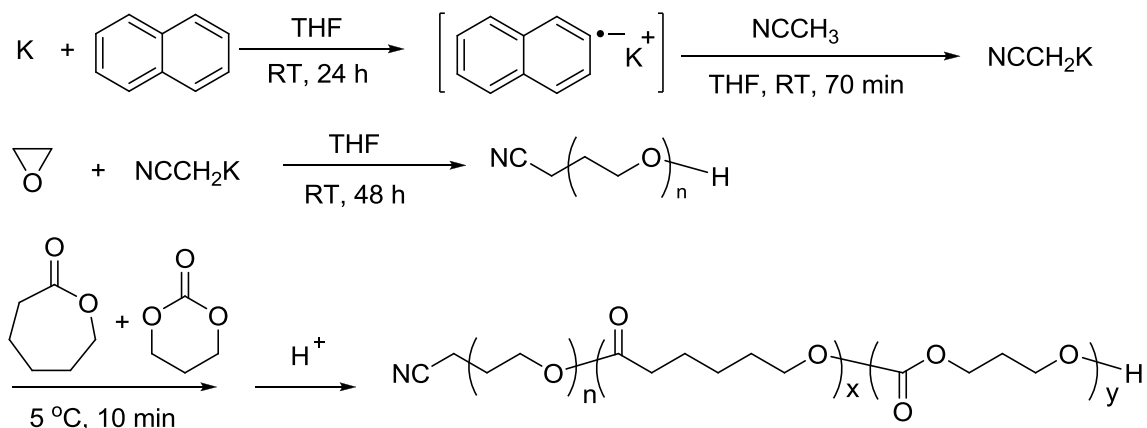
Scheme 4.2 Synthesis of PEO-b-P(CL-co-TMC) diblock copolymers by anionic living polymerization.

Anionic living polymerization: A flame-dried flask was purged with Ar and charged with 30 mL of anhydrous THF, acetonitrile (0.55 mL, 10 mmol), and potassium naphthalenide (5 ml of a 1 M THF solution). After vigorous stirring at 20 ºC for 70 min, the mixture was cooled in an ice-water bath, following which distilled EO was added via syringe. The polymerization reaction was carried out at ambient temperature; a sample of reaction product (~5 mL CN-PEO) was removed, treated with an acetone solution containing acetic acid, precipitated with excess diethyl ether, and dried under vacuum at room temperature to check the molecular weight of PEO block by NMR and GPC. Subsequently, ε-caprolactone and 1, 3-trimethylene carbonate dissolved in THF at a calculated mole ratio of ε-CL and TMC to EO, were added to the remaining reaction mixture of CN-PEO. After 10 min at 0 ºC, the polymerization was quenched by adding a small amount of acetic acid and then poured into acetone to precipitate. The reaction product was further purified by precipitation in diethyl ether and dried under vacuum at 40 ºC for two days.

4.3.1.3. Copolymer Characterization

PEO polymers and copolymers were characterized by ^{1}H-NMR spectroscopy. Weight-average molecular weight (M_w) and polydispersity index (M_w/M_n) values for each copolymer formulation were determined using a GPC system that featured two columns (PLgel 5µm mixed, 300 × 7.5mm) connected in series, and dynamic laser scattering and refractive index detectors (Enterprise System, Precision Technologies). THF was utilized as the eluting solvent. PEO standards were used to calibrate

copolymers molecular weights determined from refractive index data. And differential scanning calorimetry (DSC; TA Instruments Q100, New Castle, DE) was utilized to elucidate the thermal transitions of the polymers in bulk and within aqueous vesicle solutions. The thermal properties of the purified polymers were evaluated by differential scanning calorimetry (DSC). Samples (5-10 mg) were analyzed at a heating rate of 10 °C/min. Samples of amorphous polymers were heated from −100 °C to 100 °C, while semi-crystalline specimens were heated from −100 °C to 20 °C above their peak melting temperature. After the first heating scan, the samples were quenched rapidly (300 °C/min) to −100 °C, after 5 min at that temperature a second scan was recorded. Cyclohexane, indium, gallium and tin were used as standards for temperature calibration.

4.3.1.4. Preparation of Polymersomes

Two vesicle preparative methods, thin-film hydration and organic co-solvent/aqueous extraction, were employed to assemble the PEO-b-PCL copolymers into their equilibrium aqueous morphologies. For PEO-b-PTMC and PEO-b-P(CL-co-TMC) polymersomes, only thin-film hydration method was used. Thin film hydration has been extensively utilized for preparing non-biodegradable polymersomes comprised of PEO-b-PBD diblock copolymers; an analogous protocol was employed in experiments involving PEO-b-PCL copolymers. The biodegradable polymer (200 μL of 7 mg/mL CHCl$_3$ solution) was uniformly coated on the surface of a roughened Teflon plate, following which the sample was placed under vacuum for > 12 h. Addition of an aqueous solution (e.g. 250-300 milliosmolar sucrose or PBS) and heating at 60 °C for 48 h led to spontaneous budding of giant (5-20 μm) biodegradable polymersomes into solution. In the preparation of samples that contained 1 mol % Nile red, the dye was incorporated into

the polymersome hydrophobic bilayer during the self-assembly process noted above, which enabled facile visualization of resultant copolymer aqueous morphology via confocal fluorescence microscopy.

Small (< 300 nm diameter) unilamellar polymersomes that possess appropriately narrow size distributions were prepared via procedures analogous to those used to formulate small lipid vesicles (sonication, freeze-thaw extraction, and extrusion). The sonication procedure involved placing a sample vial containing the aqueous-based solution and a dried thin-film formulation (of polymer uniformly deposited on Teflon) into a bath sonicator (Fischer Scientific; Model FS20) with constant agitation for 30 min. Several cycles of freeze-thaw extraction were carried out by placing the sample vials (containing solutions of 300-500 nm diameter polymersomes) in liquid N_2. The vials were then transferred to a 60 ℃ water bath, and extruded to give a mono-dispersed suspension of small (100 nm diameter) vesicles; this was accomplished through the introduction of a polymersome solution into a thermally controlled stainless steel cylinder connected to pressurized nitrogen gas. The size distributions of the PEO-b-PCL suspensions were determined in each case by dynamic light scattering.

For the co-solvent/water extraction method, the PEO-b-PCl diblock copolymers were dissolved in chloroform or THF (at 10 mg/mL) and introduced at 1:100 vol% into aqueous solution (sucrose, PBS or benzene/alcohol aqueous solution) via organic co-solvent injection. The various structures formed from these diblock copolymers were extracted from the solvent mixture by aqueous dialysis (for organic co-solvent removal) at room temperature for 24 h.

4.3.1.5. Characterization of Sample Morphology in Dilute Aqueous Solution

Confocal laser scanning microscopy (BioRad Radiance 2000) and epifluorescent optical microscopy (Zeiss Axiovert 200) were employed to characterize the self-assembled aqueous morphologies of the biodegradable polymer compositions that featured dispersed Nile Red (1:99 dye:polymer). The instruments were equipped with appropriate excitation and emission filters for these experiments.

Nanometric functionalized polymersomes were formulated as described above. Vitreous samples were prepared within a controlled environment vitrification system (Vitrobot). A droplet of solution (10 ul) was deposited on a copper TEM grid coated with a porous polymer film. A thin film (< 300 nm) was obtained by blotting with filter paper. After allowing the sample sufficient time to relax from any residual stresses imparted during blotting (30 s), the grid was plunge cooled in liquid ethane at its freezing point (-180 °C), resulting in vitrification of the aqueous film. Sample grids were examined in a FEI Tecnai G²Twin transmission electron microscope operating at 200 kV, and images were recorded with a Gatan 724 multiscan digital camera.

4.3.2. Vinyl Sulfone Functionalization of PEO-*b*-PCl Diblock Copolymers

The PEO tosylation, displacement of tosylated PEO with thioacetate and deprotection to thiol, and the final divinyl sulfone attachment to PEO polymer is following the procedures previously described.[76]

4.3.2.1. Tosylation of PEO
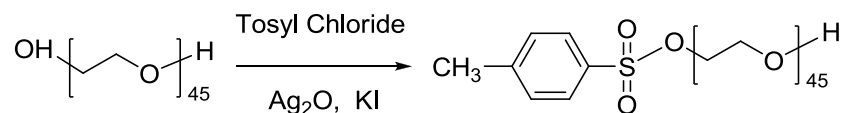
Scheme 4.3 Synthesis of monotosylated PEO.

Dihydroxy terminated PEO with molecular weight 2 kg/mol (10 g, 5 mmol) was dissolved in 200 mL dry CH_2Cl_2 and chilled to 0 °C. Ag_2O (1.75 g, 7.5 mmol) synthesized from aqueous NaOH and $AgNO_3$ was added to the chilled PEO under vigorous stirring followed by addition of KI (0.6 g, 3.6mmol) and p-toluenesulfonyl chloride (1.5 g, 7.8 mmol). The reaction mixture was stirred rapidly for 2 h at 0 °C, filtered over Celite, and reduced under vacuum to a white solid. The solid was then dissolved in 75 mL H2O, filtered, extracted into 50 mL CH_2Cl_2 three times, dried over $MgSO_4$, and precipitated into ice-cold diethyl ether. Residual solvent was removed from the resulting white solid under vacuum. The yield is 95% and the tosylation degree determined by ^{1}H NMR is 90%.

4.3.2.2. Displacement with Thioacetate and Deprotection to Thiol
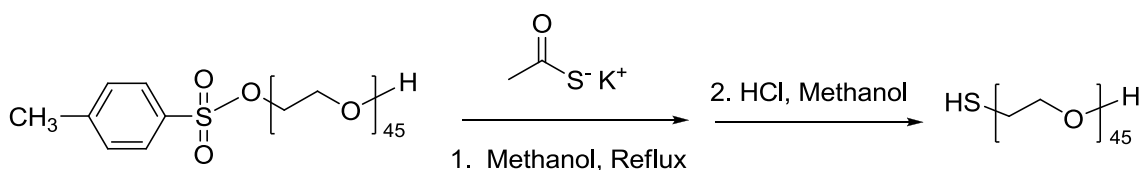
Scheme 4.4 Synthesis of monothiol-PEO.

Potassium thioacetate (5.1 g, 50 mmol) was dissolved in 125 mL dry N,N-dimethylformamide (DMF) and the mixture was added to tosylated PEO from the previous reaction (9.5 g, 4.75 mmol) and stirred until no solid was visible. The mixture was degassed by three freeze-pump-thaw cycles, backfilled with nitrogen, and allowed to react under stirring for three days at 35 °C. DMF was removed by vacuum distillation, the residue was dissolved in 200 mL H_2O, filtered, extracted three times with 60 mL CH_2Cl_2 and dried over $MgSO_4$. Volume was then reduced under vacuum and polymer

precipitated into ice-cold diethyl ether followed by solvent removal under reduced pressure. The PEO thioacetate (8.5 g, 4.25 mmol) was dissolved in 150 mL methanol containing 150mM potassium methoxide and stirred at room temperature for 1.5 h. The mixture was subsequently acidified with HCl, filtered, and solvent removed under vacuum. To reduce disulfide bonds the residue was dissolved in 300 mL of 0.1 M aqueous sodium bicarbonate to which was then slowly added sodium borohydride to 0.1 M (1.13 g, 29 mmol) followed by stirring under a nitrogen atmosphere. The solution was then acidified to pH 3 by dropwise addition of HCl, extracted three times into 50 mL CH_2Cl_2, dried over MgSO4, volume reduced under vacuum, and precipitated into ice-cold diethyl ether. The reduction–precipitation step was performed twice to yield a light-yellow solid. The yield is 75%, and the thiol modification degree is ~100% determined by ^{1}H NMR.

4.3.2.3. Divinyl Sulfone Attachment
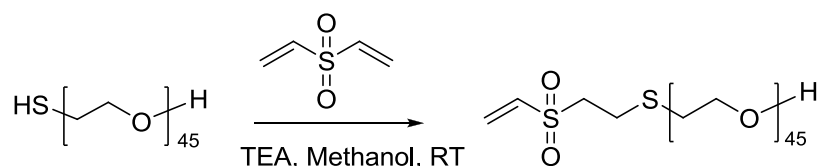
Scheme 4.5 Synthesis of vinyl sulfone terminated PEO.

Thiol-terminated PEO (2.0 g, 1 mmol) was dissolved in 50 mL tetrahydrofuran (THF) containing triethylamine (700 mL, 5 mmol) and degassed by three freeze-pump-thaw cycles. A small amount of dithiothreitol (DTT) (38 mg, 0.25 mmol) was added under nitrogen atmosphere to reduce any residual disulfide bonds and the reaction was allowed to stir for 1 h. Divinyl sulfone (DVS) (5 mL, 50 mmol) was then added rapidly under vigorous stirring. The reaction vessel was capped and allowed to react for 18 h at

room temperature. The solution was then reduced in volume under vacuum, precipitated three times into ice-cold diethyl ether and solvent removed under vacuum. The yield is 86%, and the thiol modification degree is 81% determined by ^{1}H NMR.

4.3.2.4. Polymerization of CL
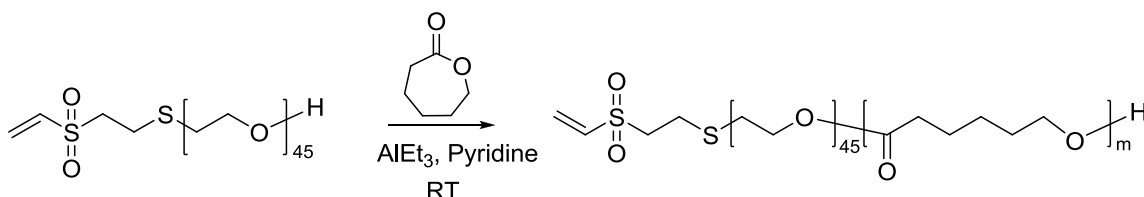
Scheme 4.6 Synthesis of vinyl sulfone terminated PEO-PCl diblock copolymer.

To a solution of VS-PEO (1.5 g, 0.75 mmol) in 50 mL of dichloromethane under nitrogen, AlEt$_3$ (1.9 M solution, 750 μL, 1.4 mmol) and pyridine (100 μL, 1.2 mmol) were added. The reaction mixture was stirred vigorously at room temperature for 3 h. Next, different amount of caprolactone was added into the reaction mixture, and the solution was allowed to react at room temperature for 42 h. The polymerization was quenched by adding 2 equivalent of HCl (1M solution) and the solution was poured in excess of methanol. Finally, the functionalized diblock copolymer (3.4 g) was isolated by precipitation three times over methanol. ^{1}H NMR showed the final VS functional degree is 60-68%.

4.4. Results and Discussion

4.4.1. Synthesis and Characterization of Biodegradable PEO-b-PCL Diblock Copolymers

A series of PEO-*b*-PCL diblock copolymers were synthesized via ring-opening polymerization (**Scheme 4.1**) of ε-caprolactone and commercially available MePEO (M$_n$

= 750, 1100, 2000 and 5000). MePEO homopolymers bearing one hydroxyl end group were used as the macroinitiator to activate polymerization (130 °C, 24 h) of ε-caprolactone monomer (ε-CL) in the presence of catalyst (stannous (II) octoate, SnOct$_2$). Such PEO-b-PCL diblock copolymers have been previously synthesized under a variety of catalyzed[21][77-79] and non-catalyzed conditons.[80, 81] Of the previously established catalysts, SnOct$_2$ is the most widely used for the production of biodegradable polyesters, as it is commercially available, easy to handle, soluble in common organic solvents and neat liquids (e.g., cyclic ester monomers), and is a permitted food additive in numerous countries.[82] For these reasons, coupled with the fact that non-catalyzed ring-opening polymerization of ε-CL must be carried out at high temperature (≥180°C) over long time periods (days), SnOct$_2$ was employed as the catalyst in the synthesis of these PEO-b-PCL copolymers (**Table 4.1**).

Although the synthesis of PEO-b-PCL copolymers from MePEO via ring-opening polymerization of ε-caprolactone is facile, the availability of MePEO homopolymers is limited. As such, we utilized anionic living polymerization of ethylene oxide monomers to produce PEOs of varying M_w; subsequent caprolactone polymerization yields PEO-b-PCL copolymers having a diverse range of number-average molecular weights (M_n: 3.6 - 57K) and PEO weight fractions (f_{PEO}: 0.08-0.33). An additional advantage of this approach is the fact that the copolymers' terminal PEO end group can be easily varied (**Scheme 4.2**). Ethylene oxide polymerization reactions utilized cyanomethyl potassium as the protected initiator, which was prepared by metalation of acetonitrile with potassium naphthalenide in THF.[69, 83-85] While anionic living polymerization had been utilized previously in the syntheses of low molecular weight, high PEO weight fraction

PEO-*b*-PCL copolymers [e.g., PEO(2.2K)-*b*-PCL(1.2K)],[85] this strategy provides PEO-*b*-PCL copolymers that possess a diverse range of PEO block molecular weights (1500, 2600, 3000, 3800, and 5800), low PEO weight fractions (f_{PEO}: 0.10-0.23), and a wide range of diblock M_n (7.8-47K).

^{1}H NMR spectroscopy was utilized to characterize the number-average molecular weight of the PEO homopolymers and the corresponding PEO-*b*-PCL diblock copolymers.[21, 77-81, 84] A typical ^{1}H NMR spectrum for MePEO-*b*-PCL is shown in **Figure 4.1**. The appearance of a resonance at ~4.20 ppm (b'), consistent with the terminal methylene end group of the PEO block in the ^{1}H NMR spectrum, indicates that the final reaction products were limited to only diblock copolymers of PEO and PCL. The sharp weak resonance at 3.38 ppm and the intense peak at 3.65 ppm correspond to methyl (a, CH_3O- terminated PEO) and methylene groups (b, repeat unit of MePEO), respectively. Resonances at 2.23 ppm, 1.63 ppm, 1.38 ppm and 4.06 ppm were assigned to protons in PCL repeat units (c, d, e, and f methylene). The peak at 3.65 ppm (the methylene proton signal for the PEO block) and the triplet at 2.23 ppm, (the methylene proton signal of the caprolactone repeating units, b, $COCH_2CH_2CH_2CH_2CH_2O$), were used to establish the degree of PCL block polymerization and M_n. ^{1}H NMR spectroscopy was further utilized to characterize the number-average molecular weight of PEO from the calculated ethylene oxide repeat unit number, by comparison of the integrated intensities of the resonances that corresponded to of the end groups (i.e. CH_3O- or $CNCH_2CH_2$-). The key difference between the ^{1}H NMR spectra of CN-PEO-*b*-PCL and MePEO-*b*-PCL diblock copolymers evident is highlighted by the two weak signals around 2.50 ppm which correspond respectively to α- and β-CH_2 groups at the diblock copolymer CN terminus.

Number-average molecular weight values of CN-PEO-*b*-PCL diblock copolymers were also calculated from the NMR spectra.

GPC was employed to characterize the molecular weight (M_w) and molecular weight distribution (M_w/M_n) (PDI) of each PEO-*b*-PCL diblock copolymer formulation. Two types of weight-average molecular masses were calculated from refractive index data using PEO standard samples and dynamic light scattering data (**Table 4.2**). Some copolymers, such as PEO(5.8K)-*b*-PCL(24K), PEO(5K)-*b*-PCL(22K), PEO(2K)-*b*-PCL(12K), and PEO(2K)-*b*-PCL(15K), exhibited similar GPC and ^{1}H NMR determined molecular weight values; in contrast, PEO(5.8K)-*b*-PCL(33.6K) and PEO(2K)-*b*-PCL(9.5K), the largest and smallest M_w copolymers synthesized, respectively, showed significant differences between ^{1}H NMR and GPC based M_w determinations. As PEO-*b*-PCL diblock copolymer standard samples are not commercially available for the calibration of RI data (GPC), the d_n/d_c values of the copolymers were calculated from internal instrument parameters calibrated from a PS standard sample; these values were then used to calculate M_w values from the DLS data. The use of polystyrene-based M_w standards likely accounts for the differences in determined GPC and ^{1}H NMR M_w at the extremes of the copolymer M_w range.

GPC data indicate that PEO-*b*-PCL diblock copolymers synthesized by anionic living polymerization having PEO molecular weights of 2600, 3000, 3800 and 5800, exhibited the narrowest molecular weight distributions (PDI: 1.2-1.27). PEO-*b*-PCL diblock copolymers synthesized from PEO(2K) via ring-opening polymerization showed narrow molecular weight distributions (PDI: 1.1-1.2) while copolymers derived from PEO(5K) displayed slightly wider distributions (PDI: 1.32-1.37). Anionic living

polymerization therefore provides the best route for synthesizing of PEO-*b*-PCL diblock copolymers with controlled PEO chain lengths, modulating PEO/PCL block ratios, and isolating block copolymers with narrow molecular weight distributions.
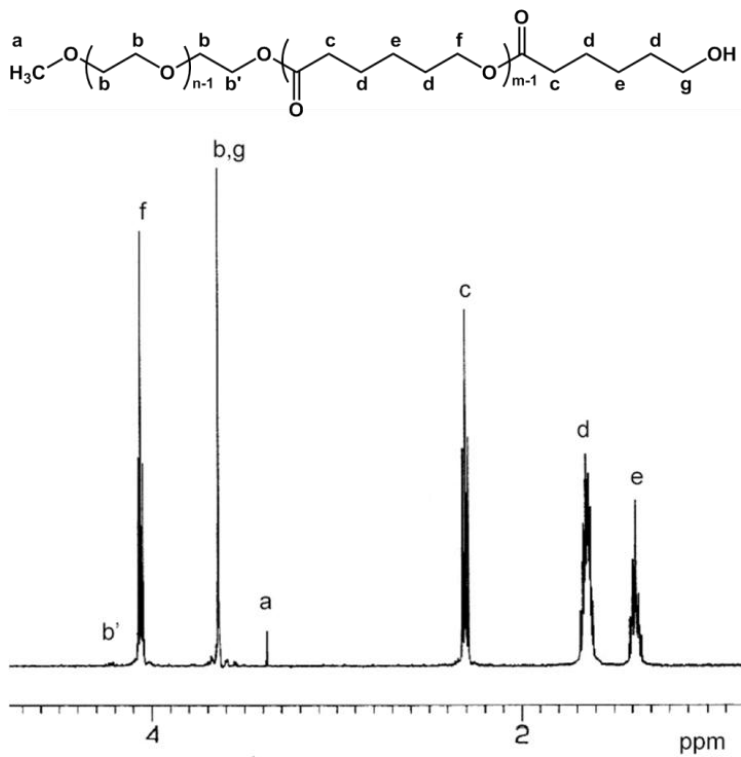
Figure 4.1 Representative ^{1}H NMR spectrum of PEO-*b*-PCL diblock copolymer.

Table 4.1 Self-Assembled Morphologies Asessed via Microsopic Studies of PEO-b-PCL

Diblock Copolymers (PEO: 0.75-5.8K) in Aqueous Media Prepared via Film Hydration.

PEO-*b*-PCL Copolymers[a]	f_{PEO}[b]	Morphologies[c]	Vesicle Yield[d]
PEO(5.8k)-*b*-PCL(22k)	0.21	Irregular particles	0
PEO(5.8k)-*b*-PCL(23.8k)	0.20	Microspheres, irregular particles	0
PEO(5.8k)-*b*-PCL(24k)	0.19	Microspheres, irregular particles	0
PEO(5.8k)-*b*-PCL(30.2k)	0.16	Irregular particles	0
PEO(5.8k)-*b*-PCL(33.6k)	0.15	Irregular particles	0
PEO(5.8k)-*b*-PCL(37.7k)	0.13	Irregular particles	0
PEO(5.8k)-*b*-PCL(41.2k)	0.12	Irregular particles	0
PEO(5k)-*b*-PCL(10k)	0.33	Irregular particles	0
PEO(5k)-*b*-PCL(16k)	0.24	Irregular particles	0
PEO(5k)-*b*-PCL(22k)	0.18	Irregular particles	0
PEO(5k)-*b*-PCL(26k)	0.16	Irregular particles	0
PEO(5k)-*b*-PCL(32k)	0.14	Irregular particles	0
PEO(5k)-*b*-PCL(52k)	0.09	Irregular particles	0
PEO(3.8k)-*b*-PCL(17k)	0.18	Polymersomes, irregular particles	30-50%
PEO(3.8k)-*b*-PCL(17.7k)	0.17	Polymersomes, irregular particles	10-20%
PEO(3.8k)-*b*-PCL(20k)	0.16	Polymersomes, irregular particles	10-20%
PEO(3.8k)-*b*-PCL(22.2k)	0.15	Polymersomes, irregular particles	<5%
PEO(3k)-*b*-PCL(16.5k)	0.15	Polymersomes, irregular particles	10-20%
PEO(3k)-*b*-PCL(19k)	0.14	Polymersomes, irregular particles	<5%
PEO(3k)-*b*-PCL(20.5k)	0.13	Irregular particles	0
PEO(3k)-*b*-PCL(24.7k)	0.11	Irregular particles	0
PEO(3k)-*b*-PCL(25.8k)	0.10	Irregular particles	0
PEO(2.6k)-*b*-PCL(11.2k)	0.19	Polymersomes, irregular particles	60-80%
PEO(2.6k)-*b*-PCL(12.3k)	0.17	Polymersomes, irregular particles	30-50%
PEO(2.6k)-*b*-PCL(13.9k)	0.16	Polymersomes, irregular particles	10-20%
PEO(2.6k)-*b*-PCL(15.5k)	0.14	Polymersomes, irregular particles	10-20%
PEO(2k)-*b*-PCL(7.4k)	0.27	Irregular particles	10-20%
PEO(2k)-*b*-PCL(9.5k)	0.17	Polymersomes, irregular particles	60-80%
PEO(2k)-*b*-PCL(12k)	0.14	Polymersomes	~100%
PEO(2k)-*b*-PCL(15k)	0.12	Polymersomes, irregular particles	30-50%
PEO(2k)-*b*-PCL(22k)	0.08	Irregular Particles	0
PEO(1.5k)-*b*-PCL(6.3k)	0.19	Microspheres, irregular particles	0
PEO(1.5k)-*b*-PCL(10.4k)	0.13	Irregular particles	0
PEO(1.5k)-*b*-PCL(12.4k)	0.11	Irregular particles	0
PEO(1.5k)-*b*-PCL(13.7k)	0.10	Irregular particles	0
PEO(1.1k)-*b*-PCL(2.9k)	0.27	Irregular particles	0
PEO(1.1k)-*b*-PCL(3.7k)	0.23	Microspheres, irregular particles	0
PEO(1.1k)-*b*-PCL(6.3k)	0.15	Microspheres, irregular particles	0

PEO(1.1k)-b-PCL(7.0k)	0.14	Microspheres, irregular particles	0
PEO(1.1k)-b-PCL(7.7k)	0.12	Irregular particles	0
PEO(1.1k)-b-PCL(9.5k)	0.10	Irregular particles	0
PEO(1.1k)-b-PCL(13.0k)	0.08	Irregular particles	0
PEO(0.75)-b-PCL(2850)	0.21	Irregular particles	0
PEO(0.75)-b-PCL(5790)	0.11	Irregular particles	0
PEO(0.75)-b-PCL(9k)	0.07	Irregular particles	0

[a] Number-average molecular weight of PEO-b-PCL diblock copolymers as determined by ^{1}H NMR spectroscopy. [b] Weight fraction of the PEO block as determined by ^{1}H NMR data. [c] Determined qualitatively from fluorescence confocal and laser optical microsopic studies of the self-assembled structures formed from thin film rehydration of 50:1 copolymer: Red Nile films. Observed polymersome and irregularly shaped particle diameters ranged from less than 1 μm to greater than 30 μm; microsphere diameters ranged from ~5-30 μm. [d] Approximate yield of polymer vesicles visually estimated from fluorescence confocal and laser optical microsopic studies qualitatively by comparison of the morphological fraction corresponding to polymersomes in aqueous solution.

Table 4.2 GPC and ^{1}H NMR Characterization Data for PEO-*b*-PCL Diblock Copolymers.

PEO-*b*-PCL Copolymers[a]	f_{PEO}[b]	M_n[b]	M_w[c]	PDI[c]	M_w[d]
PEO(5.8k)-*b*-PCL(24k)	0.20	29800	27800	1.24	28100
PEO(5.8k)-*b*-PCL(33.6k)	0.15	39400	28500	1.20	31100
PEO(5k)-*b*-PCL(22k)	0.18	27000	25300	1.37	24000
PEO(5k)-*b*-PCL(26k)	0.16	31000	31400	1.32	36200
PEO(3.8k)-*b*-PCL(17k)	0.18	20800	15100	1.20	18900
PEO(3.8k)-*b*-PCL(20k)	0.16	23800	17600	1.25	19100
PEO(3.8k)-*b*-PCL(22.2k)	0.15	26000	19200	1.26	22100
PEO(3k)-*b*-PCL(16.5k)	0.15	19000	16700	1.23	17300
PEO(3k)-*b*-PCL(19k)	0.14	22000	19400	1.24	19400
PEO(2.6k)-*b*-PCL(11.2k)	0.19	13800	16200	1.27	19000
PEO(2.6k)-*b*-PCL(12.3k)	0.17	14900	17300	1.25	20600
PEO(2.6k)-*b*-PCL(15.5k)	0.14	18100	19600	1.25	24100
PEO(2k)-*b*-PCL(9.5k)	0.17	11500	12500	1.14	16300
PEO(2k)-*b*-PCL(12k)	0.14	14000	13700	1.21	15400
PEO(2k)-*b*-PCL(15k)	0.12	17000	16100	1.21	18300

[a] Number-average molecular weight of PEO-b-PCL diblock copolymers as determined by ^{1}H NMR spectroscopy. [b] Weight fraction of the PEO block as determined by ^{1}H NMR data. [c] Polydispersity index and weight-average molecular weight of PEO-b-PCL diblock copolymers as determined from dynamic light scattering (DLS) data of samples analyzed by gel permeation chromatography (GPC). [d] Weight-average molecular weight of PEO-b-PCL diblock copolymers calculated from refractive index (RI) data of samples analyzed by gel permeation chromatography using PEO standard samples as calibrants.

4.4.2. Aqueous Assembly of Meso-scale PEO-*b*-PCL Diblock Copolymers

Two preparation methods, film hydration and organic co-solvent injection/extraction, were chosen to assemble meso-scale amphiphilic PEO-*b*-PCL diblock copolymers into their equilibrium aqueous morphologies. While both methods produced similar results, as film hydration promotes aqueous self-assembly of the copolymers, is amenable to large-scale preparation while obviating the need for post-assembly processing, this technique was used to generate the data summarized in **Table 4.1**, which describe the observed aqueous morphologies for the comprehensive set of PEO-*b*-PCL diblock copolymers that were fabricated. The equilibrium aqueous morphologies for each PEO-*b*-PCL diblock copolymer were determined using fluorescence confocal and optical microscopies under conditions where 1 mol% Nile red was incorporated into the resultant structures.

Meso-scale polymersomes were obtained uniquely, in near quantitative yield from aqueous hydration and self-assembly of the PEO(2K)-*b*-PCL(12K) diblock copolymer ($f_{PEO} = 0.14$), as shown in **Figure 4.2**. These polymersomes possessed both multilamellar (**Figure 4.2c**) and unilamellar (**Figure 4.2d**) bilayer structures. In constrast, polymersomes were found to coexist with irregular particles in aqueous preparations of PEO(2-3.8K)-*b*-PCL diblock copolymers with f_{PEO} ranging between 0.12 and 0.19. In aqueous suspensions of PEO-*b*-PCL diblock copolymers derived from higher (5-5.8K) or lower (0.75-1.5K) molecular weight PEO blocks, no polymersomes were observed regardless of the PEO/PCL ratio. Note that Disher et al. have also studied the meso-scale morphologies of a series of PEO-*b*-PCL diblock copolymers by using solvent evaporation method.[86] And our results by using thin-film hydration preparation method correspond

well with their observations on the trend of the ability of diblock copolymer compositions to self-assemble into vesicle structures.

In order to elucidate the effects of diblock copolymer molecular weight distribution on vesicle formation, PEO-*b*-PCL diblock copolymers with varying PEO block size (2600, 3000 or 3800) and narrow molecular distributions (PDI = 1.1) were separated by GPC and used to generate polymersomes. No further improvement in the yield of vesicles from these samples was observed relative to the samples with the same molecular weight but broader molecular distributions (PDI: 1.2-1.4). Furthermore, the ability of PEO-b-PCL diblock copolymers mixtures which have much wider molecular weight distributions to self-assemble into polymersomes is also assessed by scanning laser confocal microscopy. As shown in **Figure 4.3**, polymersomes can be obtained at a very high yield from these copolymer mixtures, indicates the molecular weight distribution had little influence on biodegradable polymersomes formation from involving PEO(2K)-*b*-PCL(12K) diblock copolymers.

As PEO-*b*-PCL diblock copolymers with low PEO weight fractions (<0.12) were found to be strongly adherent to the Teflon film (following aqueous hydration), an organic co-solvent water injection/extraction method was employed in an attempt to prepare polymersomes from a small subset of these copolymers. While no polymersomes were obtained by this extraction method, porous spherical particles were seen upon organic co-solvent removal via dialysis; the typical morphology of these particles is depicted in the fluorescent micrograph (**Figure 4.4**). These Nile Red encapsulated spherical particles possess porous surfaces as directly visualized by scanning laser confocal microscopy (**Figure 4.4b**), with the bright regions corresponding to the

emission of encapsulated Nile Red fluorophores in the polymersomes bilayer membrane alternate with dark regions of the porous surface without Nile Red encapsulation. Note that, while PEO(5.8K)-*b*-PCL(24K) has been previously shown to form meso-scale vesicles via a solvent injection technique,[21] no polymersomes were observed in aqueous suspensions of this diblock (PDI = 1.2) formed via thin-film hydration.

Table 4.3 Comparative Self-Assembled Meso-Scale Morphologies of PEO-*b*-PCL Diblock Copolymers in Aqueous Suspensions Obtained via Film Hydration and Organic Co-Solvent Injection/Extraction Methods.

PEO-*b*-PCL Copolymers [a]	f_{PEO} [b]	Morphologies Observed from Film Hydration[c]	Morphologies Observed from Organic Co-Solvent Injectiona/Extraction[c]
PEO(5k)-*b*-PCL(10k)	0.33	Irregular particles	Small particles
PEO(5k)-*b*-PCL(16k)	0.24	Irregular particles	Small particles
PEO(5k)-*b*-PCL(22k)	0.18	Irregular particles	Microspheres[e]
PEO(5k)-*b*-PCL(52k)	0.09	Irregular particles	Microspheres[e]
PEO(2k)-*b*-PCL(15k)	0.12	Polymersomes,[d] irregular particles	Microspheres[e]
PEO(2k)-*b*-PCL(22k)	0.08	Irregular particles	Microspheres[e]

[a] Number-average molecular weight of PEO-*b*-PCL diblock copolymers as determined by ^{1}H NMR spectroscopy. [b] Weight fraction of the PEO block as determined by ^{1}H NMR data. [c] Determined qualitatively from fluorescence confocal and laser optical microsopic studies of the self-assembled structures formed from thin film rehydration of 50:1 copolymer: Red Nile films. Observed polymersome and irregularly shaped particle diameters ranged from less than 1 μm to greater than 30 μm; microsphere diameters ranged from ~5-30 μm. [d] Less than 5% of the observed morphologies corresponded to polymersomes. [e] Formed quantitatively.
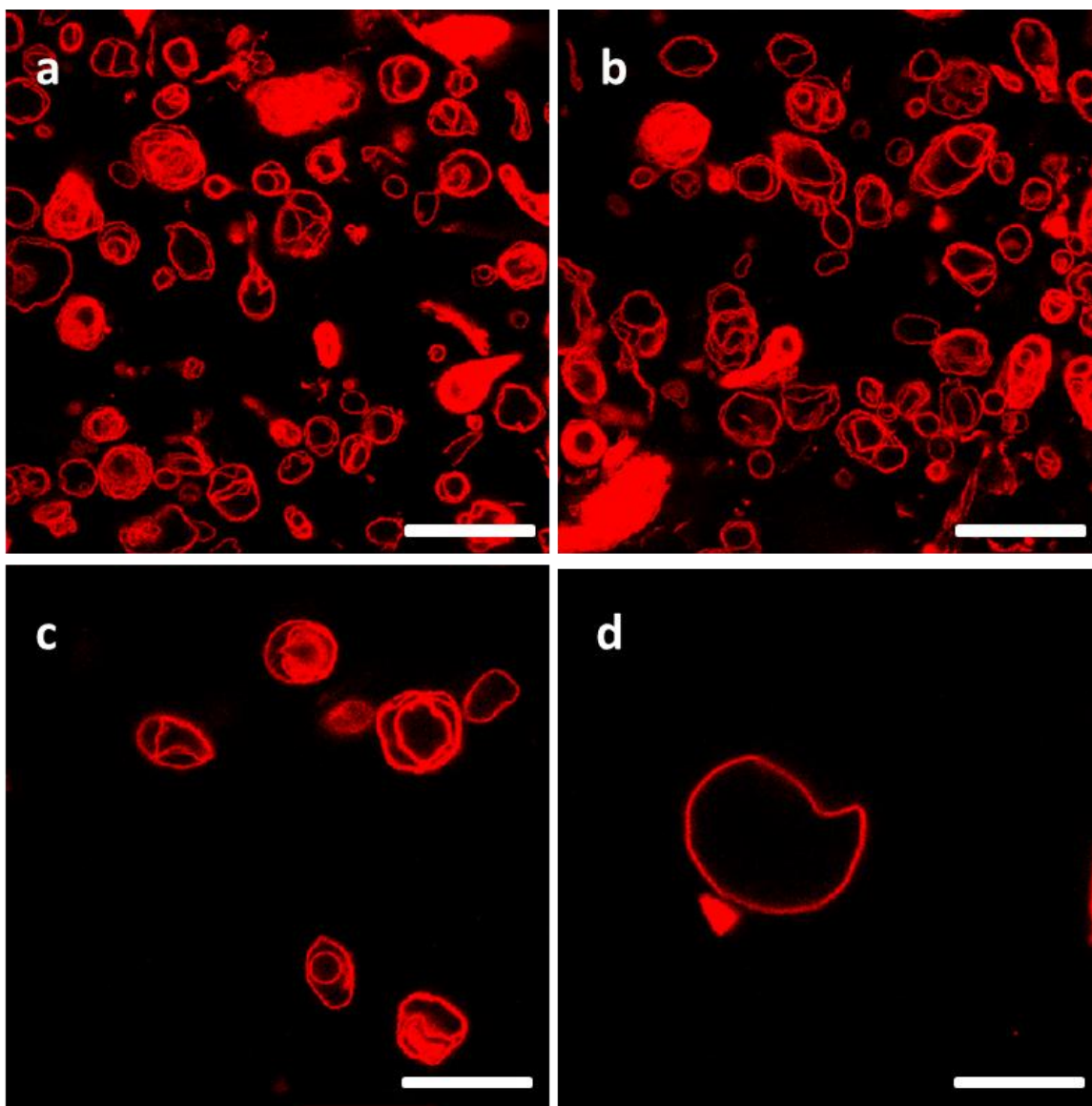
Figure 4.2 Scanning fluorescence confocal micrographs (λ_{ex} = 488 nm) of PEO(2K)-*b*-PCL(12K)-based vesicles, containing membrane-encapsulated Nile Red (peak emission = 603 nm) in DI water at 25 ° C, that display continuous spherical morphology but jagged edges supportive of solid vesicle membranes. Scale bar = 5 μm.
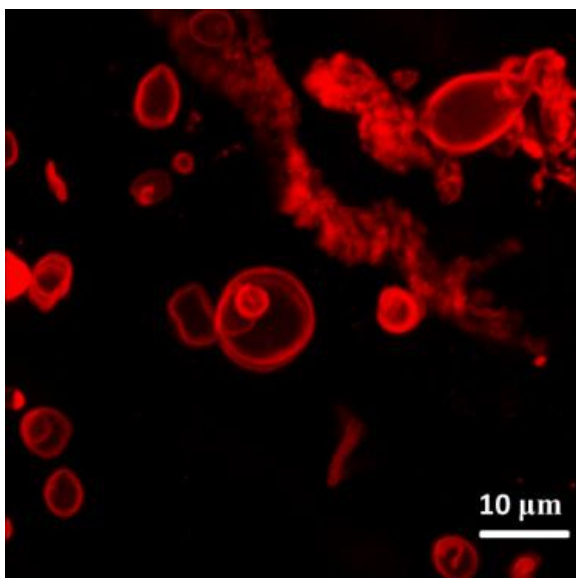
Figure 4.3 Scanning fluorescence confocal micrograph (λ_{ex} = 488 nm) of polymersomes comprised of a 1:1:1 mixture of PEO(2k)-*b*-(9.5k), PEO(2k)-*b*-(12k), and PEO(2k)-*b*-PCL(15k), containing membrane-encapsulated Nile Red (peak emission = 603 nm) in DI water at 25 °C.
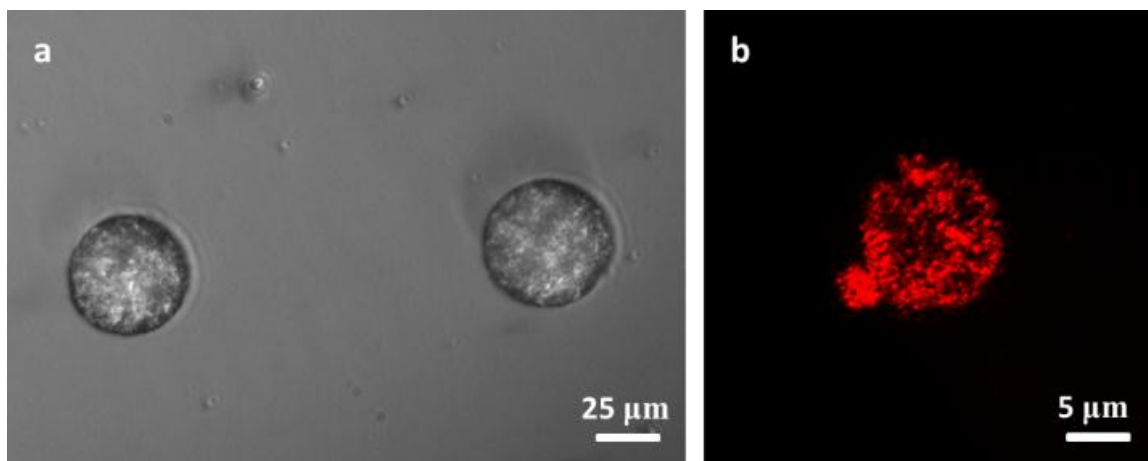
Figure 4.4 Microspheres imaged using (a) optical microscopy and (b) confocal fluorescence micrograph (λ_{ex} = 488 nm) derived from organic co-solvent extraction of PEO(5k)-*b*-PCL(52k) containing membrane-encapsulated Nile Red (peak emission = 603 nm) in DI water at 25 °C.

4.4.3. Aqueous Assembly of Nano-scale PEO-*b*-PCL Diblock Copolymers

Small, nano-scale polymersomes can be made by aqueous sonication of a dry thin-film formulation of PEO-*b*-PCL on Teflon followed by several cycles of freeze/thaw extraction. A number of diblock copolymers (**Figure 4.5** and **Figure 4.6**) were selected to prepare nano-sized self-assembles to check the effect of both hydrophilic fraction and PEO chain on the formation of vesicles. OL 1-6 are PEO-*b*-PCL diblock copolymers with the same PEO chain length (2K) but different hydrophilic PEO weight fraction, while OL A-E are PEO-*b*-PCL diblock copolymer with the same PEO weight fraction but different PEO chain length. Solution morphologies were characterized with Cryo-TEM which allows for direct visualization of the aggregate nano-sized structures formed in aqueous solution.

Very different from the meso-scale diblock copolymer particle morphologies, polymersomes constitute the dominant self-assembled nano-scale morphology. As seen in **Figure 4.5**, an increase in the molecular weight of the PCL core block, and subsequent decrease in the diblock PEO weight fraction to 0.08, results in the shape transition from bilayer vesicle structures to micellar aggregates. Through the increasing length of PCL block, the hydrophobic content of the amphiphile is increased and the interfacial curvature is decreased, which leads to the development of micelles morphologies. **Figure 4.5** shows a set of fairly uniform spherical vesicle structures formed from PEO(2K)-*b*-PCL diblock copolymers with f_{PEO} ranging from 0.14 to 0.21. The coexistence of micelles appears when the f_{PEO} is below 0.14. And for PEO-*b*-PCL diblock copolymers with a fixed f_{PEO} (~15%), a change in PEO chain length reveals diblock self-assembly into micellar and large particle aggregates. In **Figure 4.6**, micelles formed with the PEO

molecular weight lower than PEO(1.1K) or higher than PEO(3K) are clearly visible. The reduced PEO weight fractions of these polymersome-forming PEO-b-PCL compositions (f_{PEO}: 0.14-0.21) contrast sharply to the PEO-polybutadiene diblock formulations (f_{PEO}: 0.28-0.39),[87] and suggest the low PEO weight fraction to be a common theme for polymersomes generated from diblock copolymers that exploit PCL as a biodegradable hydrophobic block. This is because the strength of segregation of polybutadiene with considerably exceeds that of polycaprolactone.[86]

It is well known that the morphology of diblock copolymer assemblies is determined by the interfacial curvature,[86, 88-90] and previous work reveals that the surface elasticity of vesicle bilayer membranes is scale independent and only depends on the interface.[4, 87] Therefore, people would expect by examining the meso-scale morphology of diblock copolymers self-assemblies, it will lead to predictive insights of the nano-scale morphology. However, our nano-scale experiment results show a very distinctive trend from expectation that the diblock polymers that could not form meso-scale vesicles may be able to self-assemble into high yield of nano-scale vesicles. This evolution of structures change formed from the self-assembly of meso-scale or nano-scale PEO-b-PCL diblock copolymers in aqueous solution is very interesting. And this paper is the first example looking at this morphology transition. The reason for this morphology transition might be due to the decreased nano-scale polymersomes particle size which results in increased total surface area and decreased surface tension, core-chain stretching and the corona chain repulsion as compared to the meso-scale polymer vesicles and thus cause the change of interface curvature required for vesicle structure formation accordingly.

The effect of PEO molecular weight and PEO weight fraction on membrane thickness has also been measured for these PEO-*b*-PCl diblock copolymers in **Figure 4.5** and **Figure 4.6**. As we expected, for OL A-E which are PEO-PCL diblock copolymer with the same PEO weight fraction but different PEO molecular weight, a linear increasing of the membrane thickness is observed with the increasing of the polymer molecular weight. However, surprisingly, for OL 1-6 which are PEO-PCL diblock copolymers with the same PEO molecular weight (2K) but different PEO weight fraction, varying in the hydrophobic PCL block molecular weight doesn't result in the change of membrane thickness. Therefore, for a fixed hydrophilic PEO block length, the membrane thickness is not dependent on the hydrophobic PCL block density. We have not observed such phenomenon in any other amphiphilic diblock copolymer systems. More experiments are now undergoing to try to explain this membrane thickness independence on PCL block weight fraction.
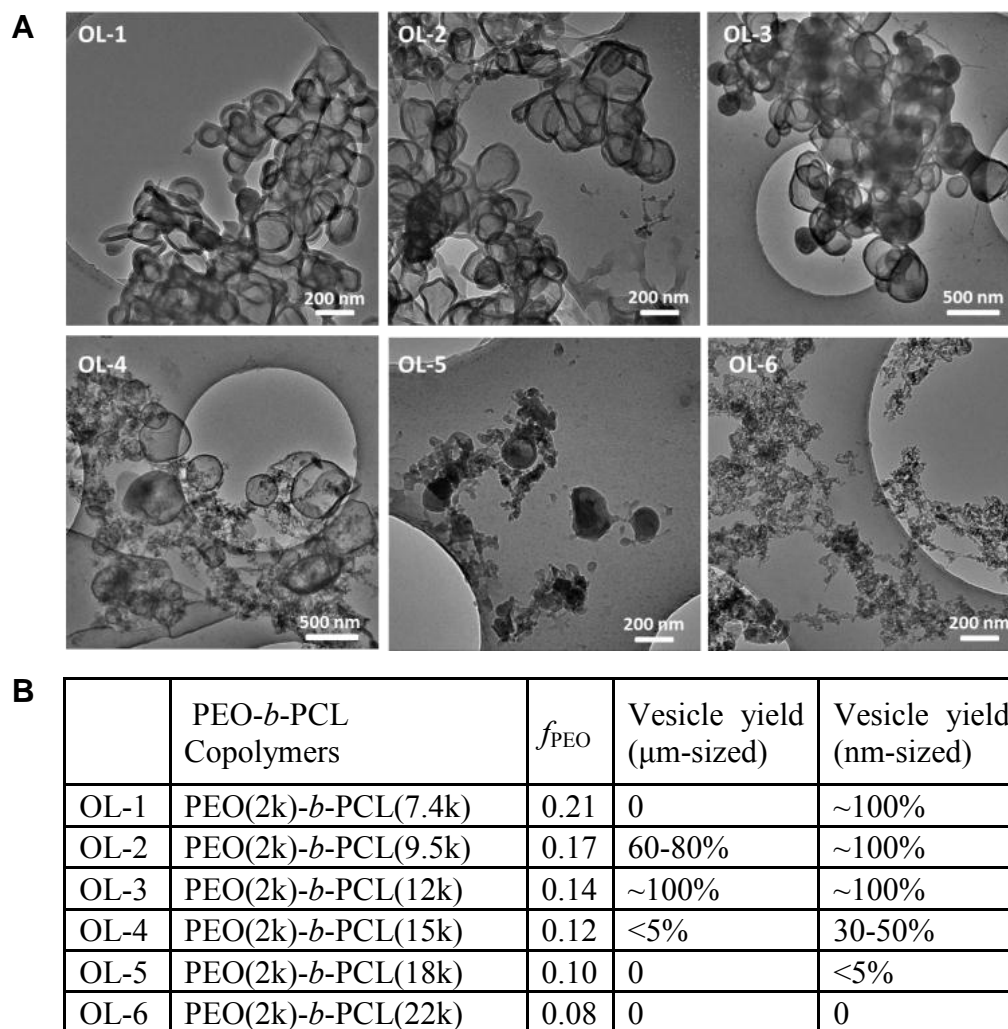
Figure 4.5 (A) Cryo-TEM images of nano-scale PEO-*b*-PCL diblock copolymers OL 1-6 particles in aqueous suspensions obtained via film hydration and subsequent self-assembly; (B) Morphology of self-assembled meso- and nano-scale structures derived from PEO-*b*-PCL diblock copolymers OL 1-6.

	PEO-*b*-PCL Copolymers	f_{PEO}	Vesicle yield (μm-sized)	Vesicle yield (nm-sized)
OL-A	PEO(1.1k)-*b*-PCL(6.3k)	0.15	0	60-80%
OL-B	PEO(2k)-*b*-PCL(12k)	0.14	~100%	~100%
OL-C	PEO(2.6k)-*b*-PCL(15.5k)	0.14	10-20%	~100%
OL-D	PEO(3k)-*b*-PCL(16.5k)	0.15	10-20%	40-50%
OL-E	PEO(3.8k)-*b*-PCL(22.2k)	0.15	<5%	10-20%
OL-F	PEO(5k)-*b*-PCL(27k)	0.15	0	0
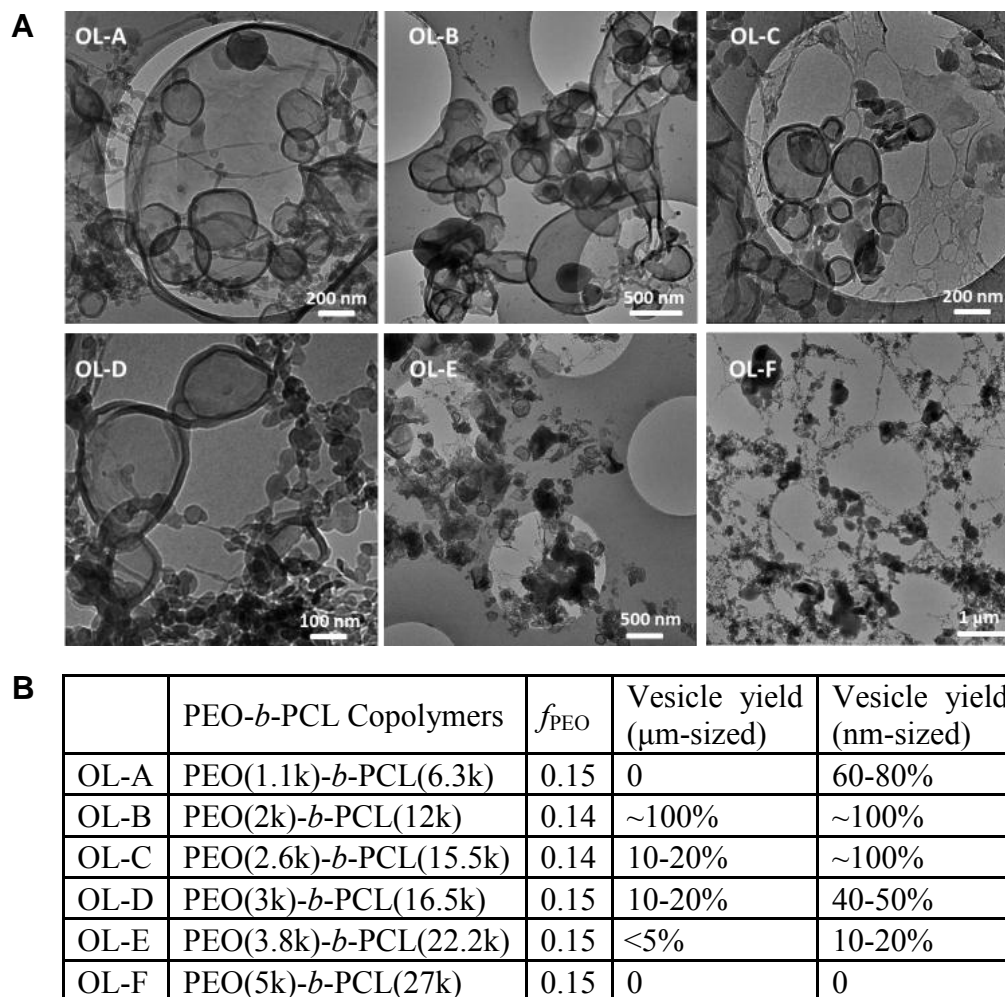
Figure 4.6 (A) Cryo-TEM images of nano-scale PEO-*b*-PCL diblock copolymers OL A-F particles in aqueous suspensions obtained via film hydration and subsequent self-assembly; (B) Morphology of self-assembled meso- and nano-scale structures derived from PEO-*b*-PCL diblock copolymers OL A-F.
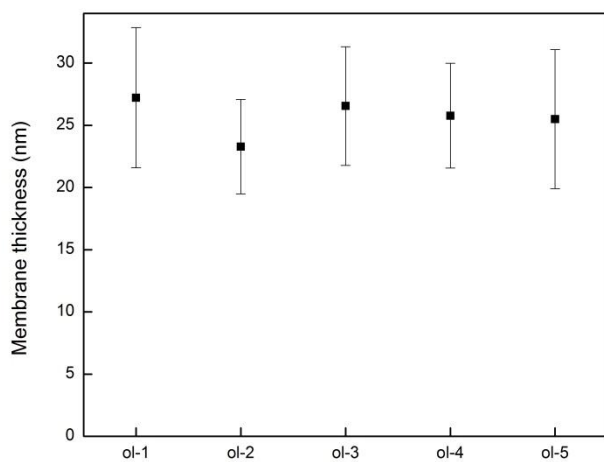
Figure 4.7 Membrane thickness of vesicles prepared from OL 1-5.
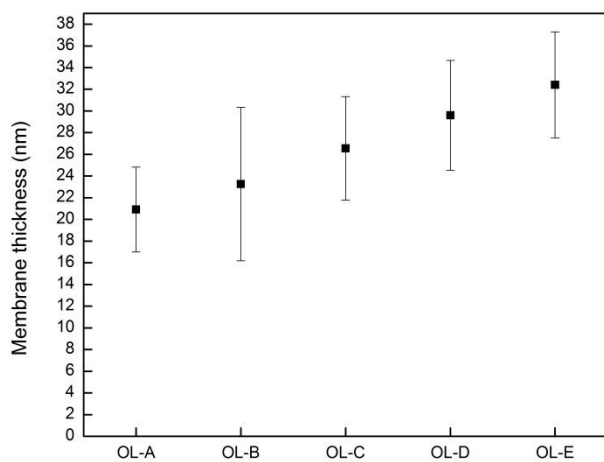
Figure 4.8 Membrane thickness of vesicles prepared from OL A-E.

229

4.4.4. Synthesis, Characterization and Aqueous Assembly of PEO-*b*-PTMC and PEO-*b*-P(CL-co-TMC) Polymers

The ideal candidates for *in vivo* imaging and drug releasing require soft biodegradable membranes. However, differential scanning calorimetry (DSC) strongly suggested that PEO(2K)-*b*-PCL(12K)-based vesicles are highly crystalline structures with glass transition temperature over 60 ℃. [27] To form functional soft resorbable, flexible and elastic materials, TMC (a highly flexible rubbery polymer) were used to copolymerize with PEO. An extensive family of FDA proved biodegradable amphilic PEO-*b*-PTMC and PEO-*b*-P(CL-co-TMC) polymers varying in a number average molecular weight (M_n: 5.7-35.6k) and PEO weight fraction (f_{PEO}: 0.10- 0.25) and TMC molar fraction of the hydrophobic block (30%, 50%, 100 %) were synthesized, characterized and examined.

These TMC containing polymers were synthesized either by ring-opening copolymerization of ε-caprolactone monomer and trimethylene carbonate monomer using commercially available monomethoxyl PEO (MePEO2K, MePEO5K) as macro-initiator in the presence of stannous(II) octoate (SnOct), or by anionic living polymerization of ethylene oxide monomers to produce PEOs of varying M_n (1.1K, 3.8K). The number-average molecular weight was characterized for each copolymer formulation by ^{1}H NMR spectroscopy (**Figure 4.9** and **Figure 4.10**). The polymers were subsequently screened for their ability to self-assemble into meso-scale polymersomes in dilute aqueous solution, the results were summarized in **Table 4.4, Table 4.5** and **Table 4.6**. While many PEO-*b*-PTMC and PEO-*b*-P(CL-co-TMC) polymers were observed to form meso-scale polymersomes, none of them produced meso-scale polymersomes quantitatively under

the thin-film rehydration conditions employed. Therefore, we sought to use blends of the PEO (2K)-*b*-PCL(12K) diblock copolymer and PEO(2K)-*b*-P(CL-co-TMC)(~12K) diblock tripolymer with different molar fractions of TMC (29% and 49%) to test their ability to self-assemble into polymersomes. PEO (2K)-*b*-PCL(12K) diblock copolymer and PEO(2K)-*b*-P(Cl-co-TMC) diblock tripolymer were mixed at different ratios: 95:5, 90:10, 80:20, 70:30, 50:50, 30:70 and followed with aqueous hydration of a dry thin-film of the blend polymers on Teflon film. Scanning confocal microscope images showed that all these blends form polymersomes, as shown in **Figure 4.11** and **4.12**, and the blend of PEO(2K)-*b*-P(CL-co-49mol%TMC)(11.9K) with PEO(2K)-*b*-PCL(12K) in 50:50 was producing polymersomes quantitatively under the thin-film rehydration conditions employed.
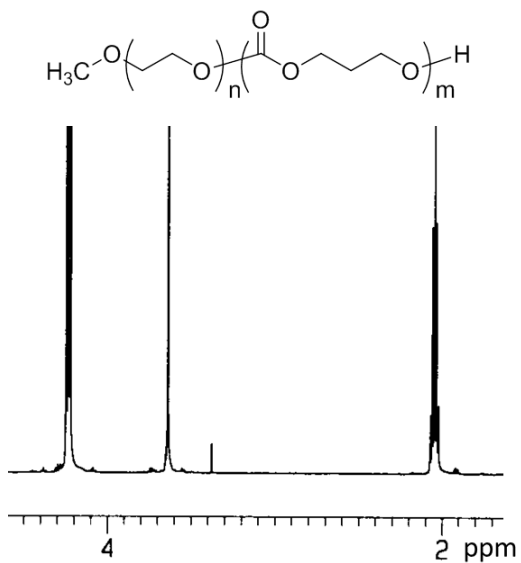
Figure 4.9 Representative ^{1}H-NMR spectrum of PEO-*b*-PTMC diblock copolymer.
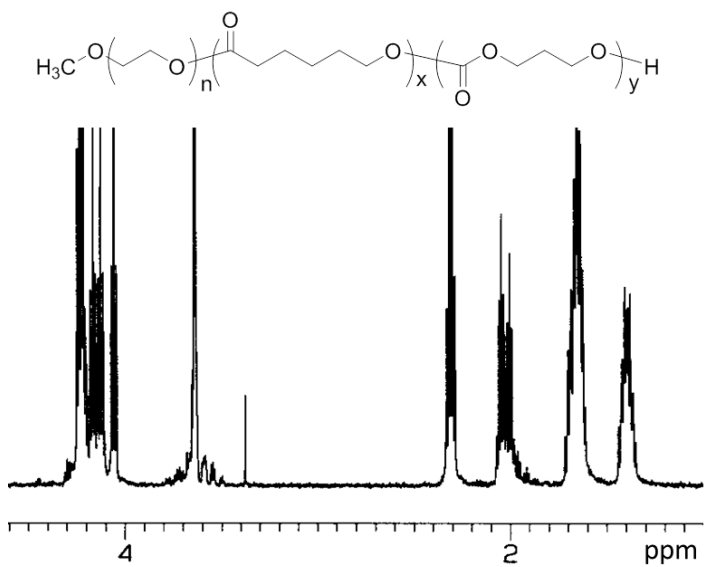
Figure 4.10 Representative ^{1}H-NMR spectrum of PEO-*b*-P(CL-co-TMC) diblock tripolymer.

Table 4.4 Self-assembly of PEO-*b*-PTMC copolymers.

PEO-*b*-PTMC[a]	M_n[b]	f_{PEO}[c]	% Yield of μm-sized polymersomes[d]
PEO(1.1K)-*b*-PTMC(4.6K)	5.7K	19.3%	0
PEO(1.1K)-*b*-PTMC(5.1K)	6.2K	17.7%	0
PEO(1.1K)-*b*-PTMC(6.2K)	7.3K	15.1%	0
PEO(2K)-*b*-PTMC(6.8K)	8.8K	22.7%	0
PEO(2K)-*b*-PTMC(9.4K)	11.4K	17.5%	5-10%
PEO(2K)-*b*-PTMC(11.2K)	13.2K	15.2%	5-10%
PEO(2K)-*b*-PTMC(13.0K)	15.0K	13.3%	5-10%
PEO(2K)-*b*-PTMC(13.8K)	15.8K	12.7%	5-10%
PEO(2K)-*b*-PTMC(15.3K)	17.3K	11.6%	0
PEO(2K)-*b*-PTMC(18.2K)	20.2K	9.9%	0
PEO(3.8K)-*b*-PTMC(17.7K)	21.5K	17.7%	0
PEO(3.8K)-*b*-PTMC(19.8K)	23.6K	16.1%	0
PEO(3.8K)-*b*-PTMC(25.8K)	29.6K	12.8%	5-10%
PEO(5K)-*b*-PTMC(18.0K)	23.0K	21.7%	< 5%
PEO(5K)-*b*-PTMC(23.0K)	28.0K	17.9%	< 5%
PEO(5K)-*b*-PTMC(25.9K)	30.9K	16.2%	< 5%
PEO(5K)-*b*-PTMC(27.5K)	32.5K	15.4%	< 5%
PEO(5K)-*b*-PTMC(30.6K)	35.6K	14.0%	< 5%

[a,b] Number-average molecular weight of PEO-*b*-PCL diblock copolymers as determined by ^{1}H NMR spectroscopy. [c] Weight fraction of the PEO block as determined by ^{1}H NMR data. [d] Approximate yield of polymer vesicles visually estimated from fluorescence confocal and laser optical microsopic studies qualitatively by comparison of the morphological fraction corresponding to polymersomes in aqueous solution.

Table 4.5 Self-assembly of PEO-*b*-P(CL-*co*-TMC) tripolymers with ~30% TMC molar fraction in the P(CL-*co*-TMC) block.

PEO-*b*-P(CL-*co*-TMC) tripolymers[a]	M_n^{b}	f_{TMC}^{c}	f_{PEO}^{d}	μm-sized Vesicle Yield[e]
PEO(2K)-*b*-P(CL-co-TMC)(11.0K)	13.0K	29%	15.4%	0
PEO(2K)-*b*-P(CL-co-TMC)(11.2K)	13.2K	27%	15.2%	<5%
PEO(2K)-*b*-P(CL-co-TMC)(12.4K)	14.4K	29%	13.9%	5-10%
PEO(2K)-*b*-P(CL-*co*-TMC)(13.1K)	15.1K	29%	13.2%	5-10%
PEO(2K)-*b*-P(CL-*co*-TMC)(14.9K)	16.9K	29%	11.8%	0
PEO(3.8K)-*b*-P(CL-*co*-TMC)(16.4K)	20.2K	30%	18.8%	5-10%
PEO(3.8K)-*b*-P(CL-*co*-TMC)(19.2K)	23.0K	32%	16.5%	5-10%
PEO(3.8K)-*b*-P(CL-*co*-TMC)(20.0K)	23.8K	33%	16.0%	<5%
PEO(5K)-*b*-P(CL-*co*-TMC)(18.5K)	23.5K	29%	21.3%	0
PEO(5K)-*b*-P(CL-*co*-TMC)(25.6K)	30.6K	29%	16.3%	10-20%
PEO(5K)-*b*-P(CL-*co*-TMC)(27.5K)	32.5K	28%	15.4%	5-10%

[a,b] Number-average molecular weight of PEO-*b*-PCL diblock copolymers as determined by ^{1}H NMR spectroscopy. [c] Molar fraction of the TMC in the P(CL-*co*-TMC) block as determined by ^{1}H NMR data. [d] Weight fraction of the PEO block as determined by ^{1}H NMR data. [e] Approximate yield of polymer vesicles visually estimated from fluorescence confocal and laser optical microsopic studies qualitatively by comparison of the morphological fraction corresponding to polymersomes in aqueous solution.

Table 4.6 Self-assembly of PEO-*b*-P(CL-*co*-TMC) tripolymers with ~50% TMC weight

fraction in the P(CL-*co*-TMC) block.

PEO-*b*-P(CL-*co*-TMC) tripolymers[a]	M_n[b]	f_{TMC}[c]	f_{PEO}[d]	μm-sized Vesicle Yield[e]
PEO(2K)-*b*-P(CL-co-TMC)(5.9K)	7.9K	49%	25.3%	0
PEO(2K)-*b*-P(CL-co-TMC)(7.0K)	9.0K	49%	22.2%	0
PEO(2K)-*b*-P(CL-co-TMC)(8.2K)	10.2K	49%	19.6%	0
PEO(2K)-*b*-P(CL-co-TMC)(9.3K)	11.4K	49%	17.7%	0
PEO(2K)-*b*-P(CL-co-TMC)(9.5K)	11.5K	50%	17.4%	0
PEO(2K)-*b*-P(CL-co-TMC)(11.9K)	13.9K	49%	14.4%	5-10%
PEO(2K)-*b*-P(CL-co-TMC)(14.3K)	16.3K	48%	12.3%	5-10%
PEO(2K)-*b*-P(CL-co-TMC)(18.4K)	20.4K	50%	9.8%	<5%
PEO(3.8K)-*b*-P(CL-co-TMC)(15.5K)	19.3K	51%	19.7%	<5%
PEO(3.8K)-*b*-P(CL-co-TMC)(19.2K)	23.0K	50%	16.5%	5-10%
PEO(3.8K)-*b*-P(CL-co-TMC)(22.0K)	25.8K	50%	14.7%	<5%
PEO(5K)-*b*-P(CL-co-TMC)(18.9K)	23.9K	49%	20.9%	0
PEO(5K)-*b*-P(CL-co-TMC)(25.3K)	30.3K	48%	16.5%	10-20%
PEO(5K)-*b*-P(CL-co-TMC)(28.4K)	33.4K	51%	15.0%	5-10%

[a,b] Number-average molecular weight of PEO-*b*-PCL diblock copolymers as determined by ^{1}H NMR spectroscopy. [c] Molar fraction of the TMC in the P(CL-*co*-TMC) block as determined by ^{1}H NMR data. [d] Weight fraction of the PEO block as determined by ^{1}H NMR data. [e] Approximate yield of polymer vesicles visually estimated from fluorescence confocal and laser optical microsopic studies qualitatively by comparison of the morphological fraction corresponding to polymersomes in aqueous solution.

Table 4.7 Self-assembly of tripolymer with 29% TMC content in the P(CL-*co*-TMC) block and PEO-*b*-PCL copolymer blends.

	PEO(2.0K)-*b*-P(CL-co-29mol%TMC)(12.4K) /PEO(2K)-*b*-PCL(12K)	Yield of μm-sized polymersomes
a	70/30	<5%
b	50/50	40-60%
c	30/70	10-20%
d	20/80	10-20%
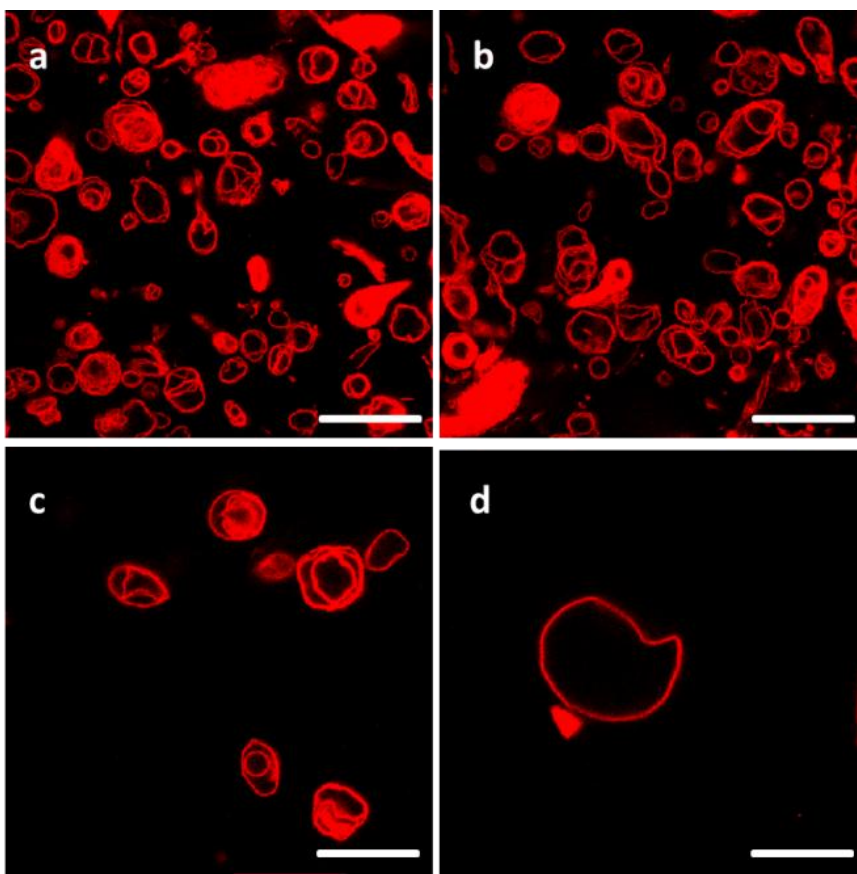
Figure 4.11 Confocal laser fluorescence micrographs of PEO(2K)-*b*-(PCL-co-49%TMC) (12.4K) / PEO(2K)-*b*-PCL(12K) blends. Scale bar = 50 μm.

Table 4.8 Self-assembly of tripolymer with 49% TMC content in the P(CL-*co*-TMC) block and PEO-*b*-PCL copolymer blends.

	PEO(2.0k)-*b*-P(CL-co-49mol% TMC)(12.4k) /PEO(2k)-*b*-PCL(12k)	Yield of μm-sized polymersomes
a	70/30	<5%
b	50/50	~100%
c	30/70	40-60%
d	20/80	10-20%
e	10/90	10-20%
f	5/95	10-20%
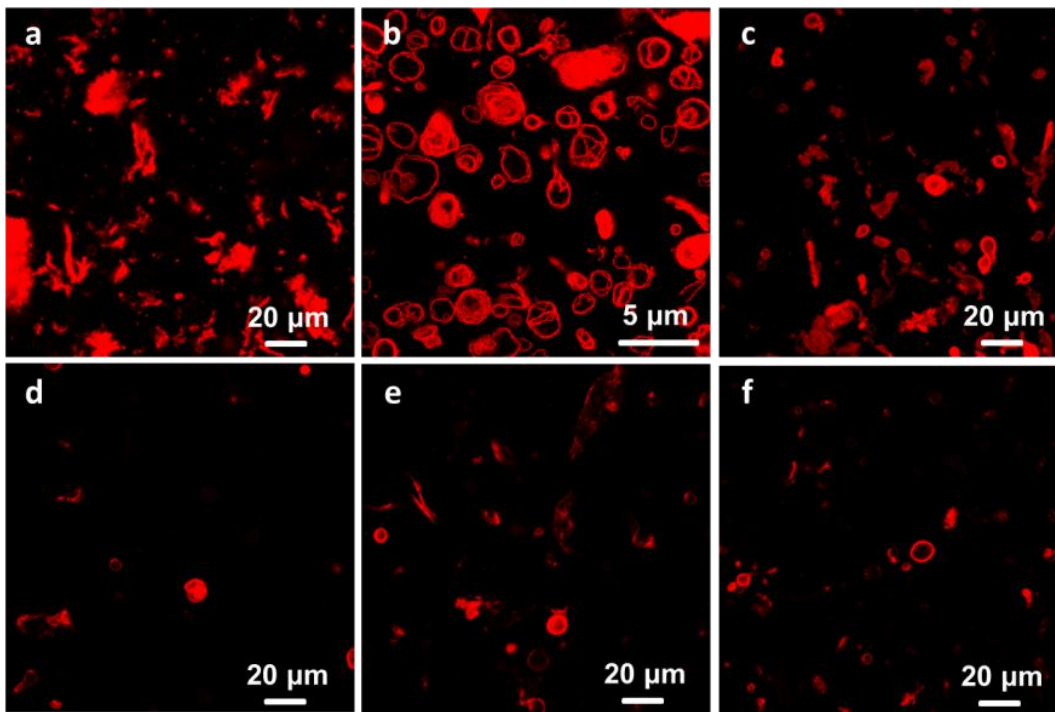
Figure 4.12 Confocal laser fluorescence micrographs of PEO(2K)-*b*-(PCL-co-49%TMC) (12.4K) / PEO(2K)-*b*-PCL(12K) blends.

Furthermore, the ability of these TMC containing PEO-*b*-PTMC and PEO-*b*-P(CL-co-TMC) polymers to self-assemble into nano-scale morphologies were examined by Cryo-TEM. The results are summerized in **Table 4.9**. As shown in **Figure 4.13**, PEO(1.1K)-*b*-PTMC(4.6-6.2K) that could not form meso-scale polymersomes self-assembled into ~100% nano-scale polymersomes, follows a similar trend with the previously reported PEO-*b*-PCL diblock copolymers that the ability to self-assemble into meso-scale and nano-scale polymersomes is different. Note that, the sizes of these PEO(1.1K)-*b*-PTMC polymersomes are much smaller compare to classic polymer vesicles. As observed from Cryo-TEM images, most polymersomes are 20-50 nm in diameter without extrusion, their small sizes will enable them to have prolonged *in vivo* circulation time and thus make them great candidate for biomedical applications.

Very interestingly, the PEO(2K, 3.8K, 5K)-*b*-PTMC with PEO molecular weight ~17% all form novel micelles with very large hydrophobic cores in a quantitative yield (**Figure 4.14**). The sizes of these micelles are very narrowly distributed as determined by both Cryo-TEM and dynamic light scattering (DLS) measurements. In addition, the sizes can be readily tuned from ~40nm (PEO(2K)-b-PTMC(9.4K)) to ~120nm (PEO(5k)-b-PTMC(25.9k)) by simply varying the diblock copolymer molecular weight. Therefore, these polymeric micelles can be served as highly effective delivery vehicles for poorly water-soluble drugs with well-defined hydrophobic volume. Moreover, the unusual large sizes of these micelles suggest enhanced mechanical stability over conventional micelles *in vitro* and *in vivo*.

Similar with PEO-*b*-PTMC, PEO-*b*-P(CL-co-TMC) diblock tripolymers also displayed similar properties of forming quantitative amount of small sized (20-50 nm)

vesicles or large sized (50-100 nm) micelles (**Figure 4.15**). So far, only a small portion of PEO-*b*-PTMC and PEO-*b*-P(CL-co-TMC) polymer self-assemblies have been observed by Cryo-TEM. More PEO-*b*-PTMC and PEO-*b*-P(CL-co-TMC) polymers will be examined soon. In addition, the self-assembling morphology of the PEO-*b*-PCL and PEO-*b*-PTMC or PEO-*b*-P(CL-co-TMC) polymer blends will also be studied for fully characterization and understanding of these TMC containing polymers.

Table 4.9 Morphology of self-assembled meso- and nano-scale structures derived from PEO-*b*-PTMC and PEO-*b*-P(CL-co-TMC) diblock copolymers.

Diblock copolymer[a]	f_{TMC}[b]	f_{PEO}[c]	Vesicle yield[d]	Nano-scale morphologies[e]
PEO(1.1K)-*b*-PTMC(4.6K)	100%	19.3%	0	~100% vesicles
PEO(1.1K)-*b*-PTMC(5.1K)	100%	17.7%	0	~100% vesicles
PEO(1.1K)-*b*-PTMC(6.2K)	100%	15.1%	0	~100% vesicles
PEO(5K)-*b*-PTMC(25.9K)	100%	16.2%	< 5%	~100% micelles
PEO(5K)-*b*-PTMC(25.9K)	100%	16.2%	< 5%	~100% micelles
PEO(2K)-*b*-P(CL-*co*-TMC)(11.9K)	49%	14.4%	5-10%	~100% micelles
PEO(3.8K)-*b*-P(CL-*co*-TMC)(19.2K)	50%	17.3%	5-10%	~100% micelles
PEO(5K)-*b*-P(CL-*co*-TMC)(25.3K)	48%	16.5%	10-20%	~100% micelles
PEO(2K)-*b*-P(CL-co-TMC)(12.4K)	29%	13.9%	5-10%	~100% vesicles
PEO(3.8K)-*b*-P(CL-*co*-TMC)(19.2K)	32%	16.5%	5-10%	~100% micelles
PEO(5K)-*b*-P(CL-*co*-TMC)(25.6K)	29%	16.3%	10-20%	~100% micelles

[a] Number-average molecular weight of PEO-*b*-PCL diblock copolymers as determined by ^{1}H NMR spectroscopy. [b] Molar fraction of the TMC in the P(CL-*co*-TMC) block as determined by ^{1}H NMR data. [c] Weight fraction of the TMC and PEO block as determined by ^{1}H NMR data. [e] Approximate yield of polymer vesicles visually estimated from fluorescence confocal and laser optical microsopic studies qualitatively by comparison of the morphological fraction corresponding to polymersomes in aqueous solution. [f] Determined qualitatively from cryo-TEM studies of the self-assembled structures formed from thin film rehydration followed by sonication.
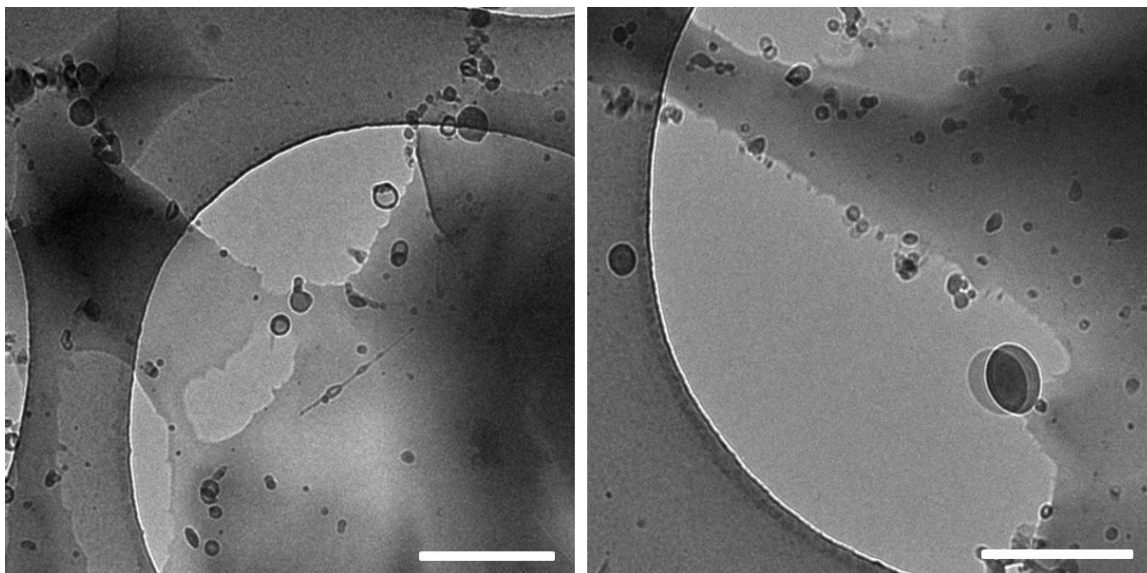
Figure 4.13 Cryo-TEM images of nano-scale PEO(1.1k)-*b*-PTMC(5.1k) diblock copolymers particles forming ~100% polymersomes in aqueous suspensions obtained via film hydration and subsequent self-assembly. Scale bar = 500 nm.
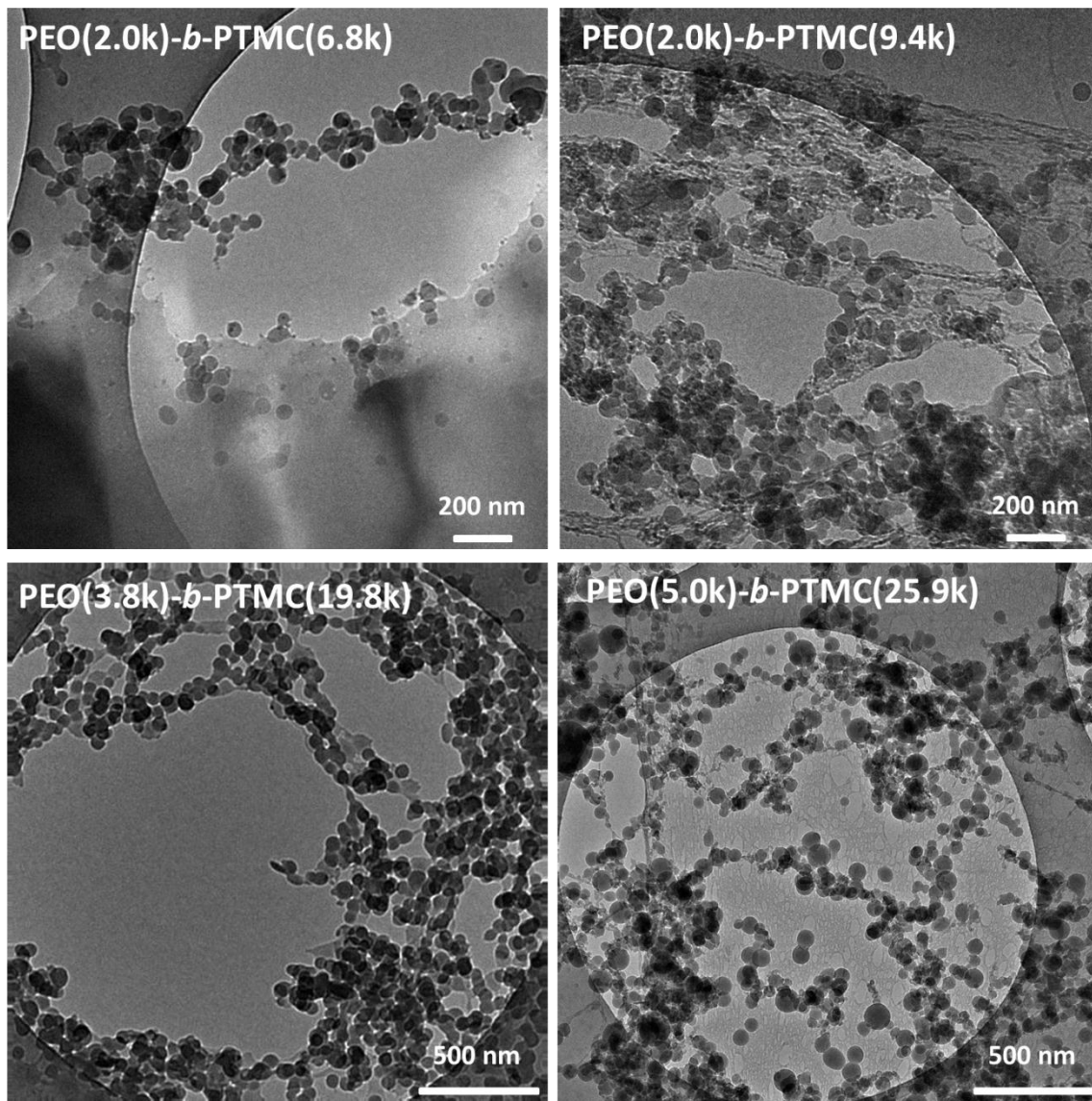
Figure 4.14 Cryo-TEM images of nano-scale PEO-*b*-PTMC diblock copolymers particles forming ~100% micelles in aqueous suspensions obtained via film hydration and subsequent self-assembly.
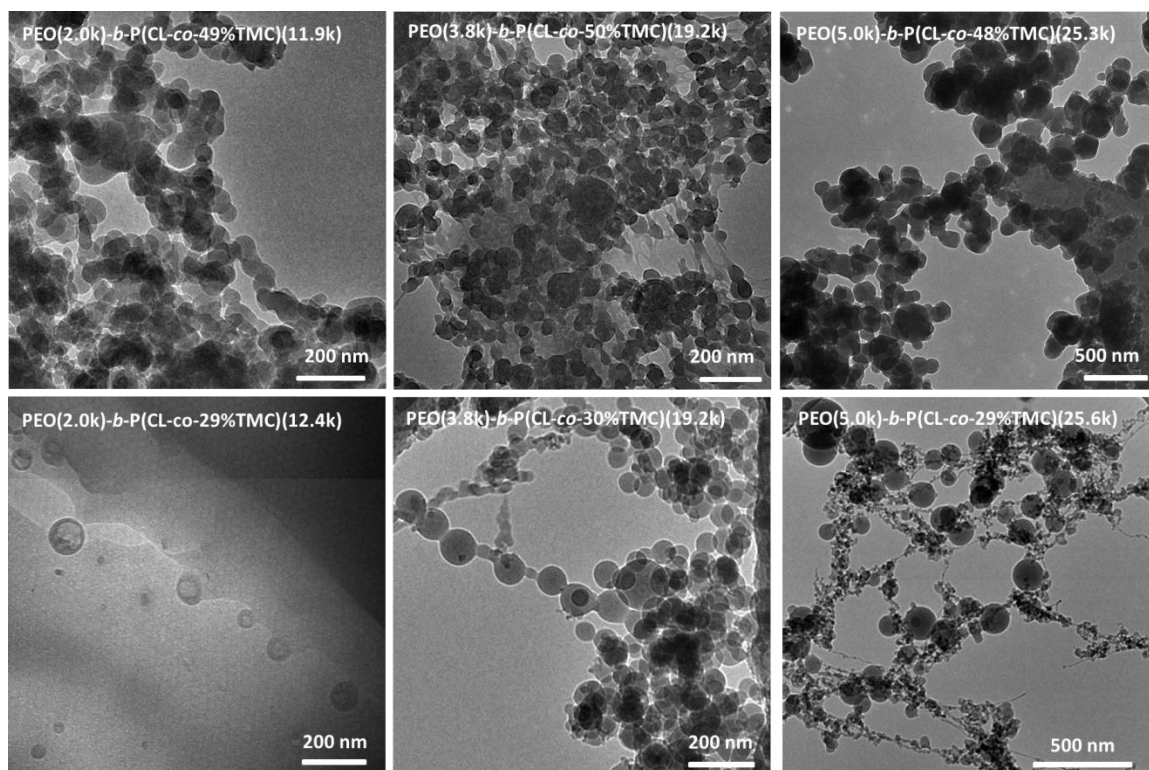
Figure 4.15 Cryo-TEM images of nano-scale PEO-*b*-P(CL-co-TMC) diblock tripolymers particles in aqueous suspensions obtained via film hydration and subsequent self-assembly.

Differential scanning calorimetry was also utilized to elucidate the thermal transitions properties of these TMC containing polymers synthesized. **Figure 4.16** compares the glass transition temperature of the five single polymers: PEO (2K), PCL(12K)-*b*-PEO(2K), P(CL-*co*-TMC(29 mol%)) (12.4K)-*b*-PEO(2K), P(CL-*co*-TMC(49 mol%)) (11.9K)-*b*-PEO(2K) and PTMC(11.2K)-*b*-PEO(2K). There is a clear big drop of glass transition temperature from 62.7 ℃ (PEO-*b*-PCL) to 40-50 ℃ for TMC containing polymers P(CL-*co*-TMC(29mol%)) (12.4K)-*b*-PEO(2K), P(CL-*co*-TMC(49mol%)) (11.9K)-*b*-PEO(2K) and PTMC(11.2K)-*b*-PEO(2K). The thermal transition properties of the polymer blends made from different ratios of P(CL-*co*-TMC(49 mol%)) (12.4K)-*b*-PEO(2K), P(CL-*co*-TMC(29 mol%)) (11.9K)-*b*-PEO(2K) and PCL(12K)-*b*-PEO(2K) are also measured as shown in **Figure 4.17**, **Figure 4.18**, and **Figure 4.19**. Again, by including TMC in the hydrophobic block, a decrease of glass transition temperature was observed. In addition, the glass transition temperature decreased with increasing the TMC content in the polymer blend.
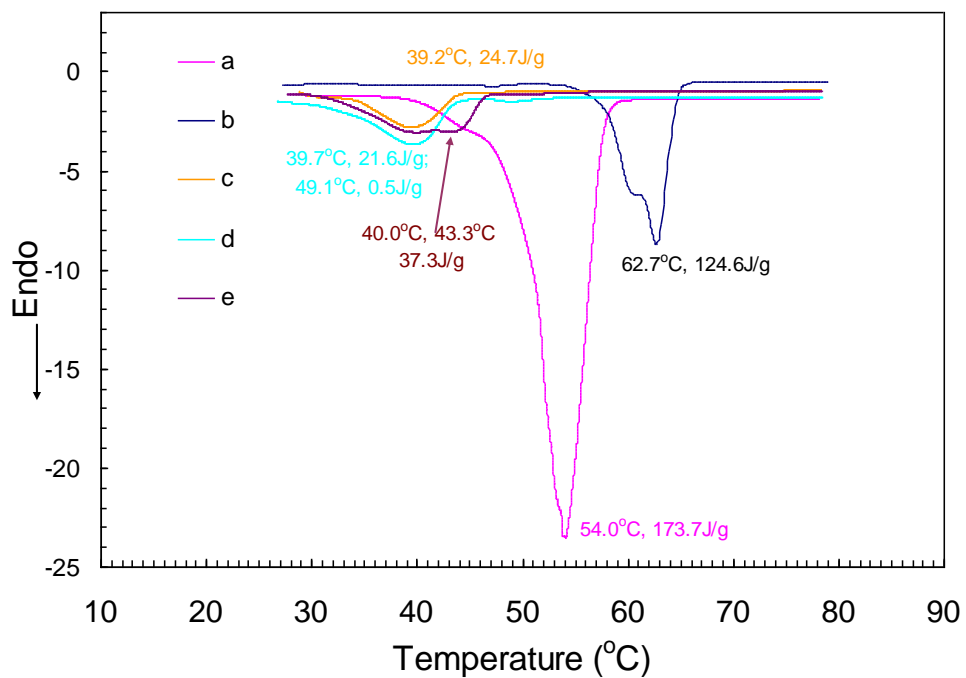
Figure 4.16 DSC data of: (a) PEO (2K); (b) PEO(2K)-*b*-PCL(12K); (c) PEO(2K)-*b*-P(CL-*co*-TMC(29mol%)) (12.4K); (d) PEO(2K)-*b*-P(CL-*co*-TMC(49mol%)) (11.9K); and (e) PEO(2K)-*b*-PTMC(11.2K).
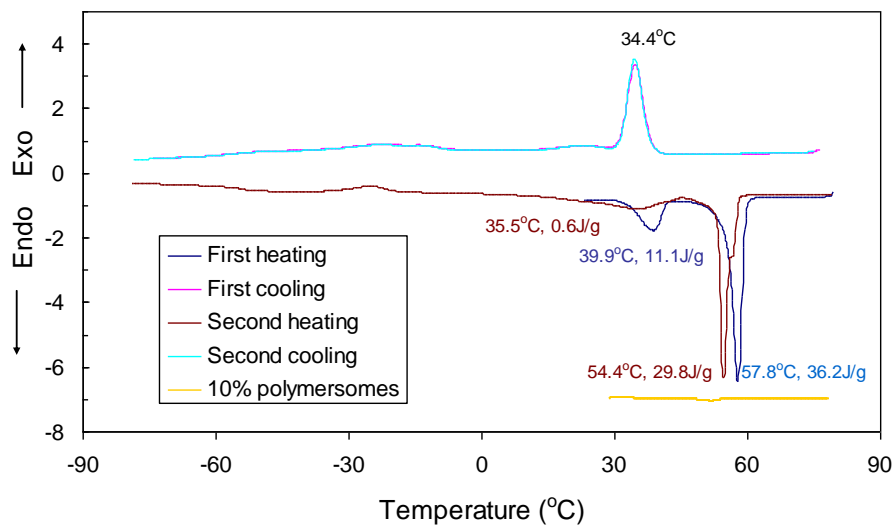
Figure 4.17 DSC data of PEO(2K)-*b*- PCL(12K) / PEO(2K)-*b*-P(CL-*co*-TMC(49mol%))(11.9K) 50/50 blend casting film (first heating, first cooling, second heating and second cooling) and its polymersomes.
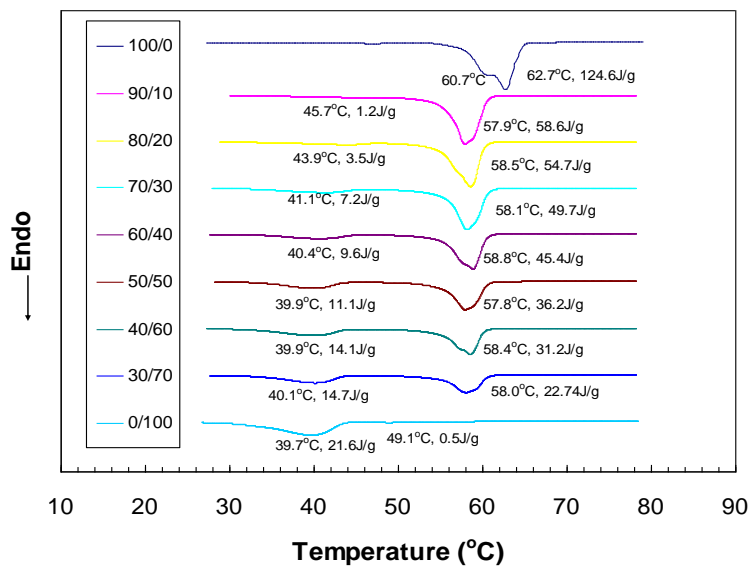
Figure 4.18 DSC data of PEO(2K)-*b*- PCL(12K) / PEO(2K)-*b*-P(CL-*co*-TMC(49mol%))(11.9K) blend casting films at a series blend ratios.
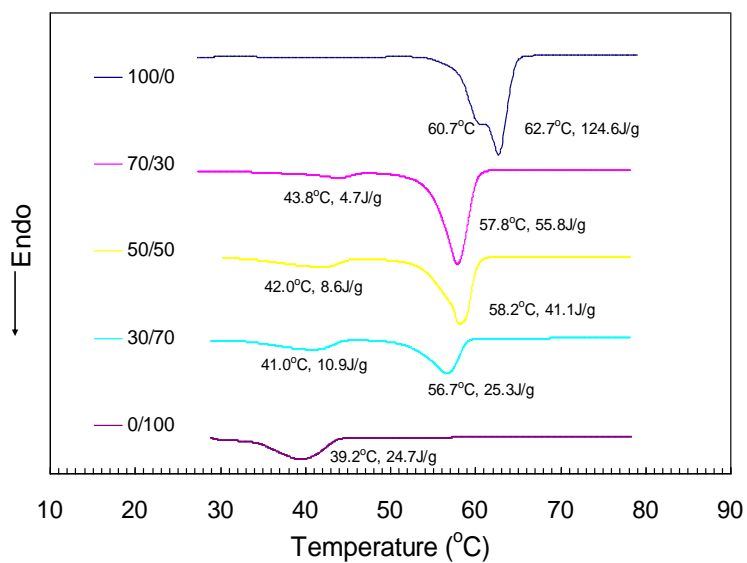
Figure 4.19 DSC data of PEO(2K)-*b*- PCL(12K) / PEO(2K)-*b*-P(CL-*co*-TMC(29mol%))(12.4K) blend casting films at a series blend ratios.

Finally, we used micropipette aspiration to probe the rheological properties of giant polymersomes. The meso-scale polymersomes prepared from PCL(12K)-*b*-PEO(2K) , P(CL-co-TMC(49 mol%)) (12.4K)-*b*-PEO(2K) / PCL(12K)-*b*-PEO(2K) 50:50 blend, and two different molecular weight PEO-*b*-PBD diblock copolymers OB2 and OB18 were progressively aspirated into a micropipette at stress rates of 0.1 pN nm^{-1} sec^{-1} up to the point of rupture. Values of the lysis tension for the TMC polymer blend as well as the three nonblend polymersomes studied are shown in **Figure 4.20**. The results generally showed that for soft PEO-*b*-PBD polymersomes, increasing molecular weight led to an increase in stability, consistent with general ideas of mesophase stability for strongly segregated copolymers. For highly crystallized PEO-*b*-PCl polymersomes that have solid membranes, they were unable to be aspirated and did not lyse at any pressure, as has been previously reported.[27, 86] However, for the PEO-*b*-PCL/PEO-*b*-P(CL-co-TMC) polymer blend, they could easily lyse at a much lower tension compare to the soft PEO-*b*-PBD polymersomes. This implicates the possible applications of using this PEO-*b*-PCL/PEO-*b*-P(CL-co-TMC) blend to prepare quantitative polymersomes vesicles that are soft and amorphous and will facilitate their location and transportation to cells in vivo.

Diblock copolymers	Lysis Tension (mN/m)
PEO(2K)-*b*-P(CL-co-**49**mol%TMC)(11.9K) /PEO(2K)-b-PCL(12K) 50: 50	2.92 + 1.10
PEO(2K)-b-PCL(12K)	does not lyse at any pressure
PEO(1.3K)-b-PBD(2.5K)	14
PEO(3.6K)-b-PBD(6.8K)	18
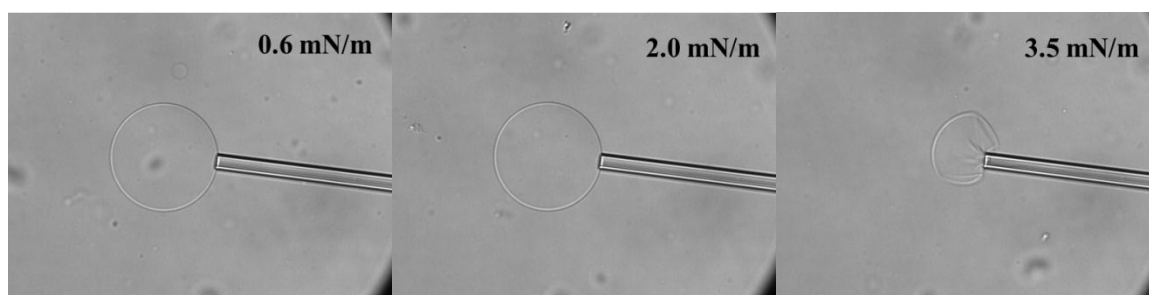
Figure 4.20 Micropipette aspiration study results of different polymers. The optical microscopy images represents the lysing process of polymersomes prepared from PEO(2K)-*b*- PCL(12K) / PEO(2K)-*b*-P(CL-*co*-TMC(49mol%))(11.9K) 50/50 blend.

4.4.5. Vinyl Sulfone Functionalization of PEO-*b*-PCl Diblock Copolymer

Various ways exist to generate functionalities on the surface of the hydrophilic leaflets of amphipilic block copolymer membranes to attach peptides and proteins for tumor targeting and drug delivery.[91] However, very few work has been done towards the biodegradable polymersomes. Herein, we reported the successfully development of a functionalization method for modification of the biodegradable PEO-*b*-PCL diblock copolymer by attaching the vinyl sulfone group. The vinyl sulfone functional group has been previously employed to attach peptides to chain ends of non-degradable PEO-*b*-PBD[92] and degradable poly(ethylene oxide)-block-poly(γ-methyl-ε-caprolactone) PEO-*b*-PMCL[76, 92] polymersome-forming systems. Using similar strategy to functionalize PEO-*b*-PCl diblock copolymers and subsequently conjuagate with peptides or proteins, we will be able to make ligand-conjugated PEO-*b*-PCL biodegradable polymersomes.

The reaction route to prepare peptide-conjugated biodegradable polymersomes is shown in **Scheme 4.7**. After silver(I) oxide-mediated tosylation of PEO, the resulting product was analyzed by ^{1}H NMR spectroscopy, and we determined that an average of about 90% of PEO chains had a tosyl group installed (**Figure 4.21A**). The tosylated PEO polymer was then reacted with an excess of potassium thioacetate in DMF to displace the tosyl groups with thioacetates. The tosyl groups were displaced to form the thioacetate and then hydrolyzed to thiol-PEO as confirmed by ^{1}H NMR analysis (**Figure 4.21B**). Vinyl sulfone functionalized PEO polymer are synthesized via conjugate addition reaction between thiols and divinyl sulfone, and the unreacted divinyl sulfone is separated by repeated precipitation into ice-cold diethyl ether. As determined by ^{1}H NMR spectroscopy (**Figure 4.21C**), the vinyl sulfone addition reaction has a nearly quantitative reaction yield toward thiol groups. After installation of vinyl sulfone, the hydroxyl end

250

groups of VS-PEO were used as initiation sites for polymerization of CL. The most commonly used method for PEO-*b*-PCL polymerization is in presence of FDA-approved SnOct$_2$ catalyst at high reaction temperature (130 ℃). However, we found the vinyl sulfone functionality in PEO is not very stable at such high reaction temperature, and the functionalization degree in the final VS-PEO-*b*-PCL polymers is significantly decreased by using this method. Therefore, a different ring-opening polymerization method was developed with a highly effective AlEt$_3$ catalyst at room temperature. Minimal loss of vinyl sulfone (from 81% to 61-68%) was detected by ^{1}H NMR spectroscopy under this polymerization condition (**Figure 4.21D**). Vinyl sulfone functionalized diblock copolymers with various different molecular weights were synthesized in **Table 4.10**, with the polymerization proceeded at a well-controlled fashion: PCL block molecular weight is linearly dependent on the amount of CL monomer added to the polymerization reaction (**Figure 4.22**). By controlling the mole ratio of CL monomer with VS-PEO, the PCL block molecular weight can be precisely tuned.

To verify that the aggregate morphology was unaffected after inducing vinyl sulfone groups, functionalized PEO(2K)-*b*-PCL(11.7K) were self-assembled into meso-scale polymersomes. The polymersomes formation were in a comparative yield to the PEO(2K)-*b*-PCl(12K) diblock copolymer. Although the meso-scale polymersomes self-assembling yield from the other functionalized diblock copolymers in **Table 4.10** is relatively lower, we would expect all of them to have a high nano-sized polymersomes formation yield based on our previous nano-sized PEO-*b*-PCL polymersomes analysis. Therefore, we have synthesized and characterized the vesicle-forming block polymer VS-PEO-*b*-PCL which can be used to develop a degradable, targeted drug delivery system.
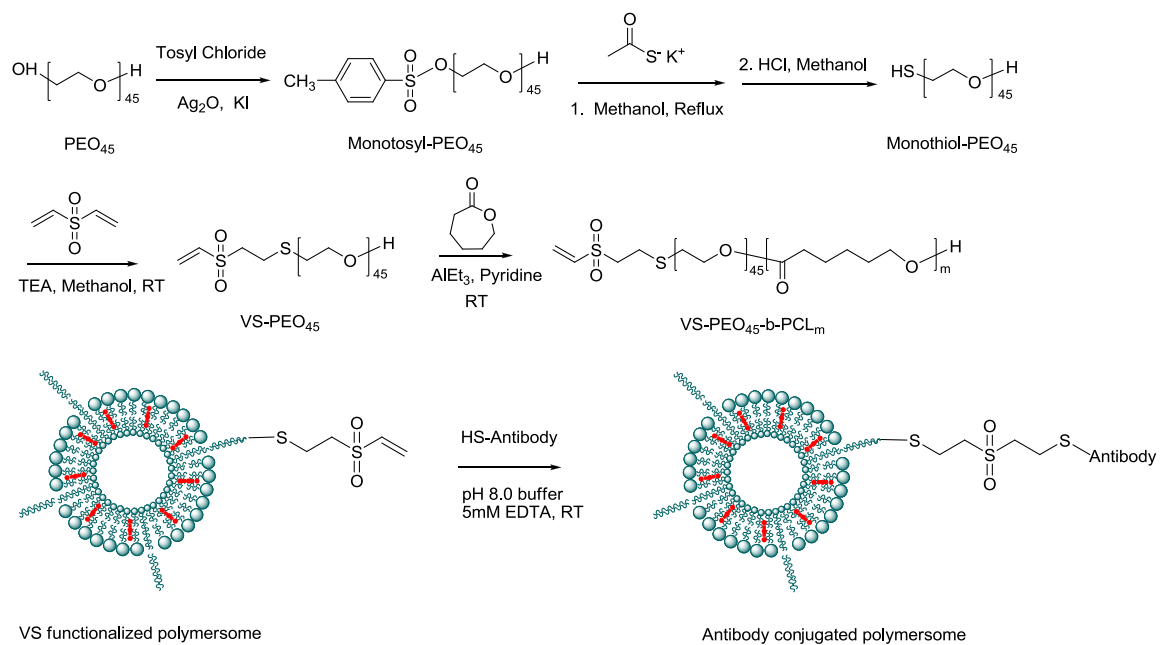
Scheme 4.7 A. Synthetic routes to VS-terminated PEO-*b*-PCL diblock copolymer. B. Michael type addition of cysteine-contained antibody to VS-functionalized PEO-*b*-PCL polymersomes.
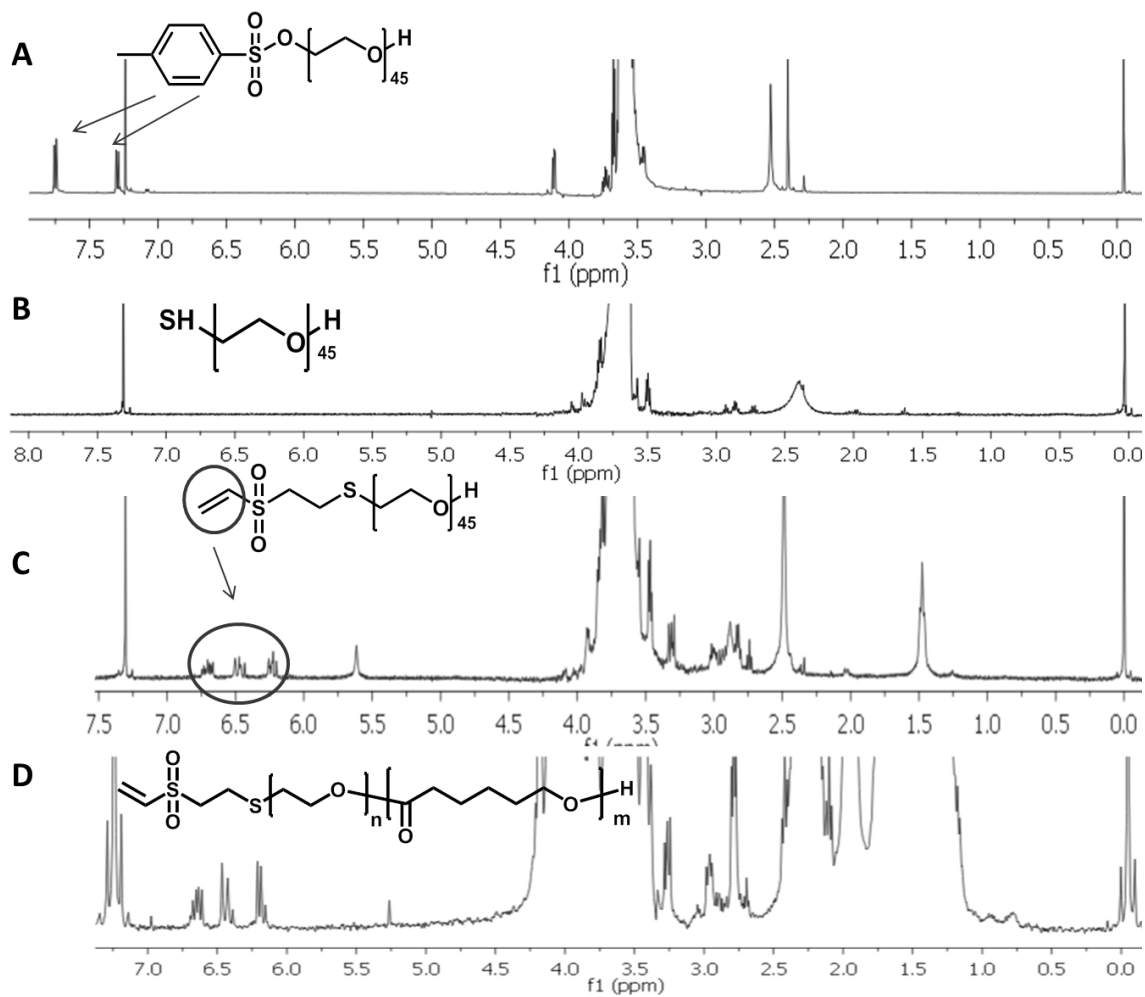
Figure 4.21 ^{1}H NMR spectra (CDCl$_3$) of (a) PEO tosylate, (b) PEO thiolate, (c) PEO vinyl sulfonate and (d) VS-PEO-PCL.
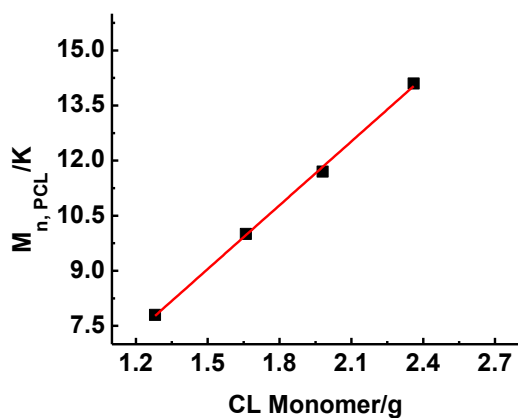
Figure 4.22 Correlation of VS-PEO(2K)-*b*-PCL molecular weight to the mass of CL monomer.

Table 4.10 Molecular weight and functionalization degree of vinyl sulfone functionalized PEO-PCl diblock copolymers.

Functionalized Polymers	f_{PEO}	Vinyl Sulfone Functionalization %
VS-PEO(2K)-*b*-PCL(6.3K)	24.1%	67.1
VS-PEO(2K)-*b*-PCL(7.8K)	20.4%	63.4
VS-PEO(2K)-*b*-PCL(8.5K)	19.0%	70.2
VS-PEO(2K)-*b*-PCL(9.4K)	17.5%	62.0
VS-PEO(2K)-*b*-PCL(10.0K)	16.7%	67.7
VS-PEO(2K)-*b*-PCL(11.7K)	14.6%	61.5
VS-PEO(2K)-*b*-PCL(14.1K)	12.4%	62.9
VS-PEO(2K)-*b*-PCL(17.7K)	10.1%	60.2

4.5. Conclusions

A series of PEO-*b*-PCL diblock copolymers varying in PEO block size (M_n: 750, 1100, 2000 and 5000), f_{PEO} (0.08-0.33), and M_n (3.6-57K) were synthesized by ring-opening polymerization of ε-caprolactone monomer using commercially available MePEO as the macro-initiator. Anionic living polymerization was also employed to synthesize PEO-*b*-PCL copolymers with a wider range of controlled PEO block sizes (M_n: 1500, 2600, 3000, 3800, and 5800), CN as the PEO block terminal group, f_{PEO} = 0.10-0.23, and M_n ranging from 7.8 to 47K. All copolymers were isolated by GPC and possessed narrow molecular weight distributions (PDI: 1.14-1.37). The PEO-*b*-PCL diblock copolymers were subsequently screened for the ability to assemble into various aqueous morphologies via two separate preparation methods: film hydration and organic co-solvent/water injection/extraction. Meso-scale polymersomes were obtained from a PEO(2K)-*b*-PCL(12K) diblock copolymer (PDI = 1.21) in nearly quantitative yield by both methods, while a much broader range of diblock copolymer varying in both the hydrophilic fraction (f_{PEO}: 0.14-0.21) and PEO chain length 1.1-3K can self-assemble into a very high yield of nano-sized polymersomes upon hydration of a dry thin film deposited on Teflon. Without the addition of co-solvent, the thin film hydration method enables controllable, large-scale synthesis, and avoids the presence of residual organic solvent which may be toxic for *in vivo* applications. Therefore, this is a pioneer work provides the entire gate of a roadmap of biodegradable PEO-*b*-PCL diblock copolymer compositions that can self-assemble into meso- and nano-scale polymersomes as biomaterials for future cosmetic, imaging, and drug delivery applications. This work also demonstrates that if nanoscale bilayer vesicles are desired, convincingly screening the

ability to form meso-scale polymersomes is inappropriate. Furthermore, we can expect by simply varying the PCL chain length or hydrophobic fraction, the biodegradable hydrophobic membranes of the nano-scale polymer vesicles can be tuned to enable the precise control of encapsulated drug release based on the effect of PCL/PEO molar ratios on the biodegradation kinetics. [93-96]

However, the thermal properties of these PEO-*b*-PCL-based biodegradable polymersomes as measured by DSC indicate that they are highly crystallized at room temperature. Recognizing the need to develop highly elastic, soft polymersomes from non-toxic, biodegradable polymers, we further designed and characterized vesicles assembled from a series of PEO-*b*-PTMC and PEO-*b*-P(CL-co-TMC) polymers by copolymerize CL with a second TMC monomer, an elastomeric aliphatic polyester with excellent flexibility and poor mechanical strength. The thermal properties of these polymers were studied by using DSC and micropipette aspiration; both indicate that we formed a soft based material. The introduction of TMC provides a route to significantly alter membrane rheological properties. Furthermore, the morphology of nano-scale self-assemblies from these TMC containing polymers varying in PEO molecular weight (2K, 3.8K and 5K), PEO weight fraction (0.15-0.20) and TMC mole fraction (30%, 50%, 100%) was examined by Cryo-TEM. Interestingly, these polymers formed either 100% polymer vesicles in much smaller sizes compare to traditional polymersomes or 100% uniformly distributed micelles structures with very large hydrophobic cores in aqueous solution; these novel and unique structures has a great deal of potential for *in vivo* and drug delivery applications.

Finally, we synthesized functionalized vesicle-forming VS-PEO-*b*-PCL biodegradable diblock copolymers varying in number-average molecular weight (Mn: 9.8 - 16.1k) and PEO weight fraction (fPEO: 12.4 – 20.4%). These functionalized block copolymers self-assemble in water to form polymersomes with high reactivity and specificity toward cysteine containing proteins under a mild conjugate reaction condition. A precise control of VS-PEO-b-PCL molecular weight is achieved by ring-opening copolymerization of VS-PEO and CL with a highly effective $AlEt_3$ catalyst. The VS functionalization groups on the exterior of the vesicles are capable of reacting with thiol-containing targeting proteins under very mild conditions in advantageous for reaction rates, yields, and stability. By including VS-PEO-*b*-PCL as the minority component prior to self-assembly, we anticipate it to serve as a versatile platform for specific delivery of a variety of therapeutic payloads with enhanced targeting due to ligand bound to vinyl sulfone groups.

4.6. Acknowledgements

4.7. References

1. Discher, D. E.; Eisenberg, A. *Science* **2002,** 297, 967-973.

2. Discher, B. M.; Won, Y. Y.; Ege, D. S.; Lee, J.; Bates, F. S.; Discher, D. E.; Hammer, D. A. *Science* **1999,** 284, 1143.

3. Lee, J. C. M.; Bermudez, H.; Discher, B. M.; Sheehan, M. A.; Won, Y.-Y.; Bates, F. S.; Discher, D. E. *Biotechnology and Bioengineering* **2001,** 73, 135-145.

4. Bermudez, H.; Brannan, A. K.; Hammer, D. A.; Bates, F. S.; Discher, D. E. *Macromolecules* **2002,** 35, 8203-8208.

5. Ghoroghchian, P. P.; Frail, P. R.; Susumu, K.; Blessington, D.; Brannan, A. K.; Bates, F. S.; Chance, B.; Hammer, D. A.; Therien, M. J. *Proceedings of the National Academy of Sciences U.S.A* **2005,** 102, 2922-2927.

6. Meng, F.; Engbers, G. H. M.; Feijen, J. *Journal of Controlled Release* **2005,** 101, 187-198.

7. Lee J.C.M., B. H., Discher B.M., Sheehan M.A., Won Y-Y, Bates F.S.; Discher D.E. *Biotechnology and Bioengineering* **2001,** 73, 135-145.

8. Yu, K.; Eisenberg, A. *Macromolecules* **1998,** 31, 3509-3518.

9. Yu, K.; Zhang, L.; Eisenberg, A. *Langmuir* **1996,** 12, 5980-5984.

10. Yu, K.; Eisenberg, A. *Macromolecules* **1996,** 29, 6359-6361.

11. Shen, H.; Eisenberg, A. *Macromolecules* **2000,** 33, 2561-2572.

12. Christian, D. A.; Cai, S.; Bowen, D. M.; Kim, Y.; Pajerowski, J. D.; Discher, D. E. *European journal of pharmaceutics and biopharmaceutics* **2009,** 71, 463-474.

13. Onaca, O.; Enea, R.; Hughes, D. W.; Meier, W. *Macromolecular Bioscience* **2009,** 9, 129-139.

14. Ahmed, F.; Photos, P. J.; Discher, D. E. *Drug Development Research* **2006,** 67, 4-14.

15. Lomas, H.; Du, J.; Canton, I.; Madsen, J.; Warren, N.; Armes, S. P.; Lewis, A. L.; Battaglia, G. *Macromolecular Bioscience* **2010,** 10, 513-530.

16. Murdoch, C.; Reeves, K. J.; Hearnden, V.; Colley, H.; Massignani, M.; Canton, I.; Madsen, J.; Blanazs, A.; Armes, S. P.; Lewis, A. L. *Nanomedicine* **2010,** 5, 1025-1036.

17. Nallani, M.; Woestenenk, R.; de Hoog, H.-P. M.; van Dongen, S. F. M.; Boezeman, J.; Cornelissen, J. J. L. M.; Nolte, R. J. M.; van Hest, J. C. M. *Small* **2009,** 5, 1138-1143.

18. van Dongen, S. F. M.; Nallani, M.; Schoffelen, S.; Cornelissen, J. J. L. M.; Nolte, R. J. M.; van Hest, J. *Macromolecular Rapid Communications* **2008,** 29, 321-325.

19. Fu, Z.; Ochsner, M. A.; de Hoog, H. P. M.; Tomczak, N.; Nallani, M. *Chem. Commun.* **2011**.

20. Kuiper, S. M.; Nallani, M.; Vriezema, D. M.; Cornelissen, J. J. L. M.; van Hest, J. C. M.; Nolte, R. J. M.; Rowan, A. E. *Organic & Biomolecular Chemistry* **2008,** 6, 4315-4318.

21. Meng, F.; Hiemstra, C.; Engbers, G. H. M.; Feijen, J. *Macromolecules* **2003,** 36, 3004-3006.

22. Adams, D. J.; Kitchen, C.; Adams, S.; Furzeland, S.; Atkins, D.; Schuetz, P.; Fernyhough, C. M.; Tzokova, N.; Ryan, A. J.; Butler, M. F. *Soft Matter* **2009,** 5, 3086-3096.

23. Johnston, A.; Dalton, P.; Newman, T. *Journal of Nanoparticle Research* **2010,** 12, 1997-2001.

24. Sanson, C.; Schatz, C.; Le Meins, J.-F.; Brulet, A.; Soum, A.; Lecommandoux, S. *Langmuir* **2009,** 26, 2751-2760.

25. Changez, M.; Kang, N.-G.; Koh, H.-D.; Lee, J.-S. *Langmuir* **2010,** 26, 9981-9985.

26. Kim, S. Y.; Lee, K. E.; Han, S. S.; Jeong, B. *The Journal of Physical Chemistry B* **2008,** 112, 7420-7423.

27. Ghoroghchian, P. P.; Li, G.; Levine, D. H.; Davis, K. P.; Bates, F. S.; Hammer, D. A.; Therien, M. J. *Macromolecules* **2006,** 39, 1673-1675.

28. Ahmed, F.; Hategan, A.; Discher, D. E.; Discher, B. M. *Langmuir* **2003,** 19, 6505-6511.

29. Ahmed, F.; Discher, D. E. *Journal of Controlled Release* **2004,** 96, 37-53.

30. Bei, J.-Z.; Li, J.-M.; Wang, Z.-F.; Le, J.-C.; Wang, S.-G. *Polymers for Advanced Technologies* **1997,** 8, 693-696.

31. Najafi, F.; Sarbolouki, M. N. *Biomaterials* **2003,** 24, 1175-1182.

32. Bellomo, E. G.; Wyrsta, M. D.; Pakstis, L.; Pochan, D. J.; Deming, T. J. *Nature Materials* **2004,** 3, 244-248.

33. Schuetz, P.; Greenall, M. J.; Bent, J.; Furzeland, S.; Atkins, D.; Butler, M. F.; McLeish, T. C. B.; Buzza, D. M. A. *Soft Matter* **2011,** 7, 749-759.

34. Harashima, H.; Kiwada, H. *Advanced drug delivery reviews* **1996,** 19, 425-444.

35. Ueda, I.; Chiou, J.-S.; Krishna, P. R.; Kamaya, H. *Biochimica et Biophysica Acta (BBA) - Biomembranes* **1994,** 1190, 421-429.

36. Drummond, D. C.; Meyer, O.; Hong, K.; Kirpotin, D. B.; Papahadjopoulos, D. *Pharmacological reviews* **1999,** 51, 691.

37. Florence, A. T.; Hussain, N. *Advanced drug delivery reviews* **2001,** 50, S69-S89.

38. Sass, W.; Dreyer, H. P.; Seifert, J. *American Journal of Gastroenterology* **1990,** 85, 255-260.

39. Jenkins, P. G.; Howard, K. A.; Blackball, N. W.; Thomas, N. W.; Davis, S. S.; O'Hagan, D. T. *Journal of Controlled Release* **1994,** 29, 339-350.

40. Moghimi, S. M.; Hunter, A. C.; Murray, J. C. *Pharmacological reviews* **2001,** 53, 283.

41. Otsuka, H.; Nagasaki, Y.; Kataoka, K. *Advanced drug delivery reviews* **2003,** 55, 403-419.

42. Photos, P. J.; Bacakova, L.; Discher, B.; Bates, F. S.; Discher, D. E. *Journal of Controlled Release* **2003,** 90, 323-334.

43. Allen, C.; Han, J.; Yu, Y.; Maysinger, D.; Eisenberg, A. *Journal of Controlled Release* **2000,** 63, 275-286.

44. Sinha, V. R.; Bansal, K.; Kaushik, R.; Kumria, R.; Trehan, A. *International journal of pharmaceutics* **2004,** 278, 1-23.

45. Coombes, A. G. A.; Rizzi, S. C.; Williamson, M.; Barralet, J. E.; Downes, S.; Wallace, W. A. *Biomaterials* **2004,** 25, 315-325.

46. Shenoy, D. B.; Amiji, M. M. *International journal of pharmaceutics* **2005,** 293, 261-270.

47. Robbins, G. P.; Lee, D.; Katz, J. S.; Frail, P. R.; Therien, M. J.; Crocker, J. C.; Hammer, D. A. *Soft Matter* **2011,** 7, 769-779.

48. Yuan, H.; Li, J.; Bao, G.; Zhang, S. *Physical Review Letters* **2010,** 105, 138101.

49. Fox, M. E.; Szoka, F. C.; Frechet, J. M. J. *Accounts of Chemical Research* **2009,** 42, 1141-1151.

50. Jain, R. K. *Cancer and Metastasis Reviews* **1987,** 6, 559-593.

51. Pego, A. P.; Van Luyn, M. J. A.; Brouwer, L. A.; Van Wachem, P. B.; Poot, A. A.; Grijpma, D. W.; Feijen, J. *Journal of Biomedical Materials Research Part A* **2003,** 67, 1044-1054.

52. Angele, P.; Abke, J.; Kujat, R.; Faltermeier, H.; Schumann, D.; Nerlich, M.; Kinner, B.; Englert, C.; Ruszczak, Z.; Mehrl, R.; Mueller, R. *Biomaterials* **2004,** 25, 2831-2841.

53. Amsden, B. *Soft Matter* **2007,** 3, 1335-1348.

54. Yang, J.; Motlagh, D.; Webb, A. R.; Ameer, G. A. *Tissue Engineering* **2005,** 11, 1876-1886.

55. Vert, M. *Biomacromolecules* **2004,** 6, 538-546.

56. Albertsson, A.-C.; Varma, I. K. *Biomacromolecules* **2003,** 4, 1466-1486.

57. Sudesh, K.; Abe, H.; Doi, Y. *Progress in Polymer Science* **2000,** 25, 1503-1555.

58. Nair, L. S.; Laurencin, C. T. *Progress in Polymer Science* **2007,** 32, 762-798.

59. Artham, T.; Doble, M. *Macromolecular Bioscience* **2008,** 8, 14-24.

60. Rokicki, G. *Progress in Polymer Science* **2000,** 25, 259-342.

61. Kobayashi, S.; Ritter, H.; Kaplan, D.; Matsumura, S., Enzymatic Synthesis of Polyesters via Ring-Opening Polymerization. In *Enzyme-Catalyzed Synthesis of Polymers*, Springer Berlin / Heidelberg: 2006; Vol. 194, pp 95-132.

62. Misfeld, M.; Scharfschwerdt, M.; Sievers, H.-H. *The Annals of Thoracic Surgery* **2004,** 78, 1060-1063.

63. Chapanian, R.; Tse, M. Y.; Pang, S. C.; Amsden, B. G. *Biomaterials* **2009,** 30, 295-306.

64. Pego, A. P.; Grijpma, D. W.; Feijen, J. *Polymer* **2003,** 44, 6495-6504.

65. Pangburn, T. O.; Petersen, M. A.; Waybrant, B.; Adil, M. M.; Kokkoli, E. *Journal of biomechanical engineering* **2009,** 131, 074005.

66. Pang, Z.; Lu, W.; Gao, H.; Hu, K.; Chen, J.; Zhang, C.; Gao, X.; Jiang, X.; Zhu, C. *Journal of Controlled Release* **2008,** 128, 120-127.

67. Pang, Z.; Feng, L.; Hua, R.; Chen, J.; Gao, H.; Pan, S.; Jiang, X.; Zhang, P. *Molecular Pharmaceutics* 7, 1995-2005.

68. Pang, Z.; Gao, H.; Yu, Y.; Guo, L.; Chen, J.; Pan, S.; Ren, J.; Wen, Z.; Jiang, X. *Bioconjugate Chemistry*, null-null.

69. Hillmyer, M. A.; Bates, F. S. *Macromolecules* **1996,** 29, 6994-7002.

70. Olivier, J.-C.; Huertas, R.; Lee, H. J.; Calon, F.; Pardridge, W. M. *Pharmaceutical Research* **2002,** 19, 1137-1143.

71. Nasongkla, N.; Shuai, X.; Ai, H.; Weinberg, B. D.; Pink, J.; Boothman, D. A.; Gao, J. *Angewandte Chemie* **2004,** 116, 6483-6487.

72. Sethuraman, V. A.; Bae, Y. H. *Journal of Controlled Release* **2007,** 118, 216-224.

73. Morpurgo, M.; Veronese, F. M.; Kachensky, D.; Harris, J. M. *Bioconjugate Chemistry* **1996,** 7, 363-368.

74. Masri, M. S.; Friedman, M. *Journal of Protein Chemistry* **1988,** 7, 49-54.

75. Seely, J. E.; Richey, C. W. *Journal of Chromatography A* **2001,** 908, 235-241.

76. Petersen, M. A.; Yin, L.; Kokkoli, E.; Hillmyer, M. A. *Polymer Chemistry* **2010**.

77. Bogdanov, B.; Vidts, A.; Van Den Buicke, A.; Verbeeck, R.; Schacht, E. *Polymer* **1998,** 39, 1631-1636.

78. Zastre, J. J., J.; Bajwa, M.; Liggins, R.; Iqbal, F.; Burt, H. *European journal of pharmaceutics and biopharmaceutics* **2002,** 54, 299-309.

79. Hsu, S.-H.; Tang, C.-M.; Lin, C. C. C.-C. *Biomaterials* **2004,** 25, 5593-5601.

80. Cerrai, P.; Tricoli, M.; Andruzzi, F.; Paci, M.; Paci, M. *Polymer* **1989,** 30, 338-343.

81. Jeong, Y.-I.; Kang, M.-K.; Sun, H.-S.; Kang, S.-S.; Kim, H.-W.; Moon, K.-S.; Lee, K.-J.; Kim, S.-H.; Jung, S. *International journal of pharmaceutics* **2004,** 273, 95-107.

82. Dong, C.-M.; Qiu, K.-Y.; Gu, Z.-W.; Feng, X.-D. *Macromolecules* **2001,** 34, 4691-4696.

83. Cammas, S.; Nagasaki, Y.; Kataoka, K. *Bioconjugate Chemistry* **1995,** 6, 226-230.

84. Nagasaki, Y.; Iijima, M.; Kato, M.; Kataoka, K. *Bioconjugate Chemistry* **1995,** 6, 702-704.

85. Deng, M.; Wang, R.; Rong, G.; Sun, J.; Zhang, X.; Chen, X.; Jing, X. *Biomaterials* **2004,** 25, 3553-3558.

86. Rajagopal, K.; Mahmud, A.; Christian, D. A.; Pajerowski, J. D.; Brown, A. E. X.; Loverde, S. M.; Discher, D. E. *Macromolecules* **2010,** 43, 9736-9746.

87. Jain, S.; Bates, F. S. *Science* **2003,** 300, 460-464.

88. Safran, S. A. *Surface Science* **2002,** 500, 127-146.

89. Bang, J.; Jain, S.; Li, Z.; Lodge, T. P.; Pedersen, J. S.; Kesselman, E.; Talmon, Y. *Macromolecules* **2006,** 39, 1199-1208.

90. Almusallam, A. S. *Physical Chemistry Chemical Physics* **2010,** 12, 12198-12207.

91. Egli, S.; Schlaad, H.; Bruns, N.; Meier, W. *Polymers* **2011,** 3, 252-280.

92. Zupancich, J. A.; Bates, F. S.; Hillmyer, M. A. *Biomacromolecules* **2009,** 10, 1554-1563.

93. Toncheva, V.; Van Den Bulcke, A.; Schacht, E.; Mergaert, J.; Swings, J. *Journal of Polymers and the Environment* **1996,** 4, 71-83.

94. Ge, H.; Hu, Y.; Jiang, X.; Cheng, D.; Yuan, Y.; Bi, H.; Yang, C. *Journal of Pharmaceutical Sciences* **2002,** 91, 1463-1473.

95. Geng, Y.; Discher, D. E. *Journal of the American Chemical Society* **2005,** 127, 12780-12781.

96. Nie, T.; Zhao, Y.; Xie, Z.; Wu, C. *Macromolecules* **2003,** 36, 8825-8829.

CHAPTER 5. Quantitative Membrane Loading of Quantum Dots into Polymersomes

5.1. Summary

Multi-functional materials that combine both hydrophilic and hydrophobic agents with novel, exceptional properties gained increasing attention in recent years for their potential applications in nanobiotechnology. By incorporating inorganic, strongly fluorescent hydrophobic quantum dots (QDs) of exceptional photostability into the bilayer membrane of polymer vesicles, we developed a new imaging system with wide-ranging potential for biomedical applications. The hydrophobic shell of diblock copolymer vesicles was successfully loaded with highly fluorescent CdSe/ZnS QDs as hydrophobic model substrates. The nano- and micro-scopic effects on the resultant vesicles' structural and material properties were studied. The combination of fluorescence microscopy studies to examine the meso-scale morphology of CdSe/ZnS QD incorporated polymersomes and cryogenic transmission electron microscopy (Cryo-TEM) experiments to observe nano-scale morphology of gold nanoparticle incorporated polymersomes showed that the nanoparticles were located within the hydrophobic interior of the shell bilayer, introducing curvature of the copolymer layers around the guest nanoparticles. In addition, to investigate whether incorporation of nanoparticles into polymersome bilayers impact physical properties of the polymer vesicles, fluorescent CdSe/ZnS QDs of two different sizes (average diameter = 2.1 and 5.2 nm, as determined by TEM) were selected as hydrophobic model substrates and quantitatively enclosed into the vesicles with polymersome membranes fabricated from three different diblock

copolymers poly(ethylene oxide)-block-poly(butadiene) PEO_{30}-b-PBD_{46} (OB2, membrane thickness 9.6 nm), PEO_{80}-b-PBD_{125} (OB18, membrane thickness 14.8 nm) and poly(ethylene oxide)-block-poly(ε-caprolactone) PEO_{45}-b-PCL_{107} (OL, membrane thickness 27.2 nm) at various QD concentrations. The self-assembled polymersome bilayer structures remained essentially unchanged, in appearance of some multilayered and aggregated structures when hydrophobic CdSe/ZnS QDs were incorporated within the vesicle shell. To note, the morphology of OL polymersomes incorporating CdSe/ZnS QDs changed from a highly crystalline, rigid vesicle structure to a noncrystallized, amorphous vesicle structure. Both the QD size and concentration impact this phenomenon. For small 2.1 nm CdSe/ZnS QDs, the vesicle structure remains crystalline at low QD concentrations, and the morphology change only happened in appearance of a high QD concentration. However, for larger 5.2 nm CdSe/ZnS QDs, vesicle morphology changes were evident at both low and high concentrations. Ongoing studies are now carried out to examine vesicle mechanical properties as a function of QD size and concentration via micropipette aspiration experiments.

Furthermore, we demonstrate the reproducible and quantitative loading of various sized hydrophobic CdSe/ZnS QD molecules within synthetic polymersome membranes. The limits for QDs incorporation inside the polymersome hydrophobic shell was systematically evaluated; revealed how far the bilayer can curve before different structural assemblies are favored. The polymersomes have a large capacity to solvate these large hydrophobic QDs within their thick membranes. These aqueous-insoluble QDs can be readily dispersed at high solution concentrations via membrane incorporation within aqueous vesicle suspensions. Due to membrane incorporation, hydrophobic

CdSe/ZnS QDs encapsulants were effectively prevented from self-aggregation, and successfully shielded from deleterious environmental interactions. Together, these studies present a generalized paradigm for the generation of promising multifunctional inorganic-organic hybrid materials suitable for *in vivo* biomedical applications.

5.2. Introduction

The incorporation of nanoparticles into artificial membranes is very important in medical science and nanotechnology, featuring a wide range of applications in drug delivery and sensor technologies.[1] Of utmost interest in this context are polymersomes because of their unique ability to form a variety of polymer-based, biocompatible nano/microstructures. Amphiphilic block copolymers tend to self-assemble into polymersomes[2-4] with hydrophobic bilayer membranes and hydrophilic inner corona similar to liposomes.[5] Such block copolymer vesicles in aqueous media have attracted increasing interest due to their enhanced stability compared to classical liposomes and due to the potential to control vesicle properties such as bilayer thickness, permeability, and surface functionalities by appropriate chemical copolymer adjustment.[2] These properties of polymersomes offer a powerful route to the formation of multifunctional nanosized materials for imaging and drug delivery applications.[6-8]

Currently, there are two different approaches for incorporation of nanoparticles into the vesicles: (1) nanoparticles are formed in situ within the polymersomes (2) nanoparticles are induced into the vesicle during self-assembling. In the first approach, metal salts are usually solubilized within the vesicle, followed by chemically reduction and production of the final metal nanoparticles at the same sites where they initially present.[9-15] The main disadvantage of this process is that the vesicles may be decomposed

and less stable during the chemical modification steps to produce metal nanoparticles, thus limits the applicable chemistry and the nanoparticles growth within the vesicles may not be well controlled. In the second approach, by providing hydrophobic properties within their high capacity hydrophobic bilayer membranes, the polymersomes enable the incorporation of large nanoparticles into the vesicle shell during self-assembly processes. Preformed nanoparticles of a specific size with defined structure and solubilizing surface groups are directly incorporated into vesicular structures via interfacial interaction. In this case, the nanoparticles have a better defined shape, size and morphology since they are preformed and characterized. In addition, interfacial interaction between the nanoparticles and the membrane can be tuned much more efficiently, enabling the controlled loading of nanoparticles into polymer vesicles.

To date, not much work has been done on nanoparticle incorporated polymersomes via self-assembling that are suitable for *in vivo* applications. Lots of nanoparticles and diblock copolymers hybrids form micelles[16-18], oligolamella "onion-like" structures[19] or or irregular polymer/nanoparticle aggregates[17, 20] rather than vesicle structures. In addition, the present nanoparticle and diblock copolymer systems that form polymersome vesicles are based on cosolvent method[21-23] which involves use of organic solvents during the preparation which can lead to *in vivo* toxicity. The only study that incorporated quantum dots and gold nanoparticles in diblock copolymers by the film rehydration method didn't show direct province of nanoparticles locating in the bilayer membrane. The authors claimed the self-assembly structures are polymersomes, however, the vesicle structure was difficult to discern and appear to have micellar properties as measured by TEM.[24, 25]

To the best of our knowledge, this report is the first to describe well-defined meso-scale and nano-scale polymersomes packed with nanoparticles in the bilayer membrane formed by thin-film hydration method. Specifically, QDs were chosen as the hydrophobic model substrate to be induced into the polymersomes. Semiconductor crystallites (known as QDs)[26-28] are excellent probes for bioimaging applications due to their broad excitation spectra, narrow emission spectra, tunable emission peaks, long fluorescence lifetimes and negligible photobleaching. [29-31] However, they must maintain three properties under aqueous biological conditions: efficient fluorescence, colloidal stability, and low nonspecific adsorption. Besides, the use of QDs in biological cells always poses concerns about potential cytotoxicity. QDs tend to aggregate, resulted in poor colloidal stability[32] and toxicity in live cells[33]. Consequently, the use of QDs in biological applications is still limited and primarily confined to in vitro studies. By incorporation of hydrophobic QDs into the polymersome membranes, we developed a generic method for making QDs water-soluble and biocompatible, well dispersed and separated in the vesicles for greatly increased colloidal stability and decreased toxicity.

Our first work involves preparation of meso-scale CdSe/ZnS QD incorporated polymersomes with three different diblock copolymers OB2, OB18, and OL at various QD concentrations. As observed by confocal microscopy, classic bilayer vesicle structures coexist with some multilayered and aggregated vesicle structures for all polymersome samples composed with different diblock copolymers, and the vesicles sizes decreased with increasing QD concentration in the vesicle shell. Very interestingly, we noticed a morphology transition of QD encapsulated OL diblock from highly crystalline vesicles to non-crystalline vesicles after nanoparticle incorporation,

underscoring the importance of the self-assembly structure and nanoparticle arrangement. Moreover, Cryo-TEM experiments were performed for the visualization of the nano-sized nanoparticle incorporated polymersomes. Due to the low dynamic contrast of these CdSe/ZnS QDs, gold nanoparticles were loaded into the hydrophobic membranes. The cryo-TEM results correspond well with confocal microscopy studies, indicate the consistency of the vesicle properties in both meso- and nano-dimensions.

To explore the capacity of polymer vesicles to stably incorporate nanoparticles non-covalently within their thick lamellar membranes, polymersomes self-assembled from three diblock copolymers with CdSe/ZnS QDs incorporated in prescribed molar ratios within their membranes were generated and characterized. The extent of vesicle membrane loading of QDs was quantitative measured by optical verification via steady state absorption. We demonstrate that polymersomes can be loaded with sizes ranging 2-5 nm QDs below a critical saturation point without significantly compromising the robust thermodynamic and mechanical stabilities of these synthetic vesicle assemblies. Abover the saturation point, there are strong aggregation interactions in-between the QDs as well as between the QDs and dibock copolymers, resulted in a low QD uptake efficiency. Finally, steady-state fluorescence spectroscopic studies were employed for delineation of intermembranous interactions of QDs and diblock copolymers. As expected, at identical membrane concentrations, the emission intensity per QD is higher for thicker membranes and smaller QDs, both accounts for the strong aggregation effect in a thin membrane and for larger QDs.

5.3. Experimental Methods

5.3.1. Preparation of Nanoparticle Incorporated Polymersomes

PEO(1300)-*b*-PBD(2500) (OB2) and PEO(3600)-*b*-PBD(6800) (OB18) copolymers under study were custom synthesized by Polymer Source, Inc (Dorval, Quebec Canada). PEO(2K)-*b*-PCL(12K) copolymers was synthesized following established ring opening polymerization methodology as described in 4.3.1. CdSe/ZnS QDs with hexadecyl amine ligand at sizes of 2.1 nm and 5.2 nm were purchased from Evidentdot Inc. 2-4 nm gold nanoparticles with oleic amine ligand were purchased from Sigma-Aldrich. Formation of giant (> 1 um) and small (< 300 nm) diameter emissive polymersomes followed thin-film hydration procedures. Briefly, diblock copolymer and nanoparticles species in toluene were combined at different molar ratios and uniformly coated on the surface of a Teflon plate, followed by evaporation of the solvent under vacuum for > 12 h. The Teflon plate consisted of a l/16" thick sheet of Teflon cut in small squares and roughened by sand paper to create macroscopically uniform digitations. Addition of aqueous solution (DI water) and heating at 60 °C for 48 h led to spontaneous budding of giant (5-50 μm) emissive polymersomes (membrane loaded at prescribed polymer:nanoparticle molar ratios) off of the Teflon and into the aqueous surroundings. Small (< 300 nm diameter) unilamellar polymersomes that possess appropriately narrow size distributions were prepared via procedures analogous to those used to formulate small lipid vesicles (sonication, freeze-thaw extraction, and extrusion). Free nanoparticles were removed by dialysis using a 1000 kDa membrane (SpectrumLab, Inc).

5.3.2. Morphology characterization of Nanoparticle Incorporated Polymersomes

<u>Confocal Laser Scanning Microscopy</u>: All confocal images were collected on a Leica SP5 laser scanning confocal microscope (Wetzlar, Germany). A 405 nm diode laser source was coupled to an inverted Leica DM16000CS microscope with a $40\times$ oil-immersion objective (Leica Plan NeoFluor, NA=1.25). An acousto-optic beamsplitter (AOBS) with a collection bandwidth of 20 nm served as a dichroic mirror to allow the 405-nm excitation light to reach the sample and to allow selection of emission wavelengths. The emission bandpass for integrated fluorescence intensity measurements was set to 500-750 nm. Cooled photomultiplier tubes (PMTs) were used to measure fluorescence through a 121 μm pinhole in a confocal arrangement with a theoretical axial resolution of 2 μm. Images were line averaged ($16\times$ per line) for improved image quality. Leica LAS AF 1.8.2 software was used for data acquisition.

<u>Cryo-TEM</u>: Specimens were prepared in a Controlled Environment Vitrification System (Vitrobot). Approximately 10 μL of solution were deposited on a holey carbon film supported on a TEM grid (200 mesh, Ted Pella). Blotting the excess solution produced 100-300 nm thick films suspended in the void spaces of the holey film. Rapid immersion in liquid ethane (-180 ℃) vitrified the solutions, which were then transferred to a liquid nitrogen cooled Cryo-TEM holder (Gatan 626). High magnification images were obtained using a FEI Tecnai G ²Twin TEM at 200 kV.

5.3.3. Quantification of QD Incorporated Polymersomes

Aqueous suspensions (in DI water) of small nano-sized CdSe/ZnS QDs emissive polymersomes were transferred to a glass vial, frozen in liquid N_2, and lyophilized (FreeZone 4.5 L Benchtop Freeze Dry System, Labconco Corporation, Kansas City, MO;

Model 77500) for 24 hours to destroy the vesicles and dry the polymer and fluorophore species. The mass of the dry samples were measured. The dry samples were then taken up in toluene and their absorption spectra recorded on a Shimadzu UV-1700 Spectrofluorimeter (Varian Inc, USA) . The concentrations of CdSe/ZnS QDs in the original polymersome solutions were calculated via Beer's Law using the toluene absorption spectra and the previously determined average molar extinction coefficients for each CdSe/ZnS QDs in this solvent. The mass of the recovered polymer was calculated by subtracting the mass of QDs from the mass of dry sample mixture.

5.3.4. Emission Profiles of QD Incorporated Polymersomes

Fluorescence spectra of emissive CdSe/ZnS QD incorporated polymersomes were obtained with Edinburge FL920 spectrophotometer (Edinburgh Instruments Ltd, UK). Emission spectra were corrected using the spectral output of a calibrated light source supplied by the National Bureau of Standards. QD incorporated polymersome solutions were produced from thin-film formulations of polymer and QDs deposited at various molar ratios. Steady state electronic absorption spectra of the solutions were obtained prior to dilution to yield fluorophore absorptions less than 0.05 ABS units in each sample. Steady state fluorescence spectra were recorded and normalized by fluorophore absorption to yield the relative fluorescence per molecule in each of the various vesicle formulations. This value was then multiplied by the number of QDs per polymersome and reported as the relative fluorescence intensity per vesicle.

5.4. Results and Discussion

5.4.1. Generation of Nanoparticle Incorporated Polymersomes in Micro- and Nano- Dimensions

Figure 5.1A depicts the steps involved in the fabrication of nanoparticle incorporated polymersomes. A solution of nanoparticles and polymers in toluene is dried on a thin teflon film to form a multilamellar polymer film, from which vesicles are spontaneously formed by hydration under water and sonication. We investigated three diblock copolymers (different hydrophobic blocks, various block lengths, etc.), as well as nanoparticle with different sizes and surface ligands and their impact upon bilayered vesicle formation. We found that the nanoparticle incorporation into polymersomes is not limited to any particular class of polymer, polymer size regime, or set of NP surface ligands. For observation by confocal microscopy, we constructed giant vesicles (1-50 μm) by classical swelling. **Figure 5.1B** shows representative confocal images of meso-scale vesicles, which appear as spherical emissive circles with a more intensive fluorescent perimeters. This result demonstrates that the hydrophobic CdSe/ZnS QDs are integrated in the hydrophobic bilayer of the vesicle, and a high yield of giant unilamellar vesicles was obtained. **Figure 5.1C** shows Cryo-TEM images of 2-4 nm gold nanoparticle incorporated into the membranes of nanoscale vesicles. The scattering contrast of gold nanoparticles is much higher compared to the diblock copolymer, enabling the gold nanoparticles to be clearly seen as dark spots inside the vesicle structure. The polymersomes are frozen in a thin water film during Cryo-TEM experiments, resulted in the projection of the three-dimensional vesicle into the two-dimensional imaging.[21] Those

gold nanoparticles appearing in the aqueous inner core are therefore also enclosed in the vesicle shell due to the projection.
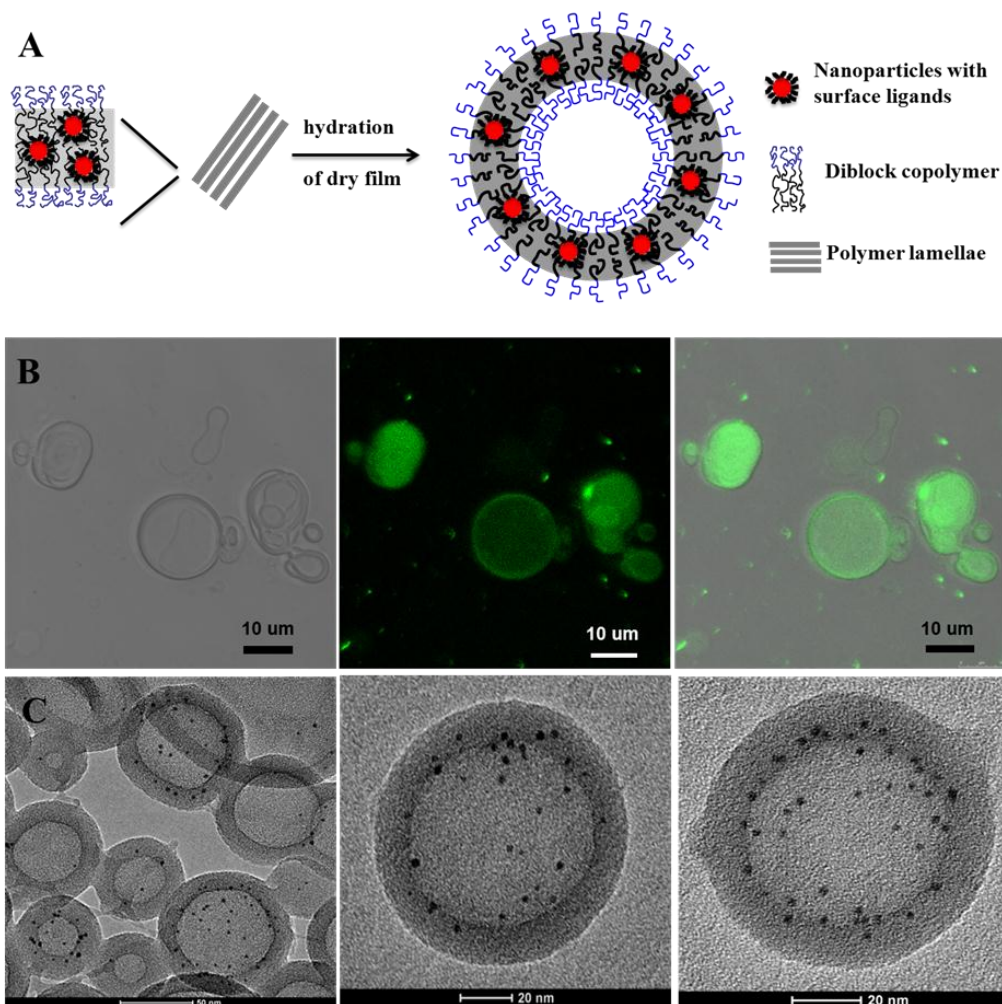
Figure 5.1 A. Steps involved in the formation of nanoparticle incorporated polymersomes.

B. Confocal fluorescence images of 2.1 nm CdSe/ZnS QD incorporated OB18 polymersomes by hydration swelling. Left column: optical microscopy images; central column: fluorescent microscopy images; right column: overlapped images.

C. Cryo-TEM images of 2-4 nm Gold nanoparticles with oleic amine ligand incorporated nanosized OB18 polymersomes by hydration, sonication and extrusion.

5.4.1.1. *Confocal Microscopy Characterization of QD Incorporated Meso-scale Polymersomes*

Confocal microscopy studies demonstrate dispersion of numerous highly emissive CdSe/ZnS QDs within the polymersome hydrophobic membranes, and show that the vesicles maintain an aqueous interior free of nanoparticles with potential for hetero-functional utility such as hydrophilic drug delivery. The accumulation of CdSe/ZnS QDs within polymersome membranes is strongly driven by their hydrophobicity. In addition, there is neither detectable leakage of nanoparticles to the external aqueous solution or internal core as observed by confocal microscopy over weeks at room temperature.

Furthermore, the morphology of QD incorporated polymer self-assemblies was studied with various QD concentrations in the copolymer bilayer membrane. For OB2 polymersomes, we observed smaller vesicles and more multilayered and aggregated structures with increasing QD concentrations (**Figure 5.2** and Figure **5.3**). Besides, the vesicle sizes varied considerably between the two OB molecular weights. Following hydration we observed mostly 5-10 μm with some 20 μm vesicles for lower molecular weight QD incorporated OB2 polymersomes, and 1-2 μm with some 10 μm vesicles for QD incorporated OB18 polymersomes.

OL diblock copolymer was also used to self-assemble into μm-sized polymersomes with CdSe/ZnS QDs. Confocal microscopy studies of this system show very interesting results. A significant phase transformation of the vesicle structure with increasing nanoparticle concentration was observed. As shown in **Figure 5.4**, for OL polymersomes with a small amount (0.08 mol%) of 2.1 nm CdSe/ZnS QDs, the vesicles remained as crystalline, irregular structures. However, when the incorporated 2.1 nm

CdSe/ZnS QDs concentration was increased to 0.5 mol%, the vesicle structures was more amorphous and appears as sphere vesicles. For larger 5.2 nm CdSe/ZnS QDs, at both low (0.08 mol%) and high (0.5 mol%) QD incorporation concentrations, the morphology changed to noncrystalline, spherical vesicles. The polymersome morphology of 2.1 nm CdSe/ZnS QD incorporated OL polymersomes at a low nanoparticle concentration of 0.08 mol% is very similar to the unincorporated OL polymersomes (**Figure 5.5**). Therefore, by simply incorporating QDs into the OL polymersomes, we achieved the transition of OL polymersome membrane from rigid crystallized membranes to soft elastic membranes as ideal candidates to successfully passivate tumor tissue *in vivo* (as described in 4.2). The surface membrane of a giant 5.2 nm CdSe/ZnS QD incorporated polymersome was also measured by Z-section confocal microscopy. The distribution of CdSe/ZnS QDs in the bilayer membrane was mostly uniform with some aggregation as observed in **Figure 5.6**.

This morphology transformation phenomenon in QD incorporated OL polymersomes can be explained by the interaction of the QDs with the polymersome hydrophobic membrane. The QDs are in dynamic state in the vesicle bilayer membrane, and the motion of QDs would disturb the crystalline structure of bilayer, resulting the decrease of phase transition temperature (T_c) and the increase of the fluidity of bilayer, thereby cause the phase transition of OL polymersomes.

Figure 5.2 Capacity of OB18 polymersome membranes to stably incorporate and solvate CdSe/ZnS QDs.

(A) Polymersomes containing equal aqueous concentrations of polymer but with different amounts of 2.1 nm CdSe/ZnS QDs, as indicated by the molar ratios of polymer:QD; (B) Polymersomes containing equal aqueous concentrations of polymer but with different amounts of 5.2 nm CdSe/ZnS QDs, as indicated by the molar ratios of polymer:QD. Aggregated and multilayered structures are shown for both 2.1 nm and 5.2 nm CdSe/ZnS QD incorporated OB2 and OB18 polymersome compositions.

OB2: 2.1nm CdSe/ZnS mole ratio:
1000:1   200:1

OB2: 5.2nm CdSe/ZnS mole ratio:
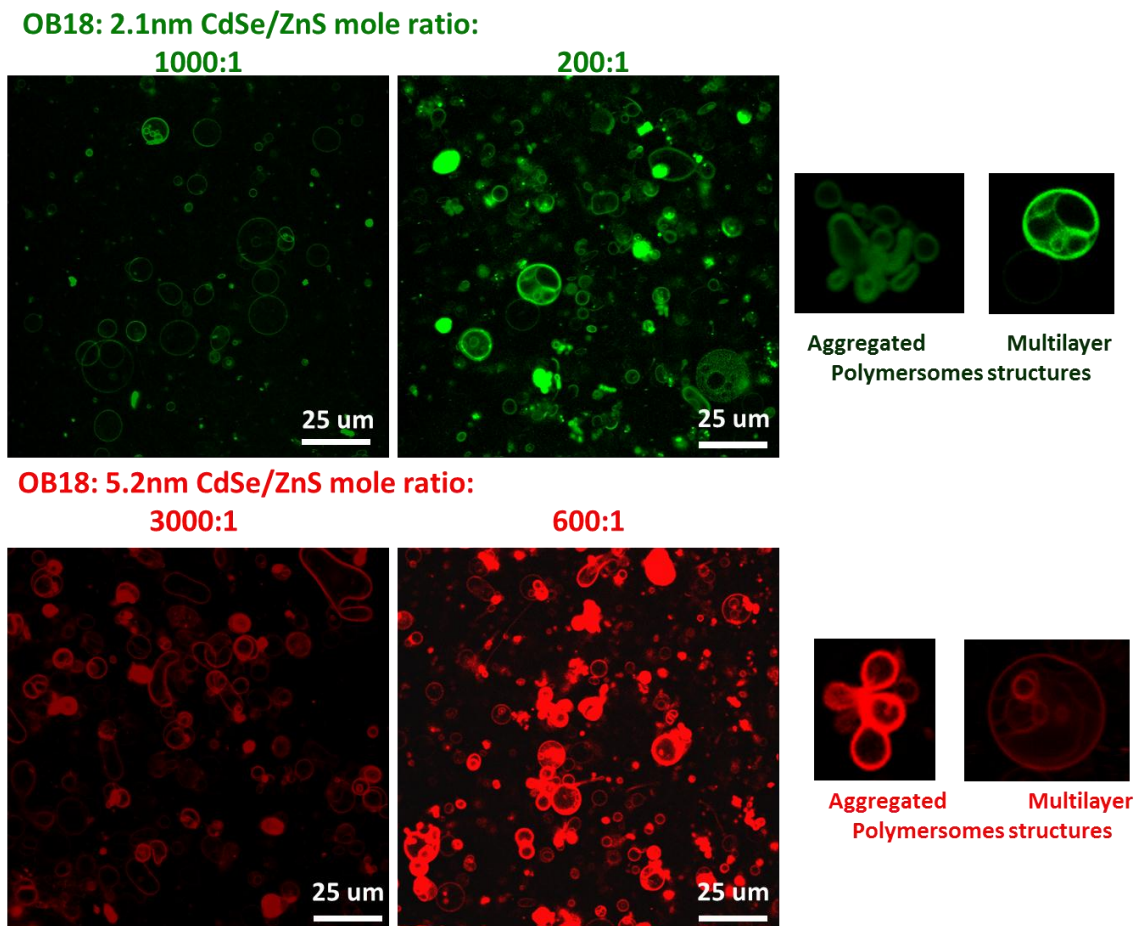3000:1   600:1
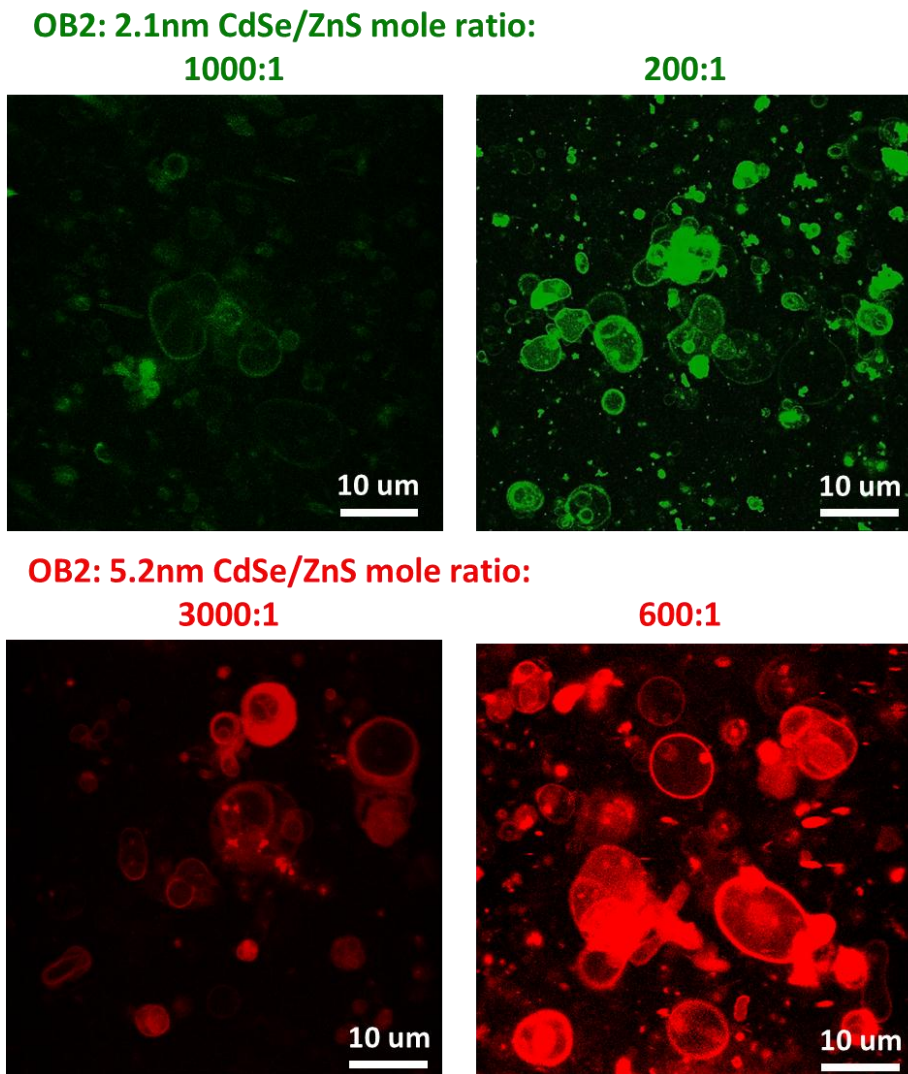
Figure 5.3 Capacity of OB2 polymersome membranes to stably incorporate and solvate CdSe/ZnS QDs.

(A) Polymersomes containing equal aqueous concentrations of polymer but with different amounts of 2.1 nm CdSe/ZnS QDs, as indicated by the molar ratios of polymer:QD; (B) Polymersomes containing equal aqueous concentrations of polymer but with different amounts of 5.2 nm CdSe/ZnS QDs, as indicated by the molar ratios of polymer:QD.

281
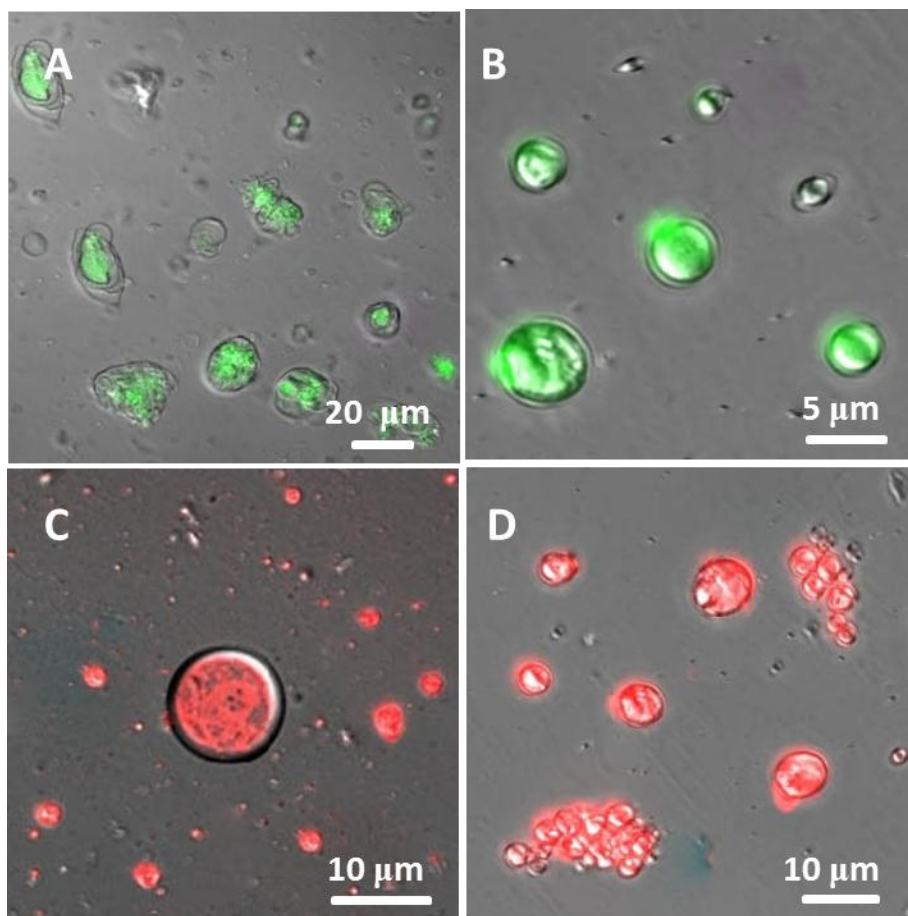
Figure 5.4 Overlapped confocal fluorescence images of different sized CdSe/ZnS QD incorporated OL polymersomes by hydration swelling.

A. OL to 2.1 nm CdSe/ZnS QD molar ratio: 1200:1; B. OL to 2.1 nm CdSe/ZnS QD molar ratio: 200:1; C. OL to 5.2nm CdSe/ZnS QD molar ratio: 1200:1; D. OL to 5.2nm CdSe/ZnS QD molar ratio: 200:1.
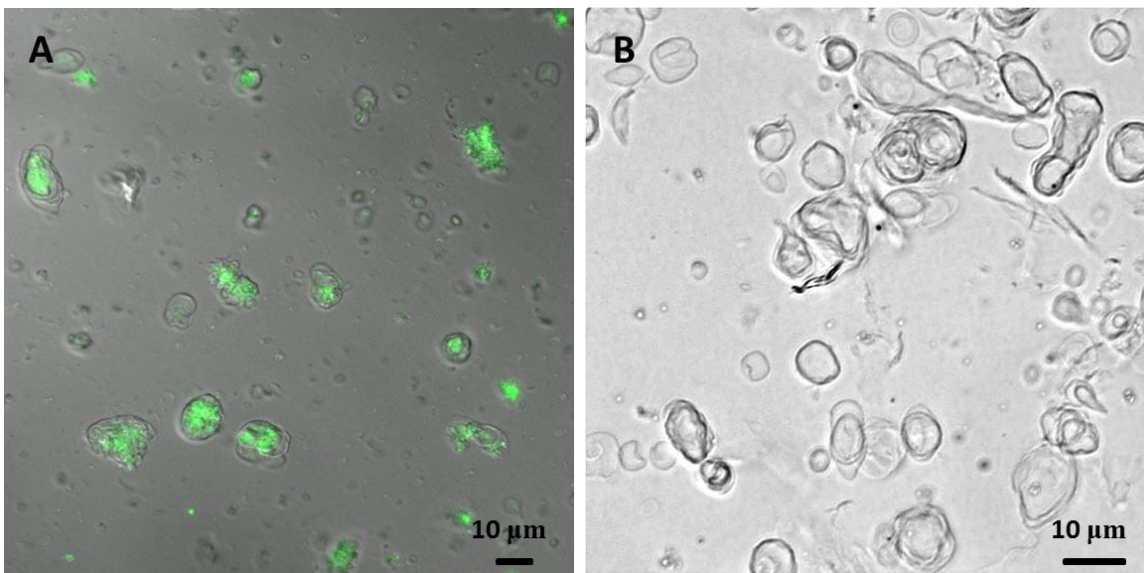
Figure 5.5 (A) Overlapped fluorescence confocal microscope image of 2.1 nm CdSe/ZnS QD incorporated OL polymersomes at OL to 2.1 nm CdSe/ZnS QD molar ratio: 1200:1 by hydration swelling. (B) Nonincorporated optical microscope image of OL polymersomes.

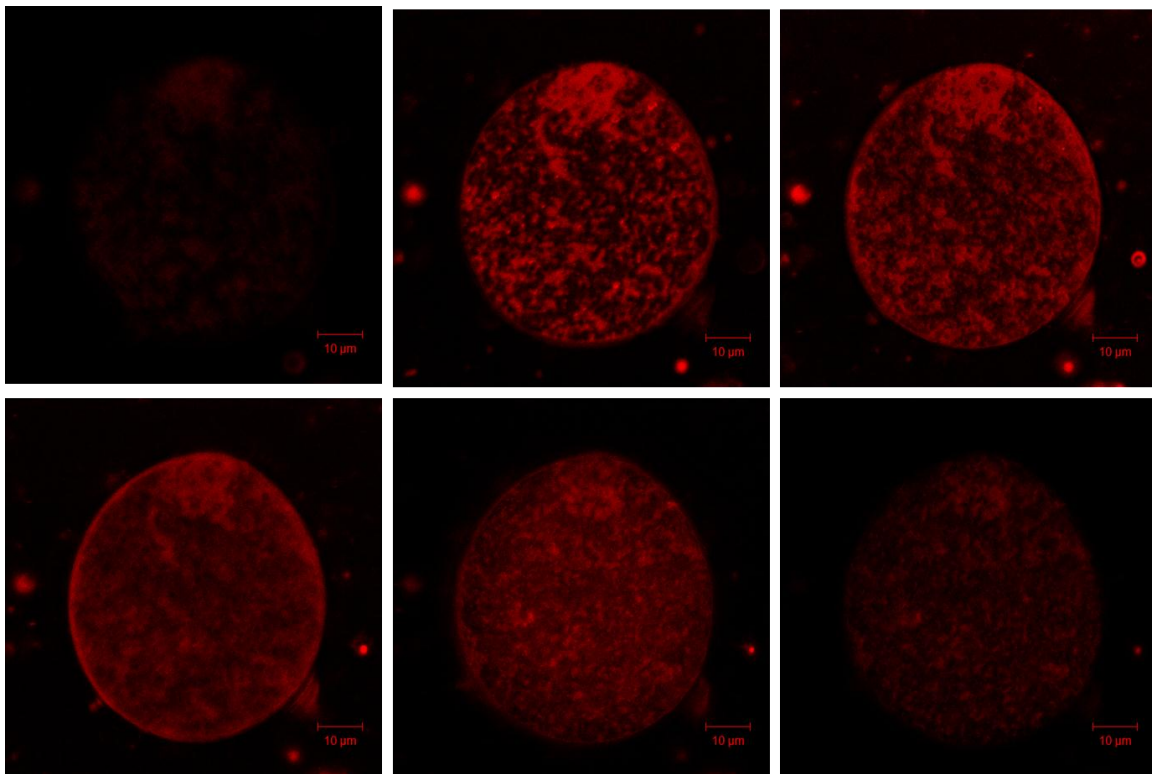**Figure 5.6** Z-section confocal fluorescence confocal images of 5.2nm CdSe/ZnS QD incorporated OL polymersomes by hydration swelling.

OL to 5.2nm CdSe/ZnS QD molar ratio: 1200:1. Total Z-sectioning was 12 μm in depth.

5.4.1.2. Cryo-TEM Characterization of Gold Nanoparticle Incorporated Nano-scale Polymersomes

The morphology of CdSe/ZnS QD incorporated polymer self-assemblies in meso-dimensions was studied by confocal microscopy and showed successful incorporation of nanoparticles into polymersome bilayer membranes. Furthermore, we want to study the morphology of nanoparticle incorporated polymer vesicles in nano-dimensions. Since these CdSe/ZnS QDs have a very low electron density, and are not able to be observed after incorporating into the polymer membranes by Cryo-TEM. The electron-dense gold nanoparticles were used to incorporate into the polymer bilayer membranes and the morphologies were subsequently examined by Cryo-TEM.

Similarly to µm-sized CdSe/ZnS QD incorporated polymersomes, gold nanoparticles with a different surface ligand (oleic acid) also self-assemble into the bilayer membrane of nano-sized polymersomes, as observed by Cryo-TEM, suggests that the surface ligands on the nanoparticles have minimal effect on the self-assembling process. In nm-sized gold nanoparticle incorporated polymersome samples, a mixture of bilayered, multilayered and aggregated structures was also observed (**Figure 5.7**). However, the amount of multilayered and aggregated structures was less than that seen in µm-sized vesicles. As visually estimated from Cryo-TEM experiments, approximate 70-90% of the gold nanoparticle incorporated OB18 polymersomes are single bilayered normal vesicle structures, with small amount multilayered and aggregated structures; while in µm-sized polymersomes, over 50% vesicles are multilayered and aggregated. This phenomenon may be caused by the sonication step that decreased the aggregation of nanoparticle incorporated vesicles during the self-assembling process for nano-scale

polymersomes formation. Also, as expected based on μm-sized CdSe/ZnS QD incorporated polymersomes results, with an increase in loading concentration of gold nanoparticles, much smaller and more aggregated polymersomes were formed (**Figure 5.8**). The membrane thicknesses of three different polymersomes with and without gold nanoparticle incorporation were also measured from Cryo-TEM (**Figure 5.9**), and were found to be consistent before and after gold nanoparticle incorporation.

This gold nanoparticle incorporated polymersome system is a well-defined example of hydrophobic vesicle shell loading, with only hydrophobic interactions between copolymer and nanoparticle. The copolymer bending around the guest nanoparticles as a function of membrane thickness, incorporated nanoparticle diameters and concentrations was examined. A mechanism hypothesis (**Figure 5.10**) is proposed based the observed phenomena that aggregation of nanoparticles affects its incorporation into block copolymers self-assembled polymersomes. Usually, the assembly of the vesicles is driven by hydrophobic/hydrophilic (or interfacial) effects,[34-37] but there are also important secondary effects[38-40] such as curving of membranes, budding of vesicles or fission and fusion of vesicles upon the interaction of nanoparticles with the interface or surface of the membrane. The interaction energy between the nanoparticles and the polymer vesicle membrane determines the polymer self-assemblies structures and the physical properties of the polymersome membrane. The size and number of the nanoparticles also play an important role for curving effects to or from the membrane, fusion or fission of the vesicles or even embedding of the nanoparticle within a membrane occurs.[24] Therefore, the change of interfacial interactions of the QDs and diblock copolymers at various QD concentrations or different QD sizes, causes the

aggregation effect and induces the change of the membrane mechanical properties. At a low nanoparticle concentration, the nanoparticle aggregation effect is small and most nanoparticles are uniformly distributed with the diblock copolymers. Thus, upon self-assembly, we observed a large amount of single dispersed bilayer vesicle structures together with a small portion of the multilayered and aggregated structures. With an increasing of the nanoparticle concentration, there will be more aggregation from the nanoparticles and more multilayered and aggregated vesicle structures were observed. Finally, at a very high nanoparticle concentration, most nanoparticles tend to aggregate together and instead of incorporation into the polymersome bilayer membranes, they formed large aggregates and directly precipitated out of the aqueous solution during self-assembling, leaving behind polymersomes with very low nanoparticle concentrations in the bilayer membranes. The observed vesicle size decreased with increasing nanoparticle concentrations can also be explained using this hypothesis. With increasing nanoparticle concentration in the polymersome bilayer membrane, the interaction energy of nanoparticles with the hydrophobic membrane increases, resulted in increased interfacial curvature, or decreased membrane bending rigidity of the membrane and thus the smaller and more aggregated structures. In addition, the membrane thickness does not change much after nanoparticle incorporation, indicating that the nanoparticles are densely compacted within the hydrophobic membrane of the polymersomes.

Double-bilayered structure

The membrane thickness of this polymersome is twice of the normal polymersome.

Aggregated structure
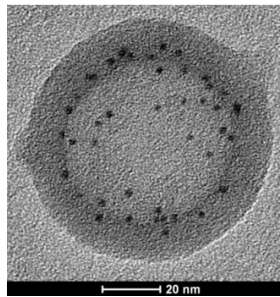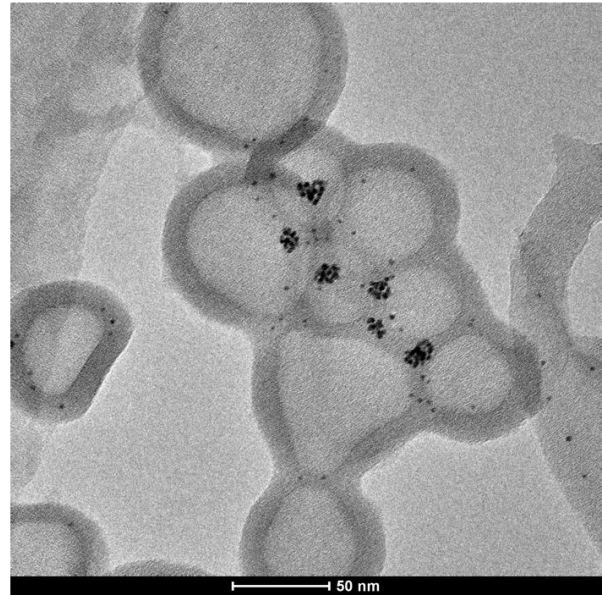
Single bilayer structure

Figure 5.7 Cryo-TEM images of 2-4 nm gold nanoparticle incorporated OB18 polymersomes show multilayered and aggregated vesicle structures.

OB2: 2-4nm Gold nanoparticles mole ratio

1000:1   600:1   400:1
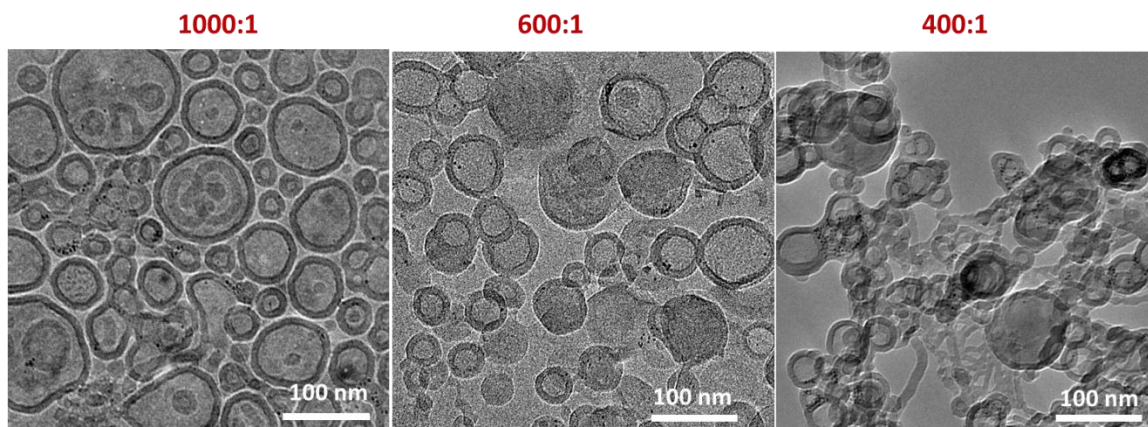
Figure 5.8 Cryo-TEM images of 2-4 nm gold nanoparticle incorporated polymersomes with increasing nanoparticle concentration, as indicated by the molar ratios of polymer:gold nanoparticle (left to right).
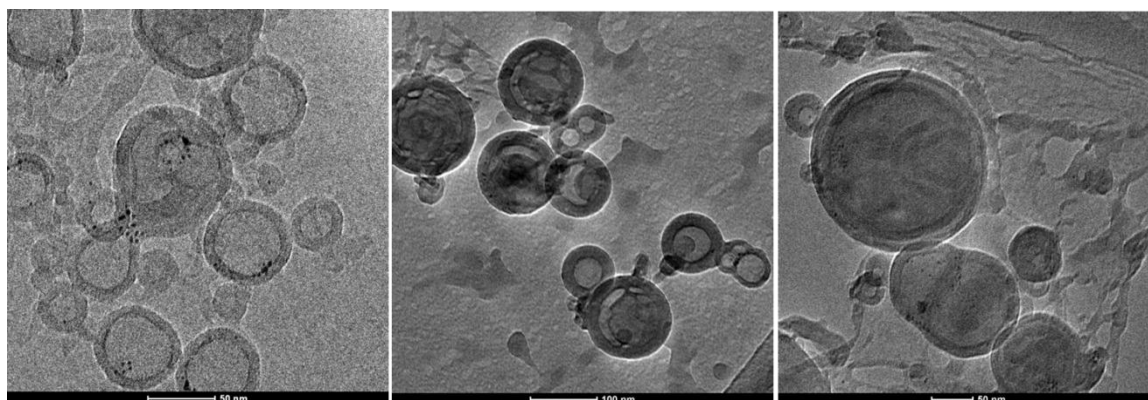
	OB2-Gold	OB18-Gold	OL-Gold
	400:1	600:1	450:1

Polymersomes composition	Membrane thickness	Polymersomes composition	Membrane thickness
OB2-Gold	9.31 ± 1.32 nm	OB2	9.6 ± 1.61 nm
OB18-Gold	14.5 ± 2.17 nm	OB18	14.8 ± 1.96 nm
OL-Gold	26.77 ± 4.62 nm	OL	27.2 ± 6.23 nm

Figure 5.9 Cryo-TEM images of 2-4 nm gold nanoparticle incorporated polymersomes with different polymer environments, and membrane thickness of the polymersomes with or without 2-4 nm gold nanoparticle incorporation.
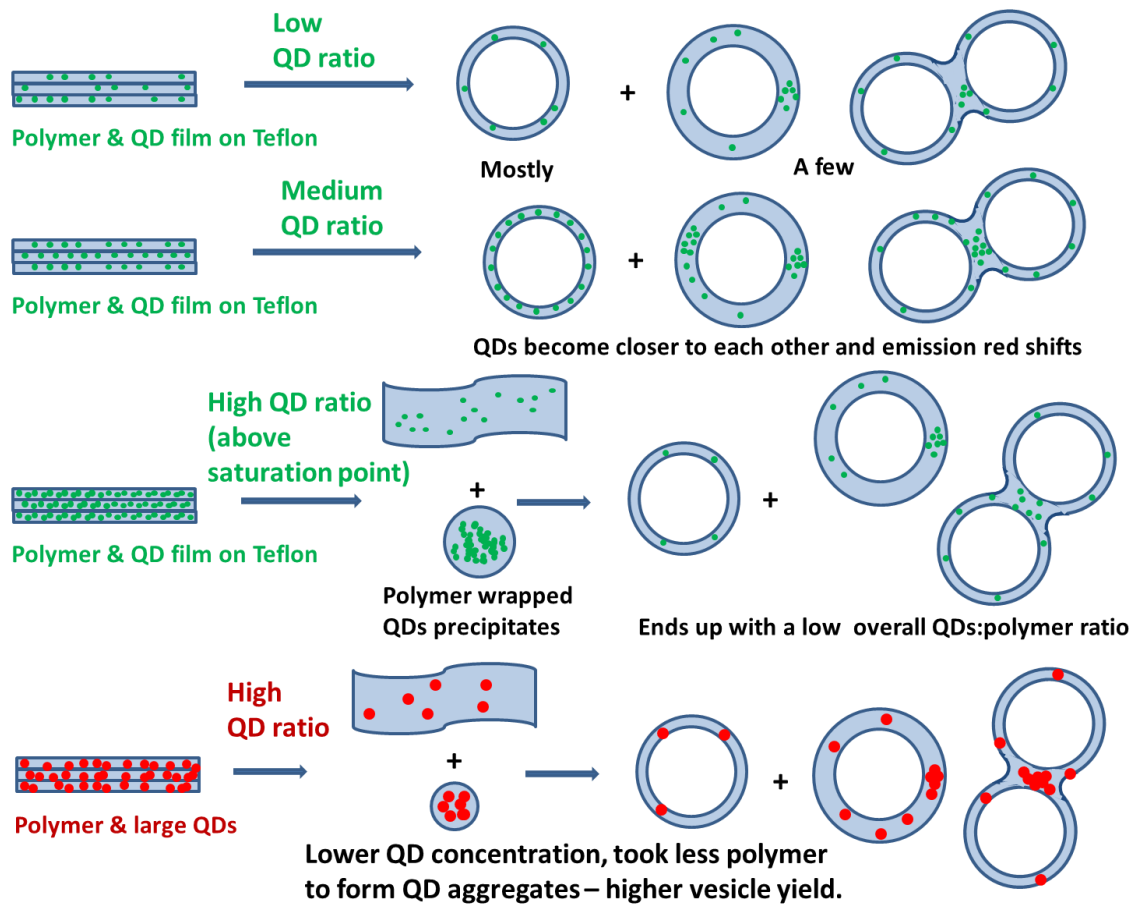
Figure 5.10 Hypothesis for CdSe/ZnS QD incorporated polymersomes formation process

5.4.2. Quantitative Loading of CdSe/ZnS QDs in Polymersomes

To correlate changes in the packing of hydrophobic QDs encapsulates with the extent of membrane loading and their relative sizes to the thickness of the polymersome membrane, further characterization is carried by steady-state absorption and fluorescence spectroscopic studies. Aqueous suspensions of small (<300 nm diameter) emissive polymersomes were formed from thin-film formulations deposited at various mole ratios of three different diblock copolymers (OB2, OB18, OL) and two different sizes emissive CdSe/ZnS QDs (2.1 nm and 5.2 nm). Since the polymer ($\lambda_{abs.max.}$= 255 nm) and 2.1 nm CdSe/ZnS QDs ($\lambda_{abs.max.}$ = 428 nm) or 5.2 nm CdSe/ZnS QDs ($\lambda_{abs.max.}$ = 515 nm) have non-overlapping absorption in aqueous vesicle suspensions, the electronic absorption spectra of the redissolved solution of lyophilized QD incorporated polymersomes in toluene were monitored and the concentrations of CdSe/ZnS QDs were calculated using Beer's Law.

Very different from porphyrin fluorophores incorporated polymer vesicles which can incorporate large payloads of porphyrin chromophores up to 20 mol% for a varies sizes of porphyrins,[41] there is a saturation point for QD incorporation. When the molar ratio of polymer:QD deposited on Teflon were below that saturation point, which is 75:1 for OB2, 50:1 for OB18, 35:1 for OL with 2.1 nm CdSe/ZnS QDs; or 600:1 for OB2, 400:1 for OB18, and over 200:1 for OL with 5.2nm CdSe/ZnS QDs, there was a near perfect correlation with the resultant polymer:QD molar ratio composing the vesicles' membrane structures (**Figure 5.11**), as well as a greater than 80% uptake of the mass of Teflon-deposited fluorophore into the membranes of the water-soluble polymersomes (**Figure 5.12A**). However, when the QD concentration is above the saturation point, the

final QD concentration in vesicle membranes and the uptake efficiency significantly decreases.

The theoretical maximum QD concentration within polymersome membranes can be calculated by assuming the vesicular hydrophobic volume is completely filled up with QDs. Therefore, the maximum 2.1 nm CdSe/ZnS QD concentration (mole ratio of polymer:QD) that can be incorporation in polymersomes is: 24.8:1 for OB2, 15.3:1 for OB18, 9.1:1 for OL; while for 5.2 nm CdSe/ZnS QDs, it is 198.7:1 for OB2, 122.4:1 for OB18, and 74.9:1 for OL. Interestingly, these numbers are all about 3 times multiplex of the experimental data. It is known that there is a critical interaction between nanoparticles and diblock copolymers, below the critical value, there is significant aggregation and above it there is almost no aggregation.[42] Therefore, our study demonstrated that the critical value for CdSe/ZnS QDs incorporation into polymersomes is 1/3 of the theoretically calculated maximum loading concentration. This determined critical value can be used to guide the quantitative loading of any nanoparticles with specific sizes into the polymersome membrane.

The membrane-uptake of QDs into solution corresponds well with the maximum QD loading concentration within vesicle membranes; the uptake of QDs is as high as ~ 70-90% below the saturation concentration and greatly decreased to 10-20% above the saturation concentration. The vesicle yields for 2.1 nm CdSe/ZnS QDs incorporation follow the same trend with the membrane-uptake ability of QDs in vesicles; there is minimal aggregation of QDs and polymers below the saturation point with a high vesicle yield and more aggregation above the saturation point, resulted in the decreased vesicle yield. However, the vesicle yields of 5.2 nm CdSe/ZnS QD incorporated polymersomes

changes differently, without much decreasing above the saturation point as seen in **Figure 5.12B.** A possible explanation for this phenomenon is described in our hypothesis (**Figure 5.10**) that the formation of CdSe/ZnS QD incorporated polymersome is mainly affected by the aggregation effect. The interactions between QDs and the interactions between QDs and segments of the block copolymer both have strong aggregation effect. Above the saturation concentration, the CdSe/ZnS QDs and diblock copolymers form large aggregations which precipitate out of solution (as observed during the sample preparation of 2.1 nm CdSe/ZnS QD incorporated polymersomes), resulted in decreased vesicle yield. Therefore, for larger CdSe/ZnS QDs that are saturated at quite low QD concentration, very few polymers were co-precipitated with the CdSe/ZnS QDs and resulting in small change of the vesicle yield.
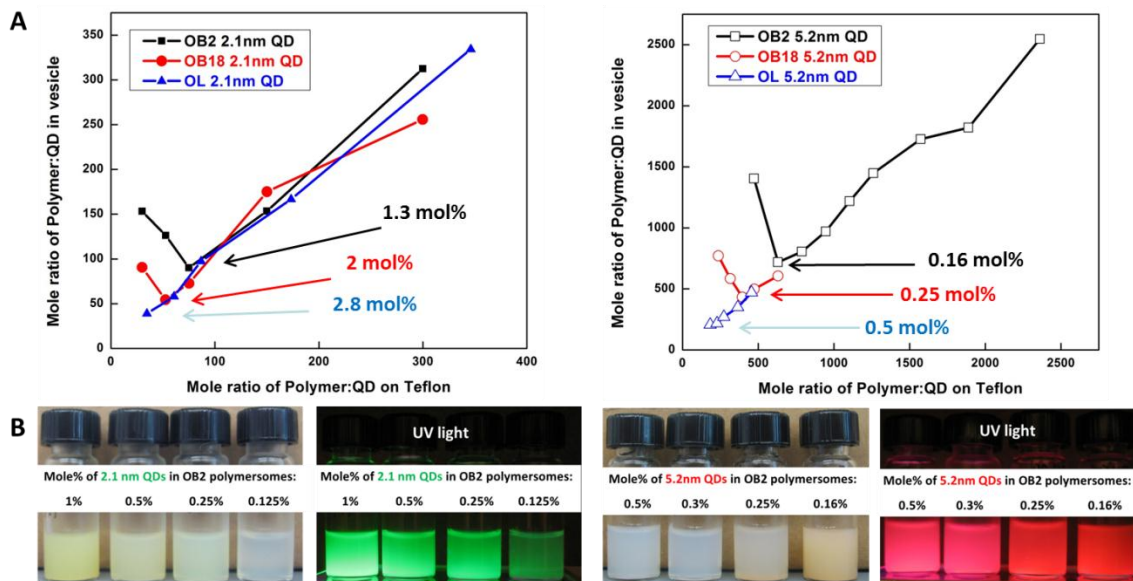
Figure 5.11 Capacity of polymersome membranes to stably incorporate and solvate 2.1 nm and 5.2 nm CdSe/ZnS QDs.

(A) The polymer:QD ratio composing the vesicles' membranes as a function of the polymer:QD molar ratio originally deposited on Teflon, as determined by electronic absorption spectroscopy. Experimental conditions: $T = 23$ °C, DI water.

(B) Solution vials containing equal aqueous concentrations of polymer but with decreasing amounts of CdSe/ZnS QDs, as indicated by the molar ratios of polymer:QD (left to right), under both room light and UV light.

Figure 5.12 Polymersomes accommodating hydrophobic CdSe/ZnS QDs of various sizes.

(A) The membrane-uptake of CdSe/ZnS QDs into aqueous vesicle suspensions and (B) the yield of emissive polymersomes in aqueous solution as a function of the polymer:QD molar ratio originally deposited on Teflon, as determined by electronic absorption spectroscopy. Experimental conditions: $T = 23$ °C, DI water.

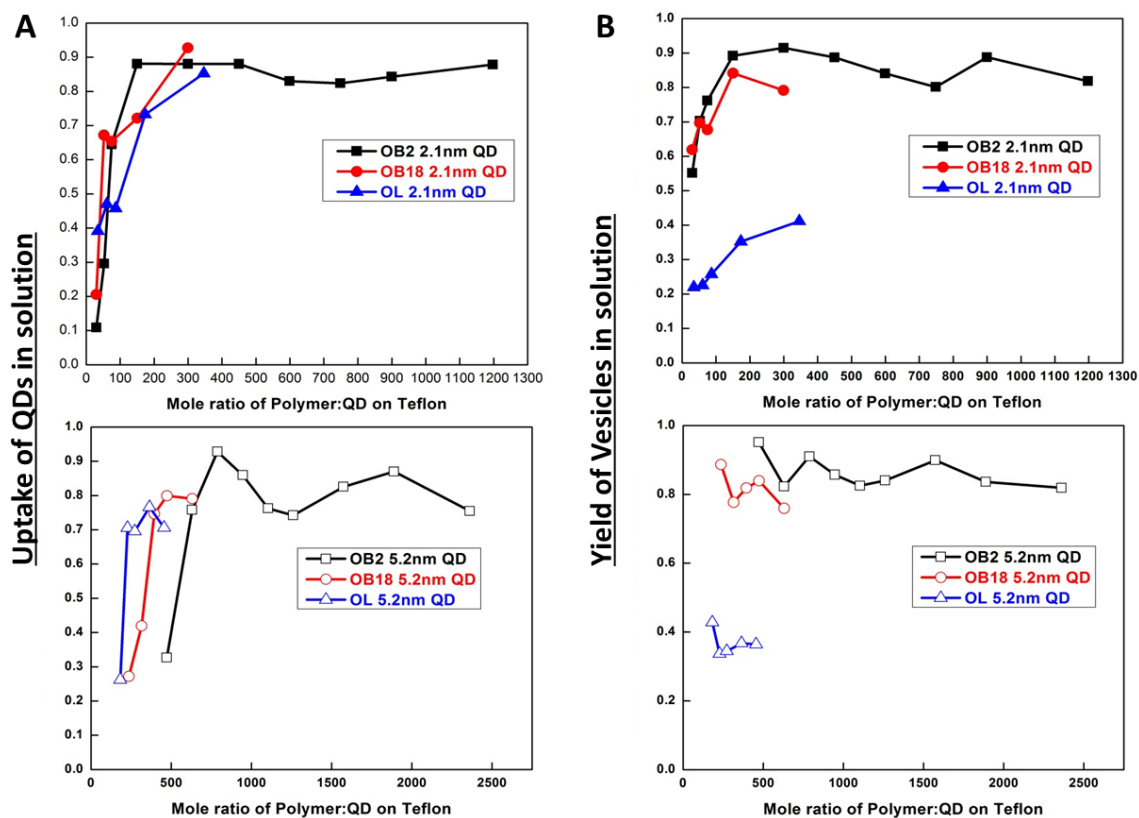Upon further quantitative examination, the solutions of CdSe/ZnS QD incorporated polymersomes were diluted, in order to obtain concentrations of QDs within the linear range of fluorescence detection (i.e. less than or equal to 0.05 absorbance units), and their fluorescence spectra were recorded (**Figure 5.13**). Spectrophotometer analysis of aqueous solutions of QD incorporated polymersomes verified strong fluorescence emission from large numbers of membrane-soluble nanoparticles, indicating excellent QD dispersion and light-harvesting characteristics. Nanoparticles manifest photophysical properties within the polymersomal matrix that are similar to those previously established in organic solvents. In addition, increasing QD concentrations augments the absorption oscillator strength and shifts the emission maximum progressively to longer wavelengths. By spectral comparison, emissive polymersomes formed from increasing QD concentrations showed marked decreases in their respective fluorescence signal intensities, when normalized by the total number of QDs per vesicle. The reduced photoluminescence intensity per QD and bathochromic shift of photoluminescence band with increasing QD concentration both indicate aggregation of QDs. Nanoparticle aggregation results in attenuated fluorescence due to self-absorption and augmentation of non-radiative decay channels, therefore both segregation of the nanoparticle and control of their microenvironment are imperative.

In order to explore the relative distribution of 2.1 nm and 5.2 nm CdSe/ZnS QDs within the polymersome membrane, we compared concentration-dependent fluorescence emission of each QD when loaded within vesicles of different membrane core-thicknesses. By increasing membrane thickness, the relative fluorescence emission of both 2.1 nm CdSe/ZnS nanoparticles and 5.2 nm CdSe/ZnS nanoparticles displayed a

linear increase in relative fluorescence signal intensity at identical fluorophore membrane concentrations (**Figure 5.13**), indicating a change in the relative distribution of the QD fluorophore when incorporated in the thicker polymersome membrane. In addition, this increase in the relative emission per molecule was more pronounced in the case of 5.2 nm CdSe/ZnS QDs relative to 2.1 nm CdSe/ZnS QDs (**Figure 5.14**) and indicates that the larger QDs experience, as expected, a greater number of aggregation effect, resulting in loss of fluorescence emission. These results suggest that the diminished QD emissive output with increasing vesicle membrane-loading derives mainly from the QDs emission quenching dominated by loading-dependent aggregation.
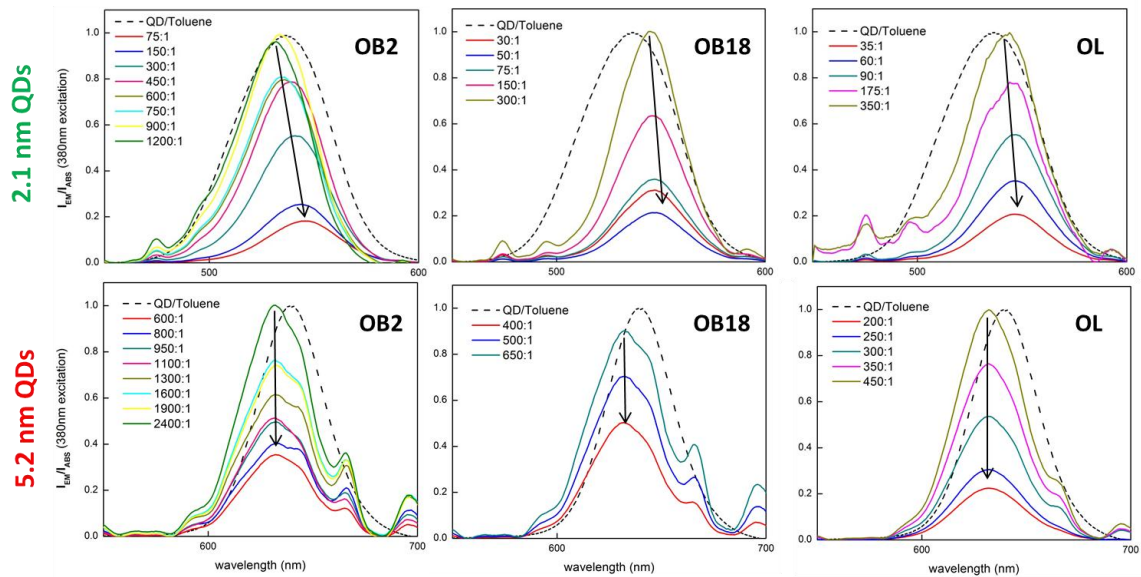
Figure 5.13 Fluorescence spectra of CdSe/ZnS QD incorporated polymersomes dependent on the molar ratios of polymer:QDs constituting the vesicles' membranes. Spectra were normalized by QD concentration and plotted on a relative scale of emission intensity.
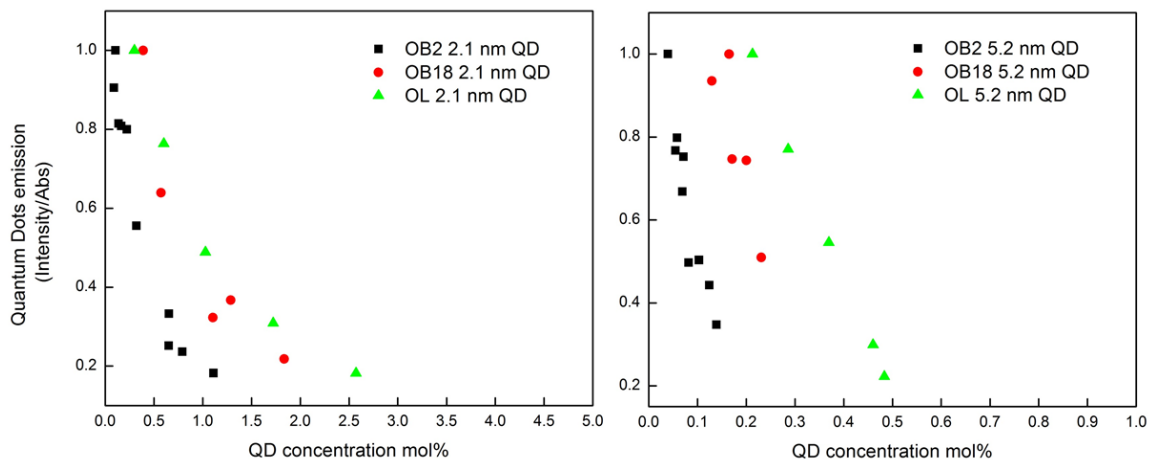
Figure 5.14 Comparison of relative fluorescence signal intensity per CdSe/ZnS QD in aqueous polymersome suspensions as a function of membrane mol% loading (experimental conditions: T = 23 °C, DI water).

5.5. Conclusions

In this chapter, we report an interesting observation of wide-ranging potential for cellular imaging and manipulation by readily disperse aqueous-insoluble nanoparticles at high solution concentrations via membrane incorporation within aqueous vesicle suspensions. The hydrophobic shell of diblock copolymer vesicles was successfully loaded with highly fluorescent QDs and gold nanoparticles as hydrophobic model substrates, which suggests that polymersome incorporation is an effective way to make nanoparticles water-soluable and biocompatible. The combination of independent methods of characterization by fluorescence microscopy imaging and Cryogenic TEM both confirmed that the hydrophobic substrates were enclosed inside the hydrophobic vesicle shell. Further experiments with differently sized nanoparticles and different diblock copolymers determined the limits for particle enclosing inside the vesicle shell, revealing how far the double-layer can curve before different structural assemblies are favored. Moreover, we described the fabrication and controlled quantitative loading of CdSe/ZnS QDs to the polymersomes membranes, and outlined a basic protocol for determining loading-dependent effect of different sized nanoparticles when confined into the synthetic vesicle membranes. Compared to other systems, they simultaneously provide efficient fluorescence, a great reduction in photobleaching and the augment of QDs colloidal stability with tunable size and switchable physical properties. These results indicate that vesicle-encapsulated QDs fulfill the promise of generating novel intracellular fluorescent probes to revolutionize bioimaging of living cells and tissues both *in vitro* and *in vivo*.

5.6. Acknowledgements

5.7. References

1. Sukhorukov, G. B.; Rogach, A. L.; Zebli, B.; Liedl, T.; Skirtach, A. G.; Köhler, K.; Antipov, A. A.; Gaponik, N.; Susha, A. S.; Winterhalter, M.; Parak, W. J. *Small* **2005,** 1, 194-200.

2. Discher, D. E.; Eisenberg, A. *Science* **2002,** 297, 967-973.

3. Antonietti, M.; Förster, S. *Advanced Materials* **2003,** 15, 1323-1333.

4. Mecke, A.; Dittrich, C.; Meier, W. *Soft Matter* **2006,** 2, 751-759.

5. Barenholz, Y. *Current Opinion in Colloid & Interface Science* **2001,** 6, 66-77.

6. Arruebo, M.; Fernandez-Pacheco, R.; Ibarra, M. R.; Santamaria, J. *Nano Today* **2007,** 2, 22-32.

7. Kim, J.; Piao, Y.; Hyeon, T. *Chemical Society Reviews* **2009,** 38, 372-390.

8. Gao, X.; Cui, Y.; Levenson, R. M.; Chung, L. W. K.; Nie, S. *Nat Biotech* **2004,** 22, 969-976.

9. Faure, C.; Derrie, A.; Neri, W. *The Journal of Physical Chemistry B* **2003,** 107, 4738-4746.

10. Korgel, B. A.; Monbouquette, H. G. *The Journal of Physical Chemistry* **1996,** 100, 346-351.

11. Koetz, J.; Jagielski, N.; Kosmella, S.; Friedrich, A.; Kleinpeter, E. *Colloids and Surfaces A: Physicochemical and Engineering Aspects* **2006,** 288, 36-43.

12. El Rassy, H.; Belamie, E.; Livage, J.; Coradin, T. *Langmuir* **2005,** 21, 8584-8587.

13. Jang, H.; Pell, L. E.; Korgel, B. A.; English, D. S. *Journal of Photochemistry and Photobiology A: Chemistry* **2003,** 158, 111-117.

14. Yaacob, I. I.; Nunes, A. C.; Bose, A. *Journal of Colloid and Interface Science* **1995,** 171, 73-84.

15. Kim, D.-W.; Oh, S.-G.; Yi, S.-C.; Bae, S.-Y.; Moon, S.-K. *Chemistry of Materials* **2000,** 12, 996-1002.

16. Ai, H.; Flask, C.; Weinberg, B.; Shuai, X. T.; Pagel, M. D.; Farrell, D.; Duerk, J.; Gao, J. *Advanced Materials* **2005,** 17, 1949-1952.

17. Berret, J.-F.; Schonbeck, N.; Gazeau, F.; El Kharrat, D.; Sandre, O.; Vacher, A.; Airiau, M. *Journal of the American Chemical Society* **2006,** 128, 1755-1761.

18. Kim, B.-S.; Qiu, J.-M.; Wang, J.-P.; Taton, T. A. *Nano Letters* **2005,** 5, 1987-1991.

19. Krack, M.; Hohenberg, H.; Kornowski, A.; Lindner, P.; Weller, H.; Forster, S. *Journal of the American Chemical Society* **2008,** 130, 7315-7320.

20. Zhu, J.; Hayward, R. C. *Journal of the American Chemical Society* **2008,** 130, 7496-7502.

21. Mueller, W.; Koynov, K.; Fischer, K.; Hartmann, S.; Pierrat, S.; Basche, T.; Maskos, M. *Macromolecules* **2008,** 42, 357-361.

22. Mai, Y.; Eisenberg, A. *Journal of the American Chemical Society* **2010,** 132, 10078-10084.

23. Hickey, R. J.; Haynes, A. S.; Kikkawa, J. M.; Park, S.-J. *Journal of the American Chemical Society* **2011,** 133, 1517-1525.

24. Binder, W. H.; Sachsenhofer, R.; Farnik, D.; Blaas, D. *Physical Chemistry Chemical Physics* **2007,** 9, 6435-6441.

25. Sachsenhofer, R.; Binder, W. H.; Farnik, D.; Zirbs, R. In *Polymersome Embedded Nanoparticles*, 2007; Wiley Online Library: 2007; pp 375-377.

26. Alivisatos, A. P. *Science* **1996,** 271, 933-937.

27. Hines, M. A.; Guyot-Sionnest, P. *The Journal of Physical Chemistry* **1996,** 100, 468-471.

28. Murray, C. B.; Norris, D. J.; Bawendi, M. G. *Journal of the American Chemical Society* **1993,** 115, 8706-8715.

29. Chan, W. C. W.; Maxwell, D. J.; Gao, X.; Bailey, R. E.; Han, M.; Nie, S. *Current Opinion in Biotechnology* **2002,** 13, 40-46.

30. Chang, C. W.; Sud, D.; Mycek, M. A. *Methods in cell biology* **2007,** 81, 495-524.

31. Chang, Y. P.; Pinaud, F.; Antelman, J.; Weiss, S. *Journal of biophotonics* **2008,** 1, 287-298.

32. Aldana, J.; Wang, Y. A.; Peng, X. *Journal of the American Chemical Society* **2001,** 123, 8844-8850.

33. Derfus, A. M.; Chan, W. C. W.; Bhatia, S. N. *Nano Letters* **2003,** 4, 11-18.

34. Zhang, L.; Hong, L.; Yu, Y.; Bae, S. C.; Granick, S. *Journal of the American Chemical Society* **2006,** 128, 9026-9027.

35. Zhang, L.; Granick, S. *Nano Letters* **2006,** 6, 694-698.

36. Gopalakrishnan, G.; Danelon, C.; Izewska, P.; Prummer, M.; Bolinger, P.-Y.; Geissbühler, I.; Demurtas, D.; Dubochet, J.; Vogel, H. *Angewandte Chemie International Edition* **2006,** 45, 5478-5483.

37. Haryono, A.; Binder, W. H. *Small* **2006,** 2, 600-611.

38. Sackmann, E. *FEBS Letters* **1994,** 346, 3-16.

39. Lipowsky, R.; Dobereiner, H. G. *EPL (Europhysics Letters)* **1998,** 43, 219.

40. Noguchi, H.; Takasu, M. *Biophysical journal* **2002,** 83, 299-308.

41. Ghoroghchian, P. P.; Lin, J. J.; Brannan, A. K.; Frail, P. R.; Bates, F. S.; Therien, M. J.; Hammer, D. A. *Soft Matter* **2006,** 2, 973-980.

42. Chen, H.; Ruckenstein, E. *The Journal of Chemical Physics* **2009,** 131, 244904.

43. Hong, K.; Friend, D. S.; Glabe, C. G.; Papahadjopoulos, D. *Biochimica et Biophysica Acta (BBA)-Biomembranes* **1983,** 732, 320-323.

44. Paasonen, L.; Laaksonen, T.; Johans, C.; Yliperttula, M.; Kontturi, K.; Urtti, A. *Journal of Controlled Release* **2007,** 122, 86-93.

45. Wu, G.; Mikhailovsky, A.; Khant, H. A.; Fu, C.; Chiu, W.; Zasadzinski, J. A. *Journal of the American Chemical Society* **2008,** 130, 8175-8177.

CHAPTER 6. Major Results and Future Directions for the Development of NIR-Emissive Polymersomal Markers

6.1. Chapter 2: Synthesis, Characterization and Properties of Conjugated (Porphinato)zinc(II) Compounds Featuring Benzothiadiazole Spacer Units

6.1.1. Major Results

We synthesizied a class of quinoidal spacer conjugated (porphinato)zinc(II) **(PZn-(BTD-PZn)$_n$, (PZn)$_2$-(BTD-(PZn)$_2$)$_n$)** and **(BTD-(PZn)$_n$-BTD)** complexes that featuring conjugated BTD spacer with varying degrees of porphyrin conjugation. The performance of electronic and optical devices based on these conjugated species is optimized by reducing and tuning energy gaps between the highest occupied molecular orbital (HOMO) and the lowest unoccupied molecular orbital (LUMO). These compounds possess very high emission dipole strength with great enhancement of emission intensity and tremendous luminescence quantum yields (18% to 38% in THF, and 18%-49% in toluene) in the NIR region (700−1100 nm), make them extremely bright NIR emitters as electrooptic materials in a range of photonic applications, especially for optical imaging purpose after incorporation into polymersomes. The synthesis, optical spectroscopy, potentiometric studies, and electronic structural calculations are reported and show that the magnitudes of the potentiometric HOMO−LUMO gap (E_p) and quantum yields in conjugated organic materials can both be modulated.

6.1.2. Future Directions

- Study the solvent relaxtion pathways that augment excited-state polarization and cause an increasing of quantum yield in nonpolar solvent toluene than polar solvent THF.

- Incorporate these BTD conjugated porphyrins into polymersomal vesicles and engineering the optical properties of these emissive polymersomes.

6.1.3. Papers Related To This Chapter

Synthesis, Characterization and Properties of Conjugated (Porphinato)zinc(II) Compounds Featuring Benzothiadiazole Spacer Units

Wei Qi, Jaehong Park, Ian Stanton, Michael J. Therien. In prepration.

6.2. Chapter 3: Antibody Conjugated Near-Infrared Emissive Polymersomes for Active Targeting

6.2.1. Major Results

We have established targeted NIR-emissive polymersomal structures that emit over the 700-950 nm spectral domain. These nanoscale, NIR-emissive bilayered vesicles feature hundreds-to-thousands copies of a single member of a larger family of conjugated multi(porphyrin) structures engineered to possess high emission dipole strength. And the hydrophilic PEO terminus is functionalized with selected activated functional groups to enable conjugation to proteins and proteins. This is the first work that systematically studies the functionalization chemistries for direct antibody conjugation to polymersomes. Six different coupling procedures were developed and we evaluated all these method in terms of antibody conjugation degree and polymersomes recovery yield to find the

optimized universal method for antibody attachment. The surface functionality degree and antibody concentration effect is also studied for controlled antibody conjugation on surface of polymersomes.

Based on the functionalization techniques we developed for direct conjugation of antibody to polymersomes surface, we have created a universal method to make immunopolymersomes for tumor cell targeting and cell tracking. Two different tumor cells are studied. Anti-ErbB2 NIR emissive polymersomes is developed to enable efficient intracellular delivery for HER2 breast cancer cells targeting with these optical probes. And a few different NIR emissive immunopolymersomes are also prepared for detecting of prostate cancer cells. NIR imaging allows quantitative, repetitive, in vivo detection of fluorophore-laden cells, at centimeter tissue depths without disturbing cellular function. Flow cytometry and confocal microscopy results indicate that anti-ErbB2 immunopolymersome polymersome delivery to HER2 cells is concentration and time dependent, resulting in punctate intracellular localization. We observe significant uptake of NIR emissive polymersomes when conjugated to the peptide, with a lower detection limit of 5000 labeled cells. The extent of polymersome delivery is estimated to be $86,000 \pm 2,500$ vesicles/ cell with the uptake efficiency as high as 37%. Further, loading prostate cancer cells with different immunopolymersomes showed specific delivery of the immunopolymersomes to the tumor cells. Our studies will enable future in vivo tracking of labeled tumor cells by NIR fluorescence based imaging.

6.2.2. Future Directions

More studies on comparison of the coupling procedures and find the optimized antibody density on polymersomes surface for targeted cell binding:

- Polymer concentration (mM) effect on antibody coupling efficiency.

- Effect of chemical manipulation of antibody on its antigen binding activity.

- Efficiency of antibody-conjugated polymersomes (ACP) on target binding for different coupling procedures.

- Effect of Ab surface density on ACP on target binding.

    For Anti-ErbB2 polymersomes (AEP), there are a lot of further characterizations we need to carry out. And also we can load drugs such as DOX to these AEP for targeted delivery:

- Pharmacokinetics of AEP.

- Stability of AEP-dox *in Vivo*.

- Antitumor Efficacy of AEP-dox against HER2 Human Breast Cancer Xenografts.

- Toxicity of AEP-dox.

- Antitumor Efficacy of AEP-dox *versus* Combination Therapy.

6.2.3. Papers Related To This Chapter

Antibody Conjugated Near-Infrared Emissive Polymersomes for Active Targeting

Wei Qi, Diane Fels, Mark W. Dewhirst, Michael J. Therien. In prepration.

6.3. Chapter 4: Synthesis, Characterization, Polymersome Preparation, Morphology Assessment and Functionalization of Biodegradable Diblock Copolymers

6.3.1. Major Results

A series of FDA-approved, biodegradable PEO-*b*-PCL diblock copolymers varying in PEO block size (M_n: 750-5000), f_{PEO} (7.7%-33.3%), and M_n (3.6k-57k) were synthesized by ring-opening polymerization and anionic living polymerization. The PEO-*b*-PCL diblock copolymers were subsequently screened for the ability to assemble into nano-scale and meso-scale polymersomes morphologies by different preparation methods. We found that only PEO-*b*-PCL diblock copolymers possessing a PEO block size of 2k-3.8k, and f_{PEO} ranging from 11.8-18.8%, were found to assemble into meso-scale biodegradable polymersomes. And meso-scaled polymersomes were obtained uniquely in nearly quantitative yield from a PEO(2k)-*b*-PCL(12k) diblock copolymer (PDI:1.21). However, very interestingly, these diblock copolymer form nano-scale vesicle morphologies in nearly quantitative yield on a much broader range. The compositions that form none or very little meso-scale polymersomes could form ~100% nano-scale polymersomes, which implicts a various applications for this diblock copolymers as nano-sized dilvery vesicles.

To improve the mechanical properties of these highly crystalized polymersomes made from degradable PEO-*b*-PCL diblock polymers, we copolymerized with a flexible and elastic TMC to make PEO-*b*-PTMC diblock copolymers and PEO-*b*-P(CL-co-TMC) diblock tripolymers. The thermal properties of these polymers are studied by using both DSC and micropipette aspiration. Both experiments indicates that we formed a soft based

310

material by using this polymer blend. Althought these polymers have a low yield on forming meso-scaled vesicles, we expect they will show a similar trend on formation of nano-scaled polymersomes to PEO-*b*-PCL diblock copolymers, study on the ability of these polymers to self-assembly into nano-scaled vesicles is now undergoing.

We functionalized this biodegradable PEO-*b*-PCL diblock copolymer with reactive vinyl sulfone groups at the terminus of the corona-forming PEO block. These groups are capable of tethering high concentrations of a thiol-containing targeting peptide after self-assembly of vesicles in mild conditions. This is the first example of functionalized biodegrdable diblock copolymers, and this system should serve as a versatile platform for specific delivery of a variety of therapeutic payloads in a carrier capable of utilizing a wide range of targeting moieties.

6.3.2. Future Directions

1.   Study the ability of TMC-based diblock copolymer to self-assemble into nano-sized polymersomes.

2.   Use these vinyl sulfone functionalized biodegradable PEO-*b*-PCL polymers to prepare nano-scale polymersomes, and conjugate peptides to the surface of these biodegradable polymersomes while incorporating drugs in the aqueous inner core to achieve targeted drug delivery.

6.3.3. Papers Related To This Chapter

1. Nano- and Meso-Scale Polymersomes, Based on Biodegradable Poly(ethylene oxide)-block-Polycaprolactone (PEO-b-PCL) Copolymers

Wei Qi, Guizhi Li, Peter Ghoroghchian, Daniel A. Hammer, Michael J. Therien. In preparation.

2. Synthesis of Highly Elastic Biodegradable Polymersomes Featuring a Soft Segment of Trimethylene Carbonate (TMC)

Wei Qi, Guizhi Li, Michael J. Therien. In preparation.

3. Functionalized biodegradable polymersomes: a new approach to targeted drug delivery

Wei Qi, Ying Ma, Michael J. Therien. In preparation.

6.4. Chapter 5: Quantitative Membrane Loading of Quantum Dots into Polymersomes

6.4.1. Major Results

1. Successful incorporation of hydrophobic highly fluorescent quantum dots and gold nanoparticles into the bilayer membrane of both meso-scale and nano-scale polymer vesicles based on PEO-*b*-PBD and PEO-*b*-PCl diblock copolymers.

2. Interestingly, the mechanical properties of PEO-*b*-PCl polymersomes change with incorporated nanoparticle concentration and incorporated nanoparticle sizes.

3. Quantitative loading of quantum dots into nano-sized polymersomes is studied. The loading process shows very different trend compare to the porphyrin incorporation in polymersomes, which could be explained by our loading mechanism hypothesis. Together, these studies present a generalized paradigm for the generation of complex multi-functional materials that combine both highly emissive quantum dots and polymers through cooperative self-assembly.

6.4.2. Future Directions

- Study the interesting photoluminescent properties of the quantum dots after incorporation into polymersomes.

- Use these quantum dots incorporated polymersomes for cell imaging and compare them to porphyrin based emissive polymersomes.

- Incorporate up-converting nanoparticles in the bilayer membrane of polymersomes to make UV-degradable polymersomes for controlled drug releasing.

6.4.3. Papers Related To This Chapter

1. Nanoparticles Incorporation into nano- and meso-Scale Polymersomes

Wei Qi, Michael J. Therien. In preparation.

2. Quantitate loading of Quantum dots into Polymersomes

Wei Qi, Michael J. Therien. In preparation.